Molecular Studies in Mercury Toxicity Using X-ray Absorption Spectroscopy and High Energy Resolution Fluorescence Detection X-ray Absorption Spectroscopy

A Dissertation

Submitted to the College of Graduate and Postdoctoral Studies

In Partial Fulfillment of the Requirements

For the Degree of Doctor of Philosophy

In the Department of Geological Sciences

University of Saskatchewan

Saskatoon, SK, Canada

By

Susan Nehzati

PERMISSION TO USE

In presenting this dissertation in partial fulfilment of the requirements for a Postgraduate degree from the University of Saskatchewan, I agree that the Libraries of this University may make it freely available for inspection. I further agree that permission for copying of this dissertation in any manner, in whole or in part, for scholarly purposes may be granted by the professor or professors who supervised my dissertation work or, in their absence, by the Head of the Department or the Dean of the College in which my dissertation work was done. It is understood that any copying or publication or use of this dissertation or parts thereof for financial gain shall not be allowed without my written permission. It is also understood that due recognition shall be given to me and to the University of Saskatchewan in any scholarly use which may be made of any material in my dissertation.

DISCLAIMER

Reference in this dissertation to any specific commercial products, process, or service by trade name, trademark, manufacturer, or otherwise, does not constitute or imply its endorsement, recommendation, or favoring by the University of Saskatchewan. The views and opinions of the author expressed herein do not state or reflect those of the University of Saskatchewan, and shall not be used for advertising or product endorsement purposes.

Requests for permission to copy or to make other uses of material in this dissertation in whole or part should be addressed to:

Head of the Department of Geological Sciences
University of Saskatchewan
114 Science Place
Saskatoon, Saskatchewan, Canada S7N 5E2

OR

Dean
College of Graduate and Postdoctoral Studies
University of Saskatchewan
116 Thorvaldson Building, 110 Science Place
Saskatoon, Saskatchewan, Canada S7N 5C9

ABSTRACT

Molecular understanding of mercury compounds is of considerable interest as the element is pervasive in the environment and certain chemical forms are highly toxic to humans at very low doses. Chalcogenides have high affinity for mercury and one in particular, selenium, may play a major role in the mechanisms involved with mercury toxicity *in vivo*. In this dissertation, conventional X-ray absorption spectroscopy (XAS) and high-energy resolution fluorescence detection X-ray absorption spectroscopy (HERFD XAS) have been employed to identify the chemical coordination of mercury with various ligand types relevant to mercury toxicity. XAS and density functional theory (DFT) calculations were used to identify the molecular structures responsible for the drastic changes in toxicity in zebrafish larvae exposed to a common hypopigment-inducer 1-phenyl-2-thiourea. Next, XAS and X-ray fluorescence imaging (XFI) were used to investigate the fate of mercury localization in zebrafish larvae following treatment with the dithiol 1,3-benzene-diamido-2-carboxylethanethiol. During the course of exploring the molecular structure of various mercury-ligand complexes, it was evident that current methods to probe the electronic structure of mercury compounds are met with challenges, and capabilities to observe richer spectroscopy would significantly benefit molecular studies of mercury toxicity. Hence, the quest to develop methods for enhanced chemical characterization using HERFD XAS was pursued to reveal the potential of increased chemical specificity and improved concentration sensitivity of this technique in natural relevant levels of a series of mercury and selenium compounds. The results present substantial improvements in chemical characterization of mercury and selenium compounds for applications in the study of mercury toxicity. HERFD XAS was thereupon employed as a complementary tool to conventional XAS in the investigations of species identification of mercury and selenium compounds in cases of biological organisms. XAS, HERFD XAS, and quantum-mechanical/molecular-mechanical (QM/MM) studies were employed to examine the interaction of Hg(II) with 1-methylthymine and a canonical DNA helix to understand this mode of biological coordination of Hg(II). Finally, mammalian tissue is examined to reveal unreported chemical species in a historical specimen showing signs of organomercury poisoning from Minamata Bay, Japan.

ACKNOWLEDGMENTS

I would like to thank my advisors, Dr. Graham George and Dr. Ingrid Pickering for their guidance and support throughout this journey. For their contributions to my growth as an academic researcher, I will be forever grateful. To my committee members, Dr. Jonathan Dimmock, Dr. Lee Wilson, and Dr. Derek Peak for their thoughtful inquiry and inspiration. To Dr. Erik Nelson for sponsoring me as an Exchange Scholar at the Stanford Synchrotron Radiation Lightsource (SSRL) – without which I would not have been able to carry out much of my research. Thank you to the overwhelmingly supportive staff of SSRL – Dr. Cynthia Patty, Dr. Matthew Latimer, Dr. Dimosthenis Sokaras, Dr. Thomas Kroll, and Dr. Sam Webb. To Dr. Mariam Alaverdashvili, Dr. Julien Cotelesage, Dr. Natasha Dolgova, Marlon Forsberg, Dr. Mark Hackett, Ashley James, Dr. Tracy MacDonald, and Dr. Jake Pushie for their technical coaching, comedy, wisdom and encouragement along the way.

Acknowledgements for work conducted at national research facilities are detailed in individual chapters (Stanford Synchrotron Radiation Lightsource, Chapters 5, 6, 7, 8, 9, 10; Advanced Photon Source, Chapter 5).

I would also like to acknowledge the funding support which has allowed me to carry out this research – the Dr. Rui Feng Scholarship, Natural Sciences and Engineering Research Council of Canada (NSERC), Canadian Institutes of Health Research (CIHR), and CIHR – Training in Health Research Using Synchrotron Techniques (CIHR–THRUST).

This dissertation is dedicated to my family – my father who has encouraged me to explore; my mother who has given me my strength; my brother for his love and support.

TABLE OF CONTENTS

LIST OF TABLES

LIST OF FIGURES

LIST OF ABBREVIATIONS

µg	microgram
µL	microliter
µm	micrometer
µM	micromolar
µ-XAS	micro X-ray absorption spectroscopy
AB9	1,3-benzene-diamido-2-carboxylethanethiol
Ag	silver
ALA	α-lipoic acid
ANOVA	analysis of variance
APS	Argonne Photon Source
As_2O_3	arsenic oxide
a.u.	atomic unit
B9	1,3-benzenediamidoethanethiol
BAL	2,3-dimercapto propanol
BBB	blood brain barrier
BDET	1,3-benzenediamidoethanethiol
BN	boron nitride
br	brain
Br	bromine
°C	degrees Celsius
C	carbon
Cd	cadmium
CGPS	College of Graduate and Postdoctoral Studies
CH_3HgCl	methylmercury chloride
CH_3HgOH	methylmercury hydroxide
$(CH_3Hg)_2Se$	dimethylmercury selenide
Cl^-	chloride ion
cm	centimeter
CN^-	cyanide ion
COSMO	conductor-like screening model
CSD	Cambridge Structural Database
Cu	copper
Cys	cysteine
DFT	density functional theory
DHLA	dihydrolipoic acid
DI	deionized water
DMPS	2,3-dimercapto-l-propanesulfonic acid
DMSA	2,3-dimercaptosuccinic acid
DMSO	dimethyl sulfoxide
DNA	deoxyribonucleic acid
dpf	days post fertilization
DOE	Department of Energy
eV	electron volt

EtOH	ethanol
EXAFS	extended X-ray absorption fine structure
Fe	iron
G	guanosine
Ga_2O_3	gallium oxide
Ge	germanium
GeV	giga electron volt
GSH	glutathione
gt	gut tube
GUI	graphical user interface
h	Planck's constant
h	hour
H&E	haematoxylin and eosin stain
H_2O	water
HERFD	high energy resolution fluorescence detection
HF	Hartree and Fock
Hg	mercury
Hg^{2+}	divalent mercury ion
Hg^{II}	divalent mercury ion
$HgCl_2$	mercuric chloride
$Hg(NO_3)_2$	mercuric nitrate
HgO	mercuric oxide
$Hg(OAc)_2$	mercuric acetate
HgS	mercuric sulfide
$HgSO_4$	mercuric suflate
HgSe	mercuric selenide
HIV	human immunodeficiency virus
hpf	hours post fertilization
HXN	hard X-ray nanoprobe
IR	infrared
K	Kelvin
K-B	Kirkpatrick-Baez
keV	kilo electron volt
kg	kilogram
kJ	kilojoule
LAT	large amino acid transporter
LC_{50}	lethal concentration killing
LN_2	liquid nitrogen
LOAEL	lowest observed adverse effect level
lv	liver
mA	milliamp
MCA	multi channel analyzer
MeHg	methylmercury
MeOH	methanol
mL	milliliter
mm	millimeter

mmol	millimolar
mM	millimolar
mo	medulla oblongata
Mol	mole
ms	millisecond
N	nitrogen
NaOH	sodium hydroxide
N_2	nitrogen gas
ng	nanogram
NMR	nuclear magnetic resonance
NSLS	National Synchrotron Light Source
O	oxygen
oe	olfactory epithelium
Pb	lead
PBS	phosphate buffer saline
PBST	phosphate buffer saline with Tween
pd	pronephric duct
PFA	paraformaldehyde
ppb	parts per billion
ppm	parts per million
PTU	phenylthiourea
QM/MM	quantum mechanic/molecular mechanic
RANOVA	repeated measures of analysis of variance
Rh	rhodium
RIXS	resonant inelastic X-ray scattering
ROI	region of interest
S	sulfur
Se	selenium
SeMet	selenomethionine
Si	silicon
SLAC	Stanford Linear Accelerator Center
sm	somatic muscle
Sn	tin
SSRL	Stanford Synchrotron Radiation Lightsource
SSSC	Saskatchewan Structural Sciences Centre
Std dev	standard deviation
mT	1-methylthymine
UV	ultra violet
v/v	volume/volume
XAS	X-ray absorption spectroscopy
XFI	X-ray fluorescence imaging
XRD	X-ray diffraction
yl	yolk
Zn	zinc

CHAPTER 1. Introduction

Mercury (Hg) compounds are some of the most powerful toxins humans are exposed to on Earth (Korbas et al., 2012). Historically mercury has had many uses in medicine, art, ceremonial practices, and industrial processes. The wealth of research on the toxic effects of mercury compounds, as well as the numerous mass poisoning events that have occurred (Takeuchi et al., 1962; Bakir et al., 1973) have decreased its utility as it is now evident that the risks associated with some mercury compounds far outweigh the benefits. Global agencies and over 100 country parties have agreed to concerted objectives in recent years to encourage the reduction in the accumulation of mercury in the environment from anthropogenic sources, restrict the use of mercury compounds and lower the exposure of mercury compounds to humans (Selin, 2014; Minamata Convention on Mercury, 2019). The Minamata Convention on Mercury ratified in 2014 outlines reduction efforts which include, yet are not limited to, an embargo on the manufacturing, import and export of consumer goods containing mercury, the reduction of mercury use in gold mining, as well as managing the mercury emission from industries (Minamata Convention on Mercury, 2019).

Mercury is pervasive in the environment and certainly a major concern to human health. Mercury is maintained in the environment through a biogeochemical cycle involving both natural and anthropogenic activities (Selin, 2009). Natural sources contributing to the global cycling of mercury include volcanic activity and forest fires (Morel et al., 1998). Anthropogenic sources of mercury include artisanal gold mining, burning of fossil fuels, chlor-alkali plants, incinerators, pulp industries, and waste handling (Selin, 2009; Morel et al., 1998). Mercury has also been used in the manufacturing of products such as dental amalgams, fluorescent lamps, switches, and thermometers (Selin, 2014). The biogeochemical cycle of mercury circulates mercury in air, water, soil, and organisms, with varying amounts of differing chemical forms (Selin, 2009). The atmosphere predominantly holds elemental mercury, and water systems and soil contain mostly inorganic and organic forms of mercury (Selin, 2009). Organic forms of mercury readily bioaccumulate and biomagnify up the food web depending on the bioavailability, chemical species, lipid solubility, and relative abundance of organisms (Morel et al., 1998). Bioaccumulation of organomercury compounds start from alkyl mercury accumulation in plankton which is then consumed by predators up the food web so that animals along the trophic web (*ie*. larger animals) will have more accumulated organomercury compounds (Morel et al., 1998).

Common sources of mercury exposure to humans today are through the consumption of contaminated fish, use of dental amalgams, and nominally through the administration of vaccines (Clarkson et al., 2003). The damaging toxic effects from excess mercury exposure (Clarkson et al., 2003; Magos and Clarkson, 2006; Guzzi and La Porta, 2008) underscores the importance of increasing the body of knowledge with regard to treatments in accidental exposures and occupational hazards to mercury. Chalcogenides have long been known to have high affinity for mercury and it is becoming increasingly apparent that the toxicity of mercury is intimately connected to the biochemistry of selenium *in vivo* (Beijer and Jernelöv, 1978; Ralston et al., 2007; MacDonald et al., 2015a). The ongoing investigations were designed to accumulate concepts for improving the therapeutics in cases of mercury poisoning, as well as exploring methodologies to better analyze this highly potent toxicant.

1.1 Mercury Toxicity

The well-documented outbreak of methylmercury poisoning which occurred in Minamata Bay, Japan in the 1950s, later evolved into the naming of Minamata disease, a neurological disorder associated with severe methylmercury poisoning (Kurland et al., 1960). As a result of the release of methylmercury from nearby factory effluent into Minamata Bay, residents in the local communities consuming fish and shellfish from the bay experienced a broad range of neurological symptoms from paresthesia and ataxia, and in extreme cases resulting in death (Kurland et al., 1960). The toxicological profile of mercury is heavily dependent on the chemical form and route of exposure (Korbas et al., 2012). Often symptoms arise after a latency period and organic mercury compounds usually exhibit the more serious toxic effects (Clarkson et al., 2003). Target organs in humans are commonly the kidney and brain with pathological symptoms including ataxia, loss of vision and hearing, proteinuria, tremors, tubular necrosis, and in extreme cases, death (Clarkson et al., 2003). The developing fetus is also a major vulnerable subject to mercury exposure as certain mercury compounds are capable of crossing the placental barrier (Rooney, 2007). As with other divalent metal ions, mercuric ions have also shown to react with DNA. Hg(II) binds strongly to nucleobases in between the two helices and has the highest relative affinity among other divalent ions (Eichhorn and Shin, 1968). Organomercurial binding to DNA has also been extensively studied, identifying the binding of $CH_3Hg(II)$ to the endocyclic N and C atoms of nucleobases as possible mechanisms of mutagenicity (Onyido et al., 2004).

1.1.1 Elemental Mercury

Elemental mercury is a naturally occurring metal released from volcanic eruptions and the erosion of rock ores containing mercury (Selin, 2009). Elemental mercury is a metallic liquid at room temperature and highly volatile (Gonzalez-Raymat et al., 2017). Mercury vapour can be transported to the most remote regions of the arctic due to global cycling (Mason et al., 2005) making it a truly global issue. Anthropogenic sources include the burning of fossil fuels, incinerators, dental amalgams, and a number of industrial applications (Guzzi and La Porta, 2008). The two major sources of human exposure are through occupational hazards and dental amalgam use, the latter of which has no known reports of toxic cases (Aposhian et al., 2003). Ingestion of Hg^0 in liquid form is not readily absorbed by the gastrointestinal tract and dermal absorption is limited. However, exposure to the vapour form is well absorbed by the lungs (Cantor, 1951; Gochfield, 2003; Clarkson and Magos, 2006). Hg^0 as an uncharged monoatomic gas is highly lipophilic which may cross cell membranes including the blood brain barrier (BBB) and placental barrier (Rooney 2007). Catalase-mediated oxidation to Hg^{2+} occurs in cells throughout the body which lowers the lipophilicity so that the cation is trapped in the site of oxidation which can determine the final body deposition (Magos et al., 1977). A study by Hursh et al. (1976) found about 74% of mercury was retained in the body following a single inhaled dose of mercury vapour. Toxic effects from acute exposure include dyspnoea, chest pain, nausea, vomiting, and in severe cases death (Magos and Clarkson, 2006). Chronic exposures show symptoms of tremors, psychological symptoms and proteinurea (Clarkson et al., 2003).

1.1.2 Inorganic Mercury

Risks of elevated inorganic mercury exposure is mostly associated through occupational exposures. Bodily distribution of Hg^{2+} is not well understood. Absorption and distribution following oral ingestion of inorganic mercury salts varies depending on the compound. Reports have shown $Hg(NO_3)_2$, $HgCl_2$, and $HgSO_4$ all to produce symptoms of anuria following acute exposure (Magos and Clarkson, 2006). Most of the ingested inorganic mercury is excreted in urine or retained by the kidneys however the exact mechanisms of renal toxicity are unknown (Magos and Clarkson, 2006). Inorganic mercury exposure can induce metallothionein synthesis which are a group of cysteine-rich, metal-binding proteins that can stimulate mercury accumulation in kidney

tubules (Tanaka-Kagawa et al., 1993). Inorganic forms of mercury are unable to cross the BBB (Rooney, 2007). Other symptoms of elevated inorganic mercury exposure following oral ingestion include stomatitis and gastroenteritis (Magos and Clarkson, 2006). Exposure through dermal contact can cause acrodynia and blistering and occupational exposure has been linked to lung damage in workers (Magos and Clarkson, 2006).

1.1.3 Organic Mercury

Methyl- and ethylmercury are the most toxic organic mercury compounds humans are exposed to which cause harmful toxic effects. Methylmercury exposure is usually with the ingestion of contaminated fish (Gochfield, 2003). Ethylmercury exposure is usually from vaccines containing Thiomersal, an organomercury compound with fungicidal properties (Aschner and Ceccatelli, 2010). These organomercurials can cross the BBB and placental barrier (Rooney, 2007), affecting both the central nervous system and the developing fetus which can promote permanent developmental damage. Methylmercury is mostly present in the body attached to thiol groups in amino acids, peptides, and proteins and circulates through the enterohepatic cycle (Gochfield, 2003). The mechanism of methylmercury demethylation into inorganic mercury by microflora has been reported to occur in the intestine yet the mechanism is currently unknown (Clarkson et al., 2007). Furthermore, inorganic mercury is poorly absorbed by the intestines, therefore most of the transformed mercury will be eliminated in feces (Clarkson and Magos, 2006). Methylmercury complexed with L-cysteine is thought to absorb from the intestines via large neutral amino acid carriers (Leaner and Mason, 2002). Once in the bloodstream methylmercury complexes are distributed to different organ systems of the body. A similar methylmercury-cysteine complex is hypothesized for transport into endothelial cells of the BBB as studies have found the transport of methylmercury-cysteine complexes across the membrane was competitively inhibited with large neutral amino acids (Kerper et al., 1992; Simmons-Willis et al., 2003). The liver was found to circulate methylmercury into bile complexed with reduced glutathione via glutathione carriers (Ballatori and Truong, 1995). This complex is then broken down to the methylmercury-cysteine complex which can be reabsorbed into the bloodstream via the gallbladder or re-enter the intestines (Clarkson et al., 2007). Symptoms of elevated exposure to organomercurials can cause mental impairments such as paraethesia and ataxia, as well as

disturbances in speech, sight, and auditory function, with severe cases of mercury loading causing death (Clarkson et al., 2003).

1.2 Minimizing of Mercury Exposure in Biological Organisms

Mercury exposure is a global issue. Reduction of anthropogenic sources of mercury is one way to help minimize mercury exposure in humans and possibly reduce the occurrence of negative health effects. Emissions from fossil fuel burning are the largest source of mercury into the atmosphere (Pirrone et al., 2010). Steps to eliminate the use of burning fossil fuels and instead harness the utility of renewable energy sources such as sunlight, wind, and geothermal heat would greatly reduce anthropogenic sources. While total elimination is unrealistic, striving to lessen the human exposure is essential. Mercury scrubbers in power plant flue gas in an attempt to reduce mercury emissions could be an alternative line of protection. Chemical forms of mercury in coal-fired flue-gas are either elemental Hg^0 or oxidized $HgCl_2$ with chemical fractions dependent on the coal type and combustion efficiency (Gale et al., 2008). Capabilities to isolate and remove mercury from flue gas are available. Investigations into wet scrubbers using a desulfurization slurry showed effective removal of Hg(II) from the flue gas, while elemental Hg^0 required an extra step of oxidation via halogens such as sodium chlorite (Krzyżyńska et al., 2018). In addition, innovative sorbent materials can aid in highly effective mercury traps for environmental remediation efforts in aqueous systems. Li et al. (2014) developed a nano-trap comprising of a highly-porous thiol-based polymer for a record-high saturation of mercury uptake, and effectively lowered the Hg(II) levels in aqueous systems from 10 ppm to as low as 0.4 ppb. The aforementioned lines of protection depend highly on economic resources which limit actions that would be appropriate for the decrease in anthropogenic sources of mercury. Therefore there is a fundamental need in the continued research into the mechanisms by which different chemical forms of mercury may exert their individual toxic effects for the development of effective therapy options and remediation arrangements to be achieved.

The course of sequestering mercury is complicated due to its varied toxicological profiles depending on the route of exposure, chemical form, and rate of exposure. The rate or amount of exposure will not be discussed in this dissertation, but the targets of mercury compounds do play a critical role in its toxicological outcome and will be broadly discussed. This is a direct result of the chemical form in question which would suggest the treatments designed to sequester mercury

may require site specific targeting. Furthermore, speciation plays a significant role in the fate of cellular mercury accumulation (Korbas et al., 2012). With the development of more sensitive techniques, the ability to investigate individual site specific chemical information will only improve the body of knowledge that can be gained from targeting the root of the problem. As technologies improve, researchers are better equipped to understand the results observed so that the more direct the investigation, the less need for interpretation of observations.

Chelators are multidentate ligands, which form stable ring complexes and are the typical model for mercury sequestrating agents. Ideal chelators would achieve strong, irreversible, and conservative binding to a target metal ion. In addition, further criteria for an ideal chelator include high specificity and affinity, safe delivery to target organs and excretion, as well as inherent drug nontoxicity. With respect to mercury, most therapeutics involve organic dithiols (Fu et al., 2011). To date the most prescribed treatment for mercury poisoning is *meso*-2,3-dimercaptosuccinic acid (DMSA), however a few other dithiol candidates have shown promise (Figure 1.1) (Rooney, 2007). Treatments to acute exposure of excess mercury compounds work best when administered soon after exposure to avoid accumulation in target organs. Removal of mercury from the body in chronic cases is met with more challenges since once mercury reaches the target organ it attaches to local tissues making the transportation and elimination very difficult. A number of dithiol compounds have been developed and are prescribed for the treatment of heavy metal poisoning but studies have shown they may not be specific to mercury (Fu et al., 2011; Packer et al., 1995). *meso*-DMSA is the leading treatment for mercury poisoning; however experiments have shown that *meso*-DMSA does not form true chelate complexes with inorganic Hg(II), instead at a 1:1 Hg:chelator ratio, a binuclear ring complex is predicted (George et al., 2004). Researchers predicted the angle between the vicinal dithiols was too restrictive to accommodate a mercury ion, as well as maintaining the close-to-linear structure observed in the vast majority of two-coordinate Hg compounds (George et al., 2004).

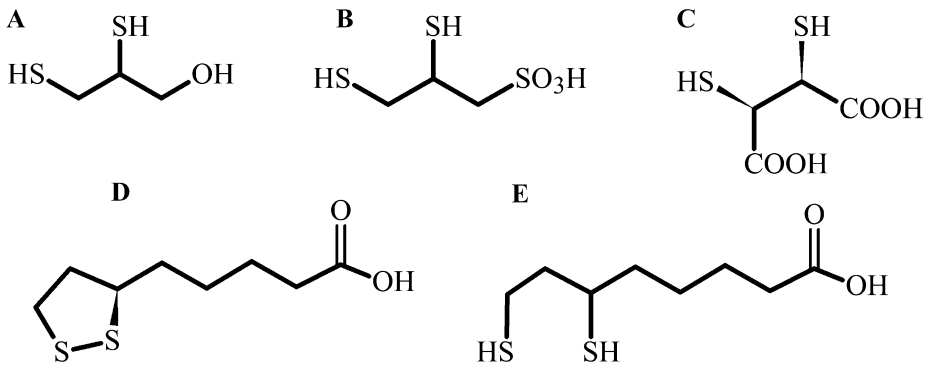

Figure 1.1. Structure of dithiol candidates for metal chelation. **A**: 2,3-dimercaptopropanol (BAL); **B**: 2,3-dimercapto-1-propanesulfonic acid (DMPS); **C**: *meso*-2,3-dimercaptosuccinic acid (*meso*-DMSA); **D**: α-lipoic acid (ALA); **E**: dihydrolipoic acid (DHLA).

Furthermore, *meso*-DMSA has been shown to chelate essential minerals like copper and zinc in the body (Rooney, 2007) and therefore the potential of harmful effects from competition subjugates the original intent of chelators and may jeopardize homeostasis. These dithiols (Figure 1.1) provide a structural foundation for mercury treatment agents, however their results are suboptimal in cases of mercury poisoning (Rooney, 2007; George et al., 2004).

1.3 Selenium

Selenium (Se) is an essential element with a narrow threshold of safety (Roman et al., 2014). As a Group VIA element and with other chalcogenides, it has high affinity for mercury compounds, approximately a million times greater than sulfur (Dyrssen and Wedborg, 1991). Selenium is present in L-selenocysteine, the 21st essential amino acid, and plays critical roles in enzymatic protection from oxidative damage in cells. The chemical properties of selenium are similar to sulfur (Reich and Hondal, 2016).

1.3.1 Selenium Sources

Selenium is a natural trace element, essential to animal life (Roman et al., 2014). In the earth's crust, $[Se]^{2-}$ is the most common state and is released from rocks through water-rock interactions (Torres et al., 2011). The world mean average of selenium in soil is 0.4 mg kg^{-1} (Sharma et al., 2015). Anthropogenic activity can accelerate the mobilization of selenium through mining, agriculture, petrochemical, and industrial processes (Torres et al., 2011). Due to bioaccumulation, selenium is also considered a major contaminant in aquatic ecosystems, however this is dependent on the concentration of chemical species (Santos et al., 2015). Plants accumulate selenium from soil and the concentration is highly dependent on the inherent accumulative abilities, as well as geoavailability relating to the physicochemical conditions of the surrounding soil such as pH, redox conditions, salinity, and organic matter (Roman et al., 2014). Once taken up, plants are able to biotransform selenium to organo-selenium compounds (Schiavon and Pilon-Smits, 2017). Selenium intake for humans is largely from diet with a minimum recommended daily intake of ~20 µg for adults before the onset of Keshan disease, a cardiomyopathy disease treated with selenium supplementation (Roman et al., 2014). The recommended daily intake of ~50 µg is

suggested for maintenance of normal functions and it is estimated one billion people are deficient in selenium (Schiavon and Pilon-Smits, 2017; Lyons et al., 2003).

1.3.2 Selenium Biochemistry

To date, only a small fraction of the twenty-five identified classes of selenium proteins have been functionally characterized in the human proteome (Roman et al., 2014). Selenium is a key component to several important processes such as redox regulation with glutathione peroxidase and thioredoxin reductase (Roman et al., 2014). Further processes include regulation of apoptosis, immunomodulation, regulation of thyroid hormones, and protein folding and degrading of misfolded proteins in the endoplasmic reticulum (Roman et al., 2014; Rayman, 2012). Absorption of selenium compounds in humans mainly occurs in the small intestine and most selenium compounds are readily absorbed to 70-90% completion for both inorganic and organic forms (Roman et al., 2014). Selenite is an exception with < 60% absorption (Roman et al., 2014). Once absorbed, selenium species are transported to the liver for selenium metabolism which include the synthesis of most selenoproteins and regulation of selenium metabolite excretion (Roman et al., 2014). Excreted selenium takes the form of methylated products which include dimethyl selenide, and the trimethyl selenide cation (Kuehnelt et al., 2007).

In higher plants, selenium is considered a beneficial element for normal growth and stress resistance (Schiavon and Pilon-Smits, 2016). Selenium supplements have shown to benefit the growth of many plant species (Lyons et al., 2003; Pilon-Smits et al., 2009). As well, low doses of selenium supplementation have protected plants from environmental stresses including UV light, heavy metal stress, and pathogens (Schiavon and Pilon-Smits, 2016). Soils with exceedingly high levels of selenate or selenite contaminate the agricultural and industrial wastewaters. The Kesterson National Wildlife Rescue in California had a reservoir in the late 20th century that resulted in the death and deformity of fish and migratory birds due to high selenium accumulation (Ohlendorf et al., 1990). Conversely, geographical areas with low selenium content tend to have local human populations with selenium deficiency. Keshan disease, discovered in a district in northeast China, claimed many lives relating to selenium deficiency (Johnson et al., 2000). Scientists analyzed the soil, crops, and hair of individuals in China and found lower selenium levels in communities from northeast China down to the southwest (Johnson et al., 2000). The level of selenium in plants depends on the level and chemical form of selenium in the soil they

grow in. Another component of selenium content in plants depends on the inherent ability of selenium accumulation in the plant. Certain plants, the genus *Astragalus* for example, are hyperaccumulators of selenium which can accumulate > 1000 mg Se kg^{-1} DW (Schiavon and Pilon-Smits, 2016; Brown and Shrift, 1982; Pickering et al., 2003). As previously mentioned, once in the plant, inorganic selenium biotransforms into organic forms selenocysteine and selenomethionine (Schiavon and Pilon-Smits, 2016). Defense mechanisms to selenium toxicity in plants include the reduction of Se(IV) and Se(VI) to Se(0), methylation of selenocysteine and selenomethionine, and metabolism to dimethyl diselenide for excretion (Shrift, 1969; Sors et al., 2009).

1.3.3 Selenium and Mercury

Selenium has considerable relevance concerning mercury toxicity through both direct and indirect mechanisms. Glutathione peroxidase and thioredoxin reductase, each with one selenocysteine amino acid, protect by way of redox-related reactions (Lu and Holmgren, 2008). More directly, selenium can partake in reducing the toxicity of certain mercury forms. Khan and Wang (2010) have reported the cleaving of the Hg–C bond in methylmercury through a mechanism involving $(CH_3Hg)_2Se$. As previously mentioned, both elevated mercury or elevated selenium levels can be detrimental to human health but the presence of certain chemical forms of each element together, in a certain order, may be beneficial. The mutual detoxification of selenium and mercury has been investigated by Gailer et al. (2000) who have identified a Hg–Se–S species readily formed, following venous injections of sodium selenite and mercuric chloride to rabbit subjects. Analysis of the rabbit plasma identified the molecular structure of a mercuric selenide core, surrounded by glutathione molecules (Gailer et al., 2000). Furthermore, mercury is known to have high affinity to endogenous selenium. Korbas et al. (2010a) found evidence of mercuric selenide formation in samples of human brain exposed to inorganic mercury. In another study, MacDonald et al. (2015a) have shown in a model vertebrate system, the co-localization of mercury and endogenous selenium when zebrafish larvae were exposed to inorganic mercury. Mercury-selenium interactions may be a good indicator of the mechanisms underlying the detrimental effects from mercury exposure. The rat progeny of 16 generations of selenium-deficient diets maintained 60% of selenium concentration in the brain (Behne et al., 2002) which emphasizes the tight regulation of selenoproteins in the brain. Raymond and Ralston (2004) have reasoned that

the ‘protective effects’ of selenium against mercury poisoning can be through the maintenance of sufficient selenium levels to support normal selenoprotein activity in the brain. Subsequent to this, Ralston et al. (2007) have identified the importance of mercury to selenium molar ratios in food as a more comprehensive marker for risks associated with dietary methylmercury exposure than methylmercury alone (Ralston et al., 2007). Following numerous examples, investigations of selenium with regards to mercury toxicity are continuing to be studied extensively.

1.4 Analytical Methods in Molecular Toxicology

Molecular toxicology examines the adverse effects of chemical compounds by investigating the structural components influencing harmful effects from toxins. A wide range of analytical methods are available to identify and quantify toxic compounds and to observe their interactions with living organisms. Concerning mercury toxicity, the toxicological profile of mercury compounds are commonly categorized through identifying the chemical species – limited to elemental, inorganic, or organic compounds (Clarkson and Magos 2006; Bernhoft, 2012; Guzzi and La Porta, 2008; Rooney, 2007). Speciation of mercury compounds from biological or environmental sources concerning human health effects is generally focused on resolving between inorganic mercury species and organomercury species (Leermakers et al., 2005). These organomercury compounds are presumed to be predominantly methylmercury, due to the generation of methylmercury compounds mediated by methylating bacteria in aquatic environments (Puk and Weber, 1994). In general, speciation involves three analytical steps – extraction, separation, and detection. Extraction of mercury from environmental or biological samples commonly involves acid or alkaline digestion depending on the sample type (biological, sediment, etc.) followed by solvent extraction (Leermakers et al., 2005). The different forms of mercury are then separated and quantified by means of gas or liquid-phase chromatography and identified using one of a number of detection methods such as mass spectroscopy (Leermakers et al., 2005). Mass spectrometry is a suitable detection tool for mercury due to the highly characteristic distribution of mercury isotopes (Hoffmeyer et al., 2006). These analytical methods are straightforward and economical enough to pursue in a number of situations. However, they provide only limited structural information on the specific chemical species of mercury which is important in understanding the mechanism of mercury toxicity. For example, the extraction method of aqueous phase ethylation using sodium tetraethylborate isolates compounds by forming

methyl-ethylmercury or diethylmercury as representatives of methylmercury and Hg(II) species, respectively (Liang et al, 1994). However, the detection of these compounds only describes the former reactant species CH_3Hg^+ and Hg^{2+}, and not the factual species present before ethylation.

The structure and physical properties of a compound impacts the route of exposure (uptake), as well as the fate and toxic outcome to a living organism. Furthermore, recognizing the structure of a toxin in the environment or in a living organism can be applied in the development of treatments used to mitigate harmful effects or sequester and safely manage the toxin. Therefore identifying the structure of mercury compounds is significant. Korbas et al. (2012) used X-ray fluorescence imaging (XFI) to show different mercury species accumulate differently in zebrafish larvae. Results showed methylmercury-cysteine species targeted the outer eye lens, differently from mercury(II)-*bis*(cysteinate) which had decreased uptake, and inorganic mercury which accumulated in the olfactory epithelium and kidneys (Korbas et al., 2012). Therefore the toxicity of mercury compounds goes beyond the divide of inorganic mercury species and organomercury species. Detailed structural information can be gathered using other analytical techniques which take advantage of light in different regions of the electromagnetic spectrum. Among the structural techniques to be broadly discussed, include nuclear magnetic resonance (NMR) spectroscopy, infrared (IR) spectroscopy, Raman spectroscopy and X-ray absorption spectroscopy (XAS).

1.4.1 Nuclear Magnetic Resonance (NMR) Spectroscopy

Nuclear magnetic resonance (NMR) spectroscopy is a non-destructive analytical technique providing structural information on nuclei with nuclear spin. This analytical technique uses electromagnetic radiation to manipulate the nuclear spin and garner structural information due to the orientation and shielding influences of electrons around the nucleus. The location of peaks, or chemical shifts, represents the resonant frequency of the energy transition of each unique chemical environment of the nuclei targeted. NMR can be determined in samples of solid, liquid, and gas phases. Identification of chemical environments using NMR is widely used in chemistry. ^{1}H NMR is extensively used due to the odd number of proton in nuclei, however isotopes of other elements are observable, including ^{199}Hg with an isotopic abundance of 16.94% (Blum et al., 2014). While the number of determined structures entered into the Protein Data Bank (PDB) has been steadily increasing over the years, the number of structures solved by NMR has plateaued. Of the total of 668 listed entries of ligands and macromolecules containing Hg, only 5 entries were solved by

solution NMR (Berman et al., 2019). Nevertheless, facets of structural information through NMR have been supportive in a number of studies. Sugiura et al. (1978) used ^{1}H NMR to measure the binding affinity of selenium-containing ligands compared to sulfur-containing ligands toward methylmercury. Results indicated a greater affinity of selenium-containing ligands which they later suspected could suggest the presence of high selenohydryl-containing proteins in sea animals, such as tuna, analogous to metallothioneine (Sugiura et al., 1978). Melnick et al. (2007) used ^{1}H NMR to emulate the coordination environment of the organomercurial lyase MerB in cleaving the mercury-alkyl bond. Using a series of simple thiol complexes, they determined the reactivity of thiol complexes to cleave the Hg–R bond is facilitated by a higher coordination of thiol ligands towards $[HgR]^{+}$ (Melnick and Parkin, 2007). Kim et al. (2017) used ^{1}H NMR to test the tolerance of *Arabidopsis* seeds to divalent cations Cd, Cu, Zn and Hg in the presence of exogenous glutathione. Their results support the impediment of Hg uptake with exogenous GSH, different from the other divalent cations (Kim et al., 2017). ^{1}H NMR is a useful analytical technique and has been instrumental in solving a number of structural questions of small molecules in chemistry. However, due to the abundance of protons in all living things, any structure determination will require pre-treatment of the sample in the form of extraction and/or separation. Furthermore, since the molar ratio of mercury within a molecule is typically very low, the extent of structural information to be obtained by ^{199}Hg is limited.

1.4.2 Vibrational Spectroscopy

Infrared (IR) spectroscopy is also a non-destructive technique probing the presence, or absence, of functional groups in a chemical compounds. Functional groups absorb photons at the infrared region of the electromagnetic spectrum at characteristic frequencies resulting in diagnostic vibrational patterns. IR spectra can be collected on solids, liquids, and gases. The information gathered from an IR spectrum is on molecular fragments, in which case other complementary techniques would be useful. IR spectroscopy has not been widely used in molecular studies of mercury compounds, as is evident with the limited publications using this analytical technique. One recent publication by Sharma and Uttam (2017) identified the changes in cell wall components of wheat seedlings when exposed to different levels of mercury. The changes in levels of certain functional groups were used as a quantitative estimation of heavy metal stress to plants (Sharma and Uttam, 2017). In another study, Terkhi et al. (2008) characterized the different carboxylic

functional groups in humic acid in the presence of Hg(II). Researchers characterized model carboxylate components of humic acid to use as a guide for monitoring the changes to these characteristic frequencies with the addition of Hg(II) (Terkhi et al., 2008). There are no established characteristic IR frequencies for mercury coordination environments. Therefore this analytical technique is limited in investigations of mercury speciation. In addition, due to the abundance of common organic functional groups, analysis of specific mercury compounds in environmental and biological samples will require pre-treatments.

Raman spectroscopy measures inelastic scattering of monochromatic light and is a non-destructive analytical tool. Raman scattering occurs when light interacts with molecular vibrations and is shifted to either a lower or higher frequency than the incident light. Samples could be of solids, liquids, or gas phases to give molecular fingerprints of compounds. Intensities of Raman bands can give information on the concentration of particular components. Raman and IR spectroscopy form a pair of complementary analytical tools. According to the rule of mutual exclusion, a centrosymmetric compound cannot be simultaneously IR and Raman active. Raman spectroscopy has been useful in a number of mercury thiolate investigations. A strong vibrational band between 180–400 cm^{-1} is considered a sensitive probe for the coordination of Hg with longer Hg–S bond lengths corresponding to a lower Raman band (Pires et al., 2012). Jalilehvand et al. (2013) monitored the decreasing Raman bands for Hg–S vibrations with increasing coordination binding of the ligand N-acetylcysteine.

1.4.3 X-ray Absorption Spectroscopy (XAS)

X-ray absorption spectroscopy (XAS) is another non-destructive technique providing accurate interatomic information of any element on the periodic table. With the use of synchrotron radiation, we can study the electronic structure of matter. The first users of synchrotron radiation were particle physicists interested in studying the building blocks of matter through high energy particle collisions. Today, with third generation synchrotron facilities, the highly tunable intense light is applied to several areas of research from material chemistry, art history, biochemistry and drug design. The vast range of the electromagnetic spectrum used by XAS can be applied to essentially any element of the periodic table and allows the probing of specific binding sites of large macromolecules, visualization of elemental distribution *in situ*, and monitoring of atomic bonds. One of the first uses of XAS in the study of toxic compounds was by Pickering et al. (1999)

identifying the speciation of a series of selenium-containing amino acids. Results showed distinct spectra which allowed the speciation of components within a composite biological sample using curve-fitting (Pickering et al., 1999). Other examples of structure determination of toxic compounds using XAS include the arsenic coordination identified in Indian mustard plants (Pickering et al., 2000a); the synergistic relationship between two toxic elements, mercury and selenium (Gailer et al., 2000) as well as arsenic and selenium (Gailer et al., 2002). Examining the chemical form within a biological samples is challenging since most exposures to toxins are low doses in chronic time-scales. Nonetheless, a number of studies of the specific chemical forms of mercury in biological samples have been published in fish (Harris et al., 2003), in dental amalgams (George et al., 2009), human hair (George et al., 2010), and brain (Korbas et al., 2010b), each requiring essentially no pre-treatments.

1.4.4 General Remarks

Choosing an analytical tool to investigate structural properties of mercury compounds requires a number of considerations. Avoiding pre-treatments to an environmental or biological sample is important to avoid possible chemical changes to the constituents of the sample. Furthermore, the extraction and separation processes may fail to isolate recalcitrant compounds, thus providing only a snapshot of the chemical components. The existing quantity of a sample would also influence the appropriate analytical technique to be used. The oral reference dose (RfD), which is the amount of a toxin consumed daily without the expectation of adverse effects, for methylmercury is 1 µg/kg/day (Harper and Harris, 2007). Mercury compounds can exhibit their toxic effects at very low doses and analytical results would be most meaningful when gathered from probing samples in their most natural conditions. Each of the above spectroscopic techniques are excellent for structurally characterizing small molecules, however applications of speciating composite biological or environmental samples in molecular toxicology are challenging. Of the shortlist of analytical techniques described above, XAS stands out as being the only technique requiring essentially no pretreatment and can probe the natural sample entirely intact. Raman spectroscopy (Bumbrah and Sharma, 2015) and ^{199}Hg NMR (Isab and Perzanowski, 1990), in contrast, exhibit low concentration sensitivity. Indeed, the structural information from XAS is generally limited to within 5–6 Å away from mercury, and consequently other complementary

tools would be useful in determining a comprehensive understanding of the structural framework involved in molecular toxicological studies.

1.5 Research Objectives

The following work in this dissertation uses X-ray absorption spectroscopy (XAS), computational chemistry, and other X-ray-based analytical methods to study the chemical interactions between different mercury compounds and various ligands that in one way or another relate to mercury toxicity. Understanding mercury toxicity through X-ray methods at a molecular level and in living organisms largely depends on the characterization of the molecular species in question. Chapter four establishes the technique development of a common pigment blocker 1-phenyl-2-thiourea (PTU) used in *in vivo* studies of zebrafish larvae. PTU is an organosulfur compound which in preliminary work unexpectedly either strongly protected or strongly exacerbated the toxic effects of mercury compounds in zebrafish larvae. As is common with mercury compounds, it is theorized that the protective or harmful effects observed in zebrafish larvae exposed to PTU is determined by the chemical form of mercury and its interaction with PTU. Chapter five studies the suitability of the sequestering agent 1,3-benzene-diamido-2-carboxylethanethiol in the treatment of acute inorganic Hg(II) exposure in zebrafish larvae through treatment trials and synchrotron X-ray fluorescence imaging (XFI). XAS and density functional theory (DFT) are used to evaluate the dithiol molecular structure complexed to mercury, and its candidacy as a true chelator of inorganic mercury.

The study into mercury toxicity at the molecular level can be difficult using conventional XAS, especially with *in situ* investigations. Ensuing from these experiments, the opportunity to develop new methods contributing to the molecular study of mercury toxicity manifested into the succeeding chapters. Chapters six and seven probe the potential of advanced X-ray absorption spectroscopic techniques to overcome the limitations of conventional XAS and considerably enhance detection methods for applications in, and concomitant to, mercury toxicity. Chemical characterization of mercury and selenium compounds is pertinent to the underlying mechanisms involved in mercury toxicity as well as the design of adequate mercury chelating agents. The ability to enhance chemical identification of mercury and selenium species at biological and environmentally relevant levels would strongly enrich investigations into the molecular basis of mercury toxicity. High energy resolution fluorescence detection XAS (HERFD XAS) capabilities

provide the depth in measurements never seen before. It was becoming apparent during the course of this dissertation work that the opportunity to observe richer spectroscopy with HERFD XAS would significantly improve the detection of different molecular species and revolutionize the investigations into the chemical structures involved in mercury toxicity.

Chapter eight examines the quantum-mechanical/molecular-mechanical (QM/MM) results of inorganic Hg(II) complexed to double stranded DNA as well as XAS results of inorganic Hg(II) complexed to 1-methylthymine, an analogue of the nucleobase thymine. Mercury has high affinity for DNA helices, though the binding site is between the base pairs and not on the exterior phosphate backbone. Therefore, DNA coordination to Hg(II) is through either nitrogen or oxygen-based ligands of thymine. X-ray-based techniques as well as DFT are used to determine the molecular structures involved in Hg–thymine binding and to determine its implication on the integrity of DNA structure. HERFD XAS was used as a complementary tool to conventional XAS in the identification of characteristic spectroscopy of mercury coordinated to 1-methylthymine compared to other biological modes of binding of mercury(II). Chapter nine highlights these new advancements in chemical speciation using HERFD XAS for the investigation into the molecular and electronic environment of mercury compounds responsible for the symptoms of Minamata disease.

CHAPTER 2. Introduction to Synchrotron Radiation Spectroscopic Methods

2.1 X-ray Absorption Spectroscopy (XAS)

X-ray absorption spectroscopy (XAS) is a versatile technique used to resolve the local atomic coordination and electronic structure of nearly any element on the periodic table. A brief review of this technique has been presented by George and Pickering (2007) (George and Pickering, 2007). XAS relies on the photoelectric effect which occurs when X-rays are absorbed by matter and a core electron is ejected. XAS exploits the characteristic binding energies (E_0) of electrons in elements to gather chemical information by investigating the patterns of photoelectrons that are ejected by X-ray excitation. When X-ray photons reach the characteristic binding energy of core electrons, photoelectrons are emitted resulting in multiple scattering events that make up the edge jump observed in spectra (Figure 2.1). The core hole created by photoabsorption is filled by the decay of an outer electron with concomitant emission of an X-ray fluorescent photon. In the hard X-ray regime the X-ray absorption spectrum is typically recorded using one or both of two main methods. Transmission detection measures the transmission of X-rays through a sample by comparing the photons measured before and after the sample using gas-filled ion chambers. Fluorescence detection measures the fluorescence emission and is assumed to be proportional to absorption processes. The spectra can be divided into two sub regions – Near-edge and Extended X-ray Absorption Fine Structure (EXAFS) (Figure 2.1). The near-edge region spans ~100 eV below and above the absorption edge, and provides information on the coordination geometry of the absorbing atom. The spectral shape of the near-edge is derived from core electron transitions to quasi-bound states. Comparing the near-edge to a library of standards can identify coordination chemistry and oxidation states of specific elements within a sample. At higher kinetic energies core electrons are excited beyond the absorbing atom and interact with neighbouring atoms. The interaction of photoelectrons with neighbouring atoms creates a backscattering wave vector with phase and amplitude functions which are characteristic of the backscatterer type. When

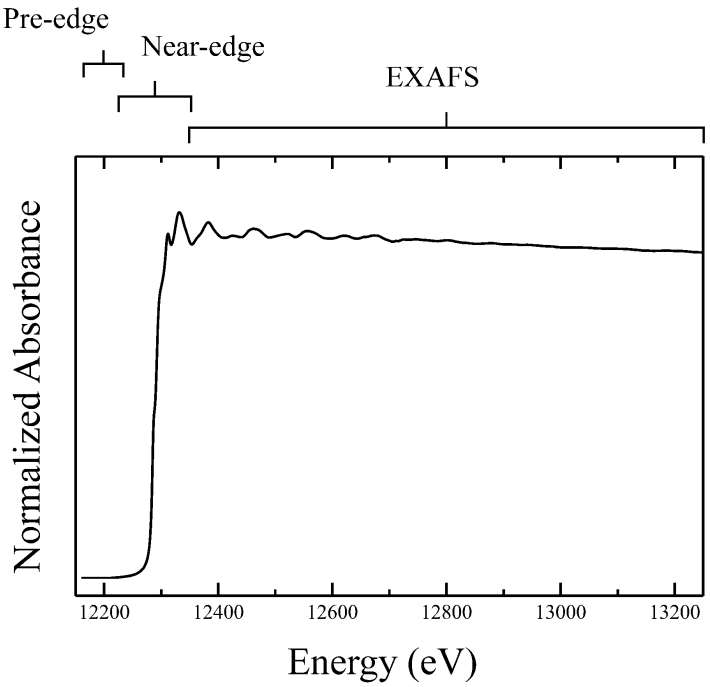

Figure 2.1. A mercury L_{III}-edge X-ray absorption spectrum.

the backscattering wave is in phase with the outgoing wave, the X-ray absorption coefficient is at a maximum and when the two waves are out of phase they are at a minimum. This constructive and destructive interference of the backscattering wave with the absorbing atom's photoelectrons create the oscillatory structure in spectra and is known as EXAFS. The phase and amplitude of the backscattering wave depends on the backscattering atom, which is how nearby atoms are identified. As the incident energy above E_0 increases, the kinetic energy of the emitted photoelectrons increase, and accordingly the wavelength decreases as described by the de Broglie equation (Equation 2.1), where E represents the energy, h represents Planck's constant, c represents the speed of light, and λ_e represents the de Broglie wavelength.

$$E = {}^{hc}\!/_{\lambda_e} \tag{2.1}$$

2.1.1 X-ray Absorption and X-ray Absorption Spectroscopy Theory

When the incident energy of an X-ray beam exceeds a core electron binding energy, the absorption coefficient increases sharply. This sharp increase is often called the absorption edge. The change in X-ray intensity through a given material is defined by Equation 2.2. The linear absorption coefficient (μ) describes the exponential of the fraction of the beam that is absorbed from an absorbing material at a certain thickness. I_0 and I are the incident and transmitted intensities, respectively, and x is the thickness of the sample.

$$\mu x = \log_e \frac{I_0}{I} \tag{2.2}$$

Absorption edges are named according to the energy level shell of the ejected core electron which are based on the principal quantum number (K (n=1), L (n=2), M (n=3), etc.). When the incident energy is equal to or greater than the core electron binding energy, the core electron is ejected as a photoelectron, creating a core hole. The core hole is then filled by the decay of an electron from a higher orbital, with the concomitant emission of a fluorescence photon. The energy of the emission line is the difference in the binding energies of the decaying and core electrons (Figure 2.2).

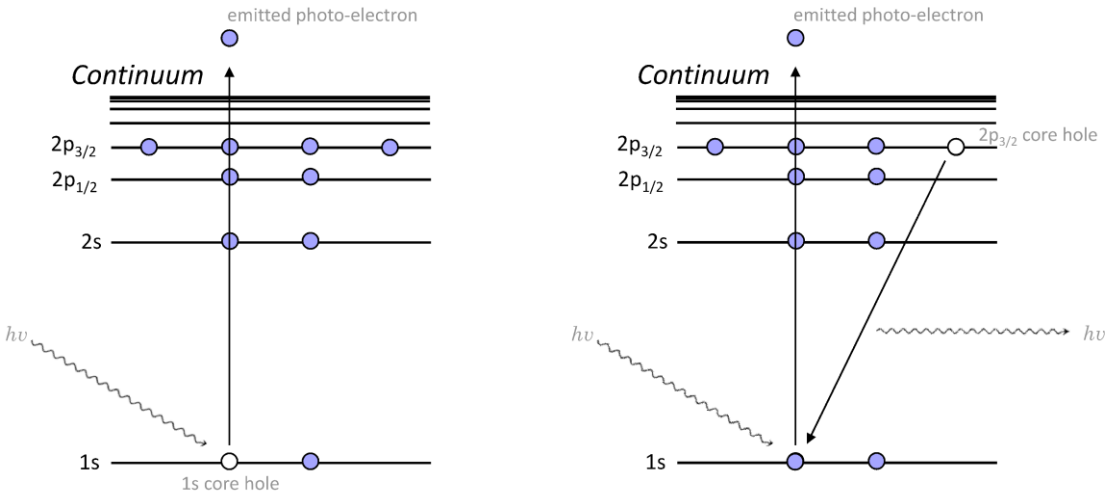

Figure 2.2. Illustration of K-edge X-ray absorption (*left*) and $K\alpha_1$ fluorescence emission (*right*).

As previously mentioned, near-edge spectra, comprising ~100 eV of the absorption edge can expose information on coordination geometry and oxidation states. Occasionally, spectral features before the absorption edge are visible, corresponding to various bound states within the absorber atom. The EXAFS oscillations (χ) above the absorption edge are defined by the absorption coefficient (μ) and the absorption coefficient in the absence of any photoelectron backscattering terms (μ_0) (Equation 2.3). In practical terms, this is isolated by subtracting the smooth background absorption coefficient from the absorption coefficient and then normalized by the smooth background absorption coefficient.

$$\chi(E) = \frac{\mu(E) - \mu_0(E)}{\mu_0(E)} \tag{2.3}$$

The simple EXAFS equation (George and Pickering, 2007) is expressed in Equation 2.4 which can be fit with parameters of a structural model to gather information on the atomic number, quantity, and distance of neighbouring atoms.

$$\chi(k) = \sum_i \frac{N_i A_i(k,R)}{kR_i^2} e^{-2R_i/\lambda(k)} e^{-2\sigma_i^2 k^2} \sin[2kR_i + \varphi_i(k)] \tag{2.4}$$

N_i is the coordination number of atom type i; A_i is the total amplitude function; R_i is the interatomic distance of the scattering path; σ_i^2 represents the mean-square deviation in R_i; $\varphi_i(k)$ represents the total phase shift function. The EXAFS equation is a combination of an amplitude component, which represents the intensity of the wave, and a phase component, which represents the oscillatory part. The amplitude component includes the amplitude function, $\frac{N_i A_i(k)}{kR_i^2}$, the mean free path term $e^{-2R_i/\lambda(k)}$, which increases the EXAFS intensity in higher k-range, and the Debye-Waller term, $e^{-2\sigma_i^2 k^2}$, which is a pair distribution function that describes the mean-square displacement between the absorbing and backscattering atoms, taking into consideration the combination of both vibrational and static disorder. The phase component, $[2kR_i + \varphi_i(k)]$, among other things, depends on the atomic number of the backscatterer. The EXAFS equation is expressed as a function of the photoelectron wave vector, k, which is defined from E using Equation 2.5. The electron rest mass is represented by m_e and the reduced Planck's constant is $\hbar$. The EXAFS oscillations are dampened

at higher kinetic energies, therefore it is good practice to weight the EXAFS by multiplying by k^3 in order to compensate for the attenuation.

$$k=\sqrt{\frac{2m_e(E-E_0)}{\hbar^2}} \tag{2.5}$$

The EXAFS oscillations can be fit to a structural model through the EXAFS equation which employs amplitude and phase functions from *ab initio* theory (Rehr et al., 1991). Non-linear optimization analysis is then used to refine parameters and obtain structural information. The EXAFS region holds information on the number and type of neighbouring atoms, as well as the interatomic distance between absorbing and neighbouring atoms.

Data reduction of EXAFS usually involves the conversion of *k*-space to *R*-space using a phase-corrected Fourier transform (Equation 2.6) (George and Pickering, 2007), where $\phi(k)$ represents the total phase function. The phase-corrected Fourier transform illustrates peak positions representing the interatomic distances between absorber and backscatterer atoms.

$$\rho(R)=\frac{1}{4\sqrt{\pi}}\int_{k_{min}}^{k_{max}}\chi(k)k^3e^{[i2kR+\phi(k)]}dk \tag{2.6}$$

The resolution of *R* is dependent on the *k*-range of EXAFS oscillations. This value represents the minimum interatomic distance required to resolve between two shells of similarly distant backscattering atoms of similar atomic numbers and is defined by Equation 2.7.

$$\Delta R = \pi/2\Delta k \tag{2.7}$$

The scattering path from the absorbing atom can involve more than one backscattering atom and in certain structures, these can be modelled to identify 2nd or 3rd backscattering shells.

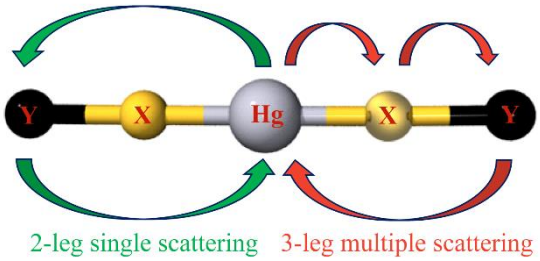

Figure 2.3. Schematic of 2-leg single scattering path (*green*) and 3-leg multiple scattering path (*red*).

In the Y–X–Hg–X–Y example (Figure 2.3), the single scattering path is observed as the two-leg path of Hg → Y → Hg, and the three-leg path is represented by Hg → X → Y → Hg. There could also be the alternative three-leg path (Hg → Y → X → Hg), or four-leg path (Hg → X → Y → X → Hg), and so on. These multiple scattering paths can be modelled to give information on geometry or angle of the complex. For example, a linear S–Hg–S complex is expected to have multiple scattering effects, showing features at twice the 2.35 Å Hg–S bond-length (Fu et al., 2011). Deviation from 180° is expected to weaken the multiple scattering feature at 4.7 Å.

2.1.2 Strengths and Limitations of XAS

Strengths of XAS include its suitability with disordered materials in non-crystalline solids and solutions. In fact, XAS can be performed on any type of sample in all phases – solid, liquid, and gas. This strength extends to the study of heterogeneous systems with mixtures of species. As well, XAS can be measured on almost any material with very little pre-treatment from real biological tissues, live plants, fossils, and synthetic materials. Interatomic distances determined using EXAFS are accurate with measurements of absorber-ligand interatomic distances up to a margin of ±0.02 Å.

EXAFS often lacks the ability to provide 3D geometric information. In addition, near-edge fitting by comparing to a library of reference standards gives only a representation of the atoms nearby within 5–6 Å. Therefore, complementary methods, such as density functional theory (DFT) calculations are useful to model a 3D structure. In addition, EXAFS resolution (ΔR) is approximated by $\pi/2\Delta k$ and can be a limiting factor if there are two different backscatterers with similar interatomic distances. As well, the dose on samples can introduce X-ray induced photochemistry to cause changes to the sample. This can be an issue in solutions of biological samples that are often dilute with a major factor being the flux density of the X-ray beam (George et al., 2012). This is increasingly problematic as the increased brilliance of synchrotron radiation sources has improved considerably which results in increased rates of X-ray induced photochemistry. Careful consideration of the flux density of the X-ray beam on the sample and condition of the sample must be maintained to ensure the same molecule at the beginning of the experiment is likely still the same molecule at the end of the experiment. One way to minimize X-ray induced photochemistry is to place the sample in a low temperature sample environment with

the use of a cryostat. Another limitation of EXAFS is its inability to distinguish between backscattering atoms of similar atomic numbers at similar distances as these elements would carry a similar number of electrons and similar phase and amplitude. Furthermore, the availability of synchrotron radiation is highly competitive, which means access to beamtime is finite and could be difficult to acquire.

2.2 X-ray Fluorescence Imaging (XFI)

X-ray fluorescence imaging (XFI) is another synchrotron technique providing 2D maps of elemental distribution *in situ* with information on the location and approximate concentrations of multiple elements in the material with minimal manipulation of the sample. This technique has been reviewed by Pushie et al. (2014). A simplified beamline setup is shown in Figure 2.4A. Micro-focus optics, used to generate a small beam size, could include using simple apertures, Kirkpatrick–Baez (K–B) mirrors, Fresnel zone plates, or a number of other methods (Pushie et al., (2014). The procedure sets the incident energy above the absorption edges of multiple elements of interest thereby simultaneously exciting their absorption edges and collecting the emission spectra of all elements absorbing in the sample (Figure 2.4). The sample is raster scanned (Figure 2.4B) and fluorescence emission peaks corresponding to different elements are windowed (purple shaded band in (Figure 2.4C)), counted and collected pixel by pixel producing element specific maps (Figure 2.4D). Image resolution depends on the size of the X-ray beam, which can be defined by various micro-focus optics, and the step size used in scanning the sample. Image resolution can allow visualization of elemental distribution at subcellular levels. Quantification can be performed by comparing the fluorescence intensity of the sample to the fluorescence intensity of standard foils of known concentrations and can provide useful information in a number of applications. Examples of applications of XFI include, yet are not limited to, plant physiology, health sciences, geology, and even fine arts. Swanston et al. (2018) used confocal XFI to investigate lead (Pb) distribution of bone and teeth of men aboard Franklin's lost expedition to conclude that Pb did not play a major role in the loss of the crew. Vermeulen et al. (2016) examined the arsenic (As) content in various 17^{th} century paintings and identified As(III) and As(V) compounds in degradation products of paint pigments. Pickering et al. (2009) developed methods for chemically specific imaging at the sulfur (S) K-edge in onion samples as an *in vivo* probe of sulfur metabolism.

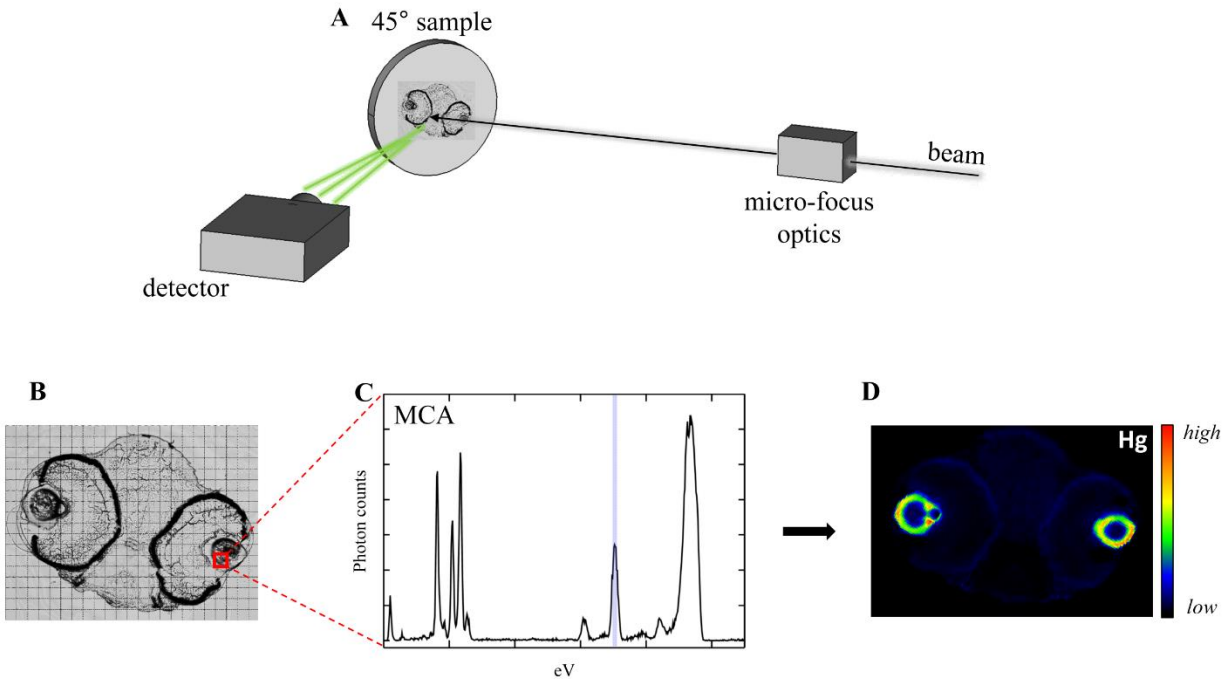

Figure 2.4. Schematic illustration of X-ray fluorescence imaging data acquisition. A: Schematic illustration of simplified X-ray fluorescence imaging beamline setup (not to scale); B: Example of raster-scanning of sample; C: Multichannel analyzer (MCA) output of all element emissions. Purple band signifies 'window' of element of interest; D: Element specific map of mercury with XFI. Color bar displays high and low levels of mercury.

2.2.1 Strengths and Limitations of XFI

Strengths of XFI include high spatial resolution to detect intracellular elemental distribution. Currently, certain beamlines can approach a very small beam size. For example beamline HXN at NSLS-II can approach a beam size of 12 nm for XFI and chemically specific imaging at 12-16 keV. XFI is element specific and the advantage of simultaneously collecting multiple elements can give a more complete picture of possible interactions of co-localized elements. As well, very little pre-treatment is needed to perform experiments. Chemically specific imaging allows investigations on the spatial distribution, concentration, and chemical forms of elements. As well, an extension of XFI is the use of µ-XAS which investigates the chemical species of elemental hotspots from XFI scans. Bacquart et al. (2010) used µ-XAS to investigate arsenic speciation in subcellular compartments of cultured cancer cells by identifying arsenic redox states in cytosol, nucleus and mitochondrial networks.

XFI experiments can be time consuming depending on the concentration of the elements of interest and the speed of data collection. And as previously mentioned, beamtime allocations are highly competitive. To get enough data for a complete project can come with a high cost. Often small compromises in all aspects, including image resolution, and number of replicates are necessary. On occasion, there is the complication of two elements with neighbouring fluorescent peaks. The mercury $L\alpha_1$ emission at 9,988.8 eV and mercury $L\alpha_2$ emission at 9,897.6 eV could overlap with zinc $K\beta_{1,3}$ emissions at 9,572.0 eV if there are high levels of either element. In these cases, checking that the software windows for each fluorescence emission are narrow and separate can help alleviate this issue. Optimal quantification of elemental levels in X-ray fluorescent images involves uniform sample thicknesses. The best scenario for quantifying would be to compare experimental samples to similar reference standards of known thickness and concentrations but to have an extensive library is costly. In the hard X-ray regime, samples thicker than 0.2-10 µm should be corrected for thickness by applying the X-ray attenuation of both incident and fluorescence X-rays from the sample and experimental setup (windows, flight paths, etc.) (Pushie et al., 2014). Synchrotron radiation sources are increasing in brilliance with higher photon flux which can cause changes to a delicate tissue sample. Samples with low concentrations would require longer exposure to the intense microfocused X-ray beam to attain adequate signal-to-noise ratios which may cause photoreduction or photooxidation. This raises concerns in making wrong

conclusions due to beam damage, and consequently prevents any following experiments with the sample. Employing a low temperature sample environment with the use of a cryostat can minimize X-ray beam damage.

2.3 High-Energy Resolution Fluorescence Detection (HERFD) XAS

High-energy resolution fluorescence detection XAS (HERFD XAS) provides improved signal-to-noise and enhanced chemical characterization abilities over conventional XAS fluorescence detection. This technique is described by Glatzel and Bergmann (2005) with beamline configuration described by Sokaras et al. (2013). The detected energy bandwidth of conventional XAS is largely influenced by the convolution of two factors; first, optical contributions of approximate Gaussian structure from the monochromator crystal, and second, by the core hole lifetime contribution of approximate Cauchy-Lorentz structure. The former is sometimes referred to as the Darwin width which is the inherent dispersion angle of the radiation wavelength of Bragg reflections. The contribution of the Darwin width depends on the quality of the crystal and is absent at 90° of the Bragg reflection (Kleimenov et al., 2009). The core hole effects are described by the Heisenberg Uncertainty Principle (Equation 2.8), where core hole lifetime is defined by Δt. This principle states that energy uncertainty is inversely proportional to the core hole lifetime. HERFD XAS spectrometers improve the signal-to-noise ratio by isolating and detecting only a small portion at the strongest intensity of the emission peak. Therefore, in addition to energy dispersive detectors which count windowed incoming photos and disregard background scattering, HERFD XAS spectrometers neglect much of the broad emission peak.

$$\Delta E \Delta t \approx \hbar/2 \tag{2.8}$$

When a photon is absorbed by a 1s electron, a photoelectron is ejected which creates a core hole (Figure 2.2, *left*). The Δt_{1s} of a 1s core hole is short lived, a fraction of a femtosecond (Föhlisch et al., 2007), since 1s is a tightly bound state. Hence, the shorter the Δt, the larger the ΔE, or energy uncertainty, and by reason, a wider spectral width. This fluorescence event creates a core hole in the $2p_{3/2}$ level (Figure 2.2, *right*) which has a longer core hole lifetime ($\Delta t_{2p3/2}$) than the 1s core hole due to its relatively weaker bound state. Hg L_{III}-$L\alpha_1$ fluorescence is the result of an electronic

transition from a 3d to $2p_{3/2}$ orbital and the apparent spectral linewidth (Γ_{app}) due to core hole lifetime broadening is described by Equation 2.9, where Γ_{int} represents the intermediate core hole lifetime broadening at the $2p_{3/2}$ level and Γ_{fin} represents the final core hole lifetime broadening at the 3d level (Proux et al., 2017).

$$\Gamma_{app} = \frac{1}{\sqrt{1/(\Gamma_{int})^2 + 1/(\Gamma_{fin})^2}} \tag{2.9}$$

HERFD XAS implements multiple crystal analyzers to tune the emission scan so that only a narrow center slice of the emission scan is preferentially diffracted to the detector. This instrumentation offers a detected energy bandwidth much less than the core hole lifetime broadening of the absorption edge, which exposes spectral features in the near-edge spectra as the lifetime of the initial core hole no longer limits the spectral resolution. The improved resolved fine structure and bonus of greater chemical sensitivity is useful in detecting and identifying different molecular species in *in situ* samples. The crystals are in Rowland geometry (Figure 2.5) with sample and solid state detector which will selectively count the emission line of interest and accordingly vastly improve the signal.

The crystal analyzers are bent Bragg crystals with optimum resolution at 90°, though this is not possible as the sample would have to be right on top of the detector. The more the Bragg angle deviates form 90°, the lower the energy resolution of the spectrometer and this is due to the Darwin width effects in the crystals (Sokaras et al., 2013). Different elements of interest require different sets of crystals to satisfy the Bragg equation (Equation 2.10), where n represents the order of diffraction, λ is the de Broglie wavelength, d represents the d-spacing for the lattice planes in the crystal, and θ represents the Bragg angle between a crystal analyzer and the fluorescence radiation path. Using Bragg optics, a large amount of the fluorescence energy uncertainty that is inherent in X-ray fluorescence can be discarded and the energy (or wavelength) that satisfies the Bragg condition is registered, broadened by the Darwin width of the particular set of crystals.

$$n\lambda = 2d \sin\theta \tag{2.10}$$

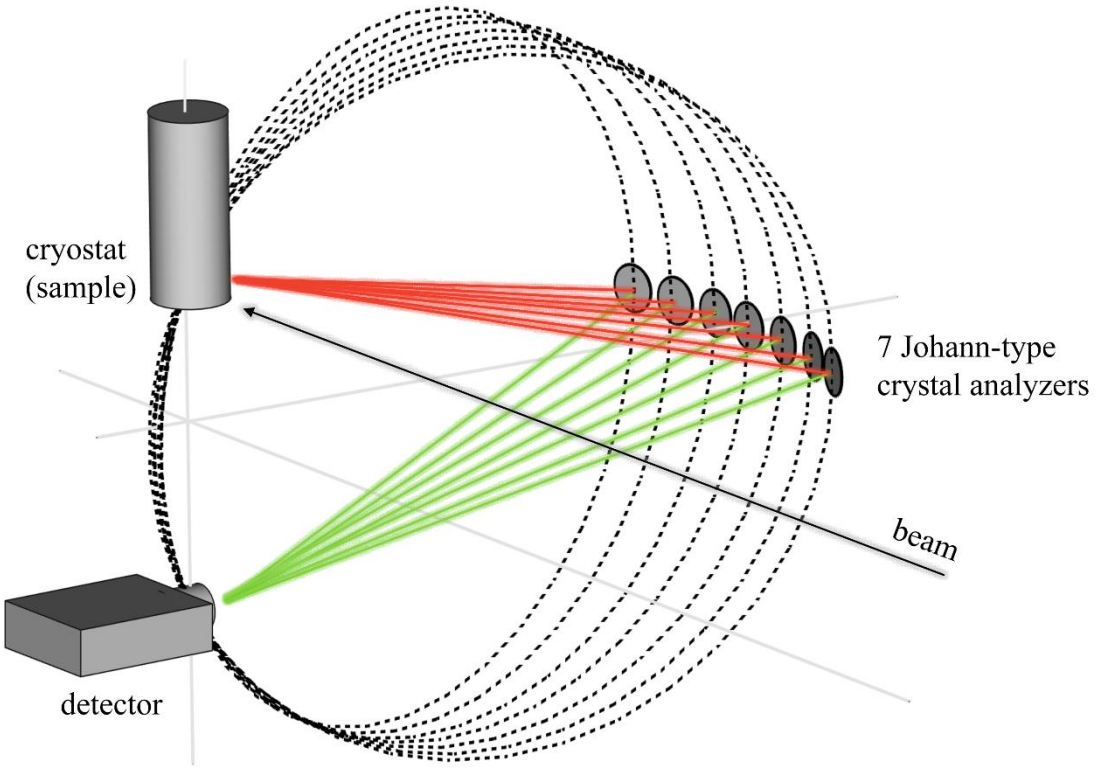

Figure 2.5. Schematic representation of HERFD XAS beamline setup. Sample (in cryostat), set of crystal analyzers, and detector aligned in overlapping Rowland geometry.

The improvements in energy resolution with a HERFD XAS spectrometer produce improvements in spectral resolution, but this is critically on the Bragg geometry – with a Bragg angle that is far from 90° the experiment becomes sensitive to the finite size of the illuminating X-ray beam on the sample (Kleimenov et al., 2009). Conversely, true HERFD XAS is only achieved when $\theta \rightarrow 90°$. Consequently, to measure a given chemical element typically requires a unique set of Bragg crystals to achieve a Bragg angle close to 90°.

2.3.1 Resonant Inelastic X-ray Scattering (RIXS)

Resonant inelastic X-ray scattering (RIXS) can be used to probe the electronic structure of an atom through inelastic scattering processes (Glatzel and Bergmann, 2005). RIXS is a two-step process which includes excitation of an electron to an intermediate state, followed by decay of an electron to a final state (Glatzel et al., 2009). A two-dimensional contour plot, also known as a RIXS plane, can be represented by plotting the intensity (*z*-direction) as a function of the incident energy (Ω; x-axis) and the energy transfer (Ω–ω; y-axis) (Glatzel et al., 2009a). Diagonal lines through the RIXS plane represent HERFD XAS spectra at fixed emission energies (Hämäläinen et al., 1991; Glatzel et al., 2009a). Furthermore, the RIXS plane contains information of both conventional XAS and resonant X-ray emission spectroscopy (RXES). Conventional XAS, which lacks the measuring of energy transfer, is represented by the integrated intensity of each vertical line to obtain the intensity of each energy point of a conventional XAS scan (Glatzel and Bergmann, 2005). A vertical line through a RIXS plane (associated with a constant incident energy) shows a single RXES spectrum corresponding to a constant intermediate state scan (Glatzel and Bergmann, 2005). Both XAS and RXES monitor the activity following the promotion of a core electron to unoccupied orbitals in the atom to investigate atomic structure. With RXES, information about occupied valence states can be obtained since RXES monitors the emission of an X-ray photon when a valence electron fills the core hole. With XAS, information about the unoccupied valence states can be obtained since XAS monitors the promotion of electrons following absorption of photons. Another method for probing the valence states is non-resonant XES (NRXES) where the incident X-ray energy is tuned well above the absorption edge so that electrons are excited to the continuum (Glatzel et al., 2009b).

2.3.2 Strengths and Limitations of HERFD XAS

HERFD XAS offers a number of profound strengths. The improved spectral resolution of HERFD XAS near-edge spectra allows for better speciation among similar compounds (See Chapters 6 and 7). HERFD XAS could be very useful in environmental or toxicological studies with natural elemental levels below the adequate detection limit of conventional XAS. Also as a benefit, collecting data is relatively quick which means more data can be collected within a shift of beamtime.

Limitations of HERFD XAS include challenges arising from the very powerful beam, carrying a high dose of radiation which can cause beam-induced photochemistry and result in challenging data analysis. Maintaining a low temperature sample environment with a cryostat can minimize X-ray-induced beam damage. Furthermore, for optimal results, each wavelength of interest, corresponding to element-specific emission energies, generally requires its own set of analyzer crystals. Not only is this a costly expense, but beamline setup can take a few hours and makes switching to investigate different elements more time consuming. As well, very few beamlines in the world can perform this technique which makes the request for beamtime extremely competitive. Another challenge with HERFD XAS is the care that needs to go into aligning the spectrometer to a consistent, reproducible position of the emission peak. If the alignment is off by a few tenths of an eV, this shift will be translated to the HERFD XAS spectra which may result in species misidentification (see Chapters 6 and 7). This is especially challenging when investigating natural samples with dilute concentrations due to the noisy emission scans.

2.4 Density Functional Theory (DFT)

Density functional theory (DFT) is a robust complementary tool used to understand experimental data in chemistry which employs a quantum mechanical approach to generate energy minimized and geometry optimized models of molecules. The theory is built upon the work of Hartree and Fock (HF) which approximates the wavefunction and energy of a many-body Schrödinger equation, however their theorem neglected an exchange-correlation energy component between electrons, limiting its performance (Corminboeuf et al., 2006). The theory has evolved to current post-HF methods which corrects the limitation, based on work by Pierre Hohenberg and Walter Kohn (Hohenberg and Kohn, 1964). Hohenberg and Kohn presented a

theorem which stated that all the information of a many-body system is contained in the density functional represented by 3 spatial coordinates. Therefore in theory, knowing the universal density functional would allow us to solve the Schrödinger equation in iterations until the lowest-energy minimum is realized which represents the exact density and energy of the system in ground state. This is however difficult to solve because the universal density functional is not known (Corminboeuf et al., 2006). The Kohn-Sham formalism (Kohn and Sham, 1965a; Kohn and Sham, 1965b) introduced a simplified density functional as a single-particle potential, instead of a many-body interacting system, that gives the exact ground-state density. From this, various approximations to explain the exchange-correlation of the Kohn-Sham system are incorporated into modern DFT software. One example of a functional is the local-density approximation (LDA) which approximates the exchange-correlation energy functional dependent on the value of electron density at each point in space. Weaknesses of LDA include underestimating the core electron energies of an atom and overestimating the binding energies of a molecule (Perdew et al., 1992). To correct for these weaknesses, another functional referred to as generalized gradient approximations (GGA) has been developed which implements a gradient correction to the charge density to correct for variations in electron density. Meaning the value of an electron at point *r* is dependent on its density and the density gradient moving away from point *r*. Modern DFT software solve the Kohn-Sham system (Kohn and Sham, 1965b) in iterations until user-defined convergence criteria are met.

CHAPTER 3. Procedural Methods

Synchrotron facilities provide intense sources of light which can be used to investigate materials in a variety of fields from condensed matter physics, material sciences, medicine, and environmental sciences. X-ray absorption spectroscopy (XAS), X-ray fluorescence imaging (XFI), and high energy resolution fluorescence detection X-ray absorption spectroscopy (HERFD XAS) for this dissertation were performed using synchrotron radiation at the Stanford Synchrotron Radiation Lightsource (SSRL) and the Advanced Photon Source (APS). SSRL employs the SPEAR3 storage ring operating at 3.0 GeV with a current of 350 mA. APS operates its 7.0 GeV electron storage ring in top-up mode at 102 mA. This chapter consolidates the Materials and Methods sections in the forthcoming chapters to serve as a reference source. Unless explicitly stated, the following procedures and configurations were used in the proceeding chapters.

3.1 X-ray Absorption Spectroscopy Methods

3.1.1 Sample Preparation

Solution samples were prepared as 1 mM concentration of absorbing atom, including 20% v/v glycerol to avoid ice diffraction effects. Samples were then loaded into 2 mm × 3 mm × 22 mm acrylic or Delrin cuvettes wrapped in metal-free adhesive Mylar or Kapton tape and flash frozen in a slurry of liquid nitrogen-cooled isopentane. Solid samples were prepared as 5% weight of the compound of interest with boron nitride (BN), ground to a fine powder, and then loaded into metal powder holders windowed with metal-free Mylar or Kapton tape.

3.1.2 Stanford Synchrotron Radiation Lightsource Beamline 7-3

Selenium K-edge and mercury L_{III}-edge X-ray absorption spectra were measured on the structural molecular biology beamline 7-3 at SSRL. The beamline was equipped with a Si(220) double-crystal monochromator. Incident X-ray intensity was monitored using a nitrogen-filled ionization chamber. X-ray absorption of samples were measured by the X-ray fluorescence excitation spectrum using a 30-element germanium detector array placed at 90° and in the same plane of the incident X-ray beam to minimize scattering contributions. Soller slits and arsenic or

gallium containing X-ray filters (EXAFS Materials, Danville, California, USA) were utilized for selenium and mercury measurements, respectively, to prevent unwanted scatter radiation and non-linearity of the detector. Transmittance was monitored using nitrogen-filled ionization chambers before and after the sample. Samples were placed in a liquid helium cryostat holding an approximate temperature of 10 K to minimize thermal contributions at 45° to the incident X-ray beam for fluorescence measurements, and 90° to the incident X-ray beam for transmittance measurements. Simultaneous absorption of standard grey hexagonal Se or Hg–Sn amalgam metal foils were measured downstream by transmittance using nitrogen-filled ionization chambers for internal energy calibration which was accomplished using the lowest-energy inflection points of the standard foils assumed to be 12,658 and 12,285 eV, respectively.

3.1.3 Data Analysis, Reduction, and Fitting

Near-edge and extended X-ray absorption fine structure (EXAFS) oscillations $\chi(k)$ were analyzed using the EXAFSPAK program suite (George, G.N., 2000). As previously mentioned, all data were energy calibrated using the lowest-energy inflection points of standard grey hexagonal Se or Hg–Sn amalgam metal foils, assumed to be 12,658 and 12,285 eV, respectively. Individual data scans, called 'sweeps', are averaged to increase the signal-to-noise. Background contributions to the measured total absorption observed in the pre-edge is fit with a polynomial or Gaussian function then subtracted from the measured total absorption, rendering the absorption from the sample. In order to extract the EXAFS, the experimental data is fit with a polynomial spline function defined over a series of intervals, and used to fit through the middle of the EXAFS oscillations and subtracted. Near-edge spectra are normalized to the spline whereas EXAFS spectra are normalized to an idealized absorption coefficient estimated by the Victoreen approximation (Equation 3.1); where *C* and *D* are tabulated Victoreen constants for a particular element and edge, and λ is the wavelength.

$$\mu_{\text{th}}(E) = C\lambda^3 - D\lambda^4 \tag{3.1}$$

The extracted EXAFS is then fit to a structural model using structural parameters and refined using least-squares refinement (Equation 3.2). The photoelectron wave vector is defined by *k*, and the

experimental and calculated spectra are defined by χ_{expt} and χ_{calc}. Structural parameters used for fitting include coordination number (N); interatomic distances (R); Debye-Waller factor (σ^2); with an energy offset representing the threshold energy (E_0), which is assumed to be 12,675 and 12,305 eV, for selenium and mercury, respectively. The program FEFF v8.25 (Rehr and Albers, 2000) was utilized to perform theoretical phase and amplitude functions calculations.

$$F = \sqrt{\frac{\Sigma k^6(\chi_{expt} - \chi_{calc})^2}{\Sigma k^6 \chi_{expt}^2}} \tag{3.2}$$

3.2 X-ray Fluorescence Imaging Methods

3.2.1 Zebrafish Exposures

Zebrafish embryos collected from breeding tanks were triple rinsed with fresh system water and stored in 25 cm Petri dishes (100 zebrafish embryos per dish). Petri dish medium contained 0.1% v/v methylene blue and system water to prevent fungal growth in the dish and were stored in an incubator at 28°C. Petri dish medium was replaced every 24 hours, dead embryos were discarded, and remaining embryos were rinsed daily. Dechorionated zebrafish larvae were triple rinsed at 3 days post fertilization (dpf) in preparation for exposure tests. Twenty-five larvae were randomly selected per Petri dish for the number of total Petri dishes necessary. Each experiment had four replicates (Petri dish) per control (system water) or treatment group. Exposures lasted four days with appropriate solution medium being replaced daily. Death and deformities of larvae were recorded daily with dead larvae removed prior to the addition of fresh medium.

3.2.2 Embedding and Fixing

The following outlines the procedures for embedding and fixing zebrafish in preparation for XFI as developed by Sullivan-Brown et al. (Sullivan-Brown et al., 2011). Following treatment days, zebrafish larvae were euthanized with 0.2% tricaine then randomly selected and fixed in 4% paraformaldehyde (PFA) at 4°C or room temperature for 2 hours. The larvae were dehydrated in a step-wise series of 0%, 25%, 50%, 75%, and 100% MeOH/EtOH:PBST buffer (30mM PBS +

0.01% Tween 20) solutions and stored under rocking conditions at room temperature or −20°C. Larvae were then slowly rehydrated in the reverse order of the MeOH/EtOH:PBST buffer washes described above and fixed in 1% 2-hydroxyethyl methacrylate and left to harden. The blocks of resin were then dehydrated in absolute MeOH or EtOH and incubated under rocking conditions for 5-8 hours at 4°C. The blocks were infiltrated overnight at 4°C with infiltration solution (0.625g benzoyl peroxide per 50mL JB-4 Solution A). The solution was replaced in the morning with fresh infiltration solution and shaken for 5-6 hours at 4°C. The resin blocks were placed in embedding molds and filled with a JB-4 polymerization mixture (1mL JB-4 Solution B per 25mL infiltration solution) which was wrapped in plastic and placed on ice and stored at 4°C overnight for polymerization to occur. Molds were gently removed and allowed to dry completely before sectioning. Transverse sections 6 μm thick were cut using a microtome and glass knife. Sections were placed in distilled water then transferred on Thermanox metal-free cover slips (Thermo Scientific, Nunc) and ready for imaging. Adjacent sections were transferred on glass slides and stained for morphological comparisons.

3.2.3 Advanced Photon Source Beamline 20-ID-B

XFI experiments of zebrafish larvae were collected at beamline 20-ID-B at APS. The endstation was equipped with a Si(111) double-crystal monochromator employing harmonic rejection. The incident X-ray intensity was tuned to 13.45 keV to remain below the Br K-edge while still monitoring the Zn Kα and Hg $L\alpha_{1,2}$ fluorescence lines. Samples were mounted on a motorized stage at 45° to the incident X-ray beam and raster scanned using a 5 μm step size with a beam exposure time of 0.6 seconds per pixel. A beam diameter of 5 μm was achieved with Kirkpatrick-Baez (K-B) Rh-coated focusing mirrors. Fluorescence was detected at 90° to the incident X-ray beam using a four-element Vortex silicon-drift detector.

3.2.4 Stanford Synchrotron Radiation Lightsource Beamline 2-3

XFI experiments were collected at beamline 2-3 at SSRL. This beamline utilizes a Si(111) double-crystal monochromator and incident X-ray intensity was tuned to 13.45 keV to be above the absorption edges of elements of interest but below the Br K-edge to avoid contributions from plastic components in the experimental setup. Samples were mounted 45° to the incident X-ray

beam and scanned with a beam diameter of 2 μm achieved with a microfocus Rh-coated Kirkpatrick-Baez (K-B) system. X-ray scanning was 'on the fly' with a dwell time of 0.6 seconds per pixel. Fluorescence was detected at 90° to the incident X-ray beam using a one-element Vortex silicon-drift detector.

3.2.5 Data Analysis

Quantification of elements, excluding mercury, was achieved by imaging uniform thin film standards (6.3 μm thick) which were mounted on Mylar substrates. Quantification of mercury was estimated using gold and thallium Mylar film standards which were used to interpolate the mercury fluorescence intensity since a mercury standard slowly loses mercury content over time and is ineffective for our use. XFI images were processed using SMAK software (Webb, 2016). X-ray fluorescence levels for each windowed element were normalized to the incoming beam and background signal was subtracted from each pixel by subtracting the average intensity of an area around larvae tissue. Units used in XFI are $\mu g/cm^2$ and expresses the amount of element within a pixel as a function of the surface area. Significant differences were evaluated in livers using a Student's *t*-test on the amount of mercury or zinc in each treatment group.

3.3 High Energy Resolution Fluorescence Detection XAS Methods

3.3.1 Sample Preparation

Experimental solution samples were prepared as 1 mM absorbing atom and loaded into 2 mm × 3 mm × 22 mm Delrin cuvettes wrapped in metal-free adhesive Mylar tape and flash frozen in a slurry of liquid nitrogen-cooled isopentane. Solid samples were prepared as 5% weight compound diluted with BN and grounded to a fine powder, then loaded into metal powder plates windowed with metal-free Mylar tape.

3.3.2 Stanford Synchrotron Radiation Lightsource Beamline 6-2

Selenium $K\alpha_1$ and mercury L_{III}-$L\alpha_1$ HERFD XAS spectra was measured at SSRL using beamline 6-2. The beamline was equipped with a Si(311) double-crystal monochromator together with a single or 6-element array of Si(844) crystal analyzers to record the Se $K\alpha_1$ emission line (Figure 3.1) or a 5 or 6-element array of Si(555) crystal analyzers to record the Hg L_{III}-$L\alpha_1$

emission line (Figure 3.1). Incident and transmitted X-ray intensity was monitored using a helium and nitrogen-filled ionization chambers, respectively. Samples were placed in a liquid helium cryostat 45° to the incident X-ray beam holding an approximate temperature of 10 K to minimize thermal contributions. Energy calibration of the monochromator was relative to the lowest-energy inflection of standard foils; grey hexagonal Se foil inflection point assumed to be 12,658 eV, and Hg–Sn foil inflection point assumed to be 12,285 eV. Fluorescence of samples were measured using a single-element silicon-Vortex solid-state detector.

Optical precision is crucial to optimize the energy resolution in HERFD XAS. Therefore, operating procedures for HERFD XAS begin with alignment of the sample cuvette. The entire sample space is monitored to identify the minima and maxima limits of the sample in 3D Cartesian space, as well as the 45° offset of the cuvette. This is followed by a spectrometer scan which produces an emission scan (ω) encompassing the entirety of the emission line of interest – $K\alpha_1$ or Hg L_{III}-$L\alpha_1$ (Figure 3.1). Each crystal analyzer, the detector and cryostat are positioned on intersecting Rowland circles and the geometry is maintained by motorized stages as the spectrometer is being scanned (refer to Figure 2.5). The signal from the crystal analyzers is simultaneously recorded. The centroid of the emission scan is selected and the spectrometer is then positioned in such a way to satisfy the Bragg geometry which produced the highest intensity of the emission scan. An in-hutch photon shutter was used when data was not actively being recorded and aluminum filters upstream of the incident ion chamber were used to control X-ray exposure on the sample. Following this, a HERFD XAS scan can be performed with increasing incident energy (Ω) spanning the desired near-edge region. Scans are typically collected from one corner of the sample space and moved to a fresh spot for each subsequent scan. The sequential scans are mapped along, similar to a raster scan pattern, in steps to fresh spots when needed. The SPEC data acquisition software (Certified Scientific Software, Cambridge, Massachusetts, USA) allows for user control on the number of scans per spot as well as the desired position of the spot on the sample. Resonant inelastic X-ray scattering (RIXS) (see Chapters 6 and 7) was performed similar to the regular HERFD XAS described above, although instead of collecting one near-edge spectra at the highest intensity of the emission peak, multiple near-edge spectra are collected at 0.25 eV incremental segments along the emission scan to produce the RIXS plot. The 3D RIXS plots show the energy transfer ($\Omega-\omega$) (incident energy – emission energy) as a function of the incident energy (ω), with the photon count illustrated in the *z*-direction.

3.3.3 Data Analysis, Reduction, and Fitting

Data reduction and analysis was carried out using the EXAFSPAK program suite (George, G.N., 2000). Calibration, background subtraction, and normalization was performed as described in section 3.1.3.

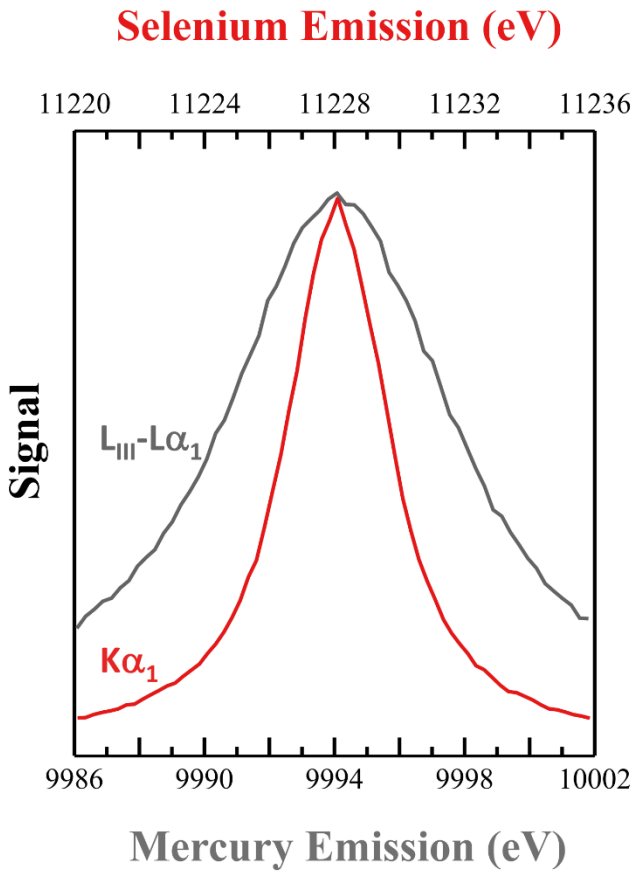

Figure 3.1. Mercury L_{III}-Lα_1 (*grey*) and selenium Kα_1 (*red*) emission scans for HERFD XAS.

CHAPTER 4. Phenylthiourea Alters Toxicity of Mercury Compounds in Zebrafish Larvae

4.1 Preface

Previous work on investigating the effects of mercury compounds in zebrafish larvae found direct accumulation of mercury compounds in sensory cells which may have implications on the neurological symptoms associated with mercury poisoning (Korbas et al., 2012). This led to the interest in understanding the effects of mercury on neuromasts, which are mechanosensory hair cells in fish responsible for sensing mechanical changes in water (Dambly-Claudière et al., 2003). In order to better visualize fluorescent stains, such as those tagged for neuromasts, researchers commonly use 1-phenyl-2-thiourea (PTU) to block pigment formation before first melanisation in order to produce transparent zebrafish and achieve optical transparency. Preliminary studies have shown that zebrafish larvae exposed to PTU early in development, followed by the addition of mercury compounds, had dramatically altered toxicological responses relative to zebrafish larvae not treated with PTU. Zebrafish larvae exposed to organic mercury following PTU hypopigmentation had poorer survival rates, while zebrafish larvae exposed to inorganic mercury appeared to be protected. This drastic variation motivated the following investigation using X-ray absorption spectroscopy into the mercury species responsible for the change in toxicity.

Author Contributions

This chapter has been published in the *Journal of Inorganic Biochemistry* and reformatted to abide by the guidelines of CGPS.

MacDonald, T.C., Nehzati, S., Sylvain, N.J., James, A.K., Korbas, M., Caine, S., Pickering, I.J., George, G.N. and Krone, P.H. (2015). Phenylthiourea alters toxicity of mercury compounds in zebrafish larvae. *J Inorg Biochem*, **151**, 10-17.

This chapter also appears in the PhD dissertation of Tracy C. MacDonald (2015) titled "Effects of inorganic mercury on developing zebrafish (*Danio rerio*) larvae".

T. C. MacDonald performed inorganic mercury trials on zebrafish, collected and analyzed XFI data, performed statistical analysis, and drafted the manuscript.
S. Nehzati prepared, collected and analyzed EXAFS data, conducted DFT calculations, and drafted XAS analysis in manuscript.
N. J. Sylvain performed preliminary trials on zebrafish and exposure procedures.
A. K. James performed organic mercury trials on zebrafish and collected XFI data.
M. Korbas performed deformity and mortality organic mercury trials on zebrafish.
S. Caine performed statistical analysis.
I. J. Pickering, G. N. George, and P. H. Krone provided scientific guidance, edited the manuscripts, and provided funding for the research.

4.2 Abstract

In recent years larval stage zebrafish have been emerging as a standard vertebrate model in a number of fields, ranging from developmental biology to pharmacology and toxicology. The tyrosinase inhibitor 1-phenyl-2-thiourea (PTU) is used very widely with larval zebrafish to generate essentially transparent organisms through inhibition of melanogenesis, which has enabled many elegant studies in areas ranging from neurological development to cancer research. Here we show that PTU can have dramatic synergistic and antagonistic effects on the chemical toxicology of different mercury compounds. Our results indicate that extreme caution should be used when employing PTU in toxicological studies, particularly when studying toxic metal ions.

4.3 Introduction

Zebrafish (*Danio rerio*) are fresh-water fish that have been extensively and increasingly used as an animal model in a variety of research areas over the past 30 years (Craig et al., 2006). Key characteristics that make the zebrafish an excellent model vertebrate system include nearly transparent embryos, rapid development outside the mother, large egg clutch, and a fully sequenced genome (Yang et al., 2009). As a model vertebrate system for studying the development

of the embryo, researchers have used zebrafish to explore metal toxicity (Yang et al., 2009;, Dave and Xiu, 1991; Blechinger et al., 2002; Korbas et al., 2008; Korbas et al., 2010a; Korbas et al., 2012; Korbas et al., 2013) as well as various human diseases (Craig et al., 2006; Kari et al., 2007).

In developmental biology research, zebrafish embryos and larvae offer a particular advantage over other model systems in that they are nearly transparent. Transparency and development outside the mother have allowed researchers to create a well-characterized staging series from fertilized embryo to hatched larva (Yang et al., 2009). Many techniques involve viewing fluorescent stains, probes or proteins using optical microscopy (Karlsson et al., 2001) which can be hindered by natural pigmentation in the fish as they age. Zebrafish develop black melanophores, yellow xanthophores and reflective iridophores (Rawls et al., 2001). One commonly used technique for inhibiting natural pigmentation is the inhibition of tyrosinase activity (Thanigaimalai et al., 2011) by exposing embryos to 1-phenyl-2-thiourea (PTU) (Figure 4.1) which inhibits melanogenesis in the melanophores (Karlsson et al., 2001; Whittaker, 1966). Additionally, normal pigmentation is restored in zebrafish following PTU treatment after a two week recovery period in water with no exogenous agents such as PTU (Karlsson et al., 2001).

When the PTU pigment blocking process was initially developed, no significant effects on hatching or survival were noted when a dose of 75 µM PTU was used (Karlsson et al., 2001). However, concentrations of 200 µM PTU are frequently used (Parker et al., 2013) with such concentrations considered standard protocols (Westerfield, 1995). Recently, evidence has been emerging that commonly used doses of PTU may not be as benign as previously had been assumed (Elsaliani, 2003; Bohnsack, 2011; Li, 2012). Elsalini and Rohr (2003) found that PTU can interfere with thyroid hormone production and thus may alter normal development after 60 hours post fertilization. PTU also has been reported to affect extraocular muscle development and neural crest development (Bohnsack, 2011). Its use has also been seen to result in reduced body size and specifically in smaller eye lenses and more tightly packed eye cells (Li, et al., 2012). To date, however, and despite the widespread use of zebrafish, the effects of PTU on the toxicity of exogenous chemical entities have not been studied. In the course of conventional microscopy studies of the effects of mercury compounds on the mechanosensory apparatus of the zebrafish, we uncovered dramatic changes in toxicology when PTU was used to generate transparent fish.

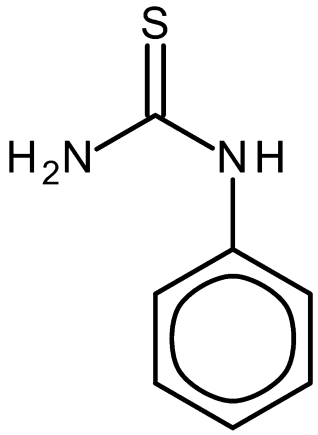

Figure 4.1. Schematic structure of the tyrosinase inhibitor 1-phenyl-2-thiourea (PTU).

We present herein a study of the effects of PTU in combination with different mercury compounds on larval stage zebrafish and show that PTU substantially perturbs these systems in ways that are totally different for inorganic mercury (Hg^{2+}) species and methylmercury species.

4.4 Materials and Methods

4.4.1 *Chemicals*

Phenylthiourea (PTU) and mercuric chloride were purchased from Sigma Aldrich (Oakville, ON) and methylmercury hydroxide from Strem Chemicals Inc. (Newburyport, MA). A 1000 ppm (3.98 mM) methylmercury chloride solution were obtained from Alfa Aesar (Ward Hill, MA).

4.4.2 *Zebrafish*

All procedures were approved by the University of Saskatchewan Ethics Board. Adult zebrafish (*Danio rerio*) were mated using the marble technique (Westerfield, 1995). Embryos were collected and raised to 22 hours post fertilization (hpf) in system water in a 28°C incubator with a 14:10 hour light:dark cycle.

4.4.3 *Statistical Analysis*

For comparisons involving deformity and death rates, significance was determined using ANOVA with a Tukey's post-hoc pairwise test to compare treatments within each day. A Student's *t*-test was used to compare Hg values in the livers of fish imaged using X-ray fluorescence imaging (XFI). For all statistical analyses a P-value <0.05 was considered to be significant.

4.4.4 *X-ray Fluorescence Imaging (XFI) Sample Preparation*

Half of the zebrafish were raised in 100 µM PTU until 3 days post fertilization (dpf) while the second half were raised to 3 dpf in system water. All zebrafish were then randomly divided into the following treatment groups: control, 100 µM PTU, both 2 and 4 µM $HgCl_2$ in the presence or absence of PTU, both 0.2 and 0.5 µM CH_3HgCl in the presence or absence of PTU. These doses were selected to represent a high mercury exposure; however, the number of deaths in the 0.5 µM

CH_3HgCl group prohibited collection of any samples. The dose 0.2 µM CH_3HgCl was selected because fish in the 0.1 µM CH_3HgCl were found to have few deformities and no deaths. After a 48 hour exposure all fish were rinsed 3 times in fresh system water to remove excess mercury on the surface of the fish. Zebrafish were fixed, embedded and sectioned as previously described (Pushie et al., 2014).

4.4.5 *X-ray Fluorescence Imaging (XFI)*

XFI data were collected at the Advanced Photon Source (APS) in Argonne, IL, USA on beamline 20-ID-B. The storage ring was operating in continuous top-up mode at 102 mA and 7.0 GeV. An incident X-ray energy of 13.45 keV was selected to avoid the Br K-edge while being able to monitor the Hg $L\alpha_{1,2}$ and Zn Kα fluorescence lines. A Si(111) double-crystal monochromator and Rh-coated mirrors were used for focusing and harmonic rejection. Samples were mounted at 45° to the incident X-ray beam and raster scanned, with a silicon-drift Vortex detector at 90° to the incident X-ray beam (Korbas et al., 2012). Kirkpatrick–Baez Rh-coated focusing mirrors were used to generate a micro-focused beam of 5 µm diameter. Samples were raster scanned using a step size of 5 µm with a beam exposure time of 0.6 s per point.

4.4.6 *X-ray Fluorescence Imaging (XFI) Data Analysis*

Data collected from X-ray fluorescence imaging were processed as previously described, with normalization to the incoming beam intensity and removal of background signal by averaging the intensity per element in the area outside of the tissue then subtracting this amount from each pixel in the entire image. Certified highly-uniform thin film standards mounted on 6.3 µm Mylar substrates for zinc, gold, and thallium were obtained from Micromatter Co. (Vancouver, BC). To quantify the amount of zinc per pixel, the zinc standard was imaged, normalized and background subtracted using a blank foil. Because mercury amalgam standards slowly decrease in mercury content over time, mercury was quantified using gold and thallium standards, as they are adjacent to mercury on the periodic table. These standards were imaged, normalized and background subtracted. Linear interpolation was then used to estimate a calibration for the mercury intensity for quantification of the mercury in the zebrafish sections. This method was verified by measurement of a new mercury-silver amalgam standard foil (Micromatter Co., Vancouver, BC).

This worked only with a fresh mercury-amalgam standard as the mercury reading was found to decrease on storage, presumably due to loss of mercury as vapor.

Due to time constraints associated with limited allocations of beamtime and long acquisition time (an average of 3.5 h per sample), only a limited number of samples can be run. Therefore 3 representative zebrafish were selected for each treatment group for synchrotron imaging. Following the quantification of mercury in each sample, significant differences were evaluated with a Student's *t*-test on the amount of mercury (in $\mu g/cm^2$) in the livers of each treatment group.

4.4.7 *X-ray Absorption Spectroscopy (XAS)*

Samples for X-ray absorption spectroscopy (XAS) were prepared at 10:1 mM PTU:Hg stoichiometries in aqueous solution (using CH_3HgOH or $HgCl_2$). Solution mixtures were incubated for 5 minutes at room temperature then were loaded into 2 mm × 3 mm × 22 mm acrylic cuvettes and were flash frozen in a slurry of liquid nitrogen-cooled isopentane.

Mercury L_{III}-edge XAS spectra was measured on the structural molecular biology beamline 7-3 at the Stanford Synchrotron Radiation Lightsource (SSRL) with the SPEAR storage ring operating at 3.0-GeV with a current of 500 mA. The beamline was equipped with a Si(220) double-crystal monochromator with harmonic rejection achieved by setting the cut-off energy of an upstream Rh-coated mirror to 15 keV. Incident X-ray intensities were monitored using a nitrogen-filled gas ionization chamber and X-ray absorption of samples was measured as the X-ray fluorescence excitation spectrum using a 30-element germanium detector array (Cramer et al., 1988). Soller slits and Ga_2O_3 X-ray filters were (EXAFS Materials, Danville, California, USA) used to attenuate unwanted scattered radiation and to preserve detector linearity. Samples were placed in a liquid helium cryostat to maintain an approximate temperature of 10 K during data collection to reduce X-ray induced photochemistry and atomic vibrations. Simultaneous absorption of a downstream standard Hg–Sn amalgam metal foil was measured by transmittance. Incident X-ray energy calibration was accomplished using the lowest-energy Hg L_{III} inflection point of the standard foil, assumed to be 12,285.0 eV. Each sample was subjected to eight sweeps approximately 22 minutes long.

Extended X-ray absorption fine structure (EXAFS) oscillations $\chi(k)$ were analyzed using the EXAFSPAK program suite (George, G.N., 2000), as previously described (George et al., 1996)

and assuming an Hg L_{III} threshold energy (E_0) of 12,305.0 eV. Phase-correction of Fourier transforms employed Hg—S backscattering. FEFF version 7 was utilized to compute theoretical phase and amplitude functions.

4.4.8 *Density Functional Theory (DFT)*

DFT calculations used the program Dmol^3 and Biovia Accelrys Materials Studio V7.0 for geometry optimization (Delley, 1990; Delley, 2000). Geometry optimization used the Perdew-Burke-Ernzerhof functionals for both the potential during the self-consistent field procedure and the energy, and employing an all-electron relativistic core treatment. Solvent effects were simulated by using the Conductor-like Screening Model (COSMO) with a dielectric value representing water (ε = 78.39) (Klamt and Schüürmann, 1993). Geometry optimization calculations integrated only enthalpy and not entropy terms.

4.5 **Results and Discussion**

4.5.1 *Toxicological Profiles*

Prior to examining the effects of mercury, range-finding studies were conducted to determine the PTU dose that combined the best pigment inhibition with the lowest rate of adverse effects. Treatment groups were 0 (control), 25, 50, 75, 100, 200 and 300 µM PTU, each with 75 larvae at 22 hours post fertilization (hpf). Consistent with normal practice, this time was chosen as zebrafish pigment formation begins at ~24 hpf, with rapid progression thereafter (Karlsson et al., 2001) and to inhibit the pigment formation larvae must be exposed to PTU before this stage (Karlsson et al., 2001). Survival, hatch, deformity and transparency rates were assessed from 1 to 5 days post fertilization (dpf). Preliminary trials found that a dose of 100 µM PTU resulted in lower death rates and fewer deformities than the more commonly used higher dose of 200 µM PTU, but with comparable suppression of pigment formation. Therefore, 100 µM PTU was used in all subsequent work. Two different categories of mercury compound were tested (mercuric chloride and methylmercury chloride), based on the differential toxicology previously reported (Korbas, 2012). In these previous studies, the highest mercury concentrations in zebrafish exposed to mercuric chloride were found in the olfactory epithelial cells (Korbas, 2012). In contrast, methylmercury chloride preferentially targeted the developing lens (Korbas, 2008; Korbas, 2010b;

Korbas et al., 2012; Korbas et al., 2013). While zebrafish exposed to mercuric chloride accumulated mercury in the ventricular region of the brain, zebrafish exposed to methylmercury chloride accumulated mercury in the muscle tissue (Korbas et al., 2012). As one would expect, mercury accumulated in the detoxification organs, the pronephros and liver, following exposure to both forms of mercury (Korbas et al., 2012).

Zebrafish were raised to 3 dpf in either system water or in 100 µM PTU solution. Treatment solutions were replaced with fresh solution every 24 hours. Fish were examined for deformities and deaths after 24, 48 and 72 hours following initial exposure, with deformities being defined as fin malformations, edema, and moribund behaviour. The results of toxicological screening with mercuric chloride and methylmercury chloride are shown in Figure 4.2 and Figure 4.3, respectively.

At 3 dpf, zebrafish larvae were exposed to 0 (control), 2 and 4 µM $HgCl_2$ in system water in the presence and absence of 100 µM PTU (n = 100 larvae per treatment). Two-way analysis of variance (ANOVA) was utilized to determine whether statistically significant differences existed for cumulative mortality between $HgCl_2$ and PTU + $HgCl_2$ treatment groups at 24, 48, and 72 hours post-exposure. The PTU + $HgCl_2$ treatment group showed very significant decreases in mortalities compared to $HgCl_2$ alone (Figure 4.2), with all P values being $<10^{-3}$. Although at first sight the data seem to suggest that there may be more deformities in the fish exposed to both $HgCl_2$ and PTU when compared to $HgCl_2$ alone, this is actually due to the fact that there are significantly more dead larvae in the latter case (Figure 4.2). Hence, the data indicate that PTU reduces the toxicity of $HgCl_2$.

Methylmercury species can be considerably more toxic than inorganic mercury compounds (Korbas et al., 2012) and can also have a very steep dose-response curve. To account for this, correspondingly lower levels of methylmercury chloride (CH_3HgCl) were used: 0.05, 0.1 and 0.5 µM CH_3HgCl in system water, in the presence and absence of 100 µM PTU. In contrast to $HgCl_2$, which had decreased toxicity in the presence of PTU, CH_3HgCl showed enhanced toxicity in the presence of PTU (Figure 4.3). While the trends were not as striking as for mercuric chloride, the increase in deaths of fish exposed to 100 µM PTU + 0.5 µM CH_3HgCl, was statistically significant at 48 and 72 hours post-exposure compared to fish exposed to 0.5 µM CH_3HgCl in absence of PTU, with $P < 0.0001$ for both (see Tables A.1 to A.3 in Appendices).

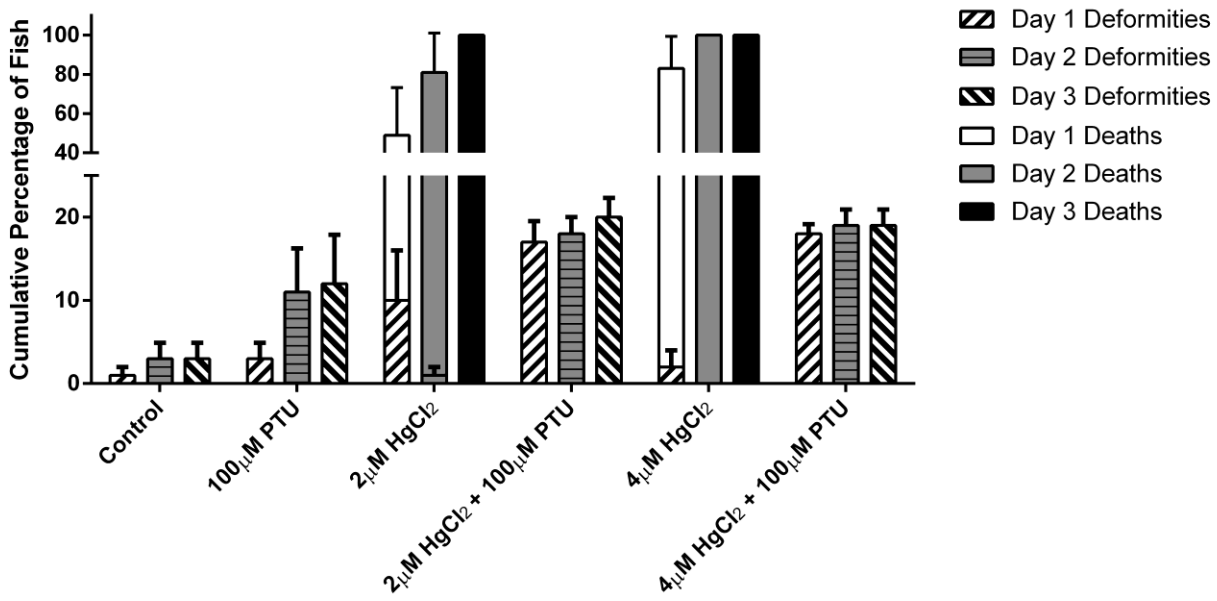

Figure 4.2. Cumulative mortality (%) stacked on top of cumulative deformity (%) (+SE) of zebrafish larvae over 3 days of exposure to various $HgCl_2$ treatments, with and without PTU. Note the absence of deaths following PTU addition, showing that PTU *decreases* the toxicity of $HgCl_2$. The control was system water from the fish facility.

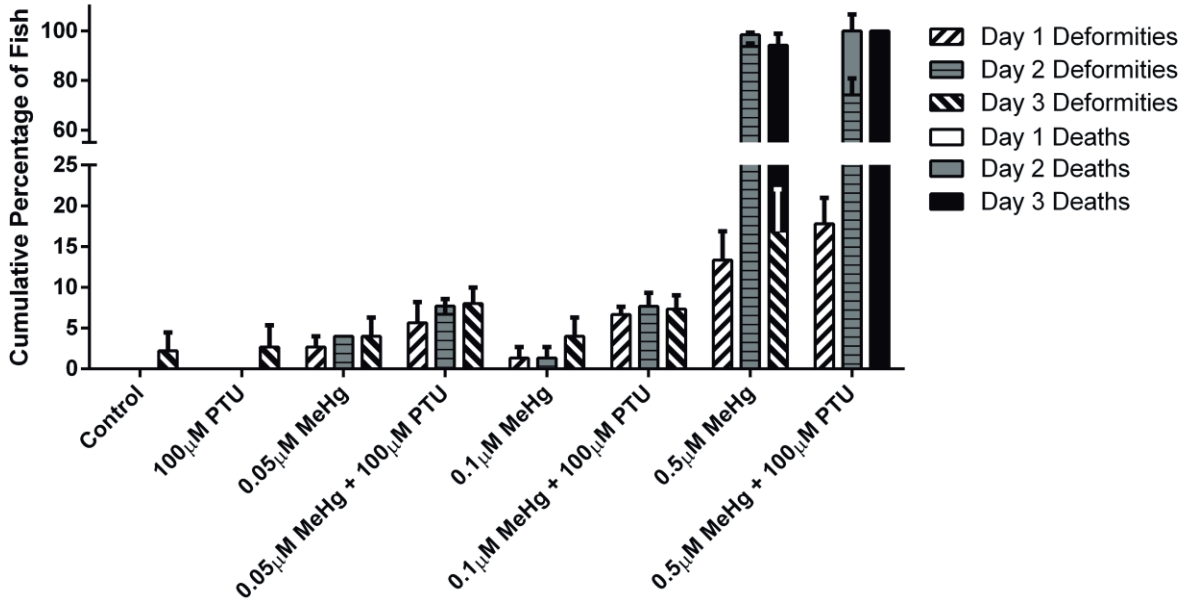

Figure 4.3. Cumulative mortality (%) stacked on top of cumulative deformity (%) (+SE) of zebrafish larvae over 3 days of exposure to various CH_3HgCl (MeHg) treatments with and without PTU. Note the increased deaths at 0.5 µM MeHg with added PTU, showing that PTU *increases* the toxicity of CH_3HgCl. The control was system water from the fish facility.

The small differences between control and 100 μM PTU in Figure 4.2 and Figure 4.3 are primarily a reflection of the fact that the tests for Figure 4.2 and Figure 4.3 were done at different times. Such variations are not uncommon and are not considered statistically significant.

4.5.2 *X-ray Fluorescence Imaging (XFI)*

XFI (Pushie et al., 2014) was used to map Hg accumulation in representative fish from each treatment group and to quantify Hg in regions of interest. The results of which are shown in Figure 4.4 to Figure 4.7, together with the corresponding histological images. Zinc, which is mapped simultaneously with mercury, is also shown for all sections; it is common practice to use the Zn image to ensure that the correct region is scanned (Korbas et al., 2012). Zinc is normally abundant in essentially all tissues but is present at notably high levels in pigment cells of zebrafish. Because PTU blocks pigment formation in the zebrafish, pigment levels in PTU treated fish were low and as expected, zinc levels were often correspondingly lower.

Figure 4.4 shows sections from zebrafish treated with $HgCl_2$ solutions in the absence and presence of PTU. The olfactory pits have previously been shown to be a target organ for $HgCl_2$ (Korbas et al., 2012); Figure 4.4 shows XFI of sections of this region. The comparative absence of mercury in the PTU-exposed larva is striking and is consistent with the protective effect of PTU observed in the toxicological profile. Figure 4.5 shows XFI of sections through the liver, gut, muscle, and pronephros. Here, the pigment spots in the absence of PTU treatment are observed to be larger and to have higher zinc levels (Figure 4.5, A & C) than the pigmented areas in the presence of PTU treatment (Figure 4.5, B & D). As with olfactory pits in Figure 4.4, the levels of mercury in the trunk region are substantially lower in PTU exposed fish, relative to fish exposed to $HgCl_2$ alone. Mercury concentrations in the livers of three separate fish from the 48-hour 4 μM exposure group were quantified and averaged. A Student's two-tailed *t*-test determined the mean mercury concentrations to be significantly greater in the $HgCl_2$ treatment compared to the PTU + $HgCl_2$ treatment with $P < 0.001$ for all. The mercury concentrations in the fish treated with solutions of PTU + $HgCl_2$ were 60-fold lower than in fish exposed to $HgCl_2$ solutions alone.

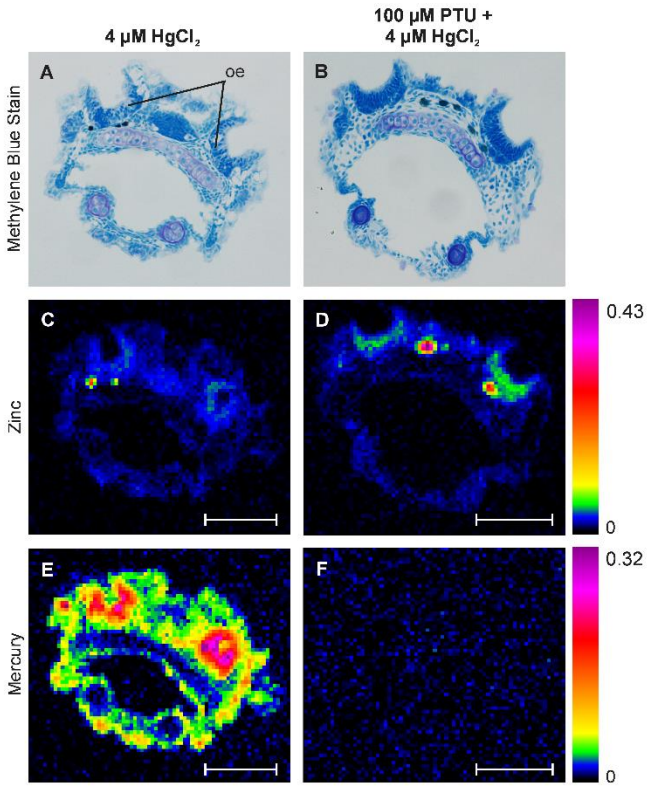

Figure 4.4. Transverse sections through the olfactory region of zebrafish treated with 4 µM $HgCl_2$ in absence (A, C and E) or presence (B, D and F) of 100 µM PTU. In each column the section stained with methylene blue for the optical image (A or B) was serial (immediately adjacent) to the unstained section used for X-ray fluorescence imaging of zinc (C or D) and mercury (E or F). White scale bars represent 100 µm. The colour bars show the quantification of zinc (C, D) and mercury (E, F) in $\mu g/cm^2$. oe= olfactory epithelium.

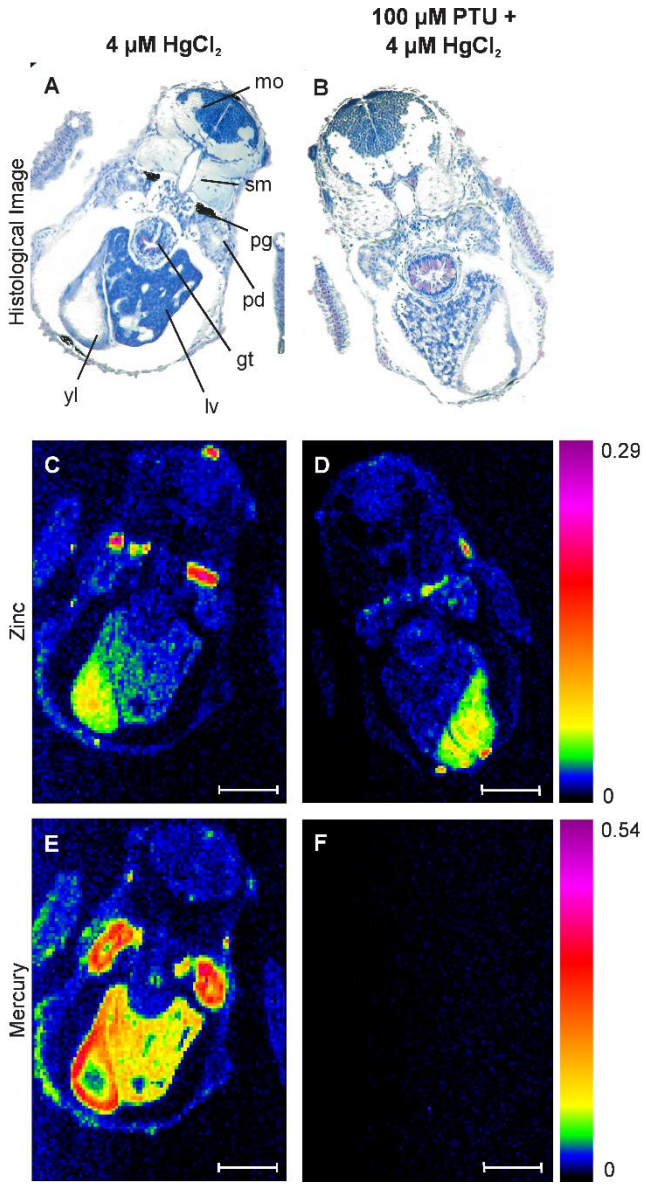

Figure 4.5. Transverse sections through the trunk region of zebrafish treated with 4 µM $HgCl_2$ in absence (A, C and E) or presence (B, D and F) of 100 µM PTU. White scale bars represent 100 µm. mo= medulla oblongata, sm= somitic muscle, pd= pronephric duct, gt= gut tube, lv= liver, yl= yolk. Additional details found in Figure 4.4.

Figure 4.6 shows zebrafish head sections from larvae exposed to 0.2 µM CH_3HgCl in absence and presence of PTU. Cells in the lens and retina are known to be among the primary targets of methylmercury compounds (Korbas et al., 2008; Korbas et al., 2010a;, Korbas et al., 2012; Korbas et al., 2013). The differences in pigment levels in the retinal pigmented epithelia in the optical micrographs can be clearly seen as a loss of black coloration in Figure 4.6B compared with Figure 4.6A, and this is paralleled by the decrease in Zn levels in those regions (Figure 4.6D compared with Figure 4.6C). Figure 4.7 shows XFI of the trunk region for the CH_3HgCl exposures; here also lower Zn levels in discrete regions that are normally pigmented are seen in the PTU-treated fish. In marked contrast to the $HgCl_2$ data, both head and trunk sections of the larvae treated with CH_3HgCl and PTU are visually higher in Hg than those treated with CH_3HgCl alone. This again is consistent with the increase in CH_3HgCl toxicity observed in PTU treated fish. Similar to the $HgCl_2$ treatment, a two-tailed Student's *t*-test with equal variance was conducted on average mercury levels in each liver of three fish per treatment group and showed $P < 0.05$. Zebrafish exposed to CH_3HgCl and PTU had approximately two fold higher mercury levels than those exposed to CH_3HgCl only.

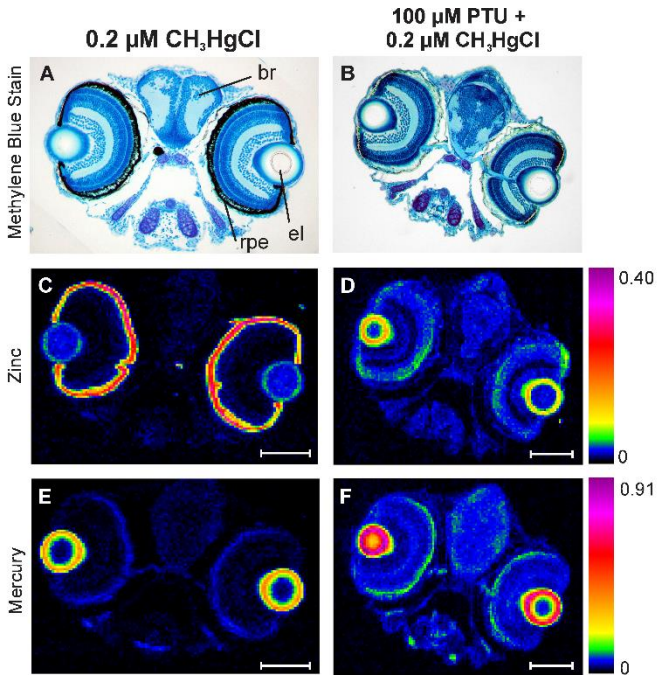

Figure 4.6. Transverse sections through the eye region of zebrafish treated with 0.2 µM CH_3HgCl in absence (A, C and E) or presence (B, D and F) of 100 µM PTU. White scale bars represent 100 µm. br= brain, el= eye lens, rpe= retinal pigmented epithelium. Additional details found in Figure 4.4.

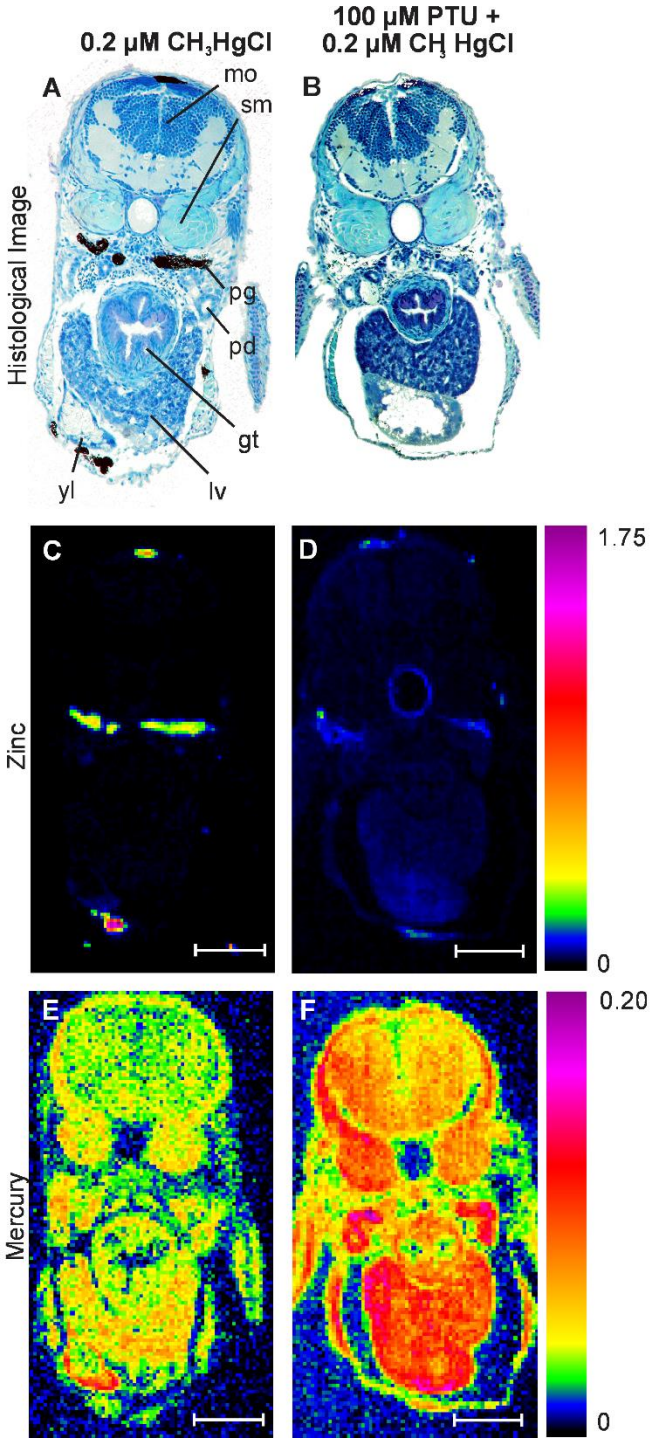

Figure 4.7. Transverse sections through the trunk region of zebrafish treated with 0.2 µM CH_3HgCl in absence (A, C and E) or presence (B, D and F) of 100 µM PTU. White scale bars represent 100 µm. mo= medulla oblongata, sm= somitic muscle, pd= pronephric duct, gt= gut tube, lv= liver, yl= yolk. Additional details found in Figure 4.4.

The XFI results together with the observations of deformity and mortality show that PTU has opposite effects on the toxicology of the two different chemical forms of mercury, being antagonistic for inorganic mercury and synergistic with methylmercury. This suggests not only that PTU is interacting chemically with the mercury species, but also that it interacts differently with the two types of mercury species. We therefore investigated the possible solution chemistry of PTU and the mercury species using X-ray absorption spectroscopy and density functional theory (DFT).

4.5.3 Extended X-ray Absorption Fine Structure (EXAFS) and Density Functional Theory (DFT)

We examined the EXAFS portion of the X-ray absorption spectrum, which can be used with quantitative analysis to obtain a radial structure (Cotelesage et al., 2012). EXAFS spectra of methylmercury and inorganic mercury in the presence of PTU, together with the associated Fourier transforms, are shown in Figure 4.8. The results of EXAFS curve-fitting analysis are also shown in Figure 4.8, with the derived structural parameters summarized in Table 4.1. Because EXAFS currently lacks the sensitivity to the micromolar levels used in the zebrafish exposures, we employed higher concentrations of both Hg and PTU, but maintaining an excess of PTU as in the fish exposures. In the case of methylmercury we used methylmercury hydroxide (CH_3HgOH) rather than the chloride because methylmercury chloride was insufficiently soluble; this species will in any case be the dominant form in dilute solution when the chloride is used (Korbas et al., 2012). Mercury typically forms compounds with either two-coordinate linear digonal coordination, three-coordinate trigonal planar coordination, or four-coordinate pseudo tetrahedral coordination (George et al., 2008). The bond-lengths to Hg change systematically with coordination type; for example for Hg—S coordination environments, two, three and four coordinate species have bond-lengths of 2.35, 2.46 and 2.54 Å, respectively (Allen, 2002).

The EXAFS of PTU with inorganic Hg^{2+} indicated a 4-coordinate complex, with 2 Hg—S donors at 2.49 Å and 2 Hg—N or Hg—O at 2.43 Å (Figure 4.8, Table 4.1). In support of this examination of the Cambridge Structural Database (CSD) (Allen, 2002) shows a marked predominance of four-coordinate Hg^{2+} compounds when coordination with thione (C=S) sulfur donors is present, with 190 database hits for 4-coordinate species, 5 hits for 3-coordinate species, and only 3 hits for 2-coordinate species. Although EXAFS cannot normally distinguish between

Hg—O and Hg—N due the similarity in ligand atomic number, the bond-lengths of four-coordinate Hg^{2+} species in CSD strongly support the assignment of an Hg—N coordination. Thus, while the average bond-length for four-coordinate species containing Hg—O bonds is 2.61 Å, that for four-coordinate species containing Hg—N bonds is 2.42 Å, which is in good agreement with our EXAFS-derived bond-length of 2.43 Å. Similarly, while there are no examples in the CSD of Hg^{2+} bound by two thione ligands with two additional nitrogen donors, the average Hg—S bond-length for thione-coordinate species is 2.52 Å, also in good agreement with our EXAFS derived Hg—S bond-length of 2.49 Å.

Table 4.1. Extended X-ray absorption structure (EXAFS) parameters[a] and curve-fitting results of phenylthiourea with mercury compounds at stoichiometry of 10:1.

Aqueous complex	Bond	N	R (Å)	σ^2 (Å^2)	ΔE_0 (eV)	F
PTU:CH_3HgOH	Hg–C	1	2.063 (3)	0.0025 (3)	– 15.0 (5)	0.3785
	Hg–S	1	2.374 (2)	0.0038 (2)		
PTU:$HgCl_2$	Hg–N	2	2.430 (2)	0.0026 (3)	– 10.3 (3)	0.2497
	Hg–S	2	2.493 (1)	0.0030 (1)		

[a]Coordination number N interatomic distances R (Å), Debye-Waller factors σ^2 (Å^2), and threshold energy shift ΔE_0 (eV). Values in parentheses represent the standard uncertainties between the curve fitting parameters and spectroscopy data. Goodness of fit function F is defined as $[\Sigma k^6(\chi(k)_{calc} - \chi(k)_{expt})^2/\Sigma k^6\chi(k)^2_{expt}]^{½}$, where $\chi(k)_{calc}$ and $\chi(k)_{expt}$ are the calculated and experimental EXAFS, respectively, with k being the photoelectron wavevector. Amplitude reduction factor (S_0^2) set to 1.0.

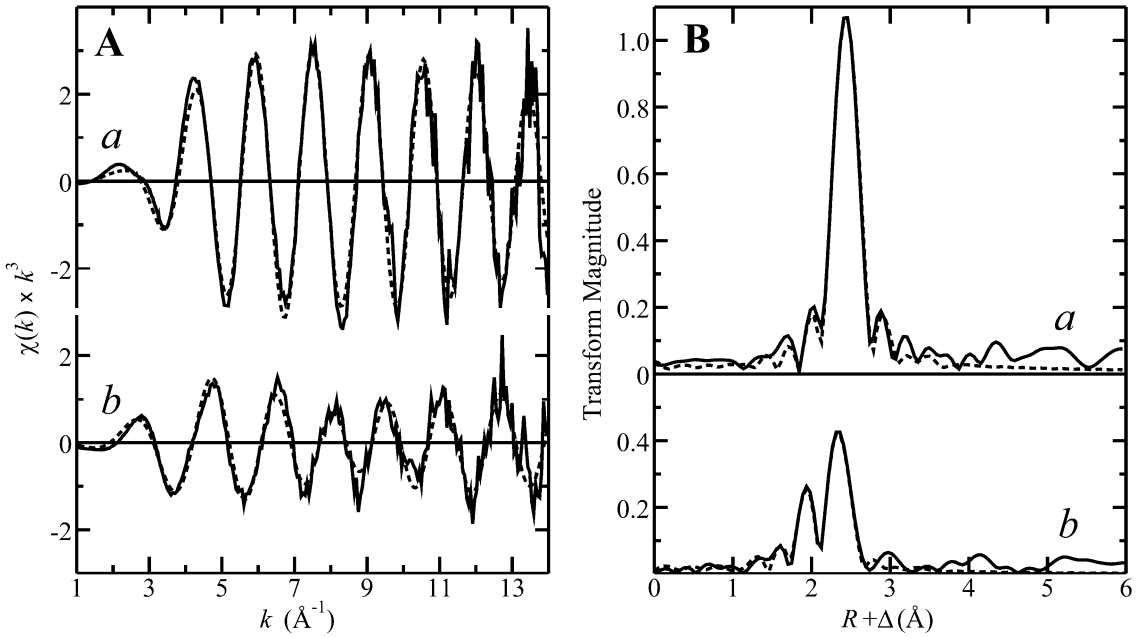

Figure 4.8. Mercury L_{III}-edge extended X-ray absorption fine structure (EXAFS) for phenylthiourea complexes with (*a*) $HgCl_2$ and (*b*) CH_3HgOH, each at a stoichiometry of 10:1. **A** shows the EXAFS oscillations and **B** the corresponding Fourier transforms phase-corrected for Hg—S backscattering. Experimental data are shown as solid lines, with results from curve-fitting analyses (Table 4.1) as broken lines.

The thiourea moiety in PTU contains amide and thione groups, both of which potentially can coordinate mercury. DFT calculations indicate that monomercury four-coordinate species with two PTU bound to one Hg^{2+} each as a bi-functional chelator through both –NH and =S (Figure 4.9A) will be unstable, because the bite angle of the (N–C=S) moiety is too acute to accommodate the Hg and DFT geometry optimizations yield two-coordinate species with Hg coordinated only through the thione sulfurs of the two PTU ligands. Coordination of a single Hg^{2+} by four PTU ligands is possible, with two PTUs bound through their thione sulfurs, and two PTUs contributing bound through their amide nitrogens. However, DFT indicates that such 4-coordinate S_2N_2 mononuclear entities are energetically unfavorable relative to the S_4 complex in which four thione sulfurs are bound, by some 40 kJ/Mol. Thus, in order to explain the four-coordinate model with mixed N and S donors to Hg^{2+}, we need to postulate the formation of a polymeric entity in solution. While there are no crystal structures of polymeric or oligomeric thiourea or phenylthiourea Hg^{2+} structures, examples do exist of polymeric Cd^{2+} structures containing bridging thione ligands derived from phenylthiourea (Yang et al., 2001). Furthermore, while the samples of Figure 4.8 were all solutions made by slow addition with stirring of Hg^{2+} to PTU solutions, it was observed that simple mixing of PTU with Hg^{2+} in solution created an amorphous precipitate, strongly suggesting the formation of some kind of polymer. A schematic fragment of one example of the very large number of possible structures for such oligomeric or polymeric species is shown in Figure 4.9B. With our postulated N_2S_2 coordination, the nitrogen donors can be either protonated or deprotonated, corresponding to cationic or neutral oligomers, respectively. DFT calculations indicate expected Hg—N bond-lengths of protonated nitrogen donors (Hg ←:NH_2—C) to be 2.47 Å, some 0.25 Å longer than the bond-length of a deprotonated nitrogen donor (Hg—NH—C) and a good match for the EXAFS derived bond-length of 2.43 Å, arguing for protonated nitrogen donors and thus a cationic oligomer. We consider the nitrogen coordinated by the phenyl group a less likely metal ligand than the amino nitrogen due to crowding by the phenyl ring. The energy minimized geometry optimized structure of one possible oligomeric fragment is shown in Figure 4.10A. Both Hg—S and Hg—N bond-lengths of 2.55 and 2.47 Å, respectively, agree well with the EXAFS-derived values of 2.53 and 2.43 Å. A number of different coordination environments might be considered plausible, including S_4, N_1S_3, N_2S_2, N_3S_1 and possibly even N_4, which might combine to give an overall average coordination of N_2S_2.

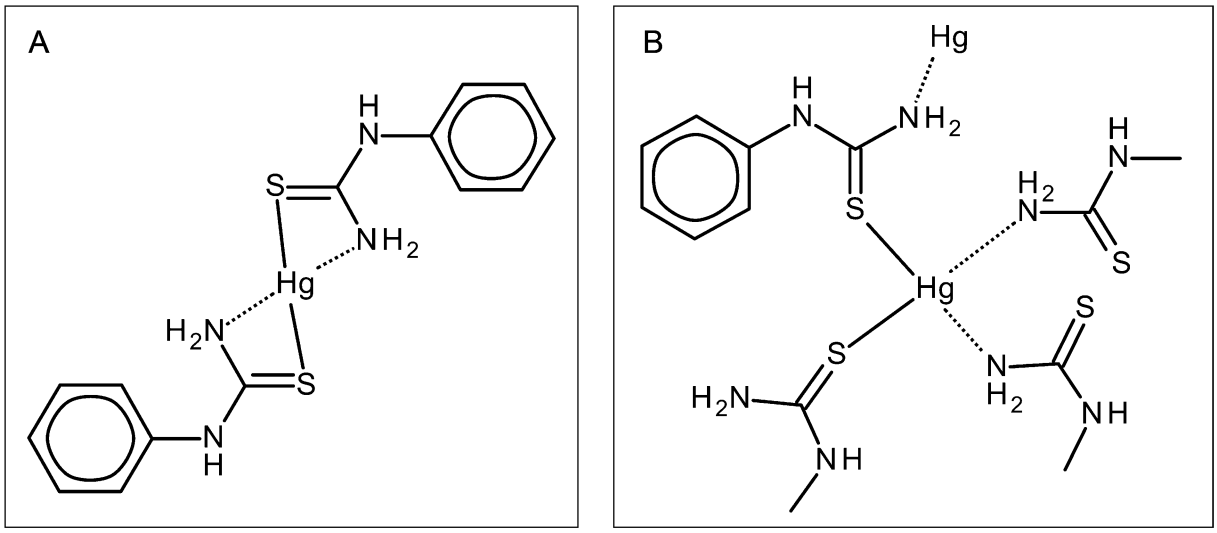

Figure 4.9. Schematic structures of four-coordinate complexes involving PTU and Hg^{2+}. (A) Hg^{2+} coordinated by two bidentate PTU ligands. As discussed in the text, density functional theory calculations indicate that A is unstable. (B) Fragment of one possible oligomeric species. See the discussion in the text for additional details.

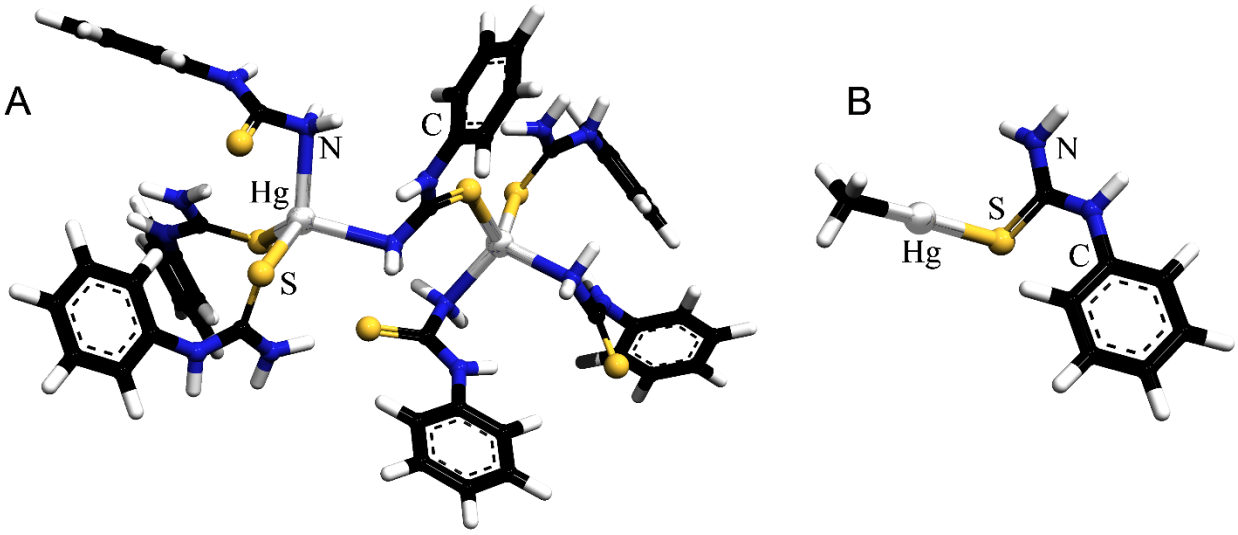

Figure 4.10. Density functional theory energy-minimized geometry-optimized structures of the products resulting from reacting phenylthiourea with (A) $HgCl_2$ or (B) CH_3HgOH in aqueous solution.

However, each of the above coordination environments will have significantly different and characteristic Hg—N and Hg—S bond-lengths, so that a distribution in coordination environments would inevitably result in a spread of Hg—N and Hg—S bond-lengths. This in turn would substantially increase the Debye-Waller factor of the EXAFS (Cotelesage et al., 2012). This is quantified by σ^2, the mean square deviation from the average bond-length R (Table 4.1). The σ^2 value has both static and vibrational components such that $\sigma = \sigma^2_{vib} + \sigma^2_{stat}$ where σ^2_{vib} is the vibrational component and σ^2_{stat} is the static component resulting from heterogeneity of the individual bond-lengths R which is not directly resolved in the EXAFS (Cotelesage et al., 2012). Because the values obtained for σ^2 (Table 4.1) are close to the expected σ^2_{vib} values (Cotelesage et al., 2012) the aforementioned heterogeneity cannot be very pronounced, and we conclude that the bulk of the Hg is actually bound with N_2S_2 coordination. The observed lack of distinct mercury-mercury interactions in the EXAFS (Figure 4.8) means that well-defined relatively rigid bridged structures, such as rhombs with two Hg separated by bridging sulfurs and/or nitrogens, cannot be uniformly present. Investigation of this possibility with DFT indicates that such structures tend to be sterically crowded in any case because of the phenyl groups on the PTU ligands.

The EXAFS data of methylmercury plus PTU clearly indicate the formation of a 2-coordinate species, with Hg—C and Hg—S bond-lengths of 2.06 and 2.37 Å, respectively (Table 4.1). The CSD (Allen, 2002) contains a number of structures in which a thione group (C=S) is coordinated to an aliphatic organo-Hg entity in a 2-coordinate complex, with mean Hg—C and Hg—S bond-lengths of 2.08 and 2.39 Å, respectively, which agree very well with the EXAFS derived bond-lengths. The presence of a two-coordinate compound with PTU is in accord both with the known stability of Hg—S complexes, and with the known predilection of CH_3—Hg species to form two-coordinate complexes; the CSD contains 178, 23 and 17 entries with two-, three- and four-coordinate CH_3Hg, respectively (Allen, 2002). The energy-minimized geometry-optimized density functional theory (DFT) model of a solution structure is shown in Figure 4.10B, for which the computed bond-lengths of 2.05 and 2.39 Å are in excellent agreement with the EXAFS derived values (Table 4.1).

Our results clearly show that oft-assumed innocuous additive PTU significantly modifies the toxicology of both inorganic mercuric and methylmercury species. In the case of inorganic mercury the toxicity is remarkably decreased, whereas with methylmercury it is substantially increased. XFI reveals that this can be attributed to differences in mercury uptake by the zebrafish

larvae, with PTU treatment causing substantially decreased Hg levels for inorganic mercury and causing increased Hg levels for methylmercury. We hypothesize that inorganic Hg^{2+} forms oligomeric or polymeric species with PTU which, due to their relatively large size, would not readily cross cellular membranes and would thus be unable to enter the zebrafish. In the case of methylmercury, XAS and DFT indicate that a molecular entity $[CH_3Hg(PTU)]^+$ is generated in solution through formation of an Hg—S bond with the PTU thione sulfur. Since such a complex would bear a single positive charge, one possible explanation for its increased toxicity may lie in the surface chemistry of cells. It is well known that glycoproteins and polysaccharide chains on cell membranes contribute a negative charge to the cell surface (van den Berg et al., 2006). Electrostatic attraction between positively charged CH_3HgPTU and the cell surface might increase the local availability of $[CH_3Hg(PTU)]^+$, which might then enter the cell and exert its lethal effects.

At the time of writing there is widespread use of PTU for generating transparent zebrafish larvae. However, other methods of obtaining essentially transparent zebrafish larvae are available as alternatives to using PTU and wild-type fish. The *roy orbison* mutant zebrafish lacks iridophores, has few melanocytes and thus has translucent skin and uniformly pigmented eyes (White et al., 2008), while Lister et al. (1999) have reported a mutant named *nacre* that lacks melanophores but has increased numbers of iridophores. White et al. (2008) subsequently created the *casper* strain that is doubly mutant for *roy orbison* and *nacre*, thus lacking both melanocytes and iridophores from embryogenesis to adulthood (White et al., 2008).

In conclusion, while PTU is used very widely in studies of larval phase zebrafish, our results indicate that it can interfere remarkably with the toxicology of mercury compounds. Our study was initiated following control experiments when we sought to use PTU together with conventional microscopy to study aspects of mercury toxicology, but our findings have broad implications that extend outside mercury toxicology. Even though the coordination chemistry of PTU itself has only been studied in few cases, a search of the CSD (Allen, 2002) indicates that PTU forms structurally characterized complexes with Cu, Zn, Ag and Cd. PTU would be expected to coordinate a wide variety of metals, and a CSD search for thiourea-related ligands to metals returns some 1,636 hits. Transition metal complexes account for 1,504 of these, including pharmacologically-relevant platinum and ruthenium species, with the remainder including complexes with toxic metals such as indium, tin, antimony, lead and bismuth. The fact that many of these metals have been studied using the larval stage zebrafish model expands the implications

of our work, and we suggest that extreme caution should be exercised when employing PTU in toxicological studies of metal ions using zebrafish larvae.

4.6 Acknowledgments

The authors thank Dr. R. Gordon at APS for assistance at beamline 20-ID-B, and the staff of SSRL for their assistance. T.C.M., S.N., A.K.J. and S.C.are Fellows in the Canadian Institutes of Health Research (CIHR) Training grant in Health Research Using Synchrotron Techniques (CIHR-THRUST). N.J.S. is a CIHR-THRUST Associate. G.N.G. and I.J.P. are supported by Canada Research Chair awards. This work was supported by the CIHR (G.N.G., I.J.P.), the Saskatchewan Health Research Foundation (G.N.G., I.J.P.), the University of Saskatchewan, and a Natural Sciences and Engineering Research Council of Canada Discovery Grant (P.H.K.). Sector 20 facilities at the Advanced Photon Source (APS), and research at these facilities, are supported by the U.S. Department of Energy (DOE) - Basic Energy Sciences, the Canadian Light Source and its funding partners, the University of Washington, and the APS. Use of the APS, an Office of Science User Facility operated for the U.S. DOE Office of Science by Argonne National Laboratory, was supported by the U.S. DOE under Contract No. DE-AC02-06CH11357. Use of the Stanford Synchrotron Radiation Lightsource (SSRL), SLAC National Accelerator Laboratory, is supported by the U.S. DOE, Office of Science, Office of Basic Energy Sciences under Contract No. DE-AC02-76SF00515. The SSRL Structural Molecular Biology Program is supported by the DOE Office of Biological and Environmental Research, and by the National Institutes of Health (NIH), National Institute of General Medical Sciences (NIGMS) (including P41GM103393). The contents of this publication are solely the responsibility of the authors and do not necessarily represent the official views of NIGMS or NIH.

CHAPTER 5. Chelator Treatment Reduces Mercury Levels in Livers of Zebrafish Larvae Following Exposure to Mercuric Chloride

5.1 Preface

Mercury poisoning in humans is often treated through chelation therapy which involves the multi-ligand binding of a chelating agent to the metal forming a stable ring complex. With the high binding affinity of thiolates (R–S–) to mercury, a number of thiolate-based chelating agents have been designed, however previous work has shown that the leading two treatments for mercury poisoning, DMSA and DMPS, do not form true chelate complexes with Hg^{2+}, thereby suggesting a less than optimal binding (George et al., 2004). Researchers at the University of Kentucky have designed a mercury chelator, 1,3-benzenediamidoethanethiol (B9), that has shown high affinity to the binding of Hg^{2+} in environmental solution settings (Matlock et al., 2002). Presented in this chapter, we extend the investigation on the activity of a more water soluble analogue of B9, 1,3-benzene-diamido-2-carboxylethanethiol (AB9), and study the fate of mercury localization without and with this dithiol in zebrafish larvae. Considering the results from Chapter 4, subsequent experiments using zebrafish larvae were performed without 1-phenyl-2-thiourea treatments. Results herein show AB9 treatment following Hg^{2+} exposure to zebrafish larvae show a promising reduction of mercury accumulation in characteristic target organs. X-ray absorption spectroscopy is used to identify the solution structure of AB9 complexed with Hg^{2+}.

Author Contributions

This chapter will be reformatted and submitted to the *Journal of Inorganic Biochemistry*.

Nehzati, S., MacDonald, T.C., Hackett, M.J., Alaverdashvili, M., Atwood, D.A., Krone, P.H., George, G.N., and Pickering, I.J. (2019) Chelator treatment reduces mercury levels in livers of zebrafish larvae following exposure to mercuric chloride. (*In preparation*)

S. Nehzati prepared the samples, collected and analyzed the XAS, XFI and DFT studies, performed statistical analysis, as well as drafted the manuscript.

T. C. MacDonald assisted with fish trials.

M. J. Hackett assisted with XFI data collection.

M. Alaverdashvili performed statistical analysis.

D. A. Atwood provided the AB9 compound.

P. H. Krone provided scientific input and aquatic facility for the fish trials.

G. N. George and I. J. Pickering provided scientific guidance, edited the manuscript, and provided funds for the research.

5.2 Abstract

Chelation treatments to tightly and specifically bind and remove mercury from the body are suboptimal and need to be improved. We tested 1,3-benzene-diamido-2-carboxylethanethiol (AB9), a water soluble dithiol, for its efficacy in the treatment of acute mercuric chloride toxicity in zebrafish larvae, a common vertebrate model for research. X-ray fluorescence imaging (XFI) results show significant removal of mercury from the livers of zebrafish larvae following treatment with AB9, demonstrating its potential as a candidate for treatment following acute inorganic mercury exposure. Mortality rates of zebrafish treated with AB9 following a dose of inorganic Hg(II) were non-significantly elevated compared to zebrafish dosed with $HgCl_2$ and treated with H_2O. X-ray absorption spectroscopy (XAS) of $HgCl_2$ mixed with AB9 at 3:1 molar ratio revealed mercury coordinated with two S ligands at 2.33 Å. Overall, the results support AB9 removal of inorganic Hg(II) from zebrafish larvae livers via a likely S–Hg–S coordination.

5.3 Introduction

Mercury can be one of the most toxic elements to humans depending on its chemical form and in some forms is a prevailing toxicant found in the environment (Zahir et al., 2005). Thiol groups have high affinity for mercury, which are abundant in proteins found in living organisms and this propensity is potentially harmful to organisms (Clarkson and Magos, 2006). The pathology of mercury toxicity depends on the chemical form as well as the route of exposure (Korbas et al., 2012). Acute inorganic mercury poisoning commonly targets the gastrointestinal

tract and kidneys, whereas organic mercury forms generally affect the central nervous system (Clarkson and Magos, 2006). Accidental exposures have been reported to result in devastating mass poisoning events which included farming communities ingesting contaminated seed wheat treated with methylmercurial fungicide in Iraq (Bakir et al., 1973) and ingestion of contaminated fish and shellfish in Minimata Bay, Japan where thousands of people had symptoms of severe morbidity and even death (Kurland et al., 1960). In industry, elemental mercury has had many applications such as in the production of caustic soda and chlorine, manufacturing of fluorescent light bulbs and batteries as well as use in artisanal gold mining processes (Clarkson and Magos, 2006). These activities can cause significant environmental hazards, therefore efforts to reduce the use of mercury compounds in industrial and commercial goods are increasing. As well, efforts to remediate mercury from environmental waste sites is important in limiting the subsequent impact of mercury exposure to the general population (Wang et al., 2004).

Chelating agents are often employed to sequester harmful metal ions and ameliorate symptoms. A chelator is a multidentate ligand which binds to metal ions using two or more functional groups from the single chelator molecule (Fu et al., 2011). Treatment of mercury poisoning often involves the administration of the dithiols *meso*-2,3-dimercaptosuccinic acid (DMSA) or 2,3-dimercapto-1-propanesulfonic acid (DMPS) (Aaseth et al., 2018), however previous work has shown that neither dithiol was capable of forming true chelates with mercuric ions (George et al., 2004). The rationale for the suboptimal binding could be due to the narrow opening between the vicinal dithiols which could not accommodate mercuric ions at ideal bond-lengths and bond angles. For a chelator to bind with high specificity towards mercury ions, the physical criteria specific to mercury ions must be met. George et al. (2004) used quantum mechanical methods to calculate a customized chelator for two-coordinate binding to mercury and found that a custom two-coordinate chelator for mercuric ions would bear an Hg–S distance of 2.35 Å with S–Hg–S bond angles of 180° ± 10° with little energetic penalty. These criteria would provide the optimal orientation specific to mercury and not other endogenous cations such as zinc ions which do have characteristic 2.35 Å bond-lengths but for four-coordinate Zn–S species, or cuprous ions which do adopt diagonal coordination but at shorter Cu–S bond-lengths of 2.15 Å (George et al., 2004).

The dithiol 1,3-benzenediamidoethanethiol (B9, BDET, MetX, and NBMI) (Figure 5.1) has high affinity and specificity for mercury compared to other soft heavy metal ions in aqueous

stock solutions forming highly stable precipitates (Matlock et al., 2003). This property is highly useful in environmental remediation and the treatment of mercury contaminants in water (Henke et al., 2000; Zaman et al., 2007). Leaching studies by Matlock et al. (2003) found BDET to form stable metal-ligand complexes, with a strong thermodynamic preference for inorganic Hg(II). Animal studies by Clarke et al. (2012) have also shown improved survival of adult rats exposed to acute Hg^{2+} levels following the abdominal subcutaneous injection of a single dose of B9. Nevertheless, B9 administration did not decrease mercury levels in tissues nor did the administration of B9 increase mercury excretion (Clarke et al., 2012). Therefore, it was suggested the strong specificity of B9 to mercury reduced the damage induced by mercury exposure through mercury sequestration without elimination of mercury (Clarke et al., 2012).

One of the limitations with B9 as a suitable chelator is its low water solubility (< 200 μM). Here, we look at 1,3-benzene-diamido-2-carboxylethanethiol (AB9), an analogue of B9 with two carboxylic acid residues which exhibit improved water solubility (Figure 5.1). The purpose of this study is to probe the effectiveness of AB9 treatments on the accumulation of mercury in zebrafish larvae following an acute mercuric chloride ($HgCl_2$) dose. Zebrafish (*Danio rerio*) are a very good vertebrate model organism for *in vivo* toxicological studies due to similarities to human physiology which comprise much of systemic biology including the nervous, gastrointestinal, renal, and endocrine systems (Lieschke and Currie, 2007). Moreover, their high fecundity, rapid and well-defined developmental stages, and simple care in animal research while simulating natural animal colony conditions are all beneficial. Low concentrations of toxicants like mercury in biological samples are easily visualized using X-ray fluorescence imaging (XFI) with results identifying the distribution of metals *in vivo* which may help deduce routes of toxicity (Korbas et al., 2012; MacDonald et al., 2015a). Here we present the fate and distribution of inorganic Hg(II) following an excess dose of AB9 in zebrafish larvae using XFI. Furthermore, X-ray absorption spectroscopy (XAS) and density functional theory (DFT) were utilized to identify the radial structure of inorganic Hg(II) complexed with AB9 in solution to qualify its candidacy as an effective mercury chelator. Both these techniques were considered because they offer different and complementary information.

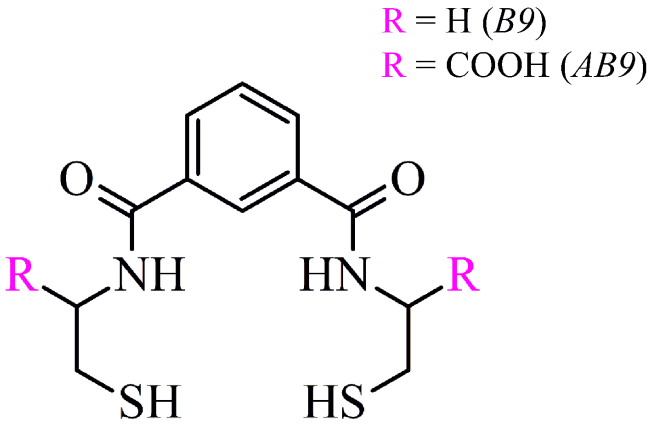

Figure 5.1. Structure of 1,3-benzenediamidoethanethiol (B9) and 1,3-benzene-diamido-2-carboxylethanethiol (AB9).

5.4 Materials and Methods

AB9 (1,3-benzene-diamido-2-carboxylethanethiol) was synthesized in Dr. David A. Atwood's research laboratory at the University of Kentucky similar to its analogue B9 (1,3-benzenediamidoethanethiol) (Figure 5.1) as previously described (Zaman et al., 2007). Mercury compounds are powerful toxicants and were handled with and disposed of with extreme care in accordance of University of Saskatchewan protocol.

5.4.1 *X-ray Fluorescence Imaging (XFI) Sample Preparation*

In vivo zebrafish experiments were performed in Dr. Patrick H. Krone's laboratory as approved by the University of Saskatchewan's Animal Research Ethics Board.

A dose of 2 µM $HgCl_2$ was selected for this experiment so that it be non-lethal to the majority of zebrafish yet still measurable in larval tissue using X-ray fluorescence imaging (XFI) elemental mapping, as described below. Range-finding studies of zebrafish larvae treated with AB9 only of concentrations up to 150 µM had 100% survival rate; a treatment concentration of 100 µM AB9 was therefore chosen to sustain a large excess with respect to Hg concentrations and also not introduce any inherent toxicity. Solutions used to incubate and treat zebrafish larvae in preparation for XFI were prepared using system water from the aquatic fish facility.

Wild-type zebrafish larvae for XFI were randomly separated into groups of 100 zebrafish per treatment and incubated in system water. Twenty-five zebrafish were randomly separated into four petri dish representing four replicates per treatment. An outline of the protocol is shown in Table 5.1. At 3 days post fertilization (dpf), mercury-dosed groups were exposed to 2 µM $HgCl_2$ for 24 hours, while the "control group" was exposed to system water. Treatment groups were then triple rinsed with system water to remove excess mercury from the exterior. At 4 dpf the "$HgCl_2$ 4 dpf" group was selected as a representative group to examine mercury distribution 24 hours following mercury exposure and were euthanized, fixed and embedded in JB-4 polymerization mixture (the details below) for further analysis. The remaining 2 treatment groups were exposed to either system water ("$HgCl_2$ + H_2O" group) or 100 µM AB9 ("$HgCl_2$ + AB9" group) for 3 consecutive days, while the "control group" was also exposed to system water for the same time period. Following the 3 day treatment (7 dpf), 20 fish were randomly selected per treatment group

and embedded and fixed following the method described by Sullivan-Brown et al. (2011). All zebrafish were euthanized with 0.2% tricaine before fixation and embedding.

Table 5.1. Experimental protocol for zebrafish dosing and treatment schedule.

Treatment Groups		**Incubation Period**	**Dosing**	**3 Day Treatment**	**Embedding**
		0 dpf / 1 dpf / 2 dpf	3 dpf	4 dpf / 5 dpf / 6 dpf	7 dpf
1	control	incubated in system water	system water	system water	prepared for XFI
2	$HgCl_2$ 4 dpf		2 µM $HgCl_2$	none; embedded for XFI	
3	$HgCl_2$ + H_2O		2 µM $HgCl_2$	system water	
4	$HgCl_2$ + AB9		2 µM $HgCl_2$	100 µM AB9	

Dose period of 24 hours; treatment period of 72 hours.

Zebrafish embryos were fixed in 4% paraformaldehyde (PFA) for 2 hours at 4°C. The embryos were slowly dehydrated using 5 minute washes in a step-wise series of 0%, 25%, 50%, 75%, and 100% MeOH:PBST buffer solutions (30 mM PBS + 0.01% Tween 20) and stored under rocking conditions at room temperature. Embryos were then slowly rehydrated in the reverse order of the MeOH:PBST buffer washes described above and fixed in 1% 2-hydroxyethyl methacrylate and left to harden. The blocks of resin were then dehydrated in absolute methanol and incubated at 4°C under rocking conditions for 5-8 hours. The ethanol solution was replaced with an infiltration solution (0.625 g benzoyl peroxide per 50 mL JB-4 Solution A) and left on a shaker at 4°C overnight. The solution was replaced again with fresh infiltration solution in the morning and shaken for 5-6 hours at 4°C. The resin blocks were then placed in embedding molds and filled with a JB-4 polymerization mixture (1 mL JB-4 Solution B per 25 mL infiltration solution) and placed at 4°C overnight for polymerization to occur. Transverse sections 6 µm thick were cut and mounted on Thermanox metal-free cover slips (Thermo Scientific, Nunc) for XFI. Images of five representative zebrafish were collected for each mercury-dosed treatment group. Hematoxylin & Eosin (H&E) staining (Harris' method) was applied to adjacent transverse sections for morphological comparisons.

5.4.2 X-ray Fluorescence Imaging (XFI) Data Collection and Analysis

XFI data were collected at the Stanford Synchrotron Radiation Lightsource (SSRL) on beamline 2-3 with its storage ring operating top-up mode at 350 mA and 3.0 GeV. This beamline utilizes a Si(111) double crystal monochromator and incident X-ray intensity was tuned to 13.45

keV, below the Br K-edge to avoid excitation of Br Kα fluorescence. Samples were mounted at 45° to the incident X-ray beam and scanned with a beam diameter of 2 µm achieved with a microfocus Rh-coated Kirkpatrick-Baez (K-B) system. X-ray scanning was 'on the fly' with a dwell time of 600 ms per pixel and a pixel size of 3 µm. Fluorescence was detected at 90° to the incident X-ray beam using a one element Vortex silicon-drift detector. Quantification of elements, excluding mercury, was achieved by imaging uniform thin film standards (6.3 µm thick) which were mounted on Mylar substrates. Quantification of mercury was achieved using gold and thallium Mylar film standards which were used to interpolate the mercury fluorescence intensity since a mercury standard slowly loses mercury content over time and is unreliable for our use.

XFI images were processed using SMAK software (Webb, 2016). X-ray fluorescence levels for each windowed element were normalized to the incoming beam and background signal was subtracted from each pixel. H&E stain images were used as a reference to mark regions of interest in XFI images for quantification. Average mercury and zinc levels in zebrafish larvae liver were compared between experimental groups.

5.4.3 X-ray Absorption Spectroscopy (XAS) Sample Preparation, Data Collection and Analysis

Aqueous samples for XAS were prepared with slow, dropwise, addition of aqueous $HgCl_2$ to AB9 solutions at 3:1 AB9:$HgCl_2$ molar ratio. Samples were mixed with 30% (v/v) glycerol at pH 7.4 then loaded into 2 mm × 3 mm × 22 mm Delrin cuvettes wrapped in metal-free adhesive Kapton tape and flash frozen in a slurry of liquid nitrogen-cooled isopentane.

Mercury L_{III}-edge spectra was measured on the structural molecular biology beamline 7-3 at SSRL employing the SPEAR storage ring operating at 3.0 GeV with a current of 350 mA. Photon source was supported by a wiggler field of 2-T. The beamline was equipped with a Si(220) double-crystal monochromator and harmonic rejection was achieved with a 15 keV mirror cut-off angle. Incident X-ray intensity was monitored using a nitrogen-filled ionization chamber and X-ray absorption of samples were measured by the X-ray fluorescence excitation spectrum using a 30-element germanium detector array. Soller slits and Ga_2O_3 X-ray filters (EXAFS Materials, Danville, California, USA) were used to reduce unwanted scatter radiation and non-linearity of the detector. Samples were placed in a liquid helium cryostat holding an approximate temperature of 10 K to minimize thermal contributions. Simultaneous absorption of a standard Hg–Sn amalgam metal foil was measured downstream by transmittance using nitrogen-filled ionization chambers

for internal calibration. Monochromator energy calibration corresponded to the lowest-energy Hg inflection point of the Hg-Sn foil, which was assumed to be 12,285.0 eV.

Extended X-ray absorption fine structure (EXAFS) oscillations $\chi(k)$ were analyzed using the EXAFSPAK program suite (George, G.N., 2000). Fourier transforms were phase-corrected for Hg–S backscattering and nominal threshold energy (E_0) was assumed to be 12,305.0 eV. The program FEFF version 8.25 (Rehr and Albers, 2000) was utilized to perform theoretical phase and amplitude functions calculations.

5.4.4 Statistical Analysis

Statistical analysis of survival studies were conducted by SPSS Statistics 24. The difference in survival rate between groups across testing days was evaluated using 2-factorial repeated ANOVA with time as the within-subject variable and treatments as the between-subject variable. When the assumption of sphericity was violated (assessed by Mauchly's test of sphericity) degrees of freedom was corrected using the Greenhouse-Geisser or Huynh-Feldt estimate of sphericity. ANOVA was then applied to treatment groups on each testing time. Bonferroni-corrected post hoc tests were applied if statistical significance was met in RANOVA and ANOVA ($P < 0.05$). $P < 0.05$ was considered as statistically significant. Significant differences of mercury levels in liver sections from XFI data were determined using a Student's t-test in each treatment group.

5.5 Results and Discussion

5.5.1 Survival Studies of Zebrafish Larvae Following Treatment with $HgCl_2$ and $HgCl_2$ + AB9

"Control" represents zebrafish larvae exposed to system water throughout the trial. "$HgCl_2$ + H_2O" group represents zebrafish larvae exposed to 2 µM $HgCl_2$ at 3 dpf, followed with 3 days of treatments with H_2O only. "$HgCl_2$ + AB9" group represents zebrafish larvae exposed to 2 µM $HgCl_2$ at 3 dpf, followed with 3 days of treatments with 100 µM AB9. Figure 5.2 summarizes the effect of treatments on the survival of zebrafish larvae across experimental days. RANOVA revealed a significant Treatment effect $F(2, 9) = 4.36$; $P < 0.05$. The negative treatment effect on survival was revealed one day after treatment and progressed afterwards (Day and Treatment interaction: $F(2.73, 12.29) = 3.66$ $P < 0.05$; Day effect: $F(1.37, 12.29) = 11.44$ $P < 0.01$). Although survival in "$HgCl_2$ + H_2O" and "$HgCl_2$ + AB9" groups decreased already one day after treatment

initiation ($P = 0.05$), ANOVA revealed statistically significant differences among groups only two days after treatment ($P < 0.05$). The difference stemmed from a significant difference of survival between "control" and "$HgCl_2$ + AB9" groups. No significant difference was observed between "$HgCl_2$ + H_2O" and "$HgCl_2$ + AB9" groups across experimental days. These results suggest that while treatments with AB9 are not more harmful than treatments with H_2O to zebrafish larvae exposed to $HgCl_2$, zebrafish dosed with $HgCl_2$ followed with AB9 treatments may be more harmed than the "Control" zebrafish not exposed to any $HgCl_2$. As previously mentioned, zebrafish larvae with AB9 treatments alone up to 150 µM had 100% survival, therefore the decreased survival of zebrafish exposed to $HgCl_2$ followed by treatments with AB9, may be the result of a redistribution of mercury to other target organs. Clarke et al. (2012) found considerable bioavailability of B9 in DMSO with distribution to the small intestine, subcutaneous fat, plasma and liver within 1 hour using abdominal subcutaneous injections. Drug delivery of AB9 in zebrafish larvae could be facilitated through the skin and gills from the surrounding environment (McGrath and Li, 2008) and is the likely route of absorption for AB9. Major vasculature is complete by 28 hours post fertilization (hpf) and major organs are functional at 5 dpf allowing for distribution of small molecules (Raluda and Pina, 2014). Once in the bloodstream, mercuric mercury binds to glutathione and sulfur-rich proteins such as metallothionein (Bernhoft, 2012).

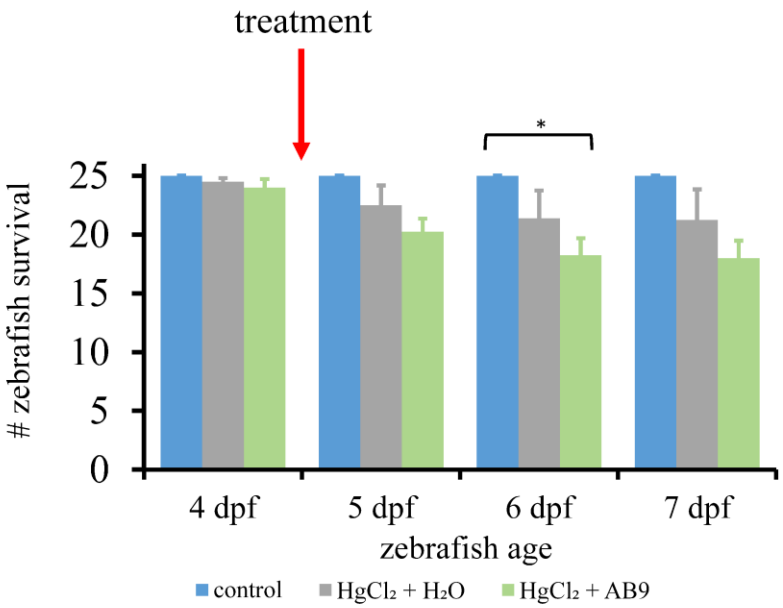

Figure 5.2. Zebrafish survival following the start of dose and treatment days. Treatment groups include "control", "$HgCl_2$ + H_2O", and "$HgCl_2$ + AB9" groups. Repeated ANOVA was performed on four replicates of 25 zebrafish per treatment group. *P*-dfp $F(1.37, 12.29) = 11.44$, $P < 0.01$. Error bars represent standard error. * indicates significant differences in zebrafish survival between "$HgCl_2$ + AB9" and "control" groups ($P < 0.05$).

5.5.2 AB9 Treatments Significantly Reduced Mercuric Chloride Accumulation in Liver Sections

As stated above, development of zebrafish larvae is rapid with major organs and vasculature functional by 2 dpf and embryogenesis complete by 5 dpf (McGrath and Li, 2008; Kari et al., 2007). The uptake and accumulation of $HgCl_2$ following acute exposure is customarily to the liver and olfactory regions of zebrafish larvae (Korbas et al., 2012). Figure 5.3 shows the histological and XFI images of the transverse trunk region showing sections of the liver as well as sections of pronephric ducts, yolk sac, gut, and brain. "$HgCl_2$ 4dpf" represents zebrafish exposed to 2 µM $HgCl_2$ at 3 dpf, then euthanized at 4dpf. $HgCl_2$ accumulation is predominantly in the pronephric ducts, liver and yolk sac wall of zebrafish larvae (Korbas et al., 2012) and the results of this study were consistent with that pattern. "$HgCl_2$ + H_2O" and "$HgCl_2$ + AB9" zebrafish are 7 dpf and have absorbed their yolk sacs by that age and therefore would not have any yolk sac wall for mercury accumulation. Figure 5.3 shows typical zinc accumulation in all tissues but is especially highly observed in pigment cells, which is consistent with previous studies (MacDonald et al., 2015b). Following treatment, the levels of mercury in the trunk region of the zebrafish treated with AB9 ("$HgCl_2$ + AB9") are lower than compared to the zebrafish treated with H_2O alone ("$HgCl_2$ + H_2O"). Mercury levels in the livers of five separate fish were quantified and averaged using a Student's *t*-test and shown in Figure 5.4. Results confirmed a significant decrease ($P < 0.05$) in mean mercury levels when measuring the liver sections of "$HgCl_2$ + AB9" zebrafish compared to the two other $HgCl_2$ treated groups. The difference in mercury levels between "$HgCl_2$ 4 dpf" and "$HgCl_2$ + H_2O" groups, euthanized at 4 dpf and 7 dpf respectively, was not significant, suggesting that excretion of mercury during depuration period is very low. Levels of mercury in the "$HgCl_2$ + AB9" group compared to the "$HgCl_2$ + H_2O" group was significantly lower ($P < 0.05$) indicating the unloading of mercury from the liver with AB9 treatment. Moreover, zinc (Zn) levels in the livers were similarly quantified using a Student's *t*-test and mean Zn levels in the liver sections are shown in Figure 5.5. Zn levels increased significantly ($P < 0.05$) between "$HgCl_2$ 4 dpf" and both "$HgCl_2$ + H_2O" and $HgCl_2$ + AB9" groups and this is attributed to the natural growth and accumulation of zinc of zebrafish.

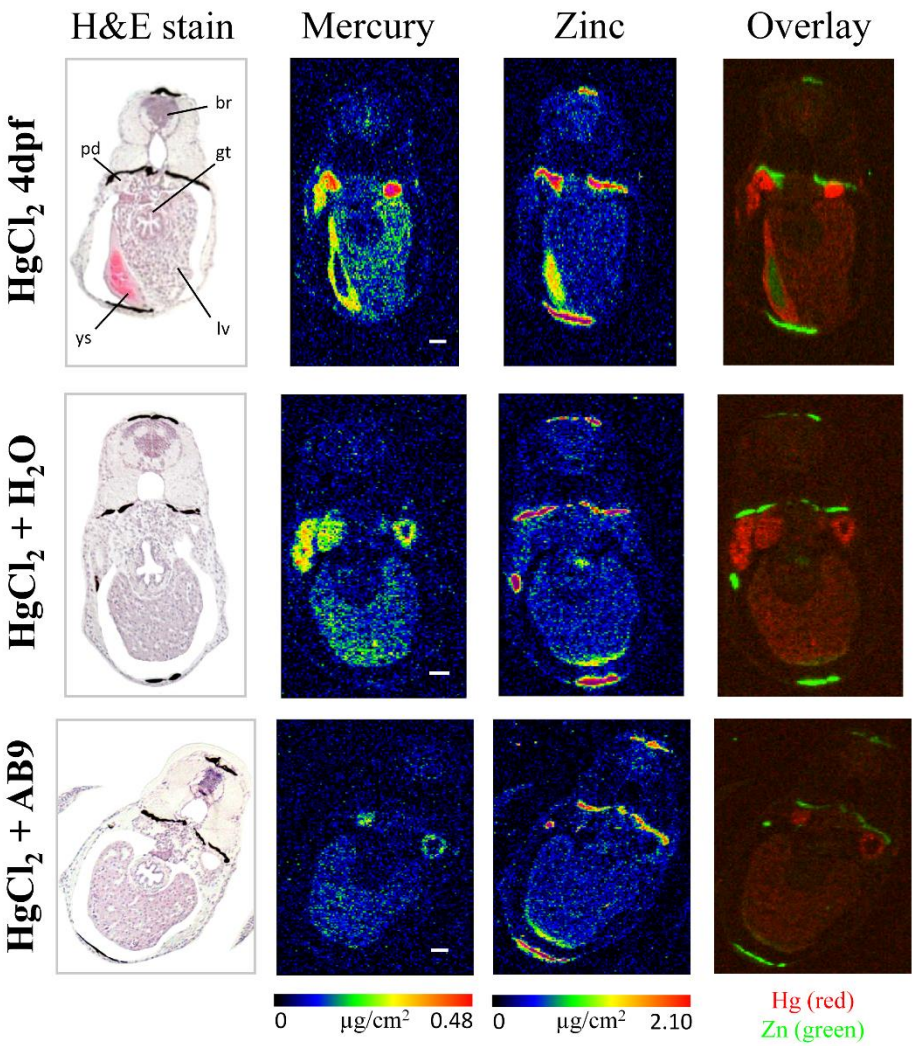

Figure 5.3. Optical (H&E) and X-ray fluorescence imaging (XFI) images of mercury and zinc distributions in sections of zebrafish larvae treated with $HgCl_2$ without and with AB9. "$HgCl_2$ 4 dpf" are zebrafish following 2 µM $HgCl_2$ dose then euthanized. "$HgCl_2$ + H2O" are zebrafish following 2 µM $HgCl_2$ dose, then 3 days of H_2O treatment. "$HgCl_2$ + AB9" are zebrafish following 2 µM $HgCl_2$ dose, then 3 days of 100 µM AB9 treatment. br = brain, pd = pronephric ducts, gt = gut, ys = yolk sac, lv = liver. White scale bars represent 30 µm. Overlay XFI images are mercury (*red*) and zinc (*green*).

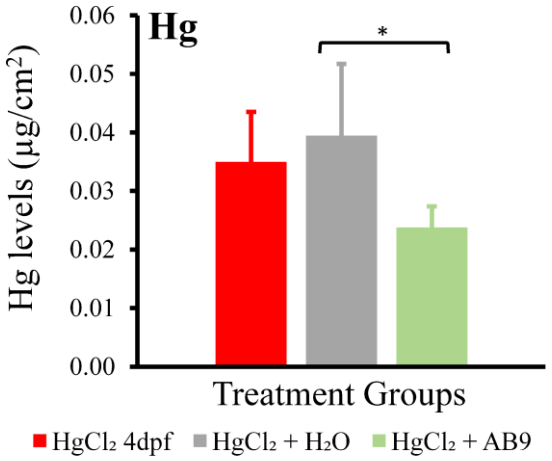

Figure 5.4. Student's *t*-test of mercury levels in zebrafish livers in µg/cm^2. Error bars indicate standard deviation. *indicates mercury levels significantly different between "$HgCl_2$ + AB9" and "$HgCl_2$ + H_2O" groups ($P < 0.05$).

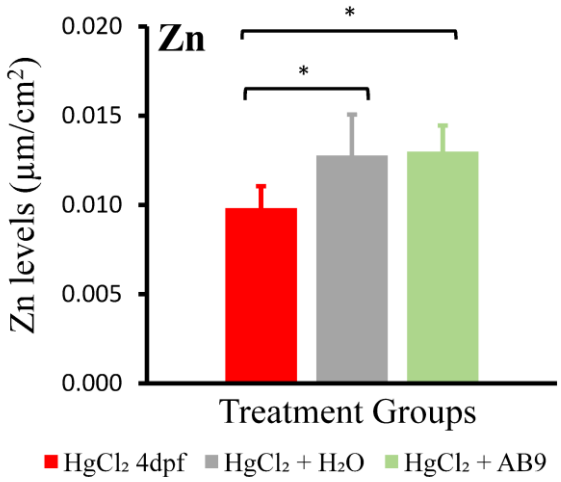

Figure 5.5. Student's *t*-test of zinc levels in zebrafish livers in µg/cm^2. Error bars indicate standard deviation. *indicates zinc levels significantly different between "$HgCl_2$ + H_2O" and "$HgCl_2$ 4 dpf" groups ($P < 0.05$) and "$HgCl_2$ + AB9" and "$HgCl_2$ 4 dpf" groups ($P < 0.05$.

As previously mentioned, zinc is an abundant endogenous divalent transition metal which might compete for binding with AB9 and therefore high AB9 treatment doses might result in dysregulation of zinc. However, no significant differences were found in Zn levels of liver sections when comparing "$HgCl_2$ + H_2O" and "$HgCl_2$ + AB9" groups which suggests preservation of homeostasis with respect to Zn in this anatomical region of interest. An excess dose of AB9 could pose a threat to the homeostasis of other biologically relevant transition metals as previous work with B9 has shown its high affinity for soft heavy metals iron (Fe), copper (Cu), and Zn, with strongest affinity for Hg (Matlock et al., 2002; Matlock et al., 2003). Biological systems are higher in Fe, Cu, and Zn with respect to Hg, and harmful effects from the depletion of these metals could be a concern, however preliminary range finding studies of zebrafish with AB9 alone found no significant increase in morbidity nor mortality of a dose up to 150 µM and XFI data showed no significant decrease in Zn levels in zebrafish larvae livers. Moreover, essential transition metals are typically tightly and efficiently regulated reducing the likelihood.

XFI clearly demonstrated decreased levels of mercury in the liver sections of zebrafish larvae treated with AB9 following an acute $HgCl_2$ exposure. The decrease in mercury levels supports the ability of AB9 to facilitate the unloading of Hg from the liver. Examination of the pronepheric ducts also show a decrease in mercury levels when treated with AB9 however quantifying the structures of the pronephric ducts at this resolution was challenging due to variances of anatomical structures and therefore was not included. The non-significant decrease in survival in the "$HgCl_2$ + AB9" group compared to the "$HgCl_2$ + H_2O" group (Figure 5.2) underscores the importance of further studies on the pharmacodynamics of AB9 in relation to the fate of mercury *in vivo* which may help explain how mercury may be unloaded from liver sections of zebrafish larvae following AB9 treatment. The mechanism of liver clearance of inorganic Hg(II) after AB9 treatment is currently unknown. Mercury could have been excreted into the environment (Petri dish) or redistributed to other areas of the body. Redistribution to essential organ systems could possibly explain the decreased survival seen in zebrafish treated with AB9. This assumption is consistent with the lower mercury concentrations reported by Clarke et al. (2012) in the urine and feces in B9 treated rats which may also suggest redistribution (Clarke et al., 2012). Zebrafish blood brain barrier (BBB) is comparable to mammalian BBB and is developed as early as 3 dpf (Korbas et al., 2012) therefore if one site of the redistribution of Hg is the brain, the AB9–Hg complex would likely have to be transported by membrane transporters. While the present study

is appreciably different to the Clarke et al. (Clarke et al., 2012) study with regards to animal model, life-stage of animal model, chelator and method of chelator administration, both studies suggest a possible beneficial role of B9 or AB9 in ameliorating toxic effects from inorganic Hg(II).

5.5.3 Extended X-ray Absorption Fine Structure (EXAFS) Characterization of $HgCl_2$ with AB9

The interaction of $HgCl_2$ in solution with AB9 at 3:1 molar ratio was examined with the analysis of Hg L_{III}-edge extended X-ray absorption fine structure (EXAFS) to look at how AB9 reacts with $HgCl_2$ in solution and investigate the solution structure of AB9–Hg complex as a possible model of how they bind *in vivo*. EXAFS provides information on the radial structure of an absorbing element and in this case could provide information on whether AB9 has the characteristics necessary to be a good chelator specific to Hg(II) ions. Compared to the $HgCl_2$ dose administered to the zebrafish larvae for the XFI experiments, higher concentrations of $HgCl_2$ and AB9 were used for EXAFS analysis due to the detection limit of EXAFS experiments. EXAFS of $HgCl_2$ with AB9 is shown in Figure 5.6 with the structural parameters used for the best fit using multiple scattering analysis in Table 5.2. Figure 5.6A illustrates EXAFS oscillations with uniform phase and large amplitude which signifies backscattering from a moderately large atom. The Fourier transform (Figure 5.6B) is dominated by a first-shell interaction at 2.33 Å corresponding to Hg—S. Other backscattering shells modelled include two Hg•••C at 3.36 Å and two Hg•••N at 3.97 Å.The multiple scattering peak at ~4.7 Å is due to the near-linear geometry of the S–Hg–S. These results are in good agreement with characteristic two-coordinate S–Hg–S structures with a close to linear bond angle of 177 ± 4° which have bond-lengths in the range of 2.34-2.36 Å (Fu et al., 2011). Geometry-optimized, energy-minimized structure of AB9 binding inorganic Hg(II) is shown in Figure 5.7. The calculated S–Hg–S bond angle of 179° is marginally lower than the characteristic linear range which can be a result of minor ring strain due to the inherant structure of the AB9 molecule and its shorter ligand length that translates to a small bite angle. Indeed, Fu et al. (2011) found that a longer ligand chain length of propanethiolate to be more energetically favourable than the ethanethiolate to provide the ideal fit to incorporate an Hg atom. In addition, as previously mentioned, a 10° deviation of the S–Hg–S bond angle from linear 180° did not result in significant energetic penalties (George et al., 2004), hence AB9 complexed with Hg^{2+} is well within the acceptable margin.

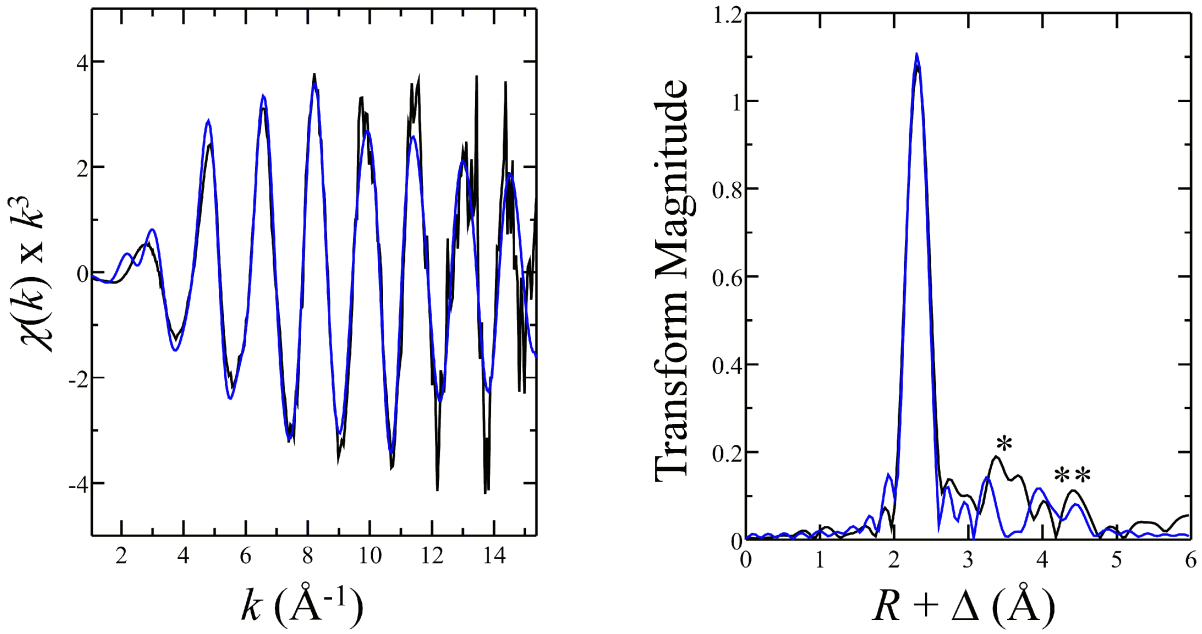

Figure 5.6. Mercury L_{III}-edge X-ray absorption spectroscopy (XAS) of $HgCl_2$ with AB9 at 3:1 molar ratio. A: EXAFS oscillations. B: Corresponding Fourier transform, phase-corrected for Hg—S backscattering. Experimental data shown in *black*; curve-fitting analyses shown in *blue*, the numerical results of which are shown in Table 5.2. *indicates unidentifiable backscattering atoms between ~3–4 Å from mercury. **indicates multiple scattering peak due to near-linear geometery of S–Hg–S.

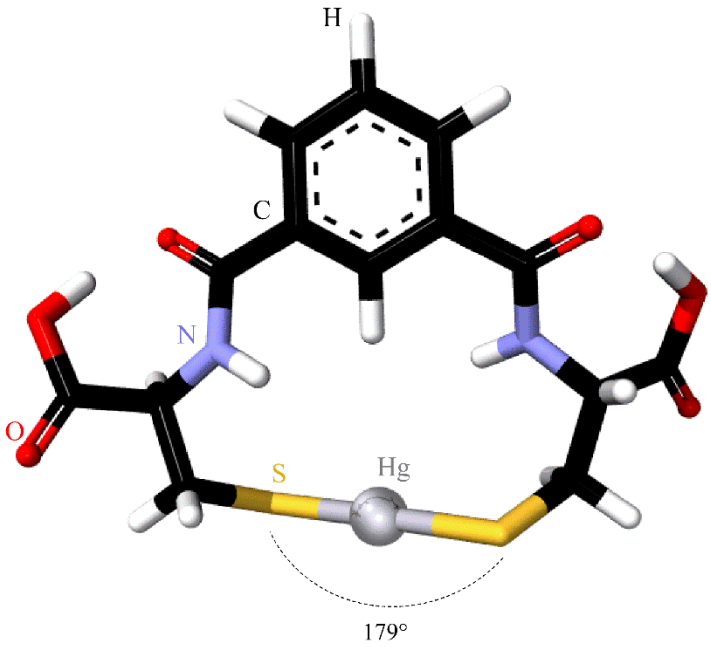

Figure 5.7. Geometry optimized, energy minimized calculated structure of 1 AB9 molecule binding to Hg(II).

The features shown between 3-4 Å correspond to further shells but could not be identified with a suitable model. The ligands of AB9 are flexible and therefore in solution could exist in any number of possible orientations.

Zaman et al. (2007) found complexes of B9 with mercuric mercury to have Hg—S bond-lengths of 2.42 Å long and had contributed the elongation to the presence of secondary interactions with other ligands. In addition, the longer Hg—S bond-length may be attributed to the large Debye-Waller factor fixed at 0.008 $Å^2$ which translates to larger static disorder in the bond distance. Polymeric species with alternating Hg^{2+} ions and dithiolate molecules can exist when mixed in solutions at higher concentrations (Fu et al., 2011) and Zaman et al. (2007) found the formation of insoluble precipitates at high concentrations of B9 with Hg^{2+} which suggests the formation of polymers. For this reason, samples for EXAFS were prepared with the slow, dropwise addition of $HgCl_2$ to AB9 solutions. Nevertheless, the EXAFS results did not indicate any significant backscattering from systemic neighbouring atoms which may indicate a non-crystalline complex. Irrespective of this, the fate of Hg^{2+} *in vivo* is expected to culminate at binding sites with endogenous thiolates so while the EXAFS results can not conclusively state whether AB9 forms true chelate complexes with Hg^{2+}, the incidental sequestering activity of AB9 *in vivo* can be expected to have a more probable chance of forming a true chelate ring complex, at a 1:1 Hg^{2+}:AB9 ratio.

Table 5.2. Curve-fitting parameters[a] used to fit extended X-ray absorption fine structure (EXAFS) of AB9 and mercuric chloride.

	Bond	N	R (Å)	σ^2 ($Å^2$)	ΔE_0 (eV)	*F*
	Hg — S	2	2.33 (1)	0.0024 (1)	–4.9 (5)	0.3696
3 AB9 : 1 $HgCl_2$	Hg ••• C	2	3.36 (1)	0.0036		
	Hg ••• N	2	3.97 (1)	0.0042		

[a] N coordination number; R (Å) interatomic distances; σ^2 ($Å^2$) Debye-Waller factor; ΔE (eV) threshold energy shift to nominal threshold value of 12,305 eV (E_0). Estimated standard deviations in the last digit of the fitted parameters are shown in parentheses. The goodness of fit function F is defined by $[\Sigma k^6(\chi(k)_{calc} - \chi(k)_{expt})^2/\Sigma k^6\chi(k)^2_{expt}]^{1/2}$, with $\chi(k)_{calc}$ and $\chi(k)_{expt}$ as the calculated and experimental EXAFS and k being the photoelectron wavevector. Amplitude reduction factor (S_0^2) set to 1.0.

In summary, this study shows AB9 to have favourable sequestering activity as treatment with 100 µM AB9 reduces the accumulation of mercury in the livers of zebrafish larvae. The EXAFS results support the characteristic properties of specific chelation binding of AB9 to Hg^{2+} with characteristic two-coordinate linear Hg—S bond-lengths of 2.33 Å, and geometry optimized, energy-minimized DFT results show the complex structure displaying an almost linear coordination within the ideal linear range. However, unfavourable results with respect to significantly decreased zebrafish survival were also observed with zebrafish larvae dosed with $HgCl_2$ followed by AB9 treatment compared to the healthy control group. In this case, more in depth *in vivo* studies to better understand the fate of AB9 removal of inorganic mercury from target organs could be useful in understanding the mechanistic activity of this sequestering agent.

5.6 Acknowledgments

The authors thank Dr. Jith K. Thomas and Dr. David M. Janz for providing the zebrafish larvae and Dr. Sam Webb and Dr. Courtney Roach for their assistance and support with running the XFI experiments. This work was supported through Discovery grants from the Natural Sciences and Engineering Research Council of Canada (NSERC, I.J.P. and G.N.G.), a grant from Innovation and Science Fund of Saskatchewan (I.J.P.), a Canada Foundation for Innovation John Evans Leader's Fund Award (I.J.P.) and by Canada Research Chairs (I.J.P. and G.N.G.). S.N. acknowledges the Dr. Rui Feng Scholarship and was a Fellow in the Canadian Institutes of Health Research-Training in Health Research Using Synchrotron Techniques (THRUST). Use of the Stanford Synchrotron Radiation Lightsource, SLAC National Accelerator Laboratory, is supported by the U.S. Department of Energy, Office of Science, Office of Basic Energy Sciences under Contract No. DE-AC02-76SF00515. The SSRL Structural Molecular Biology Program is supported by the DOE Office of Biological and Environmental Research, and by the National Institutes of Health, National Institute of General Medical Sciences (including P41GM103393). The contents of this publication are solely the responsibility of the authors and do not necessarily represent the official views of NIGMS or NIH.

CHAPTER 6. High Energy Resolution Fluorescence Detection X-ray Absorption Spectroscopy of Mercury Compounds

6.1 Preface

XAS has the advantage of element specific probing of oxidation states and coordination environments of chemical species. With the development of advanced synchrotron techniques, researchers are able to observe beyond the limitations of conventional XAS. The structural components of mercury compounds are important to the activity and fate of mercury in environmental and biological systems, therefore knowledge of the structure is of vital importance. Near-edge spectroscopy is effective in fingerprint identification of coordination environments but can be challenging with mercury compounds due to the broad spectra at the Hg L_{III}-edge. The following chapter explores the potential of high-energy resolution fluorescence detection (HERFD) XAS monitoring the mercury L_{III}-$L\alpha_1$ emission line in the molecular characterization of mercury compounds. The improved energy resolution afforded with HERFD XAS will improve the chemical speciating capabilities critically important in understanding the molecular toxicology of mercury compounds. *In situ* detection of trace accumulated levels of highly toxic compounds, like some mercury compounds, is achievable with HERFD XAS and we conclude that this spectroscopic tool will be an influential complement to EXAFS measurements in the characterization of natural, dilute levels important in environmental and health sciences.

Author Contributions

This chapter will be reformatted as a journal article and submitted to *Chemical Research in Toxicology*.

Nehzati, S., Dolgova, N.V., Sokaras, D., Kroll, T., Pickering, I.J., and George G.N. (2019) High Energy Resolution Fluorescence Detection X-ray Absorption Spectroscopy of Mercury Compounds. (*In preparation*).

S. Nehzati prepared the samples, collected and analyzed the XAS and HERFD XAS, performed DFT and ORCA calculations, and drafted the manuscript.

N. V. Dolgova collected and performed XAS and HERFD XAS analysis.

D. Sokaras and T. Kroll optimized beamline configuration and assisted with experiments.

I. J. Pickering and G. N. George directed the science, performed data acquisition, edited the manuscript, and funded the research.

6.2 Abstract

High-energy resolution fluorescence detection X-ray absorption spectroscopy (HERFD XAS) employs Bragg optics which decreases core hole lifetime broadening effects to X-ray absorption spectroscopy. This vastly improves the energy resolution which produces greater details in X-ray absorption spectra. Here, we use HERFD XAS to investigate a series of mercury compounds and develop methods for mercury L_{III}-$L\alpha_1$ HERFD XAS. Results show L_{III}-$L\alpha_1$ HERFD XAS provides improved speciating capabilities of different chemical species of mercury. The observed L_{III}-$L\alpha_1$ HERFD XAS spectra are interpreted with *ab initio* calculated electronic transitions using a density functional theory restricted-open-shell configuration interaction singles (DFT/ROCIS) method with incorporation of the spin-orbit coupling (SOC) of the molecular multiplets of L-edge X-ray absorption. This new method is used to examine mercury species in wild swordfish at natural dilute levels.

6.3 Introduction

Mercury (Hg) is the only metal pollutant with no geographic boundaries as the volatile form Hg0 is readily transported around the globe. Its atmospheric lifetime lasts several months in the form of Hg0, facilitating its global transportation (Ariya et al., 2015). The chemical transformation of Hg0 to different mercury species and oxidation states result in differing physicochemical properties that affect its environmental deposition. Mercury is a naturally occurring element comprising about 80 μg/kg of the earth's crust and 0.3 ng/L in seawater (Gonzalez-Raymat et al., 2017). Its presence in land and aquatic systems plays an important role in the redistribution of mercury in aquatic systems where the production of methylated mercury species occurs (Selin, 2009). Despite mercury's ubiquitous existence, at present time there are no

known biological roles for mercury in organisms. A possible exception may be phototrophic microorganisms which use heavy metals, including Hg(II), as electron sinks during photosynthesis (Reith et al., 2009; Gregoire and Poulain, 2016). Mercury is also part of some of the most toxic compounds on earth (George et al., 2004). The extent of toxicity from elevated exposures to mercury compounds is largely dependent on the chemical form of mercury (Bernhoft, 2012; Korbas et al., 2012). Understanding the electronic structure of mercury coordination can lead to a better understanding to the mechanisms of mercury transformation, biotransformation, and toxic effects.

Often chemical investigations of mercury are performed under sub-optimal conditions requiring the excess addition of the metal in order to meet the detection limit of the analysis. Additionally, bulk measurements of the sample are performed to meet adequate count rates which may obscure the heterogenous composition in the sample. Furthermore, the near-edge region of Hg L_{III}-edge spectra is very broad, compared to other elements like sulfur K-edge spectra which produce sharp spectral features (Sneeden et al., 2004). The lack of prominent features in Hg L_{III}-edge spectra makes the separation of different chemical species somewhat challenging. High-energy resolution fluorescence detection X-ray absorption spectroscopy (HERFD XAS) is capable of distinguishing between different chemical species by probing the local bonding environment of an absorbing element. HERFD XAS employs Bragg crystal sets that preferentially diffract only a small portion of the fluorescence emission from the sample to the detector which vastly improves the energy resolution (Sokaras et al., 2013) and produces richer spectra, and hence, greatly improves the speciating capabilities. HERFD XAS has been influential in investigating the coordination geometry of complex systems, mostly in the area of catalytic sciences where experiments directly probe the electronic levels responsible for chemical properties or *in operando* experiments probing the electronic transitions important to a chemical reaction (Atkins et al., 2012; Wierzbicki et al., 2018), but the use of HERFD XAS in environmental sciences is limited. HERFD XAS was practical in substantiating a new diiron distance in a key intermediate involved in the methane monooxygenase enzymes in methanotropic bacteria as a step forward to understanding the mechanism involved in the oxidation of methane (Cutsail et al., 2018). In another study involving mercury, HERFD XAS had been used to investigate environmental accumulation of mercury and detect the ligand form bound to mercury in hair at levels as low as 3 nM (Manceau et al., 2016). The lowest mercury level triggering adverse effects in humans was examined to be 4

μg/kg/day, correlating to a blood level of 200 μg/L or accumulation of 50 μg/g in hair (Swedish Expert Group, 1971). Here, we examine the capabilities of HERFD XAS with the chemical characterization of a variety of organic and inorganic mercury compounds and expand methodologies by monitoring the mercury L_{III}-$L\alpha_1$ emission line to demonstrate its extensive potential to better identify different chemical species of mercury.

6.4 Materials and Methods

6.4.1 Sample Preparation

Mercuric chloride and mercuric acetate were obtained from Alfa Aesar. Mercuric sulphate, yellow mercuric oxide, α-mercuric sulfide, mercuric selenide, methylmercury hydroxide, selenocystine, sodium borohydride, and methyl-imidazole were purchased from Sigma Aldrich. Elemental mercury was prepared with the reduction of mercuric chloride with sodium borohydride. β-mercuric sulfide was prepared by mixing Na_2S and $HgCl_2$, collecting, and washing the precipitate. Mercuric *bis*-L-cysteinate ($HgCys_2$), methylmercury-L-cysteine (CH_3HgCys), methylmercury-imidazole (CH_3Hg-imidazole), and *bis*-methylmercury selenide ($(CH_3Hg)_2Se$) were prepared with the mixing of mercuric chloride or methylmercury hydroxide with excess ligands. $[Hg(SR)_4]^{2-}$ was prepared by mixing mercuric chloride with excess L-cysteine in alkaline solution (Jalilehvand et al., 2006). Methylmercury selenocysteine ($CH_3HgSeCys$) was prepared from the crystallization of equimolar methylmercury hydroxide and selenocysteine in alkaline solutions. Samples were prepared as either 1 mM (final) solutions or 5 % weight solid samples diluted with BN powder. Solutions were injected into polyacetal cuvettes, covered with metal-free Mylar or Kapton tape and frozen in a slurry of LN_2-isopentane. Solution samples for conventional XAS contained 20% (v/v) glycerol. Solid samples were ground to a fine powder and loaded into metal-free sample holders windowed with Mylar or Kapton tape.

6.4.2 X-ray Absorption Spectroscopy (XAS)

Mercury L_{III}-edge X-ray absorption spectra were measured on the structural molecular biology beamline 7-3 at SSRL. The beamline uses a Si(220) double-crystal monochromator for energy tuning. The incident X-ray intensity was monitored using a nitrogen-filled ionization chamber before the sample holder. Samples were placed in a liquid helium cryostat holding an

approximate temperature of 10 K to minimize thermal contributions to atomic vibrations and radiation damage. X-ray absorption of solution samples were measured using a 30-element germanium detector array at 90° to the incident beam and in the same plane of the incident X-ray beam to minimize scattering contributions. Soller slits and gallium containing X-ray filters (EXAFS Materials, Danville, California, USA) were utilized to prevent unwanted scatter radiation. Transmittance was monitored using nitrogen-filled ionization chambers before and after the sample. The simultaneous monitoring of a Hg–Sn amalgam metal foil was measured downstream by transmittance using nitrogen-filled ionization chambers for internal calibration which used the lowest-energy inflection point of the standard foil assumed to be 12,285 eV.

6.4.3 High Energy Resolution Fluorescence Detection XAS

Mercury L_{III}-$L\alpha_1$ and selenium $K\alpha_1$ HERFD XAS spectra were collected at the Stanford Synchrotron Radiation Lightsource (SSRL) beamline 6-2. The storage ring was operating at 3.0 GeV and a current of 350 mA. The Si(311) double crystal monochromator and a 5-/6-element array of Si(555) and Si(884) crystal analyzers were used to survey the Hg L_{III}-$L\alpha_1$ and Se $K\alpha_1$ emission lines. Samples were placed 45° to the incident beam within a helium flow cryostat holding a temperature of ~10 K to minimize atomic vibrations and reduce radiation damage. The monochromator was energy calibrated relative to the lowest-energy inflection point of standard hexagonal grey Se or Hg–Sn foil, assumed to be 12,658 and 12,285 eV, respectively. Fluorescence emission was monitored using a single element silicon-Vortex solid-state detector. Data reduction and analysis was performed using the EXAFSPAK suite of computer programming (George, G.N., 2000).

6.4.4 Ab initio Theoretical Calculations

Density functional theory (DFT) geometry optimization was carried out using DMol^3 (Delley, 1990; Delley, 2000) on Biovia Materials Studio version 2018 R2. The GGA PBE functional with all-electron relativistic core treatments were used for the self-consistent field procedure and solvation effects were modeled using the COSMO model (Klamt and Schüürmann, 1993), where applicable. Geometry-optimized structures from the DFT calculations were then used to calculate electronic transitions and transition moments with the ORCA software package

(Neese, 2017). The input functional B3LYP was used for geometry optimization, with scalar relativistic zero order regular approximation (ZORA) (Pantazi et al., 2008) methods and def2-TZVP (Weigend and Ahlrichs, 2005) orbital expansion basis sets in combination with the Coulomb-fitting auxiliary SARC/J orbital basis set. Hg atoms were matched with the all-electron relativistic contracted basis set SARC-ZORA-SVP and energies were corrected for spin-orbital coupling (SOC) (Sandhoefer and Neese, 2012). Solvation effects were also accounted for using the CPCM solvation model and corresponding solvent parameters (Neese, 2017). Electron density isosurfaces were constructed with 0.05 spin per a.u.. Theoretical transition spectra were uniformly shifted to align with the experimental data. The energy deviation is due to the omission of electron correlation effects (Roemelt and Neese, 2013a).

6.5 Results and Discussion

6.5.1 Improved Speciating Capabilities

Fluorescence detected XAS monitors the secondary physical process of fluorescence emission as an indicator of the absorption coefficient. The near-edge spectra of conventional XAS of Hg species often display unremarkable broad spectra (Figure 6.1 and Figure 6.2, *dashed lines*) thus decreasing their utility for characterizing chemical forms. The full width half max (FWHM) natural linewidth of Hg L_{III}-edge X-ray line is calculated to be 5.50 eV which was extrapolated from experimental fluorescence data in conjunction with the theoretical radiative rate of mercury (Krause and Oliver, 1979). This broadening is largely governed by the core hole lifetime of the $L\alpha_1$ emission line. Furthermore, as a result of the energy resolution of current detectors, conventional XAS of Hg L_{III}–edge spectra typically monitors an averaged $L\alpha_1$ (9988.8 eV) and $L\alpha_2$ (9897.6 eV) peak, as they are close in energies. HERFD XAS instrumentation employs Bragg crystal sets which preferentially detect the desired emission line with high energy resolution. As a result of the improved energy resolution, the core hole lifetime broadening effects from the initial core hole are decreased which improves the observed spectral features. These crystal analyzer sets offer a large improvement in energy resolution, thus facilitating the direct monitoring of the $L\alpha_1$ emission line at the Hg L_{III}-edge. The high energy resolution reveals sharper spectral details which correspond to electronic structural details of the excited element, as has been previously reported by other workers (Manceau et al., 2015; Proux et al., 2017). The sharper features in the spectra (Figure 6.1 and Figure 6.2, *solid line*) reveal discernible details of different chemical species and improve speciation capabilities between different ligand types.

6.5.2 Ab initio Theoretical Calculations

The spectra for dimethyl mercury shown in Figure 6.3 illustrates the good agreement between the theoretical transition and experimental spectra. Theoretical transitions were calculated using *ab initio* wavefunctions of restricted open-shell methods with spin-orbit coupling adaptation to calculate the probability of excited states using the ORCA suite of programs (Neese, 2017; Sandhoefer and Neese, 2012). Unlike K-edge spectra where the final states are not affected by multiplicity, the open-shell $2p^5nd^{n+1}$ final states can produce molecular multiplets due to the

overlap of 2p and 3d orbitals. Furthermore, spin-orbit coupling (SOC) effects of the L_{II} and L_{III}-edges make the interpretation of 2p X-ray excited spectra somewhat difficult (Roemelt et al., 2013b). According to XAS selection rules, dipole allowed $\Delta l = \pm 1$ transitions produce intense features and quadrupole allowed $\Delta l = \pm 2$ transitions produce weaker features. The Laporte rule further expresses that transitions between states with the same symmetry ($\Delta l = 0$) are forbidden dipole transitions. The observed Hg L_{III} absorption edge is shaped by the photoexcitation of electrons from the $2p_{3/2}$ core level to unoccupied molecular orbitals, characteristic of d and s character as noted by the lowest unoccupied orbitals of Hg in Hg-ligand complexes. Figure 6.3 shows the L_{III}-$L\alpha_1$ HERFD XAS and theoretical transition stick spectrum of dimethyl mercury. Computed molecular orbitals are constructed by the linear combination of atomic orbitals (LCAO) and these are represented in each transition of the stick spectrum (Figure 6.3, *red*), but due to Laporte selection rules, theoretical transitions of quadrupole allowed or formally forbidden dipole transitions, marginally observed at lower energies than the intense peak of the stick spectrum at 12288.0 eV, will be overlooked. Using the theoretical calculations, the observed intense peak at 12288.0 eV is assigned to an electron transition from a 2p orbital to antibonding σ^* orbital populated with d character mixed with some s character. While some formally forbidden dipole transitions may be observed in some cases such as the ligand 2s to metal 1s transition (Doonan et al., 2005), mercury L_{III}-$L\alpha_1$ HERFD XAS spectra of dimethyl mercury, as seen in Figure 6.3, did not exhibit comparable ligand to metal transitions. Furthermore, the calculated excited states are composed of different configurations and multiplicities, therefore the intensities observed are not to be direct measurements of molecular orbital character (Roemelt et al., 2013b).

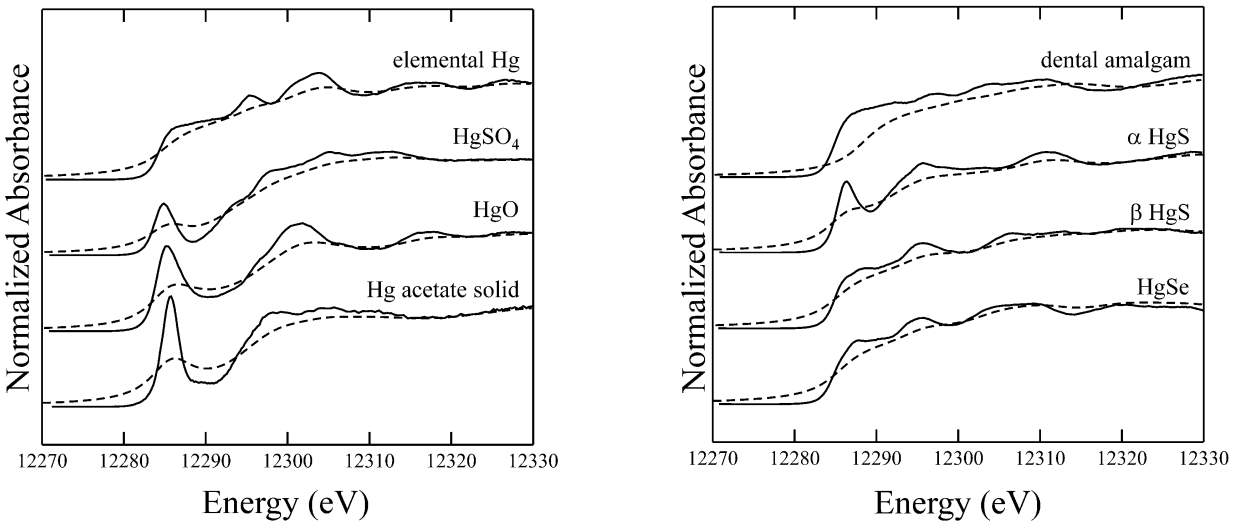

Figure 6.1. Mercury L_{III}-$L\alpha_1$ HERFD XAS compared with conventional mercury L_{III}-edge XAS of inorganic mercuric compounds. HERFD XAS dataset shown as *solid line*; conventional XAS shown as *dashed line*. HERFD XAS spectra were collected following the selection of an emission energy corresponding to the peak of the emission scan for each individual mercury compound. Solid spectra were not corrected for self-absorption effects.

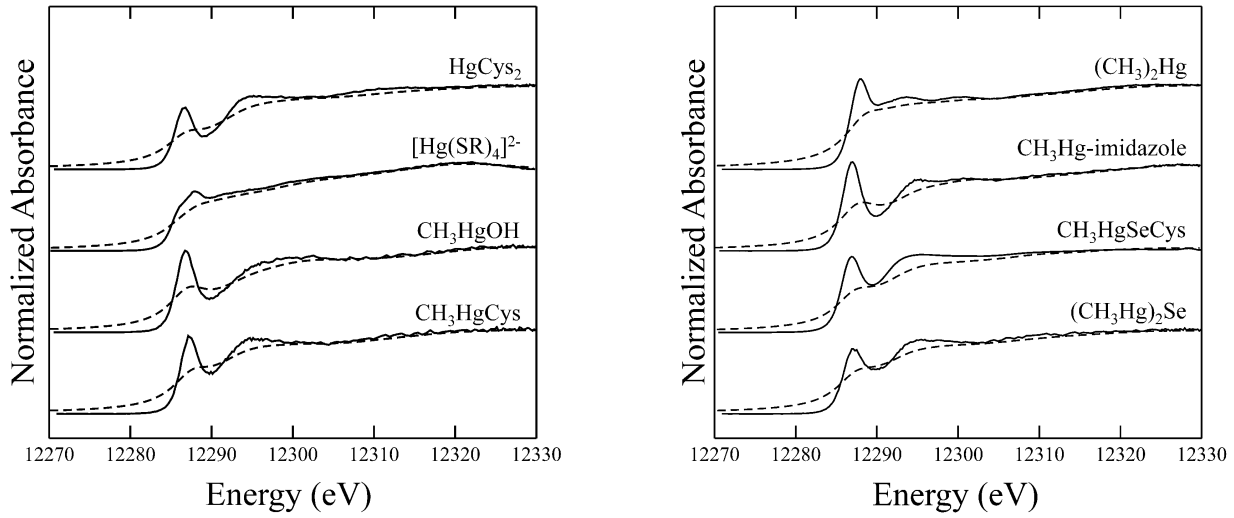

Figure 6.2. Comparison of organic mercuric compounds using mercury L_{III}-$L\alpha_1$ HERFD XAS and conventional mercury L_{III}-edge XAS. *Solid line* represents HERFD XAS, while *dashed line* represents conventional XAS. Emission energy was selected as the center peak of the emission scan of each mercuric compound.

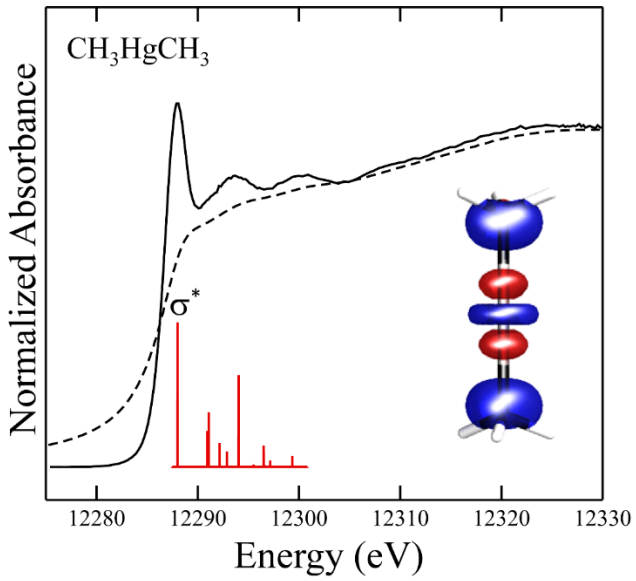

Figure 6.3. Mercury L_{III}-edge spectra of dimethyl mercury. Conventional XAS shown in *dashed line*, L_{III}-$L\alpha_1$ HERFD XAS shown in *solid line*, and theoretical transition stick spectrum shown in *red*. The highest peak which comprises the main edge feature is mostly comprised of 2p to 5d electronic transition as calculated by *ab initio* wavefunctions. Inset shows the molecular orbital most populated at the σ^* excited state.

HERFD XAS is able to distinguish signature features in the near-edge spectra of structurally similar compounds. The mercuric chalcogenides, β-mercuric sulfide (β-HgS) and mercuric selenide (HgSe), shown in Figure 6.4 (*left*) are isostructural with both crystals exhibiting zincblende crystal structures. Conventional XAS (Figure 6.4, *left*, *dotted lines*) shows very similar spectra for both mercuric chalcogenides which makes it difficult to discriminate between the two. Mercury L_{III}-$L\alpha_1$ HERFD XAS (Figure 6.4, *left*, *solid lines*), however, is able to discriminate and speciate between these two compounds with little uncertainty. The organic methylmercury chalcogenides (Figure 6.4, *right*), methylmercury cysteine (CH_3HgCys) and methylmercury selenocysteine ($CH_3HgSeCys$), were also spectrally indistinguishable with conventional XAS (Figure 6.4, *right*, *dotted lines*), however HERFD XAS, is able to distinguish between the two compounds (Figure 6.4, *right*, *solid lines*) which presents the initial rise in absorption of methylmercury selenocysteine a fraction of an eV before methylmercury cysteine. This was supported with the results of the theoretical electronic transitions calculated of the SOC corrected Hg L-edge excited states. Table 6.1 lists the theoretical electronic transitions of these methylmercury chalcogenides. Theoretical transitions of methylmercury selenocysteine were calculated to be at lower energies than methylmercury cysteine, which supports the subtle differences in the experimental spectra. The σ* molecular orbital for both compounds exhibited strong electronic transitions from a 2p orbital to a molecular orbital populated with d character mixed with s character (Figure 6.5). These results show the effectiveness of using theoretical transitions to excited states to help interpret and strengthen subtle observations in experimental X-ray absorption data.

Table 6.1. Calculated Hg L-edge electronic transitions from *ab initio* wavefunctions using the DFT/ROCIS method with spin-orbit-coupling correction.

	LUMO (eV)	LUMO + 1 (eV)	LUMO + 2 (eV)	LUMO + 3 (eV)
methylmercury cysteine	12286.46	12286.46	12286.49	12287.33
methylmercury selenocysteine	12286.34	12286.35	12286.37	12287.09

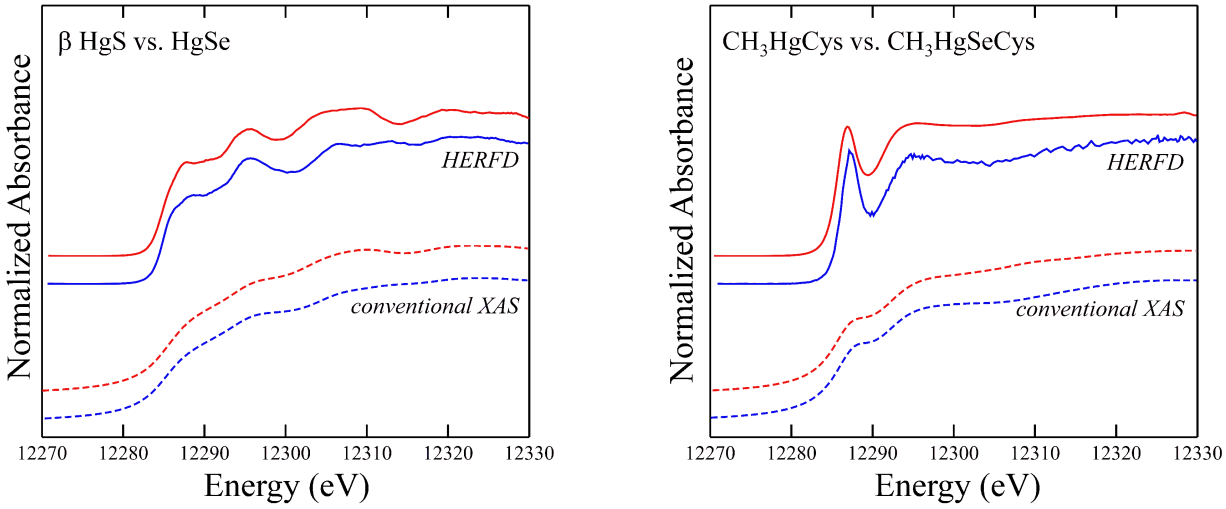

Figure 6.4. Mercury L_{III}-edge spectra of mercuric chalcogenide compounds. Selenide compounds shown in *red* while sulfide analogue shown in *blue*. Mercury L_{III}-$L\alpha_1$ HERFD XAS shown as *solid* line while conventional mercury L_{III}-edge XAS shown as *dashed line*.

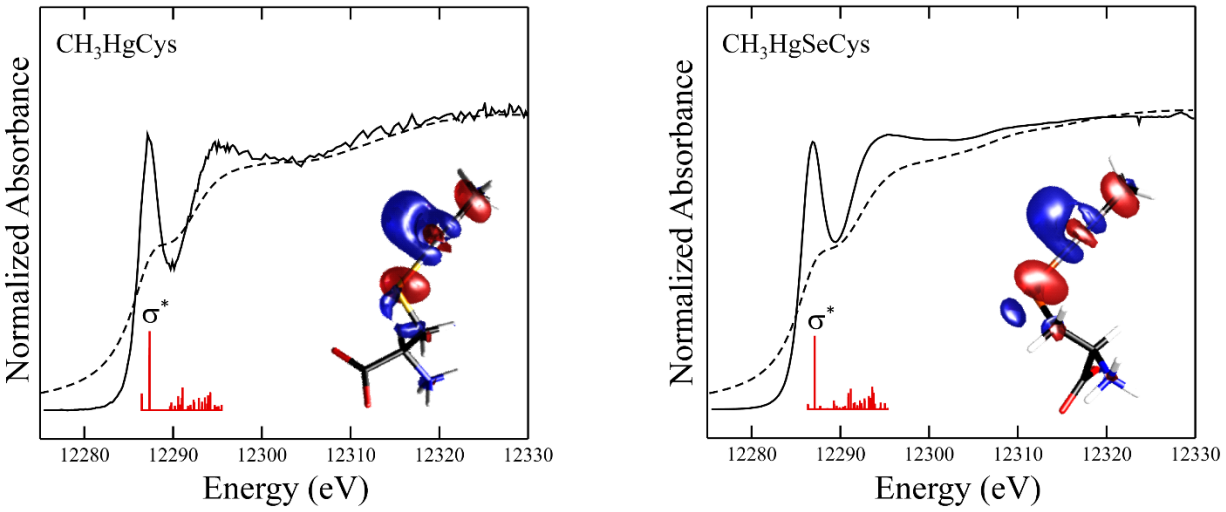

Figure 6.5. Comparison of mercury L_{III}-$L\alpha_1$ HERFD XAS (*solid line*) with conventional mercury L_{III}-edge XAS (*dashed line*) of mercuric chalcogenide compounds. Calculated *ab initio* wavefunctions of probable electronic transitions shown in *red* stick spectrum. Molecular orbital inset shows the most populated molecular orbital at the σ* excited state.

6.5.3 HERFD XAS of Biological Sample

Another benefit of using a HERFD XAS spectrometer is the rejection of unwanted scattering radiation. A considerable rejection of scattering could improve the signal-to-noise which would lower the detection limit to allow the investigation of trace elemental levels. Improvements on the detection limit would be different between K-edge and L-edge HERFD XAS because the separation between the emission line and scattering signal is smaller from a K-edge than an L-edge excitation. Hence, fluorescence signals from Se $K\alpha_1$ HERFD XAS is expected to offer greater improved concentration sensitivity than with Hg L_{III}-$L\alpha_1$ HERFD XAS. Figure 6.6A and Figure 6.6B show the HERFD XAS spectra collected from wild swordfish white muscle with estimated elemental levels of ~24 µM for Hg and ~12 µM for Se using the height of the edge-jumps compared to standards of known concentrations. For more information on selenium HERFD XAS, refer to Chapter 7. The spectra were fit using a linear combination of mercury reference standard compounds from a library of HERFD XAS mercury standard spectra with results shown in Table 6.2. Mercury and selenium species contributions were identified using a least squares fitting approach fitting the swordfish near-edge spectra to the sum of reference near-edge spectra. The best fit of the swordfish using mercury reference compounds of Hg L_{III}-$L\alpha_1$ HERFD XAS is shown in Figure 6.6A and shows main contributions from two main components of methylmercury cysteine (75 ± 3%) and methylmercury selenocysteine (25 ± 3%). Using a series of selenium reference compounds, Se $K\alpha_1$ HERFD XAS of the same swordfish tissue had a best fit comprising a combination of methylmercury selenocysteine (58 ± 2%), seleno-diglutathione (34 ± 0.8%), and selenomethionine (13 ± 1%) (Figure 6.6B). The relative level of methylmercury selenocysteine (~7 µM) contributing to the Se $K\alpha_1$ HERFD XAS is in good agreement with the relative level of methylmercury selenocysteine (~6 µM) monitoring the Hg L_{III}-$L\alpha_1$ HERFD XAS. Previous results showed a predominant contribution of methylmercury cysteine (Harris et al., 2003) only, however the improved energy resolution with HERFD XAS can discriminate the subtlety of closely similar species and perhaps offers new insights. Selenium is known to be highly attracted to mercury ions and mercury has been known to bind to endogenous selenium compounds (Korbas et al., 2010b; MacDonald et al., 2015a).

Table 6.2. Results from the best fit of a linear combination of reference mercury and selenium standards of swordfish muscle using Hg L_{III}-$L\alpha_1$ and Se $K\alpha_1$ HERFD XAS shown in Figure 6.6.

Spectra	Component	Fraction (%)
Hg L_{III}	methylmercury cysteine	75 ± 3
	methylmercury selenocysteine	25 ± 3
Se K	methylmercury selenocysteine	58 ± 2
	seleno-diglutathione	34 ± 0.8
	selenomethionine	13 ± 1

Least-squares fitting minimize function $= 1/N \sum_{j=1}^{N} (y_{j,obs} - y_{j,calc})^2$, where N is the total number of data points, j is the energy point number, $y_{j,obs}$ and $y_{j,calc}$ are the observed and calculated mixture intensities. The calculated spectrum is given by $y_{j,calc} = \sum_{i=1}^{m} x_i I_{i,j}$, where m is the number of components (user defined), i is the component number, x_i is the proportion of component i, $I_{i,j}$is the normalized intensity of the spectrum of component i at energy j.

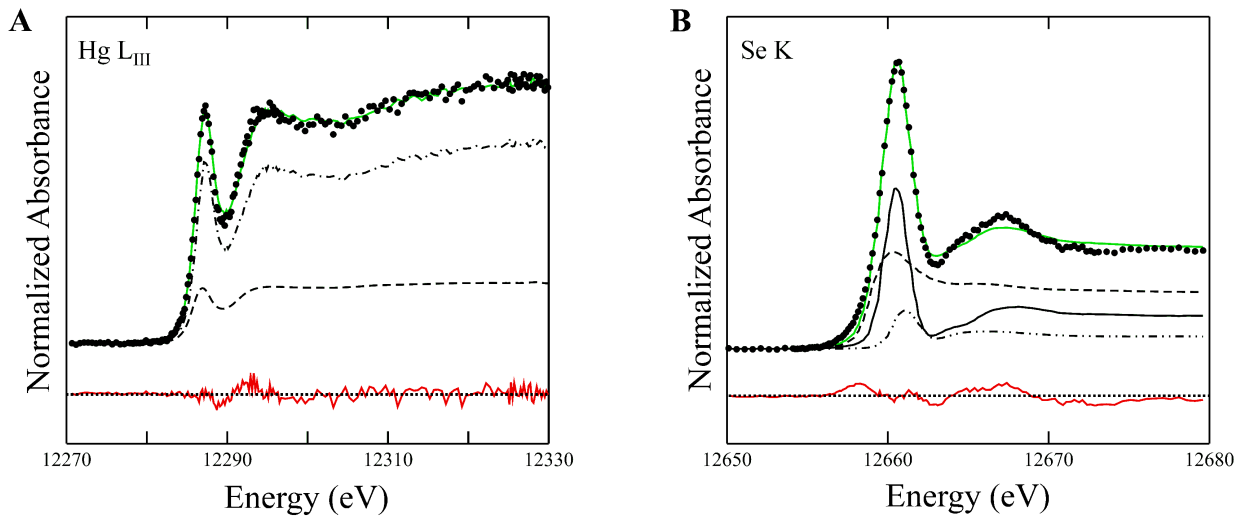

Figure 6.6. Species identification of swordfish tissue using mercury L_{III}-$L\alpha_1$ and selenium $K\alpha_1$ HERFD XAS. **A:** Mercury L_{III}-$L\alpha_1$ HERFD XAS experimental data (*circles, left*) was best fit (*solid green line)* with a major contribution from methylmercury cysteine (75 ± 3%, *dotted dashed line*) and a lesser contribution from methylmercury selenocysteine (25 ± 3%, *dashed dotted line*). **B:** Selenium $K\alpha_1$.HERFD XAS experimental data (*circles, right*) was best fit (*solid green line*) with methylmercury selenocysteine (58 ± 2%, *dashed line*), seleno-diglutathione (34 ± 0.8%, *dotted dashed line*), and selenomethionine (13 ± 1%, *solid black line*). Residual is shown in *red*.

Resonant Inelastic X-ray Scattering (RIXS)

Near-edge spectra are sensitive to electronic structure and the improved sensitivity of HERFD XAS offers great potential with natural samples. However, this technique is complex because the operation itself influences its capabilities in heterogeneous samples. HERFD XAS utilizes crystal analyzers that monitor and select just a small fraction of the fluorescence emission to be detected and with the work herein, the highest peak of the emission scan was selected due to the finest signature features. This method of choosing the highest peak of the emission scan to get the best discernable spectral features is acceptable when comparing different molecules in a series of samples (ex. titration, etc.). However, when using HERFD XAS for identifying components of a heterogeneous mixture, there can be significant challenges. Figure 6.7 shows the resonant inelastic X-ray scattering (RIXS) plot of the incident beam (Ω) as a function of the energy transfer ($\Omega-\omega$), with the relative concentration in the *z*-direction. The center diagonal of the RIXS plane delineate the HERFD XAS scan and is where most variable features are present. Noticeably, any deviation from the center of the RIXS plane would result in a different HERFD XAS spectra, therefore it is imperative to be vigilant when selecting the emission energy so that consistency is maintained and speciation is correct. Furthermore, the RIXS diagonal will be in varying positions for different compounds and this energy shift would translate to a small energy shift and change in spectral shape in the HERFD XAS which may also lead to species misidentification. The energy position of the emission scans of mercury compounds showed little variation with chemical form. However, this caution is increasingly probable with noisy datasets which is the case with natural samples with ultra-dilute levels of the elements of interest. To circumvent these challenges, a swathe of scans spanning the apex of the emission scan could be captured instead of selecting a single emission energy so that the data collected spans the range of emission peaks of different mercury species. Another possible solution would be to choose a fixed emission energy for all standards and unknown heterogeneous samples so that scans are at the very least consistent and reproducible. However, choosing scans at a fixed emission energy instead of the emission peak energy would introduce a small drawback in HERFD XAS spectral features. Fortunately the peak of the Hg $L\alpha_1$ emission is wide enough that small deviations from the center RIXS plane, and with the little variation in Hg emission line energies between different compounds, Hg L_{III}-$L\alpha_1$ HERFD XAS will likely not suffer from drastic changes to the shape of HERFD XAS spectra.

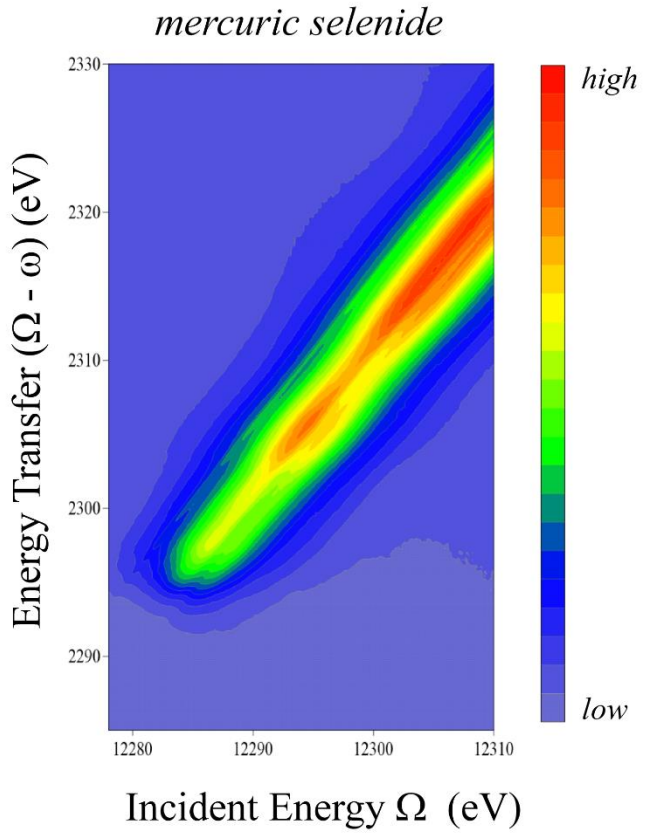

Figure 6.7. Mercury L_{III}-$L\alpha_1$ RIXS plane of mercuric selenide representing incident energy (Ω) as a function of energy transfer ($\Omega - \omega$). The most varied exclusive features unique to each compound are found on the center of the RIXS diagonal. Color bar represents photon counts measured; high signal (*red*); low signal (*purple*).

In this work, the remarkable potential of mercury L_{III}-$L\alpha_1$ HERFD XAS spectra to demonstrate signature features, that are often difficult to distinguish with conventional XAS, have been investigated. These signature features improve the speciation capabilities, allowing the distinguishing of formerly similar spectra of different chemical compounds. Mercury, like other 5d elements, has near-edge spectra with large broadening effects which are a result of beamline X-ray optics and core hole lifetime broadening effects. High energy resolution achieved from crystal analyzers omit much of the core hole lifetime Lorentzian broadening source, leaving only Gaussian-type contributions from beamline optics. Improving the energy resolution from beamline optical broadening affects could further improve the speciating capabilities. Nonetheless, the prime power with HERFD XAS will be the possibility to better distinguish various chemical forms of mercury, and will undoubtable revolutionize the investigations of mercury toxicity in biologically and environmentally relevant fields.

6.6 Acknowledgments

This work was supported by Discovery Grants from the National Sciences and Engineering Research Council of Canada (NSERC, I.J.P. and G.N.G.) an Innovation and Science Fund of Saskatchewan grant (I.J.P.), a Canada Foundation for Innovation John Evans Leader's Fund award (I.J.P.) and by Canada Research Chairs (I.J.P. and G.N.G.). S.N. acknowledges funding from the Dr. Rui Feng Scholarship and was a Fellow in the Canadian Institutes of Health Research-Training grant in Health Research Using Synchrotron Techniques (THRUST). N.V.D. was a THRUST Associate. Stanford Synchrotron Radiation Lightsource, SLAC national Accelerator Laboratory, is supported by the U.S. Department of Energy, Office of Science, Office of Basic Energy Sciences, under Contract No. DE-AC02-76SF00515. The SSRL Structural Molecular Biology Program is supported by the DOE Office of Biological and Environmental Research, and by the National Institutes of Health, National Institute of General Medical Sciences (including P41GM103393). The contents of this work are solely the responsibility of the authors and do not represent the official views of NIGMS or NIH.

CHAPTER 7. High Energy Resolution Fluorescence Detection X-ray Absorption Spectroscopy of Selenium Compounds

7.1 Preface

The toxic mechanism of elevated exposure to mercury compounds can be closely associated to endogenous selenium. The decrease of endogenously available selenium is thought to be partly responsible for the toxic effects of mercury, owing to the high affinity of selenium to mercury. Selenium can also be harmful if available in high quantities. Interestingly, a mutual detoxification of selenium and mercury compounds has been reported (Parízek and Ostádalová, 1967). Therefore, molecular characterization is important in understanding the mechanism between the relationship of mercury and selenium *in vivo*. X-ray absorption spectroscopy of the Se K-edge of some Se compounds are distinctive, with 1s–4p dipole allowed transitions producing sharp features in the near-edge spectra. However, selenium's $K\alpha_1$ emission line's proximity to the scattering peaks increases the contribution from background noise, making the sensitivity of this technique somewhat lacking. HERFD XAS rejects much of the background scatter which results in an improved signal-to-noise of the fluorescence signal and improves the sensitivity of the excited element. This chapter develops selenium $K\alpha_1$ HERFD XAS methods and examines the improved chemical sensitivity with HERFD XAS. *Ab initio* wavefunction calculations are employed to understand the electronic transitions and molecular orbitals responsible for the chemical signatures seen in the near-edge spectra of selenium compounds.

Author Contributions

This chapter will be reformatted as a journal article and submitted to *Chemical Research in Toxicology*.

Nehzati, S., Dolgova, N.V., Sokaras, D., Kroll, T., Pickering, I.J., and George, G.N. (2019) High Energy Resolution Fluorescence Detection X-ray Absorption Spectroscopy of Selenium Compounds. (*In preparation*)

S. Nehzati prepared the samples, collected and analyzed the XAS and HERFD XAS, performed DFT and StoBe-deMon calculations, and drafted the manuscript.
N. Dolgova performed XAS and HERFD XAS data.
D. Sokaras and T. Kroll optimized beamline configuration and assisted with experiments.
I. J. Pickering directed the science, performed data acquisition, reviewed the manuscript, and provided funds for the research.
G. N. George prepared some solid samples, directed the science, performed data acquisition, reviewed the manuscript, and provided funds for the research.

7.2 Abstract

Selenium K-edge high resolution fluorescence detection X-ray absorption spectroscopy (HERFD XAS) was measured for a series of selenium organic and inorganic compounds. HERFD XAS overcomes much of the core hole lifetime broadening effects and reveals new spectral features allowing for the chemical characterization of previously non-differentiable selenium compounds by conventional XAS. Electronic transitions of photoelectrons of 1s–4p transitions that make up the near-edge features of selenium, near-edge spectroscopy were deduced using calculated StoBe-deMon simulations of Kohn-Sham approximations. The sensitivity of selenium $K\alpha_1$ HERFD XAS is highlighted with the site-specific detection of selenium compounds at ultra-dilute endogenous levels of a biological sample.

7.3 Introduction

Selenium (Se) is an essential micronutrient (Winkel et al., 2015). As a member of group XVI elements, selenium shares similarities in chemical properties to another chalcogenide sulfur (S), but with a greater redox potential which may be why it is involved in some of the most important reactions in biochemistry (Jacob et al., 1999). In recent years, interest in selenium chemistry has increased due to the narrow range between essential and toxic levels, its highly reactive chemistry, and role in mercury detoxifying mechanisms (Zhang et al., 2013). Selenium is highly redox active, ranging oxidation states from –2 to +6, with the most common being elemental selenium (Se0) selenide (Se–II), selenite (SeIV), and selenate (SeVI). Selenium is represented in a large number of different chemical species, with inorganic selenium compounds usually found in soil and

aquatic systems, and both organic and inorganic species present in biological organisms ranging from bacteria to humans. In the environment, the pH of soil of vegetation plays a critical role in the chemical form of selenium oxyanions and therefore the bioavailability (Raptis et al., 1983). The levels of selenium in our diet largely depend on the selenium levels and speciation in soil and the extent of selenium accumulation of vegetation in a given geographical area (Thavarajah et al., 2007).

Selenium plays a key role in the active site of several essential Se-proteins, predominantly by means of a single selenocysteine residue (Roman et al., 2014), emphasizing its influential role in protein function (Gladyshev, 2006). Of the twenty-five Se-proteins identified in humans, only a small number of them have been functionally and structurally characterized which can be due to their understated presence, as well as the high reactivity of selenocysteine residues which increases the difficulty during investigations to keep enzymes intact (Roman et al., 2014; Avery and Hoffmann, 2018). Among them, the redox regulation of glutathione peroxidases (GPxs) and thioredoxin reductases (TrxRs) are the most studied (Roman et al., 2014). Atypical activity of seleoproteines have been known to play a role in a number of diseases including muscle disorders, cardiovascular diseases, epilepsy, inflammatory responses, HIV, endocrine disorders, male infertility, and cancer (Roman et al., 2014). A major excretion metabolite of selenium after exposure to high levels of selenium is trimethyl selenonium, produced by methyltransferases throughout the body (Kuehnelt et al., 2007). The intermediate dimethyl diselenide is kinetically favoured and exhaled through the lungs (Roman et al., 2014).

As previously mentioned, one of the challenges in studying selenium metabolism in biological organisms is its low abundance. In most organs and tissues selenium content is 1-10 µM (Dolgova et al., 2016). X-ray absorption spectroscopy (XAS) is a great tool for studying chemical speciation, particularly because it allows the determination of different chemical forms in a heterogeneous mixture without any sample preparation and therefore without artefacts. One of the limitations of XAS is that it often requires concentrations two to three orders higher than what is found in biological systems. The improved concentration sensitivity of selenium $K\alpha_1$ high energy resolution fluorescence detection (HERFD) XAS is expected to be instrumental in measuring natural selenium levels found in biological organisms. In the case of selenium, since the concentration range between essential nutrient and toxic character is very narrow, it is extremely important for the detection of chemical species of selenium at naturally relevant levels in order to

understand the fine line between health and disease. HERFD XAS can also be beneficial for other fields of study, for example geochemistry. Natural levels of selenium are highly variable in the earth's crust (Sharma et al., 2015) which may lead to challenges for analytical investigations in areas of dilute natural levels. The near-edge region of XAS is characteristically useful in identifying coordination environments and oxidation states due to the activity of unoccupied valence orbitals in excited states which are commonly chemical specific. The near-edge regions for heavier elements have poor spectral resolution with broad spectra due to the short core hole lifetime which increases energy uncertainty and has broadening effects obscuring spectral details necessary to discriminate between different compounds, especially those involving the lowest unoccupied molecular orbital (LUMO) states (Bauer, 2014). HERFD XAS data is collected by selecting a narrow window of the emission line to preferentially diffract a narrow emission energy using a multi-crystal Johann-type spectrometer (Sokaras et al., 2013). Furthermore, at low concentrations, background noise from inelastic scattering is dominating the fluorescence signal in selenium K-edge XAS which makes investigations on dilute samples more challenging. The use of HERFD XAS with improved signal-to-noise and emission-tuning produces sharper spectra for any absorbing elements and will help in establishing better structural models. Gathering information on the electronic structure is key to many scientific problems including the identification of toxic chemical species, enzyme mechanisms, and elemental distribution *in situ*.

HERFD XAS has been evidently suitable in a number of solid state and catalysis studies probing the LUMO structure to give precise measurements of molecular orbitals (Hűbner et al., 2012; Sa et al., 2012; Atkins et al., 2012; Kvashnina et al., 2013; Kleymenov et al., 2012). However, HERFD XAS in health and environmental research is only starting to be pursued. Previous work in our group has shown the formation of a new species of selenyl radical showcasing the enhanced chemical sensitivity of this technique (Nehzati et al., 2018). Removing the limitations from conventional XAS to investigate relevant chemical species at dilute concentration would offer profound information. The initiatives for the work herein were to probe the chemical and concentration sensitivity of Se $K\alpha_1$ HERFD XAS and unveil exciting opportunities with investigations pertaining to selenium compounds in a wide variety of research disciplines and to establish the foundation for prospects in further research explorations. The potential to detect molecular species at natural levels *in situ*, presently under-realized in areas of health and environmental research, will be tremendous.

7.4 Materials and Methods

7.4.1 Sample Preparation

Selenocystine, selenomethionine, oxidized glutathione, cysteine, sodium borohydride, iodomethane, and dimethyl diselenide were purchased from Sigma Aldrich. Sodium selenate, sodium selenite, grey selenium powder, selenium sulfide, arsenic selenide, iron selenide, nickel selenide, copper (I) selenide, copper (II) selenide, and zinc selenide were purchased from Alfa Aesar. Manganese selenide was purchased from Strem Chemicals. Dimethyl selenide was purchased from Fluka. Selenocysteine, selenocysteinate, seleno-sulfocystine were prepared as previously described (Pickering et al., 1999). Trimethyl selenonium was prepared from an adapted protocol (Zhao et al., 2010). Solutions for HERFD XAS were prepared as 1mM (final) aqueous solutions and injected into polyacetal cuvettes covered with metal-free Mylar tape and frozen in a slurry of LN_2-isopentane. Solutions for conventional XAS contained 20% v/v glycerol to minimize ice diffraction effects and were taped with metal-free Kapton tape. Solid samples were prepared as 5 % weight of the compound, diluted with boron nitride and grounded to a fine powder. Powder samples were loaded into metal-free sample holders windowed with Mylar tape.

7.4.2 High Energy Resolution Fluorescence Detection X-ray Absorption Spectroscopy

Selenium $K\alpha_1$ HERFD XAS spectra were collected at beamline 6-2 at the Stanford Synchrotron Radiation Lightsource (SSRL). The SPEAR3 storage ring was operating at 3.0 GeV with a current of 350 mA. A Si(311) double crystal monochromator was used for energy-tuning of the incident beam and a single or 6-element array of Si(844) crystal analyzer was used to monitor and maintain the desired portion of the Se $K\alpha_1$ emission line. Samples were placed in a helium flow cryostat at 45° to the incident beam, maintaining a temperature of 10 K to minimize thermal contributions. A helium filled ion chamber was placed before the cryostat to monitor incident X-rays. The monochromator was energy calibrated relative to the lowest-energy inflection of grey Se, assumed to be 12,658 eV. Fluorescence emission was monitored using a single element silicon-Vortex solid-state detector. Data reduction and analysis was carried out using the EXAFSPAK suite of computer programs (George, G.N., 2000).

7.4.3 X-ray Absorption Spectroscopy (XAS)

Conventional Se K-edge XAS spectra were collected at beamline 7-3 at SSRL. The endstation employs a Si(220) double crystal monochromator and nitrogen-filled ionization chamber to monitor the incident X-ray intensity. X-ray absorption was measured by the X-ray fluorescence excitation spectrum using a 30-element germanium detector. Soller slits and arsenic containing filters (EXAFS Materials, Danville, California, USA) were used to limit unwanted scattering radiation. Transmittance measurements were collected using nitrogen-filled ionization chambers placed before and after the sample to monitor the transmission of X-rays through the sample. Samples were in a liquid helium cryostat holding a temperature of 10 K at 45° to the incident X-ray beam. Simultaneous absorption of standard grey hexagonal Se was collected downstream by transmittance using nitrogen-filled ionization chambers.

7.4.4 Ab initio Theoretical Calculations

Density functional theory (DFT) calculations were performed using the program DMol^3 (Delley, 1990; Delley, 2000) on Biovia Materials Studio version 2018 R2. The GGA PBE functional and all-electron relativistic core treatments were employed for the self-consistent field procedure, and when appropriate, solvation effects were modeled using the COSMO model for water (ε = 78.54) (Klamt and Schüürmann, 1993). Near-edge spectra were simulated from Dmol^3 geometry-optimized, energy-minimized coordinates and using the StoBe-deMon code using half-core hole potentials for core hole calculations (Hermann et al., 2001). Orbital basis sets employed were as follows: selenium (ii_iglo) or selenium (63321/5321/41); sulfur (73111/6111/1); oxygen (7111/411/1); nitrogen (7111/411/1); carbon (6311/311/1); and hydrogen (311/1); with auxiliary basis sets for interpolation of the exchange-correlation potential as: selenium (5,5;5,5); sulfur (5,4;5,4); oxygen (5,2;5,2); nitrogen (5,2;5,2); carbon (5,2;5,2); and hydrogen (3,1;3,1). Theoretical calculations for molecules with two or more selenium atoms were described by means of a carbon surrogate (and corresponding basis sets) for the non-core-excited selenium to minimize complications. Electron density isovalues were mapped using 0.05 spin per a.u.. Spectra convolution was performed using parameters as described previously (Doonan et al., 2008).

7.5 Results and Discussion

7.5.1 Improved Speciation Capabilities of HERFD XAS

Figure 7.1 compares the experimental spectra of selenium Kα_1 HERFD XAS (*solid line*) and conventional selenium K-edge XAS (*dashed line*) of various inorganic selenide compounds. The selenium Kα_1 HERFD XAS reveals spectral details at the absorption edge owing to the diminished core hole lifetime broadening effects, whereas the conventional XAS exhibits a much broader absorption edge. HERFD XAS rejects much of the second-order scattering processes and allows for sharper spectra due to the improved energy resolution. Furthermore, HERFD XAS reveals spectral features within the absorption edge that are not detectable with conventional XAS. This was especially evident in spectra of manganese selenide, nickel selenide, copper (I) selenide, and zinc selenide in Figure 7.1. The improved energy resolution of selenium Kα_1 HERFD XAS leads to enhanced capabilities of differentiating between similar chemical species.

The selenium oxyanions are a group selenium compounds that partake in important redox reactions. With conventional XAS, it is difficult to distinguish between the various degrees of protonation states of selenate, and to a lesser degree with selenite. The redox reactions of the Se oxyanions present great chemical interest and in soil and sediments they vary from the oxidized Se(VI) selenate ($[SeO_4]^{2-}$, $[HSeO_4]^-$; pK_a ~1.7), or the reduced Se(IV) selenite ($[SeO_3]^{2-}$, $[HSeO_3]^-$, H_2SeO_3; pK_{a1} 2.64, pK_{a2} 8.4) (Peak, 2006). The various chemical forms of Se in soil affect sorption, bioavailability, and therefore play an important role in the cycling of Se in the environment (Navarro-Alarcon and Cabrera-Vique, 2008). Figure 7.2 illustrates the opportunities of improved chemical speciation of Se Kα_1 HERFD XAS using the selenium oxyanions as an example. Conventional XAS spectra of selenate in the two illustrated spectra (Figure 7.2, *left*) are almost identical and largely indistinguishable. Conventional XAS spectra of selenite (Figure 7.2, *right*) only shows slight deviations between the different protonation states. Contrarily, selenium Kα_1 HERFD XAS spectra shows clear separation between the different protonation states which would make identifying these chemical species more straightforward.

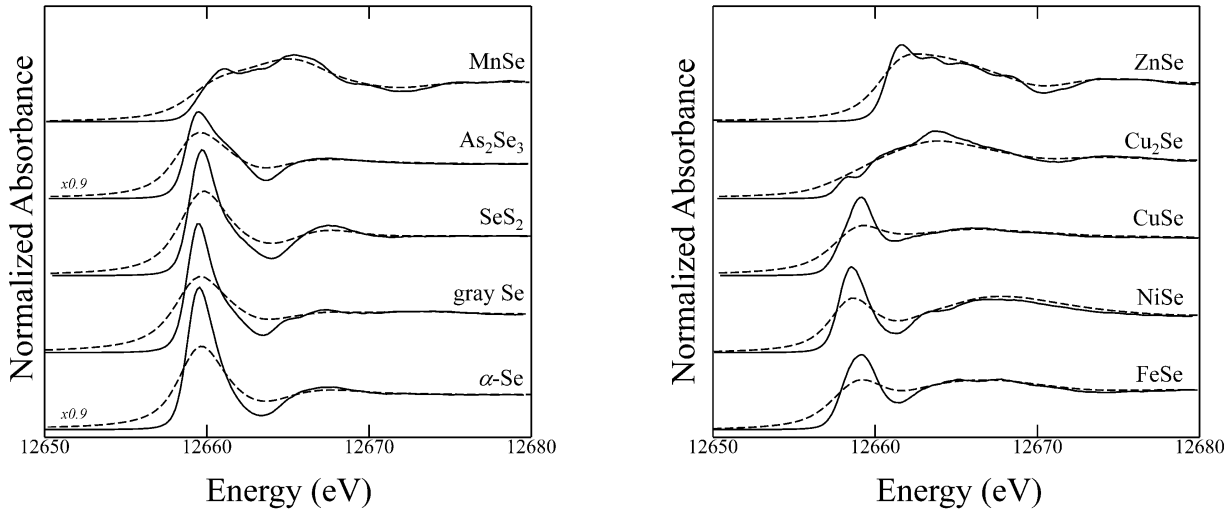

Figure 7.1. Selenium Kα$_1$ HERFD XAS spectra compared with conventional K-edge XAS spectra of inorganic selenide compounds. HERFD XAS shown in *solid line*; conventional XAS shown in *dashed line*. HERFD XAS spectra generated from selecting the emission energy at the peak of the emission scan for each individual selenium compound.

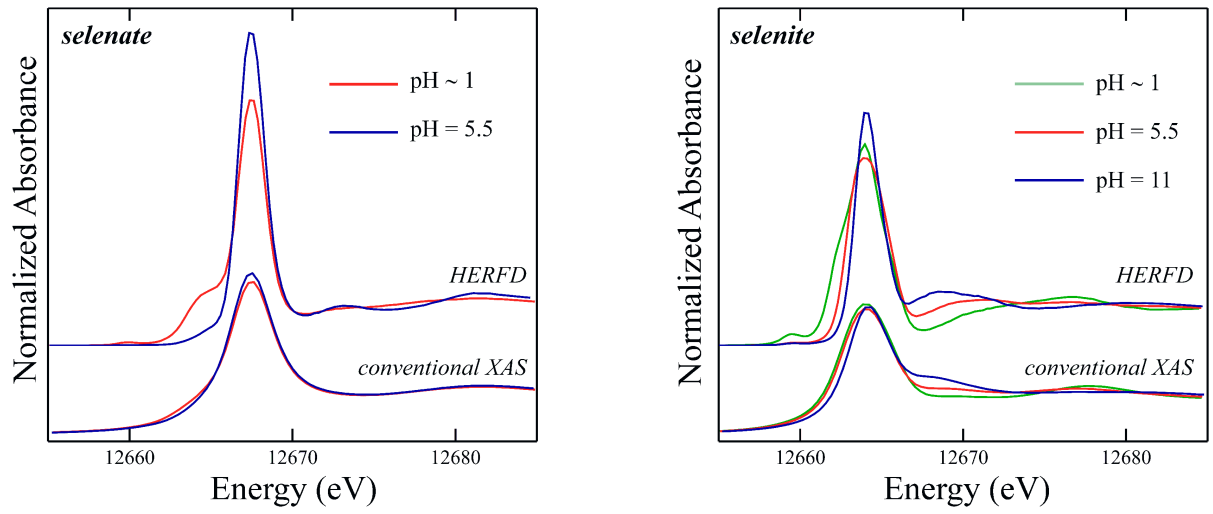

Figure 7.2. Selenium Kα$_1$ HERFD XAS spectra compared with conventional K-edge XAS spectra of selenium oxyanions. *Left*: solution sodium selenate shown at pH ~ 1 and ~ 5.5. *Right*: solution sodium selenite shown at pH ~ 1, ~ 5.5, and ~ 11. Conventional XAS scans show almost indistinguishable spectra, whereas selenium Kα$_1$ HERFD XAS scans show spectral features to distinguish between different protonation states of selenate and selenite solutions.

7.5.2 Ab initio Theoretical Calculations

The chemical speciation and chemical sensitivity improvements with HERFD XAS are substantial and this is evident by the comparison between selenium $K\alpha_1$ HERFD XAS experimental spectra and simulated spectra calculated from StoBe-deMon Kohn-Sham approximations. Figure 7.3 and Figure 7.4 show the selenium $K\alpha_1$ HERFD XAS and simulated StoBe-deMon calculated spectra of common organoselenium compounds, and corresponding major electron transitions responsible for the shape of the absorption edge. In all cases, the calculated spectra are in good agreement with the experimental spectra. The intensity and energy of the electron transition of the Se(1s) electron to the lowest unoccupied molecular orbital (LUMO) with 4p character is influenced by the bonding and chemical environment of the absorbing Se atom. Table 7.1 lists some of the major calculated StoBe-deMon transitions. The transitions are listed in order of increasing energy as LUMO, LUMO+1, and LUMO+2 transitions. All organoselenium compounds but selenourea and seleno-*bis*-methanethiol (representing seleno-diglutathione) had the highest cross section corresponding to Se(1s) excitation into the antibonding σ^* LUMO. As expected the positively charged trimethyl selenonium ion had the highest energy LUMO with a peak at 12,662.51 eV. The following molecular orbital diagrams, simulated from StoBe-deMon calculations are described in an attempt to understand the experimental selenium $K\alpha_1$ HERFD XAS spectra. LUMO, LUMO+1, and LUMO+2 were derived from DFT calculations using GGA PBE functionals for the self-consistent field procedure, and simulated using StoBe-deMon computed transitions.

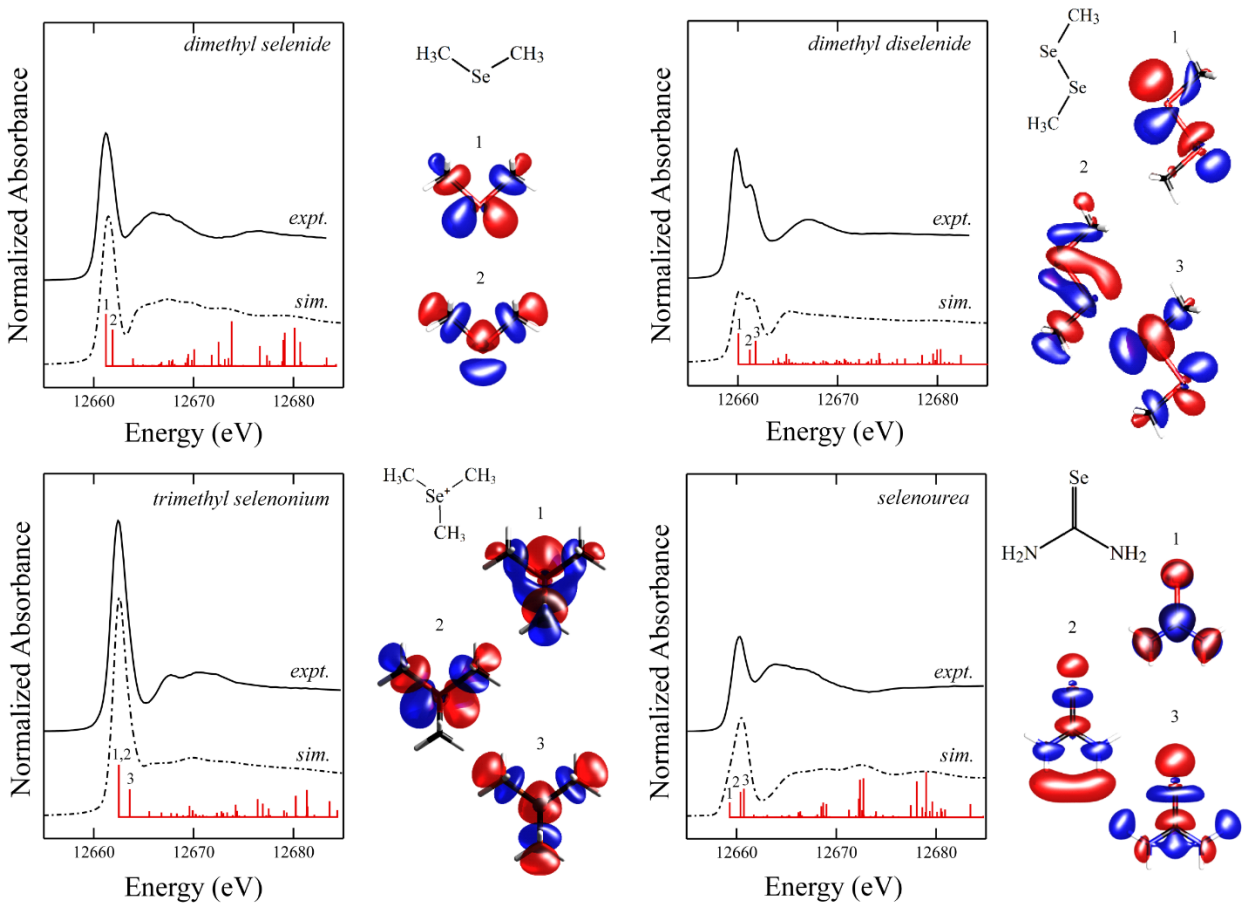

Figure 7.3. Experimental and simulated data of selenium Kα$_1$ HERFD XAS of small molecule organoselenium compounds. Experimental data shown in *solid lines*; simulated spectra shown in *dashed lines* and obtained from convoluting StoBe-deMon transition calculations shown in *red* stick spectrum. Lowest unoccupied molecular orbital (LUMO), LUMO+1, and LUMO+2 molecular orbital diagrams, corresponding to theoretical calculated transitions 1, 2, and 3, respectively (where applicable).

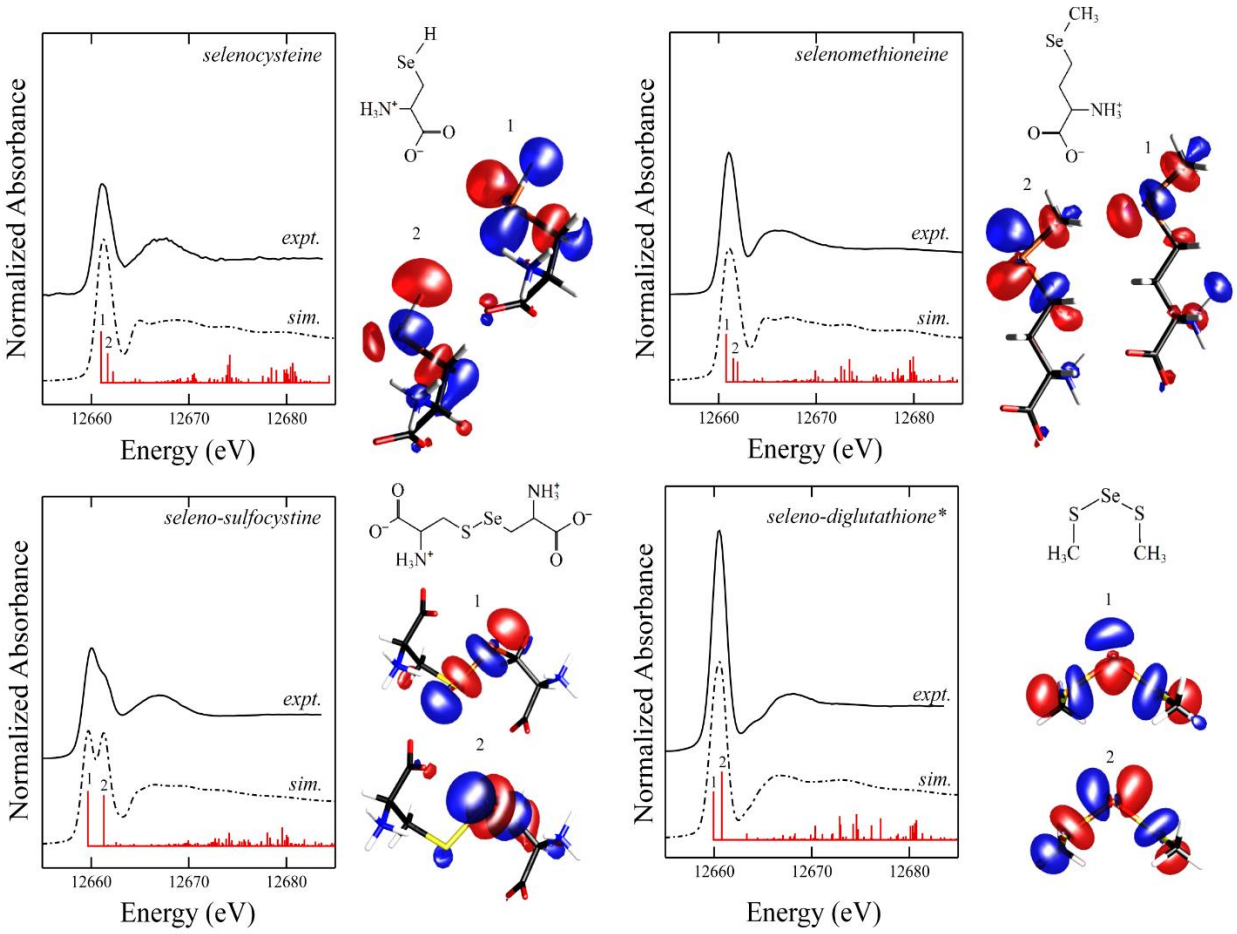

Figure 7.4. Experimental and simulated data of selenium Kα_1 HERFD XAS of extended organoselenium compounds. Experimental data shown in *solid lines*; simulated spectra shown in *dashed lines* and obtained from convoluting StoBe-deMon transition calculations shown in *red* stick spectrum. The lowest unoccupied molecular orbital (LUMO) and LUMO + 1 correspond to transitions 1 and 2 from half-core hole excited state calculations. *Simulated spectra and corresponding StoBe-deMon transition calculation are of a simplified model analogue of seleno-diglutathione, selenium-*bis*-methanethiol, due to the atom limits of the software.

Table 7.1. Calculated StoBe-deMon selenium K-edge electronic transitions of organoselenium compounds.

	Calculated StoBe-deMon transitions (eV)		
Compound	LUMO	LUMO+1	LUMO+2
dimethyl selenide	12,661.22	12,661.89	–
dimethyl diselenide	12,660.06	12,661.20	12,661.78
trimethyl selenonium	12,662.51	12,662.52	12,663.60
selenourea	12,659.33	12,660.40	12,660.74
selenocysteine	12,661.00	12,661.68	12,662.23
selenomethionine	12,660.76	12,661.50	–
seleno-sulfocystine	12,659.67	12,661.30	–
seleno-*bis*-methanethiol (model for selenium-diglutathione)	12,659.94	12,660.79	–

Small molecule organoselenium compounds. Dimethyl selenide is known to play an important role in the global cycling of selenium and is also found as a major exhalation product of selenium metabolism in humans (Vriens et al., 2014; Ohta and Suzuki, 2008). Experimental $K\alpha_1$ HERFD XAS and StoBe-deMon calculated electronic transitions are shown in Figure 7.3. The first electronic transition in the calculated near-edge spectra of dimethyl selenide at 12,661.22 eV corresponds to the LUMO antibonding σ* (Se–C) (Figure 7.3). The next transition at 12,661.89 eV corresponds to LUMO + 1 antibonding σ* (Se–C). Dimethyl diselenide is considered one of the key players in the global cycling of selenium (Groner et al., 2004). The highest intensity electronic transition of dimethyl diselenide in the calculated near-edge spectra is illustrated at 12,660.06 eV and corresponds to molecular orbitals of Se(1s) excitation to LUMO antibonding σ* (Se–Se). The next transition at 12,661.89 eV is dominated by π bonding-like character between the two Se atoms. The third transition at 12,661.78 eV has molecular orbitals dominated by antibonding σ* (Se–Se) and σ* (Se–C). Trimethyl selenonium ion is known as a major urinary metabolite in humans (Ohta and Suzuki, 2008). The calculated near-edge spectra of trimethyl selenonium has one high intensity transition at 12,662.51 eV with molecular orbitals corresponding to antibonding σ* (Se–C) to all three carbons. The transition at 12,662.52 eV corresponds to antibonding σ* (Se–C) to two of the three carbons. The third transition at 12,663.60 eV corresponds to antibonding σ* (Se–C) with all three carbons. Selenourea has no known natural

biological activity but has been shown to be efficient in free radical scavenging activity, more so than its thiourea analogue (Hussain et al., 2014). The first electronic transition for selenourea at 12,659.33 eV corresponds to LUMO antibonding π* of the Se atom. Transition 2 at 12,660.40 eV is characterized with molecular orbitals of LUMO + 1 antibonding σ* (Se=O). The next transition at 12,660.74 eV is the strongest intensity and is assigned to molecular orbitals dominated with LUMO + 2 antibonding σ* (Se=O) and antibondingσ* (Se–N).

Extended organoselenium compounds. Selenium is part of a number of amino acids found in biological systems (Pickering et al., 1999). Selenocysteine was named the 21st amino acid after the discovery of the UGA codon responsible for its biosynthesis (Turanov et al., 2011). Figure 7.4 shows the experimental Kα_1 HERFD XAS and StoBe-deMon calculated electronic transitions of various extended organoseneium compounds. The strongest intensity transition of selenocysteine at 12,661.00 eV corresponds to Se(1s) excitation to 4p LUMO antibonding σ* (Se–C) and antibonding σ* (Se–H). The next transition at 12,661.68 eV is also characterized by antibonding σ* (Se–C) and σ* (Se–H). As previously mentioned, the amino acids selenomethionine and seleno-sulfocystine have been detected in biological systems (Pickering et al., 1999). The highest transition probability for the calculated spectra of selenomethionine (Figure 7.4) assigned at 12,660.76 eV is dominated by the Se(1s) excitation to the 4p antibonding σ* (Se–C). Electronic transition 2 at 12,661.50 eV is characterized by LUMO + 1 antibonding σ* to the terminal carbon (Se – C). The first and highest electronic transitions of seleno-sulfocystine in the calculated near-edge spectra at 12,659.67 eV is assigned to the LUMO antibonding σ* (Se–S). The second transition at 12,661.30 eV is characterized by LUMO + 1 antibonding σ* (Se–C). The HERFD XAS spectra of seleno-diglutathione is shown in Figure 7.4. The calculated stick spectrum is that of a simplified model analogue, selenium-*bis*-methanethiol, due to the limits in number of atoms allowed in the StoBe-deMon software. The first most intense electronic transition of selenium-*bis*-methanethiol at 12,659.94 eV corresponds to molecular orbitals with Se(1s) excitation to LUMO antibonding σ* (Se–S). The second transition at 12,660.79 eV is again a theoretical molecular orbital with LUMO + 1 antibonding σ* (Se–S) (Figure 7.4).

7.5.3 Improved Detection of Naturally Relevant Levels with HERFD XAS

$K\alpha_1$ HERFD XAS of selenium detects only a narrow window of the $K\alpha_1$ emission peak which suppresses the core hole lifetime broadening effects on spectral linewidths and consequently improves the signal-to-noise. This rejection of the background noise greatly improves the sensitivity of this method which is especially favourable for selenium due to the proximity of the Se $K\alpha_1$ emission peak to inelastic scattering X-rays. The increased sensitivity of selenium $K\alpha_1$ HERFD XAS permitted the collection of acceptable quality spectra of aqueous solutions as low as 100 nM which would be immensely helpful in the investigations of natural elemental levels in areas of health and environmental sciences.

The improved chemical sensitivity offered by HERFD XAS is useful in investigating natural levels of chemical species. Figure 7.5A compares the $K\alpha_1$ HERFD XAS detection method compared to conventional XAS. Conventional XAS employing energy dispersive detectors with an energy resolution of ~150–300 eV produce broad signals with a dominating contribution from Comptom X-ray scattering (Figure 7.5A, *red*). HERFD XAS instrumentation provides superior energy resolution which for selenium is capable of separating the $Se\alpha_1$ and $Se\alpha_2$ emission lines (Figure 7.5A, *black*). Isolating a small band of the $Se\alpha_1$ emission line eliminates the dominating Compton X-ray scattering contribution. Figure 7.5B shows the Se K-edge spectra of the same sample of fish tissue, estimated by edge-jump analysis to comprise of ~5 µM selenium. The results show the undeniable improvements with concentration sensitivity provided by HERFD XAS compared to conventional XAS.

The HERFD XAS spectrometer requires a small focused beam which permits the detection of species at greater spatial resolution. Furthermore, the need to capture bulk sample regions of heterogeneous natural samples for acceptable signal detection are diminished due to the concentration sensitivity gains with HERFD XAS. Figure 7.6 shows an example scan of human brain of an individual that has been exposed to elevated mercury levels. With a beam size of 100 x 400 µm, adequate signal is achieved in which the detection of different chemical species is distinguishable in different scanning spots. Least-squares fitting of the near-edges of two different regions of the human brain show two different accumulation patterns. *Position A* (Figure 7.6) comprises of predominantly α-Se, whereas *Position B* showed contributions from two components of mostly selenocysteine and partly *nano*-HgSe.

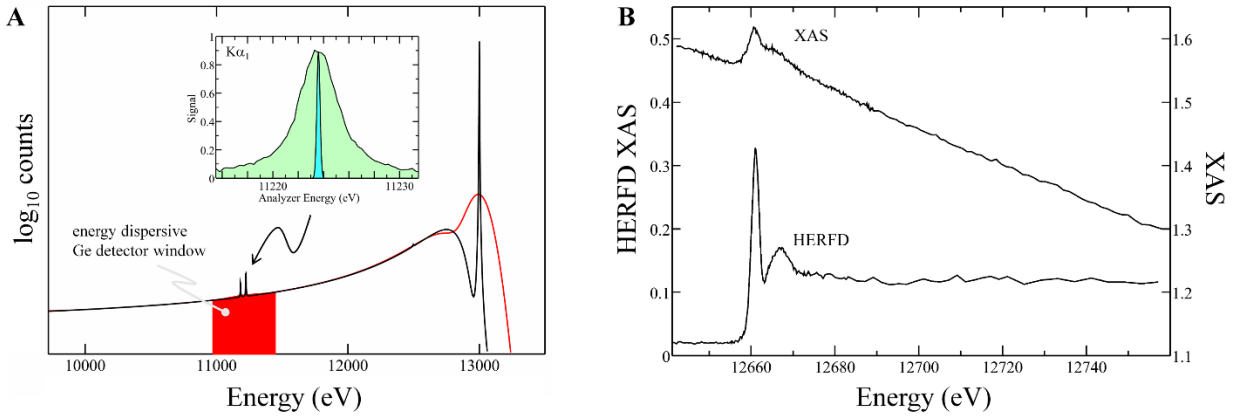

Figure 7.5. Illustrations showing improved concentration sensitivity of selenium $K\alpha_1$ HERFD XAS compared to conventional XAS. **A**: Computed Compton X-ray scatter of conventional XAS detection (*red*) with averaged Se $K\alpha_{1,2}$ signal and HERFD XAS detection (*black*) with separate distinct Se $K\alpha_1$ and $K\alpha_2$ emission lines. Inset shows band of Se $K\alpha_1$ emission line measured (*bright blue*) using HERFD XAS instrumentation. **B**: Comparison of conventional XAS and HERFD XAS scans of same fish tissue sample under similar beamline conditions. Note: conventional XAS scan was collected with ~42 × larger solid angle.

Scans on natural samples at dilute and ultra-dilute levels are however challenging due to the signal-to-noise ratio of the emission scan. A noisy emission scan would make it difficult to locate the true centroid of the emission peak which may lead to mischaracterization of results during qualitative analysis of HERFD XAS scans. Figure 7.7, *left*, shows a selenium $K\alpha_1$ resonant inelastic X-ray scattering (RIXS) spectra of zinc selenide. RIXS spectra measures an XAS spectrum (Ω) in 0.25 eV intervals of the emission energy (ω) and adds another dimension to probe both XAS and XES (X-ray emission spectroscopy). The diagonal lines through the RIXS plane correspond to HERFD XAS spectra at fixed emission energies. The highest intensity of the emission peak would reveal the most details in the HERFD XAS spectra. Dilute samples produce noisy emission scans and it is evident in the RIXS spectra (Figure 7.7, *left*) that when the emission energy is off the energy transfer diagonal, exclusive features belonging to specific chemical species begin to change shape, which makes qualitative identification of the species present very challenging. To minimize the possibility of being off the highest intensity of the emission scan, a peak deconvolution method to fit the emission peak using a sum of pseudo-Voigt peak shapes would help maintain the precision in the HERFD XAS.

Applications of HERFD XAS for species identification are straightforward when the sample is homogenous, comprising a single species. However, species identification in a heterogeneous sample, comprising more than one chemical species, is much more challenging. Figure 7.7, *right*, shows the selenium $K\alpha_1$ RIXS spectra of a 50/50 mixture of sodium selenate and dimethyl selenide. The spectra clearly show two separate RIXS diagonal planes corresponding to the highest intensity of each chemical species' emission peak, 11,223.9 and 11,223.1 eV, respectively. Therefore, it may not be sufficient to attempt fingerprint identification of a heterogeneous unknown sample with reference standard HERFD XAS spectra that have been collected using their individual emission energy peaks. Instead, choosing a fixed emission energy for the library of standards as well as any unknown samples would uphold the spectral integrity. Also, for heterogeneous mixtures especially, it may be prudent to collect spectra at a range of emission energies spanning the apex of the emission scan in order to avoid missing any important information.

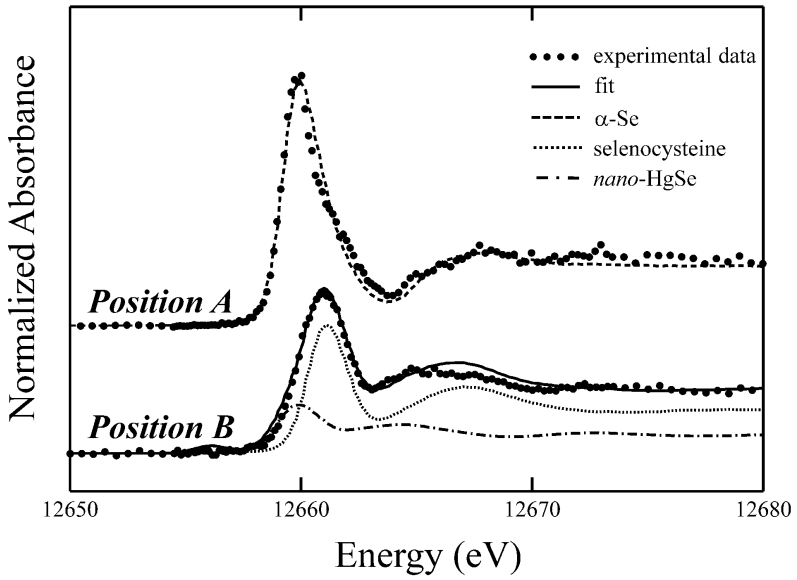

Figure 7.6. Selenium $K\alpha_1$ HERFD X-ray absorption spectra of human cerebellum sample of individual exposed to elevated mercury levels. ***Position A*** and ***Position B*** correspond to different regions of the brain being scanned. Results from near-edge fitting to a library of selenium standards clearly show different components responsible for the shape of the near-edge measured.

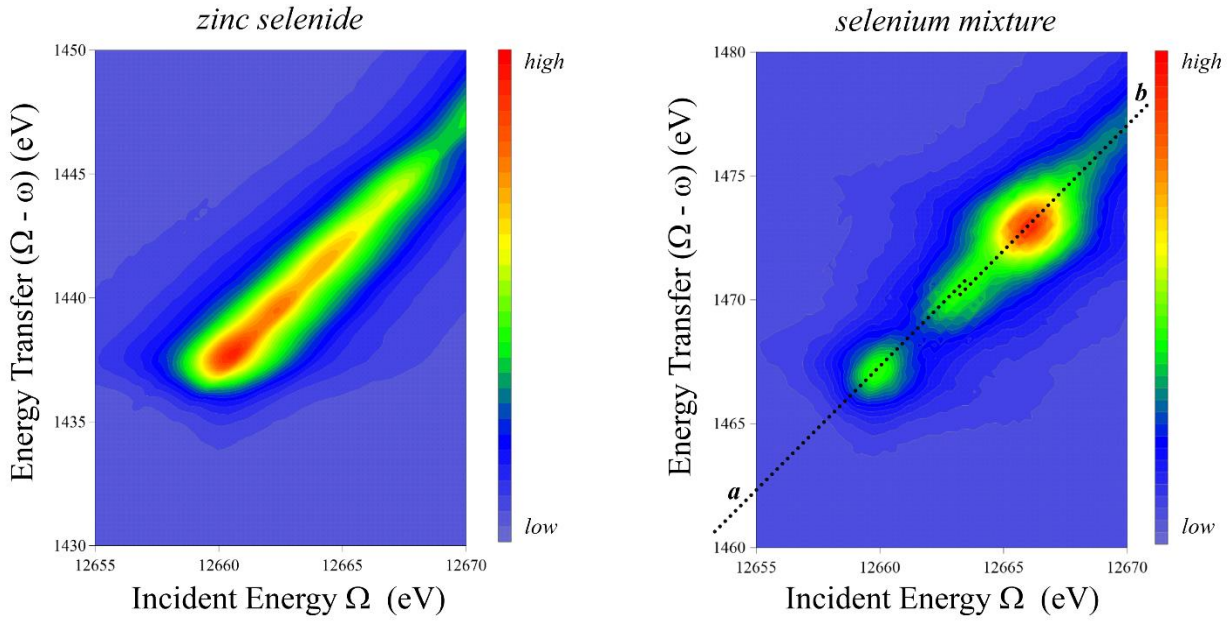

Figure 7.7. Selenium Kα$_1$ RIXS spectra of selenium compounds. *Left:* Selenium Kα$_1$ RIXS plane of zinc selenide. The RIXS diagonal gives the HERFD XAS where exclusive features to the specific chemical species are found. *Right:* Selenium Kα$_1$ RIXS plane of an equimolar, heterogeneous solution sample of ***a)*** dimethyl selenide and, ***b)*** sodium selenate. The RIXS diagonals (*black dotted lines*) gives the HERFD XAS of each species where exclusive features to each selenium species are found. Color bars represent the measured photons; high signal (*red*); low signal (*purple*).

In summary, there is a wealth of possibilities for selenium $K\alpha_1$ HERFD XAS applications in the health and environmental sciences. This technique requires a high flux density to achieve reasonable count rates and therefore X-ray induced photochemistry of samples may be problematic. Nonetheless, studies into the electronic levels that determine chemical and catalytic properties or electronic transitions during the course of a reaction are excellent targets for HERFD XAS. Beyond that, the sensitivity of this technique would provide profound opportunities in detecting natural levels of trace chemical species in a variety of disciplines.

7.6 Acknowledgments

This work was funded by Discovery Grants from the National Sciences and Engineering Research Council of Canada (NSERC, I.J.P. and G.N.G.) an Innovation and Science Fund of Saskatchewan grant (I.J.P.), a Canadian Foundation for Innovation John Evans Leader's Fund award (I.J.P.) and by Canada Research Chairs (I.J.P. and G.N.G.). S.N. acknowledges funding from the Dr. Rui Feng Scholarship and was a Fellow in the Canadian Institutes of Health Research-Training grant in Health Research Using Synchrotron Techniques (THRUST). N.V.D. was a THRUST Associate. Stanford Synchrotron Radiation Lightsource, SLAC national Accelerator Laboratory, is supported by the U.S. Department of Energy, Office of Science, Office of Basic Energy Sciences, under Contract No. DE-AC02-76SF00515. The SSRL Structural Molecular Biology Program is supported by the DOE Office of Biological and Environmental Research, and by the National Institutes of Health, National Institute of General Medical Sciences (including P41GM103393). The contents of this work are solely the responsibility of the authors and do not represent the official views of NIGMS or NIH.

CHAPTER 8. Hg(II) Binding to Thymine Bases in DNA

8.1 Preface

Mercury toxicity is thought to occur at the genetic level, binding to DNA helices and disrupting normal DNA function. One might expect mercuric ions to bind to the negatively charged phosphate backbone of DNA, however it has long been known that mercury ions can and do preferentially bridge between nucleotide bases within the DNA helix (Thomas, 1954; Eichhorn, 1963). This chapter examines the chemical speciation interaction of Hg(II) with 1-methylthymine using spectroscopic techniques, to understand the preferred binding site of the metal ion to thymine bases. Quantum-mechanical/molecular-mechanical (QM/MM) studies of canonical DNA and Hg(II) are performed to support the electronic structures observed from the spectroscopic results. HERFD XAS was used to establish a spectroscopic fingerprint of mercury coordination to *bis*(1-methylthymine) unlike other possible biological coordinations of Hg(II).

Author Contributions

This chapter will be reformatted and submitted to *ACS Omega*.

Nehzati, S., Summers, A.O., Zhu, J., Sokaras, D., Kroll, T., Pickering, I.J., and George, G.N. (2019) Hg(II) Binding to Thymine Bases in DNA. (*In preparation*)

S. Nehzati prepared the samples, collected and analyzed the XAS and HERFD XAS experiments, performed QM/MM studies, as well as drafted the manuscript.
A. O. Summers contributed to the scientific input.
J. Zhu collected and analyzed the XRD data.
D. Sokaras and T. Kroll assisted with HERFD XAS data collection.
I. J. Pickering provided scientific guidance, reviewed the manuscript, and funded the research.
G. N. George provided scientific guidance, performed QM/MM studies, reviewed the manuscript, and funded the research.

8.2 Abstract

The compounds of mercury can be highly toxic, and interfere with a range of biological processes, although many aspects of the mechanism of toxicity are still obscure. Hg(II) can bind DNA directly, and is known to bridge cross-adjacent thymine nucleotides. We have used a combination of small molecule X-ray diffraction, X-ray spectroscopy and computational chemistry to study the interactions of Hg(II) with thymine. We find that the energetically preferred mode of thymine binding in DNA is to the N3, and predict only minor distortions of the DNA structure on binding one Hg(II) to two cross-adjacent thymine nucleotides. The preferred geometry is predicted to be twisted away from co-planar through the torsion angle φ of between 32 and 43°. Using 1-methylthymine as a model, the *bis*-thymine coordination of Hg(II) is shown, to give highly characteristic X-ray absorption spectroscopy (XAS) that is quite discrete from other possible biological modes of binding of Hg(II). This work lays the foundation for future studies of the modes of Hg(II) to DNA using this method.

8.3 Introduction

Worldwide, the health and environmental effects of mercury and its compounds are a source of increasing concern (Global Mercury Assessment 2013, United Nations Environment Programme, 2013). Mercury's compounds can be more toxic than any other non-radioactive heavy element (MacDonald et al., 2015a), and because anthropogenic emissions have dramatically increased in recent decades (Streets et al., 2018) there is growing interest in the mechanisms underlying the toxicity of mercury compounds. Mercury, plus a number of other toxic heavy metal ions, are known to cause adverse biological effects by binding to DNA. There are two main sites of metal ion interaction with DNA; the external phosphate backbone, and the electron-donor groups of the purine and pyrimidine bases which will result in alterations in the DNA double helix and profound affects upon structure and function (Eichhorn and Shin, 1968). Metal-induced genotoxicity of DNA is varied but is thought to generate functional changes in DNA synthesis or DNA repair processes by obstructing the binding of important DNA enzymes such as regulating transcription factors, helicases and nucleases (Hansen and Stern, 1984). Insertion of a metal ion between base-pairs could distort DNA structure so that binding of critical DNA enzymes is either blocked or inhibited (Ariza and Williams, 1999). Mercuric species (Hg(II)) are known to be active

mutagens, with preferred binding to N3 of thymine and N1 of guanosine (Simpson, 1964; Eichhorn and Clark, 1963), which can also lead to a shift in the DNA sequence if metal binding involves cross-adjacent nucleotides. Wagida and Gabal (1991) have examined metaphase chromosomes for individuals exposed to mercury fulminate and compared them with those of unexposed persons, reporting aberrations in the mercury group in the form of gaps, breaks and fragments (Wagida and Gabal, 1991). The high selectivity of Hg(II) for thymine nucleotides has been exploited in the development of DNA-based Hg(II) colorimetric nanosensors (Chun et al., 2018; Liu et al., 2015; Liu et al., 2009) with possible applications for mercury determination in foodstuffs and environmental samples (Liu et al., 2009), although Hg(II) *bis*-thymine coordination is reversible upon addition of Cl^- or CN^- suggesting a less than optimal coordination (Nandi et al., 1965). Kosturko et al. (1974) have reported the crystal structure of Hg(II)-*bis*-1-methylthymine with an R-factor of 7.70 %, showing that in this low-molecular weight complex the Hg is bound to N3 of the thymine ring with the C2 and C4 carbonyls participating with the two nucleobase rings co-planar to form an essentially planar system with 6 atoms associated with Hg(II) (Kosturko et al., 1974). Herein we use a combination of computational chemistry, crystallography and spectroscopy to study the binding of thymine to Hg(II).

8.4 Materials and Methods

8.4.1 Sample Preparation

Mercuric oxide, mercuric chloride, and boron nitride were purchased from Alfa Aesar. L-cysteine and 1-methylthymine were purchased from Sigma Aldrich. Solution and crystal mercury-*bis*(1-methylthymine) were prepared following the protocol from Kosturko et al. (1974). A solution sample of mercury-*bis*(1-methylthymine) was collected from the reaction mixture after 1 hr of stirring. The flask was wrapped in foil, cooled to room temperature and stored until crystals had formed. White needle crystals were collected using vacuum filtration and washed with methanol and water and vacuumed to dryness. Portions were taken for purification using recrystallization but were immiscible in a number of common laboratory solvents. Two-coordinate and four-coordinate Hg(II) bound to thiolates were prepared using the protocol from Jalilehvand et al. (2006) with the thiolates L-cysteine and 2,3-dimercapto-1-propanesulfonic acid. Solid XAS samples were prepared by diluting mercuric compounds with boron nitride (5-10% weight Hg compound) and grinding to a fine powder. The powder was transferred to metal plates windowed

with metal-free Mylar adhesive tape. Solution samples were injected into polyacetal cuvettes covered with metal-free Mylar tape and frozen in a slurry of LN2-isopentane.

8.4.2 Computational Chemistry Calculations

Density Functional Theory (DFT) geometry optimizations were carried out using DMol^3 and Biovia Materials Studio Version 2017 R2 (Delley, 1990; Delley, 2000) using the meta-GGA approximation employing the M11-L functional both for the potential during the self-consistent field procedure, and for the energy (Peverati and Truhlar, 2012). DMol^3 double numerical basis sets included polarization functions for all atoms with all-electron relativistic core treatments. Environmental effects were modeled using the Conductor-like Screening Model (COSMO) (Klamt and Schüürmann, 1993) in DMol^3, with a dielectric value representing water with 25% glycerol (ε = 69.53). Quantum-mechanical/molecular-mechanical (QM/MM) calculations were performed on a segment of DNA d(GCGAATTCG)$_2$ with initial coordinates taken from a high-resolution (0.89 Å) crystal structure (Soler-Lopez et al., 2000), which was selected because of the centrally placed AT pairs. The QMERA method as implemented in Biovia Materials Studio was used, employing DMol^3 for the QM part as described above and GULP for the MM part (Gale, 2005), using the UFF force field (Rappe et al., 1992). The structure was partitioned with the QM region comprising of the thymine–Hg(II)–thymine complex, and the MM region comprising the rest of the molecule.

8.4.3 Single Crystal X-ray Diffraction (XRD)

Crystal data were collected on a Bruker APEX II Kappa CCD FR540C diffractometer, using graphite monochromated Mo Kα radiation. After coated with Paratone oil, a single crystal of Hg-*bis*(1-methylthymine) (CCDC 1898763) was mounted onto the Goniometer using a Micromount^{TM} (*MiTeGen*). The crystal was under a cold stream of N_2, at a temperature of 173K (controlled by the Oxford Cryojet attached to the diffractometer). Frames integration, data reduction, and absorption correction were then performed with the Bruker SAINT software package (SAINT and SADABS, 2013, Bruker AXS Inc. Madison, WI, USA). Finally, the structure was solved with the Intrinsic Phasing method implemented with SHELXT and refined using the Bruker SHELXTL software package (Sheldrick, 2014; Sheldrick, 2015). Non-hydrogen atoms were refined with independent anisotropic displacement parameters. Hydrogen atoms were placed

at geometrically idealized positions with respect to the attached non-hydrogen atoms and their displacement parameters were fixed to be 20-50% larger than those of the attached non-hydrogen atoms (the Riding Model). Crystallographic data are summarized in Tables B.1-B.4 in Appendices.

8.4.4 X-ray Absorption Spectroscopy (XAS) Data Collection and Analysis

X-ray spectroscopy was carried out at the Stanford Synchrotron Radiation Lightsource (SSRL) with the SPEAR3 storage ring operating at 3.0 GeV and a ring current of 500 mA. Standard XAS spectroscopy was conducted on the structural molecular biology beamline 7-3 using a Si(220) double crystal monochromator, while High Energy Resolution Fluorescence Detected (HERFD) XAS used SSRL beamline 6-2 using a Si(311) double crystal monochromator for the incident beam. For both beamlines incident X-ray energy calibration was done with reference to the transmission of an Hg-Sn amalgam foil, assuming a lowest-energy Hg L_{III} inflection point of 12,285 eV. For both experiments the incident energy was monitored with gas ionization chambers and samples were placed in a liquid helium flow cryostat (Oxford instruments, Abingdon, UK) and held at an angle of 45° to the incident X-ray beam, and maintained at a temperature of 10 K to minimize thermal contributions and protect against X-ray induced photochemistry. XAS data were collected using the XAS Collect data acquisition software (George, M.J., 2000), and HERFD XAS using SPEC (Certified Scientific Software, Cambridge MA, USA). XAS of solutions were collected by measuring the $L\alpha_{1,2}$ fluorescence excitation spectrum using a 30-element germanium array detector (Canberra Ltd. Meriden, CT, USA) (Cramer et al., 1988). In order to maintain detector count-rates in the pseudo-linear regime, Ga_2O_3 X-ray filters were employed to preferentially absorb scattered radiation, together with silver Soller slits (EXAFS Co., Pioche Nevada) to reject filter fluorescence. HERFD XAS spectra were collected by using a 6-element array of spherically bent crystal Si(555) analyzer crystals (Sokaras et al., 2013) to record the Hg L_{III}-$L\alpha_1$ emission. For transmission XAS a set of Soller slits was used to minimize calibration foil fluorescence return to the upstream ion chamber, as previously described (Tse et al., 2011). Near-edge spectra and extended X-ray absorption fine structure (EXAFS) oscillations $\chi(k)$ were analyzed using the EXAFSPAK program suite (George, G.N., 2000). For analysis of the EXAFS the threshold energy (E_0) and the zero-point for the photo electron wave vector k was assumed to be 12,305 eV, and the program FEFF v8.25 was used to calculate *ab initio* theoretical phase and

amplitude functions (Rehr and Albers, 2000). Fourier transforms were computed using phase correction for Hg–N backscattering.

8.5 Results and Discussion

8.5.1 Small Molecule Density Functional Theory (DFT) calculations

Thymine bases in DNA can potentially bind mercury via either oxygen or nitrogen functional groups of the base. Using 1-methylthymine (1,5-dimethylpyrimidine-2,4-dione) as a model for DNA thymine, we computed the energetics of different modes of Hg(II) binding. We first considered the conformational isomerism of binding via N3, N3′ (Figure 8.1). DNA enforces the synperiplanar conformation, shown in Figure 8.1a, which we compute is 1.2 $kJ \cdot mol^{-1}$ lower in energy than the antiperiplanar conformer, Figure 8.1b. Figure 8.2 shows the energetic effects of rotation about the approximately linear N3–Hg–N3′ bonds, exhibiting a well-defined minimum for the synclinal conformer with $\varphi = 90°$ which is some 11.3 $kJ \cdot mol^{-1}$ lower in energy than the synperiplanar conformer with $\varphi = 0°$; like the antiperiplanar conformer this conformation cannot be present in DNA because a co-planar structure will be enforced by the tertiary structure.

Hg(II) has a high affinity for both nitrogen and oxygen donor ligands found on nucleotide bases (Boerner and Zaleski, 2005), and we therefore used DFT to examine possible binding to the exocyclic oxygens O2 and O4 (Figure 8.1). The results of these calculations, involving binding of mercury in various combinations of N3, O2 and O4, are summarized in Table 8.1. When geometry optimizations were carried out in the absence of any constraints or restraints irrespective of the starting structures, the minimization algorithm invariably shifted the coordination from the oxygen donors to the N3–Hg–N3′ binding that we have discussed above. This behavior clearly indicates that the N3–Hg–N3′ binding is preferred, but it makes calculation of specific energy differences more challenging. We imposed harmonic-type energetic bond-angle restraints of 420 $kJ \cdot mol^{-1} \cdot rad^{-2}$ in order to calculate the geometry optimized energies appropriate for alternate modes of metal bonding. Values for the bond-angles to be used in these calculations were estimated by computing geometry optimized structures using 2-hydroxy-1,5-dimethyl-pyridin-4-one in place of 1-methylthymine. In this compound the N3 nitrogen is replaced by a carbon, and is thus unavailable for bonding Hg(II). Using the reasonable values for bond-angles obtained in this way, in combination with restraints, the dissociation of Hg from oxygen during the geometry optimization was discouraged, and we obtained the values given in Table 8.1.

Table 8.1. Density functional theory (DFT) results of Hg-*bis*(1-methylthymine) bound through different atoms of 1-methylthymine. See text for details.

Figure 1	Species/conformer	E-E_{min} (kJ·mol^{-1})
a	N3, N3′, synperiplanar	11.3
b	N3, N3′, antiperiplanar	12.2
a	N3, N3′, synclinal	0.0
c	N3, O2′, planar	83.6
c	N3, O2′, perpendicular	72.8
d	O2, O2′, bound	152.3

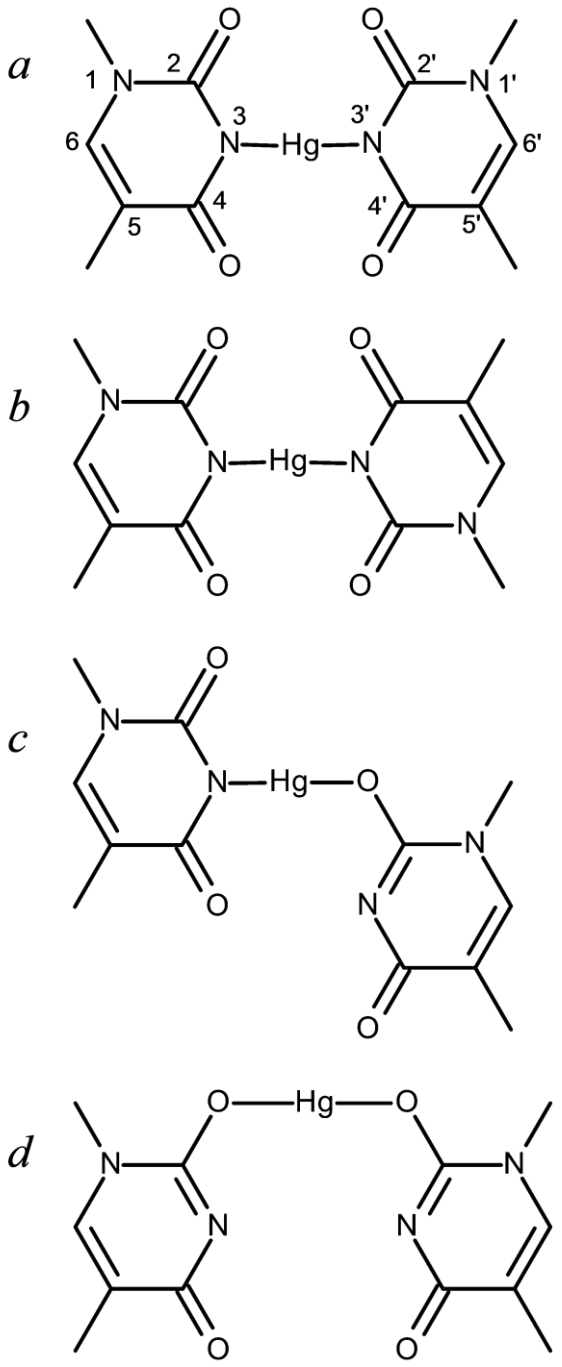

Figure 8.1. Schematic structures showing different modes of Hg(II) binding to two thymine nucleotides. The relative energies obtained with geometry optimization for the different structures are listed in Table 8.1.

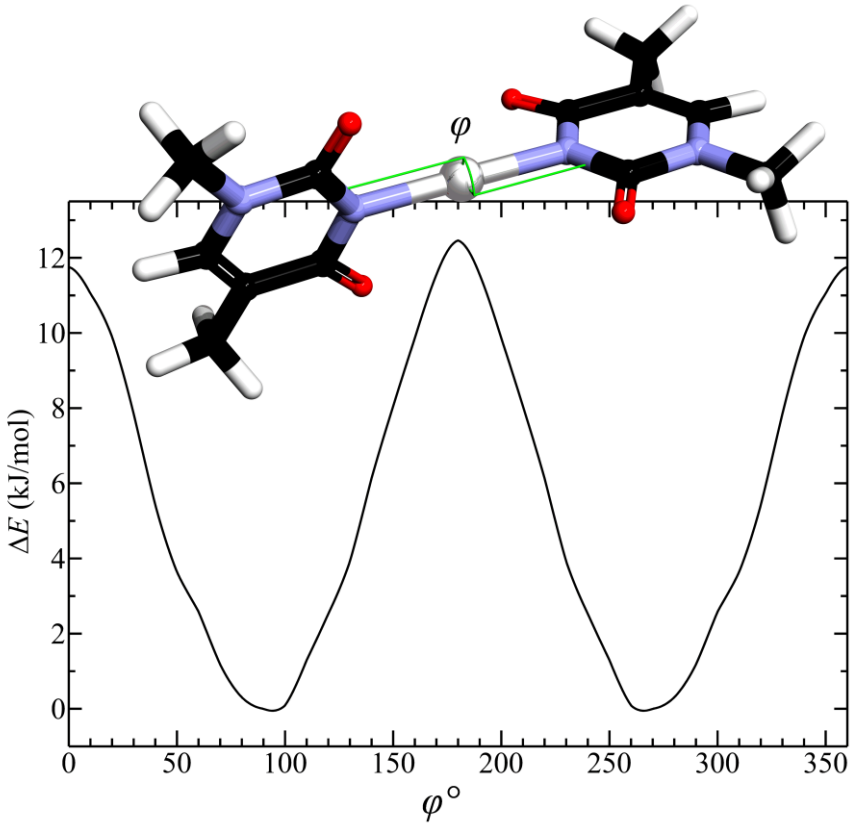

Figure 8.2. Results of DFT calculations on the effect of variation of the torsion angle φ where zero is coplanar. Energies are those obtained upon geometry optimization with φ constrained to the abscissae, calculated every 5 or 10°, depending upon rate of change of energy with φ. Energies are given relative to the minimum value, which was obtained with φ=90.

For example, for the N3 and O2′ bound species, placing restraints upon the C2′–O2′–Hg bond-angle of 117.14°, but now with geometry optimization of two coordinated 1-methylthymine donors bound through N3 and O2′, gave an energetic penalty of +83.6 kJ·mol^{-1} for this mode of binding (Table 8.1). As expected, nearly identical energies were found when constraints were used in place of restraints. In all cases conformational isomers with the ring planes orthogonal to one another were found to be approximately 11 kJ·mol^{-1} lower in energy than corresponding conformations with co-planar rings. Without any constraints or restraints, the most energetically favorable conformation was with two 1-methylthymines in orthogonal orientation bound via the ring nitrogens exhibiting a bond angle of 179.8° for N3–Hg(II)–N3′ and bond-lengths of 2.01 Å for both Hg–N bonds. Comparison of the 1-methylthymine ring in the mercury complex with that of free 1-methylthymine, similarly geometry optimized (not illustrated), gave atomic positions that were nearly superimposable, with ring atoms having a root-mean square displacement of only 0.008 Å. The co-planar conformation gave slightly longer Hg–N bond-lengths of 2.02 Å. With N3–Hg(II)–O2′ (Figure 8.1c), geometry optimization gave energies that were 83.6 kJ·mol^{-1} higher, and binding through the two oxygen atoms O2–Hg(II)–O2′ (Figure 8.1d) was least preferred energetically by some 152.3 kJ·mol^{-1}. These results clearly indicate that the energetically preferred coordination of 1-methylthymine to Hg(II) is *bis*-N3 coordination (Figure 8.1a) which is nearly coplanar with approximately C_{2v} point group symmetry.

Other workers have used computational chemistry to evaluate the binding of Hg(II) to thymine bases, but at lower levels of theory. Marino (2014) compared different levels of theory, including the M06-L functional, for hypothetical mismatched base-pairs such as (T–Hg–T)$_2$ and (T–Hg–T)$_3$, but examined only physiologically relevant synperiplanar conformations (Marino, 2014); we will revisit their findings in our discussion of Hg(II) DNA structure, below. Uchiyama et al. (2001) compared synperiplanar and antiperiplanar conformations using the B3LYP/6-31+G(d,p) level of theory, employing relativistic pseudopotential core potentials for mercury (Uchiyama et al., 2001). They calculated that the Hg–N3 bond-lengths should be substantially shorter for the antiperiplanar conformation, by some 0.1 Å. Our calculations confirm this trend, but we estimate a substantially smaller difference of 0.004 Å. The synclinal conformer with φ = 90° shows the still shorter Hg–N3 bond-length, by an additional 0.003 Å, of 2.011 Å. The absolute accuracy of bond-length determination by DFT is generally taken to be ~0.05 Å, but the relative

trends are typically much more accurate than this. We therefore compared experimentally the solid-state and solution structures of Hg-*bis*(1-methylthymine).

8.5.2 Solid State and Solution Structures of Mercury Bound to 1-methylthymine

Kosturko and co-workers have previously reported the crystal structure of *bis*(1-methylthymine)mercury(II) with an *R*-factor of 7.7% (Kosturko et al., 1974). We re-evaluated this structure using a lower temperature, which yielded an improved *R*-factor of 1.24%, but otherwise our results are in full agreement with the earlier work. Tables B.1-B.4 (see Appendices) give the refined crystal structure data; the crystal system is monoclinic with space group $P2_1/c$ (No. 14) and unit cell dimensions a=4.3903(2) Å, b=11.7232(4) Å, and c=13.2976(5) Å. Mercury is bound to two nitrogen atoms as expected, with a bond-length of 2.0235(18) Å and N3–Hg(II)–N3′ bond angle of 180.0°, with the planes of 1-methylthymine essentially antiperiplanar with φ=180.0° (Figure 8.3). Our computational studies are in excellent agreement with the crystal structure data, with an Hg–N3 bond-length of 2.0150 Å for the antiperiplanar conformation; an agreement of better than 0.01 Å, emphasizing the outstanding capabilities of the M11-L functional within the meta-GGA approximation, which we have previously observed (Nienaber et al., 2018). Also, in agreement with our computational studies (section 8.5.1), the refinement of the 1-methylthymine group in our structure closely matches the crystal structure of pure 1-methylthymine (Hoogsteen, 1963), showing differences of less than 1° for all bond-angles, suggesting only minimal distortions upon Hg complexation. The crystal packing shows a herringbone pattern (Figure 8.4), with two long Hg•••O at 3.010 Å from adjacent molecules approximately stacked along the crystallographic *a* axis, consistent with previous studies (Kosturko et al., 1974).

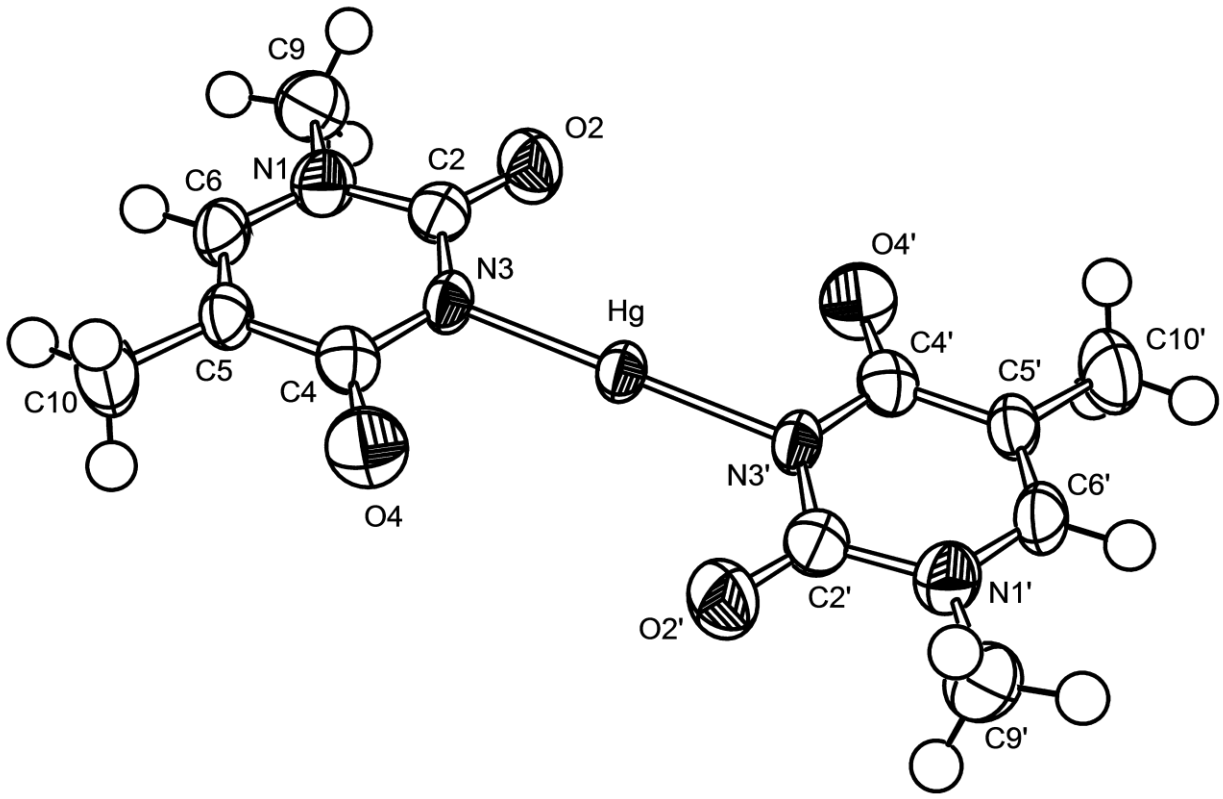

Figure 8.3. X-ray crystal structure of Hg-*bis*(1-methylthymine); non-hydrogen atoms are drawn using 95% probability thermal ellipsoids.

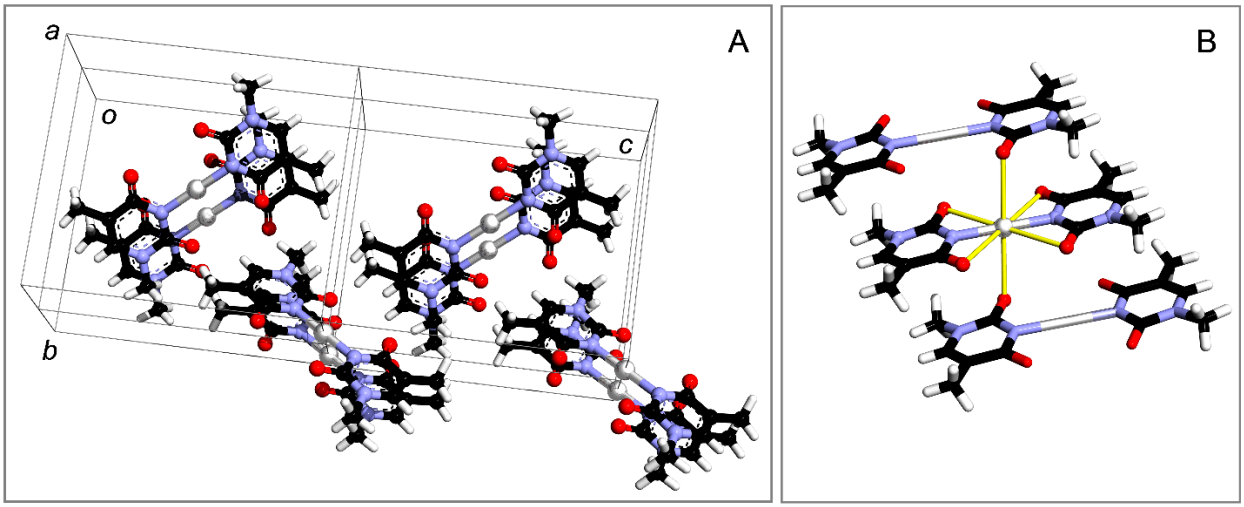

Figure 8.4. Crystal packing in the X-ray crystal structure of mercury(II)-*bis*(1-methylthymine). Panel A shows a 2×1×2 super-cell showing the herringbone molecular packing that is discussed in the text, and panel B shows the 3.0 Å shell of oxygen coordination, four from the two 1-methylthymine ligands, and two from the adjacent molecules packed above and below in the crystal, to give a skewed octahedral arrangement of six oxygens around each mercury highlighted in yellow (the skew away from octahedral is approximately 8.2°).

Figure 8.5 shows the extended X-ray absorption fine structure (EXAFS) of crystalline and aqueous solution Hg-*bis*(1-methylthymine), showing the EXAFS and the results of curve-fitting analysis, which are summarized in Table 8.2. For the solid the EXAFS is dominated by a combination of first shell and second shell interactions involving EXAFS from two Hg—N at 2.023 Å, together with four carbon atoms and six oxygen atoms at 2.925 Å and 3.016 Å, respectively. The two latter, held in a rigid arrangement due to the ring system, interactions produce intense second shell EXAFS that is seen as an unusually intense Fourier transform peak at ~3 Å (Figure 8.5). These values are in excellent agreement with those determined from crystallography of 2.920 Å and 3.014 Å, for Hg•••C and Hg•••O, respectively, plus two additional Hg•••O at 3.009 Å from the stacked methylthymine from molecules above and below in the crystal structure (Figure 8.4). The XAS of Hg-*bis*(1-methylthymine) in aqueous solution is very similar to that of the solid, noting that the k-range of the data set is somewhat reduced because of signal to noise limitations at higher k. The solutions are expected to predominantly adopt the lower energy synclinal conformer with φ~90°, and analysis of the EXAFS gives an Hg—N bond-length of 2.029 Å, slightly longer than the solid, and not subtly shorter as predicted by our DFT calculations. Possibly this small change is a reflection of greater accessibility to the solvent and consequent association with the metal in solution, but nevertheless these changes are still small and we conclude that the previously suggested changes in Hg—N bond-lengths with conformation (Uchiyama et al., 2001) are not expected, based both upon our DFT calculations and upon our XAS experiments.

The near-edge portion of the XAS spectra of Hg-*bis*(1-methylthymine) are shown in Figure 8.6, again of solid and solution, which give remarkably similar spectra. The spectra of Hg-*bis*(1-methylthymine) are compared with spectra of Hg(II) in coordination environments that are likely to occur *in vivo*; an aqueous solutions of a two-coordinate Hg(II) bound to L-cysteinyl sulfur [*bis*-(L-cysteinato)-mercury(II)] (Taylor and Carty, 1977), and Hg(II) bound to four thiolate donors (Jalilehvand et al., 2006; George et al., 2004). The improved resolution of the HERFD XAS spectra is clear from the figure. The spectra of the *bis*(1-methylthymine) complex shows an intense transition at 12287.4 eV, and a broader high-energy feature at 12327.7 eV, which is present in both solid and solution data sets. The former can be assigned to a dipole-allowed bound-state transition from the $2p^3/_2$ level to a non-bonding molecular orbital with substantial 5d and 6s character, which is most intense for linear two-coordinate coordination of Hg(II), and which is unusually intense in

the spectrum of *bis*(1-methylthymine) complexes; its weak presence in the spectrum of the *bis*-(L-cysteinato) complex is more characteristic of the intensity observed in most two-coordinate species. The second broad feature is also intense in solution spectra (Figure 8.6), suggesting that this feature is insensitive to the torsion angle φ. The unusual spectra of Hg-*bis*(1-methylthymine) can be considered as a fingerprint of this type of coordination, and the present work lays the foundation for future experimental studies of Hg(II) binding to DNA.

Table 8.2. Extended X-ray absorption fine structure (EXAFS) curve-fitting parameters*.

	N	***R* (Å)**	**σ^2 (Å^2)**	**ΔE_0 (eV)**	***F*[a]**
Solid					
Hg — N	2	2.023 (2)	0.0019 (2)	-5.2 (4)	0.371
Hg ••• C	4	2.925 (5)[b]	0.0032 (5)		
Hg ••• O	6[c]	3.016 (6)	0.0052 (7)		
Solution					
Hg — N	2	2.029 (3)	0.0023 (2)	-5.1 (6)	0.322
Hg ••• C	4	2.917 (9)[b]	0.0037 (8)		
Hg ••• O	6[d]	3.020 (1)	0.0081 (8)		

*Parameters used for cure-fitting include: N coordination number; R(Å) interatomic distances; σ^2 (Å^2) Debye-Waller factor; ΔE (eV) threshold energy shift to nominal threshold value of 12,305 eV (E_0). Values in parenthesis are estimated standard deviations of the last digit of the fitted parameters. Amplitude reduction factor (S_0^2) set to 1.0. [a]The goodness of fit function F is defined by $[\Sigma k^6(\chi(k)_{calc} - \chi(k)_{expt})^2/\Sigma k^6\chi(k)^2_{expt}]^{1/2}$, with $\chi(k)_{calc}$ and $\chi(k)_{expt}$ as the calculated and experimental EXAFS with k representing the photoelectron wavevector. [b]The value for the Hg•••C bond-length is linked to 12 different outer shell paths, including multiple scattering paths which were modelled using the crystal structure. We note that apart from this consideration the Hg•••C would not be resolvable from the Hg•••O interaction with the k-range available. [c]The total coordination of Hg•••O includes two from each of the two thymine 1-methylthymine ligands, plus two from adjacent molecules in the unit cell. These are all at approximately the same distance, and are treated as a single (unresolved) interaction in our analysis. [d]The total Hg•••O coordination assumes some contribution from two solvent molecules, in addition to the oxygens provided from each of the two 1-methylthymine ligands; these are treated as a single (unresolved) interaction in our analysis.

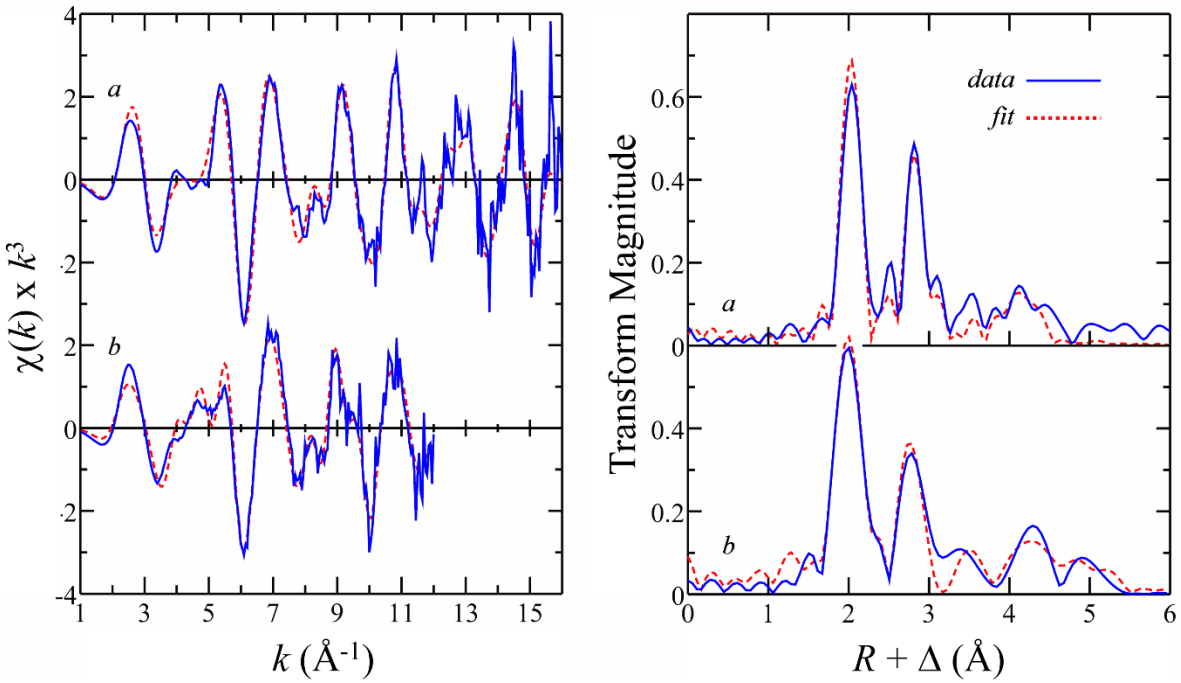

Figure 8.5. Extended X-ray absorption fine structure oscillations, plus best fit, with corresponding EXAFS Fourier transforms for Hg-*bis*(1-methylthymine) for solid crystalline (*a*) and aqueous solution (*b*). The parameters for the best fit are given in Table 8.2.

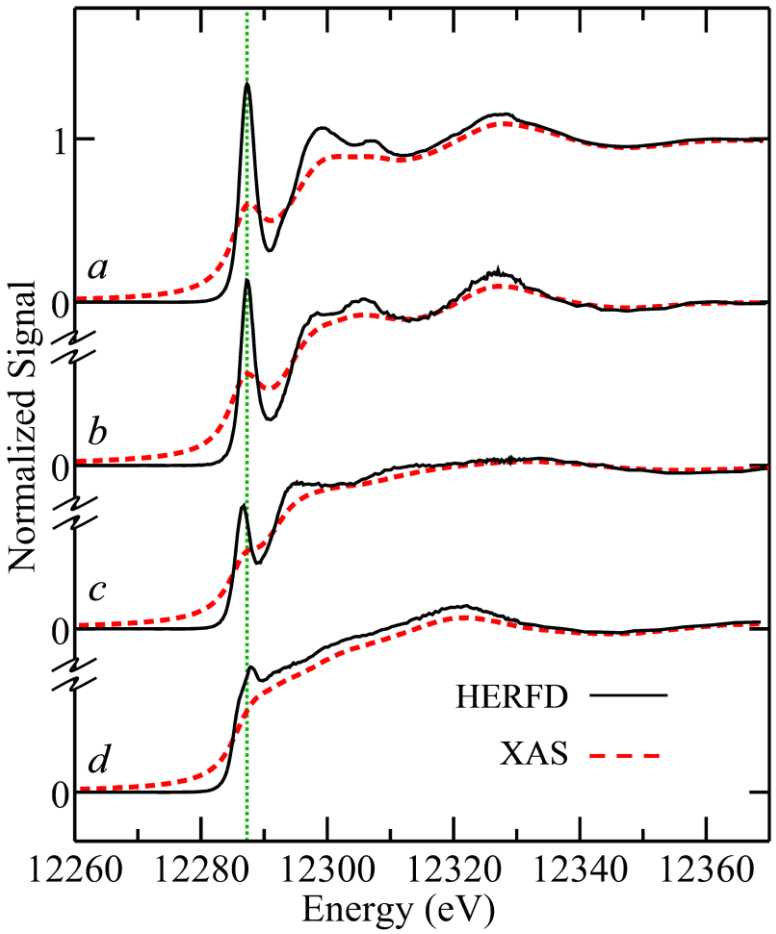

Figure 8.6. X-ray absorption spectra of Hg-*bis*(1-methylthymine). Spectrum of solid Hg-*bis*(1-methylthymine) as solid (*a*) and solution (*b*) samples, displaying the HERFD spectrum as a *solid black line* with conventional XAS as a *red broken line*. *c* and *d* show the spectra of complexes relevant to other biologically relevant Hg(II) binding modes; *c* shows the spectra for [*bis*-(L-cysteinato)-mercury(II)] containing an approximately digonal S–Hg–S arrangement, and *d* the spectra [*tetrakis*-(dimercaptopropanesulfonic acid)-mercury(II)]$^{2-}$, containing an approximately tetrahedral sulfur–bound mercury. The vertical *green broken line* is drawn to guide the eye to small shifts in the spectral peaks.

8.5.3 Mercury Binding to DNA

In an attempt at modelling the binding of mercuric ions to DNA, DFT geometry optimizations were carried out on a 4-base pair $d(AATT)_2$ segment of DNA. The total number of atoms in $d(AATT)_2$ is 244, which is close to a practical upper limit for DFT geometry optimization calculations. DFT is known for its poor treatment of long-range noncovalent interactions, such as the π–π stacking of base pairs in DNA, but the M11-L functional that we have employed is designed to overcome these difficulties. Initially, geometry optimizations were carried out upon the mercury-free $d(AATT)_2$ DNA fragment, and bound Hg(II) then introduced in various starting positions. The DFT-derived structure is compared with a crystal structure containing a core $d(AATT)_2$ segment in Figure 8.7a. The match can be seen to be excellent; with the base pairs of the DFT-derived structure showing a good match with the crystallographic results, but with some displacement of the deoxyribose phosphate DNA backbone. The mercury-bound DFT geometry optimized segment of DNA is shown in Figure 8.7b, compared with the DFT-derived structure of the short segment of mercury-free DNA. A variety of starting positions for mercury were tested, and in agreement with our small-molecule calculations, we found that Hg(II) bound to oxygen rapidly migrated so as to be coordinated by N3 of the thymine. The two Hg—N bond-lengths were computed to be 2.042 and 2.043 Å, slightly longer than our small molecule results, with a N3–Hg(II)–N3′ bond-angle of 176° and a torsion angle φ of 32.1°. The changes in the overall structure were quite small, with no atoms being displaced by more than 1 Å.

We then sought to evaluate the effects of mercury binding through calculations on a longer segment of DNA. Because DFT geometry optimizations on a substantially larger segment of DNA would become impractical in terms of computational burden, we carried out hybrid quantum-mechanical/molecular-mechanical (QM/MM) simulations in which the thymine bases and mercury ions are treated with DFT and the remainder of the structure is modelled with molecular mechanics (MM). Initial MM calculations were carried out on a segment of DNA alone, $d(GCGAATTCG)_2$ which has a double-helical $d(CGAATTCG)_2$ core with one unbound guanine base at the two 5′ ends of the double helix (Soler-Lopez et al., 2000).

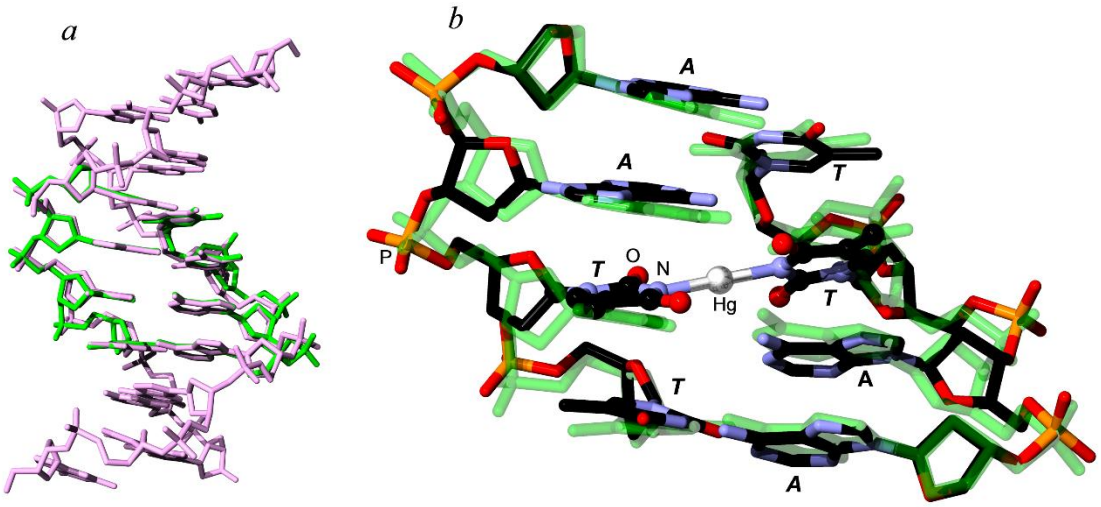

Figure 8.7. of DFT geometry optimization of a short segment of DNA $d(AATT)_2$ in the absence and presence of Hg(II). *a* shows a superimposition of the crystal structure (*pink*) of $d(GCGAATTCG)_2$ (Soler-Lopez et al., 2000) containing the same central sequence as the DFT derived structure (green). *b* shows the DFT-predicted effects of Hg(II) binding, with the structure of Hg-free $d(AATT)_2$ shown in *green*.

Figure 8.8a compares the reported crystal structure (Soler-Lopez et al., 2000) with the results of MM geometry optimization. As expected, the MM structure reproduces that observed by crystallography well, although as with DFT the DNA backbone is slightly displaced. The effects of introducing a single approximately central mercuric ion are shown in Figure 8.8b, and as expected the mercury binds N3 of the two opposing thymine bases. The two Hg—N bond-lengths in the QM/MM structure are 2.018 and 2.013 Å, which are closer to our small molecule results than those from the large DFT calculation, with a N3–Hg–N3′ bond-angle of 175° and a somewhat larger torsion angle φ of 42.8°. Overall, the results are in agreement. The bonding mode of Hg(II) is predicted to be through thymine N3, with approximately linear N–Hg–N geometry, and a torsion angle φ between 32 and 43°. The Hg(II) bound thymine bases are translated by ~0.9 Å and tilt towards the minor groove of the DNA helix to accommodate for the incorporation of Hg(II), altering the distance between N3•••N3′ of two cross-adjacent thymine bases from 4.86 to 4.03 Å. The root-mean-square (RMS) deviation of the two DNA oligonucleotides was calculated to be 0.53 Å, suggesting that binding of Hg(II) causes only minor deviations in the overall double helical structure. Experimental studies of solution and crystalline DNA duplexes containing two consecutive T–Hg–T base pairs have been previously reported showing a slightly larger RMS deviation upon Hg binding of 0.7 Å (Kondo et al., 2014; Yamaguchi et al., 2014). The higher mercury loading may explain the slightly increased RMS deviation, as a double load of mercury in adjacent sites and an Hg•••Hg separation of ~3.3 Å should provide additional stability to the metal bound conformation (Kondo et al., 2014). With higher metal loadings, some of the other mixed oxygen-nitrogen binding modes have been observed, which our calculations suggest we have concluded are not energetically preferred in isolated small molecule calculations (Liu et al., 2017). Thus Liu et al. (2007), have observed mercury bound through N3–Hg(II)–O2′ and N3–Hg(II)–O4′ in DNA duplexes that incorporate two Hg(II) ions, which may arise because of the presence of a supportive second bound mercury stabilizing what are otherwise energetically unexpected modes of binding. DNA duplex structure stabilization was observed by Kondo et al. (2014) with incorporation of a second Hg(II).

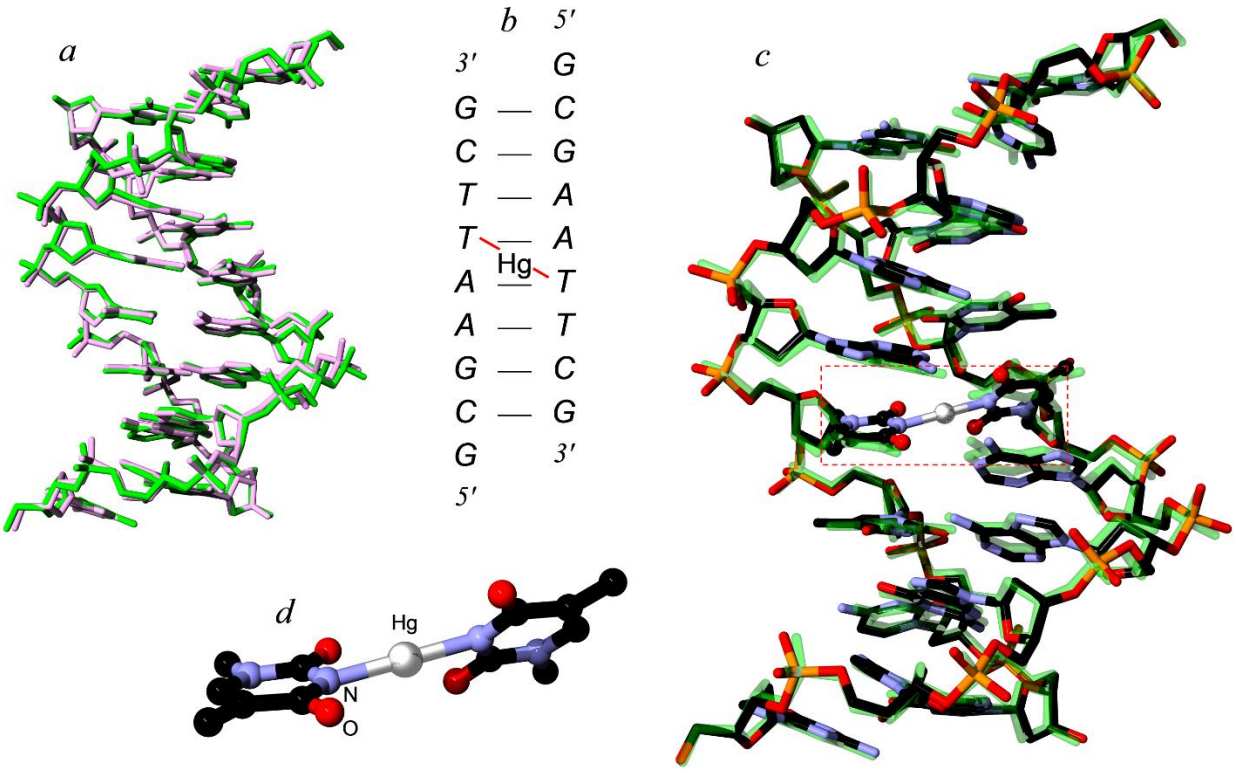

Figure 8.8. Results of QM/MM geometry optimization of d(GCGAATTCG)$_2$ (Soler-Lopez et al., 2000) in the absence and presence of Hg(II). *a* shows a superimposition of the crystal structure (*pink*) of d(GCGAATTCG)$_2$ and the MM-derived structure (*green*). *b* shows a schematic of the sequence with the centrally located Hg(II) binding site, and *c* shows a comparison of the QM/MM Hg(II) bound structure and the MM Hg(II)-free structure (*green*). *d* shows the QM atoms from the calculation in *c*.

In conclusion, our results predict that the preferred mode of thymine binding in DNA will be to the N3 atom of the base. Only minor distortions of the DNA structure on binding one Hg(II) to two cross-adjacent thymine nucleotides are predicted, with the preferred geometry predicted to be twisted from co-planar through the torsion angle φ of between 32-43°. Our results give general information on the binding of Hg(II) to cross-adjacent thymine nucleotides, but do not inform on specific genotoxic activity of Hg(II), as this will depend on specific sites of binding, and upon the ultimate function encoded by that site. The *bis*-thymine coordination of Hg(II) is shown, using 1-methylthymine as a model, to give highly characteristic XAS that is quite discrete from other possible biological modes of binding of Hg(II), laying the foundation for future studies using this spectroscopic method, and its derivatives (Pushie et al., 2014) of the modes of Hg(II) binding to DNA.

8.6 Acknowledgments

This work was supported through Discovery grants from the Natural Sciences and Engineering Research Council of Canada (NSERC, I.J.P. and G.N.G.), a grant from Innovation and Science Fund of Saskatchewan (I.J.P.), a Canada Foundation for Innovation John Evans Leader's Fund Award (I.J.P.) and by Canada Research Chairs (I.J.P. and G.N.G.). S.N. acknowledges the Dr. Rui Feng Scholarship and was a Fellow in the Canadian Institutes of Health Research-Training in Health Research Using Synchrotron Techniques (THRUST). Use of the Stanford Synchrotron Radiation Lightsource, SLAC National Accelerator Laboratory, is supported by the U.S. Department of Energy, Office of Science, Office of Basic Energy Sciences under Contract No. DE-AC02-76SF00515. The SSRL Structural Molecular Biology Program is supported by the DOE Office of Biological and Environmental Research, and by the National Institutes of Health, National Institute of General Medical Sciences (including P41GM103393). The contents of this publication are solely the responsibility of the authors and do not necessarily represent the official views of NIGMS or NIH.

CHAPTER 9. Rethinking the Minamata Tragedy: What Mercury Species Was Really Responsible?

9.1 Preface

Publications of HERFD XAS applications in biological tissues is limited, but as was described in Chapters 6 and 7, there is great potential in the areas of biological and environmental sciences. Herein, the methods of HERFD XAS are applied to study the mercury species in a sample of cat cerebellum tissue. This cat had been the subject of an experiment over 60 years ago where it was exposed to the effluent from an acetaldehyde chemical plant infamously recognized for dumping chemical wastes into Minamata Bay that later was known to be the source of severe mercury poisoning to the local population. Results of linear combination fitting of HERFD XAS using a library of mercury standards and EXAFS, together with DFT results strongly suggest an alternate mechanism for the extreme mercury poisoning exhibited in the surrounding community of Minamata Bay.

Author Contributions

This chapter will be reformatted as a journal article and submitted to *Nature*.

James, A.K.,[¶] Nehzati, S.,[¶] Dolgova, N.V., Sokaras, D., Kroll, T., Eto, K., Marumoto, M., Sakamoto, M., O'Donoghue, J.L., Watson, G.E., Myers, G.J., Krone, P.H., Pickering, I.J., and George, G.N. [¶]These authors contributed equally to this work. (2019) Rethinking the Minamata Tragedy: What Mercury Species Was Really Responsible? (*In preparation*)

A. K. James planned the experiments, performed XAS experiments and drafted the manuscript.
S. Nehzati synthesized and prepared the small molecule samples, performed XAS and HERFD XAS experiments, and contributed to the final writing of the manuscript.
N. V. Dolgova performed XAS and HERFD XAS experiments.
D. Sokaras and T. Kroll performed the HERFD XAS experiments.
K. Eto, M. Marumoto, M. Sakamoto, J. L. O'Donoghue, G. E. Watson, G. J. Myers planned the experiments and provided and prepared tissue samples.
P. H. Krone consulted with expertise in Anatomy and Cell Biology.

I. J. Pickering planned the experiments, performed the HERFD XAS experiments, and drafted the manuscript.
G. N. George planned the experiments, performed the XAS and HERFD XAS experiments, performed the DFT calculations, and drafted the manuscript.

9.2 Abstract

Industrial release of mercury into the local Minamata environment with consequent poisoning of local communities through contaminated fish and shellfish consumption is considered the classic case of environmental mercury poisoning. However, the mercury species in the factory effluent has proved controversial, originally suggested as inorganic, and more recently as methylmercury species. We used newly-available methods to re-examine the cerebellum of historic cat 717, which was fed factory effluent mixed with food to confirm the source. Synchrotron high energy resolution fluorescence detection X-ray absorption spectroscopy (HERFD XAS) revealed sulfur-bound organometallic mercury with a minor β-HgS phase. Density functional theory (DFT) indicated energetic preference for α-mercuri-acetaldehyde as a waste product of aldehyde production. The consequences of this alternative species in the "classic" mercury poisoning should be re-evaluated.

9.3 Introduction

The potentially deadly effects of organomercury compounds have been defined by tragic mass-poisonings of human populations. The most infamous is the Minamata tragedy (Kurland et al., 1960; Takeuchi et al., 1962; Eto et al., 2010), for which organomercury poisoning is named Minamata disease (Eto et al., 2010). Release of mercury-contaminated industrial waste from a chemical plant resulted in local marine pollution, leading to contamination of fish and other seafood that was ingested by local fishing villagers. Those poisoned experienced varying signs and symptoms now assumed to be typically associated with methylmercury poisoning (paresthesia, dysarthria, visual and auditory disturbances, ataxia, seizures, and ultimately death (Hunter and Russell, 1954; Kurland et al., 1960). Over 50 congenital cases were also diagnosed (Eto et al., 2001a), resulting in the first recognition that prenatal methylmercury (MeHg) exposure might harm

the fetus at levels not particularly harmful to mothers. Integral to diagnosing the etiology of Minamata disease was the identification of diseased-related signs in local feline populations, which locals called the "dancing cat syndrome" (Eto et al., 2001b). In 1959, three years after the official discovery of Minamata disease, its cause was still unknown. To test whether industrial waste from the nearby Chisso acetaldehyde manufacturing plant might be responsible, a company physician fed ten cats food on a daily basis that had been combined with effluent taken directly from the chemical plant (Eto et al., 2001b). At 4-11 weeks into the experiment eight of the cats exhibited signs similar to the human symptoms. Two cats were autopsied and biological materials preserved. One was cat 717 (Eto et al., 2001b) which is analyzed and discussed herein.

The Minamata poisoning (Minamata disease) is frequently taught in undergraduate toxicology as the prototypical example of biomethylation of inorganic mercury with magnification through trophic levels, leading to human methylmercury exposure (Fox and Boyes, 2013). Recently Eto et al. (2010) have challenged this scenario, suggesting that the Minamata poisonings were due to direct release of methylmercury, rather than inorganic mercury, from the Chisso factory into Minamata bay (Eto et al., 2010). They studied brain tissue of cat 717 and found that methylmercury was only a minority fraction of total mercury (Eto et al., 2001b). They attributed this to the prolonged preservation. Here we re-examine the chemical forms of mercury and selenium from the same cat 717 using state-of-the-art synchrotron techniques only recently developed to show that the predominant form of mercury in cat 717 brain tissue is sulfur-bound organometallic. We complement these results with density functional theory (DFT) calculations relevant to the chemical process and plausible biotransformation to show that the most probable dominant neurotoxic chemical form of mercury was neither methylmercury nor inorganic mercury, but rather α-mercuri-acetaldehyde or a chemically related species.

9.4 Materials and Methods

Sample Preparation. Reagents were purchased from Sigma-Aldrich (Oakville, Ontario, Canada) and were of the highest quality available. Mercury L-cysteinate was prepared as previously described (Hoffmeyer et al., 2006). Mercury L-selenocysteinate was prepared following the method of Carty et al. (Carty et al., 1983) except employing L-selenocystine rather than the racemate. β–HgS was prepared as a black precipitate by mixing aqueous solutions of Na_2S and $HgCl_2$, which was filtered, washed with de-ionized water, and then dried. Other selenium

compounds were prepared according to published literature (Pickering et al., 1999; Gailer et al., 2000). Solutions and tissue samples were loaded or packed into 2 mm thick poly-acetal cuvettes closed with a polyimide adhesive tape window, and then frozen by immersion into a partly-frozen isopentane slurry with a temperature of approximately 120 K. Solution samples for conventional XAS contained 20% (v/v) glycerol. Solids were finely powdered and mixed with a boron nitride diluent and packed into 1 mm thick aluminum plates sealed on either side with polyimide adhesive tape. Samples were transported and stored at liquid nitrogen temperatures until data acquisition.

X-ray Absorption Spectroscopy. Standard X-ray absorption spectroscopy (XAS), including EXAFS and high energy resolution fluorescence detected (HERFD) XAS were both carried out at the Stanford Synchrotron Radiation Lightsource (SSRL) using beamlines 7-3 and 6-2, respectively with the SPEAR3 storage ring containing 500 mA at 3.0 GeV. On both beamlines in-hutch photon shutters were employed to prevent exposure of the sample to the X-ray beam when data were not being actively recorded. Samples were maintained at a temperature of 10 K using a helium flow cryostat (Oxford instruments, Abingdon, UK) with cuvettes inclined at an angle of 45° to the incident X-ray beam to facilitate measurement of X-ray fluorescence, giving an incident X-ray path length of 2.8 mm. On both 7-3 and 6-2 the incident beam energy calibration was relative to the lowest-energy inflection of Hg-Sn amalgam foil for the Hg L_{III}-edge, or a grey hexagonal selenium foil for the Se K-edge, values for which were assumed to be 12284.0 eV and 12658.0 eV, respectively.

On 7-3 a Si(220) double crystal monochromator was used for the incident beam, with harmonic rejection accomplished by detuning the monochromator to 60% of peak intensity. Incident and transmitted X-rays were monitored using nitrogen-filled gas ionization chambers, while X-ray absorption was measured as the $L\alpha_{12}$ fluorescence excitation spectrum using an array of 30 germanium detectors (Cramer et al., 1988) (Canberra Ltd. Meriden, Connecticut, USA). In order to maintain detector count-rates in the pseudo-linear regime, Ga_2O_3 X-ray filters were employed to preferentially absorb scattered radiation, together with silver Soller slits (EXAFS Co., Pioche, Nevada, USA) to reject filter fluorescence. Data were collected using the XAS Collect data acquisition software (George, M.J., 2000).

On 6-2 a Si(311) double crystal monochromator was used for the incident beam with harmonic rejection achieved through the cutoff energy (*ca*. 18 keV) of upstream Rh-coated specular optics. Incident and transmitted X-rays were monitored using gas ionization chambers

filled with helium and nitrogen, respectively. High resolution X-ray fluorescence was measured by means of a 6-element array of spherically bent crystal analyzers, using Si(555) and Si(844) crystals (Sokaras et al., 2013) to select a narrow energy band of the Hg $L\alpha_1$ or Se $K\alpha_1$ emission, respectively. The emission intensity was measured using a single-element silicon drift detector with aluminum filters upstream of the incident ion chamber used to adjust X-ray exposures and to maintain the detector count-rates in the pseudo-linear regime. Data were collected using the SPEC data acquisition software (Certified Scientific Software, Cambridge, Massachusetts, USA).

Data reduction and analysis was carried out as previously described (George et al., 1996) using the EXAFSPAK suite of computer programs (George, G.N., 2000). Extended X-ray absorption fine structure (EXAFS) phase and amplitude functions were calculated using the program FEFF (Rehr et al., 1991).

Density Functional Theory (DFT) Calculations. DFT geometry optimizations and energy calculations were carried out using DMol^3 and Biovia Materials Studio Version 2018 R1 (Delley, 1990; Delley 2000) using the meta-GGA approximation employing the M11-L functional both for the potential during the self-consistent field procedure, and for the energy (Peverati and Truhlar, 2012). DMol^3 double numerical basis sets included polarization functions for all atoms with all-electron relativistic core treatments. Transition state search and optimization used the linear synchronous transit/quadratic synchronous transit/conjugate gradient (LST/QST/CG) method implemented within DMol^3.

9.5 Results and Discussion

Figure 9.1 shows the HERFD XAS Hg L_{III} spectrum of cerebellar brain tissue from cat 717. HERFD XAS uses enhanced energy resolution (Figure 9.2) to probe the local atomic and electronic environment and hence speciation of a target element, here mercury, and can do so in complex materials such as biological tissues (Manceau et al., 2016; Nehzati et al., 2018). The HERFD XAS Hg L_{III} spectrum of cat 717 cerebellar brain tissue was fit to binary linear combinations of a library of HERFD XAS spectra of standard compounds. The best match (Figure 9.1) is with organometallic and inorganic mercury standard compounds, 78±4% sulfur-bound organometallic mercury in a C–Hg–S linear two-coordinate environment and 22±4% inorganic as β-mercuric sulfide (β–HgS). Of the ten best binary combinations (Table 9.1), all included sulfur-

bound organometallic mercury as the majority component with around 20% of a minor inorganic component. The best fit (Figure 9.1) used β–HgS (metacinnabar) as the minor component, the kinetically preferred but thermodynamically less-stable of the mercuric sulfide dimorphs, which exhibits a zincblende structure (Lehman, 1924) with four sulfurs bound to the metal. Other reasonable fits were found with other four-coordinate Hg–S species. Since spectra are sensitive to local environment, specific molecular identities are not available from HERFD XAS or conventional XAS. For example, analogous methyl and ethyl mercury compounds have similar spectra (not illustrated) due to similarity in immediate coordination of mercury, such that our measurements cannot distinguish between different sulfur-bound organometallic mercury compounds. The predominant form of mercury in the cerebellum of cat 717 is therefore identified as sulfur-bound organometallic mercury, with a minor phase that strongly resembles β–HgS.

Table 9.1. Top 10 best binary linear combination fits.

f_1	component 2 identity	f_2	$F^2\times10^6$	*fit-index*
0.775	β-HgS	0.225	1.5105	0.22
0.809	$[Hg(SR)_4]^{2-}$	0.191	1.8842	0.59
0.848	$[Hg(SPh)_4]^{2-}$	0.152	1.9211	0.63
0.824	HgSe	0.176	1.9316	0.64
0.847	$[Hg(SR)_3]^{-}$	0.153	1.9579	0.66
0.833	$[Hg(SePh)_3]^{-}$	0.167	1.9790	0.68
0.658	CH_3Hg–Se(L–Cys)	0.342	2.1631	0.87
0.899	$[HgCl_4]^{2-}$	0.101	2.2316	0.94
0.903	$(CH_3)_2Hg$	0.097	2.2737	0.98
0.893	Hg(0)	0.107	2.4263	1.13

Linear compound fits of the Hg L_{III} HERFD XAS spectrum of cat 717 cerebellum were carried out using the EXAFSPAK program MATCHIT using a library of 21 different Hg L_{III} HERFD XAS spectra. In all of the best 10 binary combinations (listed in the table) the first (majority) component was found to be methylmercury L-cysteineate [CH_3Hg–S(L–Cys)], corresponding to fraction f_1 in the fits, with the remainder fraction (f_2) corresponding to a minor component identified in the table. The function F^2 (often called χ^2, called F^2 here to distinguish it from the EXAFS χ) is defined by $F^2 = \sum(\mu - \mu_{calc})^2/(n-2)$ where μ and μ_{calc} are the experimental and computed signal, respectively, and the sum is over n data points included in the fit. The *fit-index* is given by $(F^2 - F^2_{min}) \times 10^6$, where F^2_{min} is F^2 computed between Fourier filtered (free of high-frequency noise) data and raw data. The fit-index effectively and approximately lacks contributions from high-frequency noise, so that a fit-index value of zero would represent a best possible fit, and higher values represent poorer fits.

.

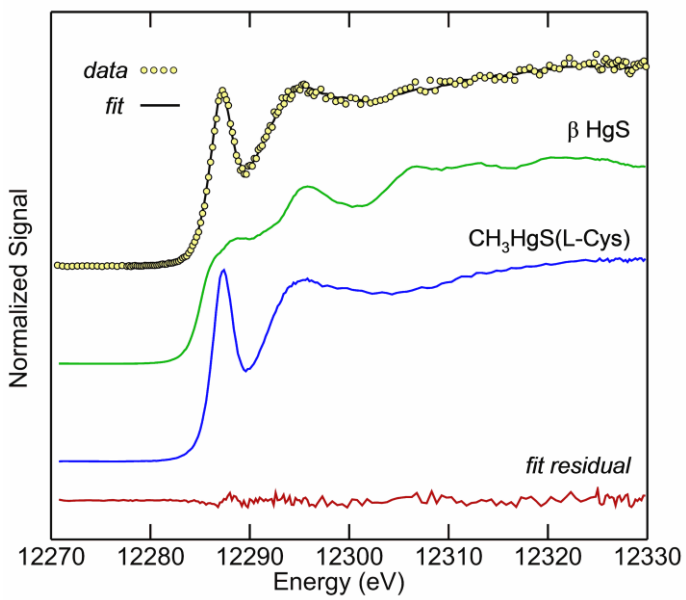

Figure 9.1. High energy resolution fluorescence detected Hg L_{III} X-ray absorption near-edge spectra. The HERFD XAS spectrum of cat 717 cerebellum (circles) is compared with those of methylmercury L-cysteinate, and β–HgS. The striking resemblance between the spectrum of cat 717 and methylmercury L-cysteinate is clear from the figure. The best fit (solid black line) was obtained with 78±4% methylmercury L-cysteineate and 22±4% β–HgS; errors are three times the estimated standard deviation (99% confidence limits) from the diagonal of the variance-covariance matrix.

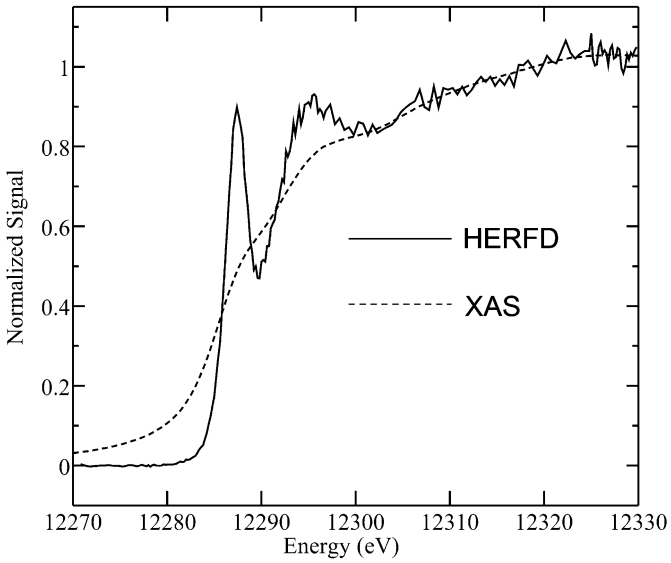

Figure 9.2. Comparison of Hg L_{III} HERFD XAS and standard Hg L_{III} XAS of cat 717 cerebellum showing the dramatically improved spectroscopic resolution obtained with HERFD XAS

Selenium is important in mercury toxicology (Gailer et al., 2000; Gailer, 2007; MacDonald et al., 2015a), so we also examined the Se K-edge HERFD XAS (Nehzati et al., 2018) and found no involvement of mercury-selenium interactions in the brain tissue. We used Hg L_{III} and Se K HERFD XAS absorption edge-jumps to estimate the effective concentration to be 70.9 μM Hg and 5.6 μM Se (wet weight), or some 13-fold excess of mercury. Previous conventional analysis of cat 717 cerebellum (Eto et al., 2001b) showed selenium below detection limits and total mercury dry weight of 62.5 $\mu g.g^{-1}$, which is commensurate with our value. Previous analyses also determined fractions of methylmercury and inorganic mercury to be 30% and 70%, respectively (Eto et al., 2001b); the analytical method for methylmercury, however, would be misleading if mercury was in a different organometallic form.

The Hg L_{III} extended X-ray absorption fine structure (EXAFS) spectra and corresponding Fourier transforms of cat 717 cerebellum (Figure 9.4) enable us to determine radial structural metrics of the mercury environments (Table 9.2). Curve-fitting analysis indicates 2.11 Å Hg–C and 2.37 Å Hg–S contacts, characteristic of two-coordinate organometallic mercury. Consistent with a minor component of β–HgS, the EXAFS also shows a 2.55 Å Hg–S interaction characteristic of its four-coordinate site, together with diagnostic weaker long-range Hg•••Hg and Hg•••S interactions. Constraining first-shell coordination numbers to the species fractions obtained from fitting the Hg L_{III} HERFD XAS spectra gave the excellent fit shown in Figure 9.4. The EXAFS is therefore quantitatively in agreement with the HERFD XAS result that mercury in the cerebellum of cat 717 is present as 78% sulfur-bound organometallic mercury, with 22% inorganic mercury as β–HgS. Because cat 717 was given the acetaldehyde plant waste directly, our results provide experimental evidence related to the composition of the waste. Since there are no known plausible pathways to convert inorganic to organometallic mercury in mammalian tissues, the presence of predominantly organometallic mercury in the brain of cat 717 clearly shows that the primary mercury species in the plant waste was organometallic, and not inorganic as suggested in some early reports. In agreement with this, the pathology exhibited by cat 717 (Eto et al., 2001b) was that expected for organomercury but not inorganic mercury poisoning.

Table 9.2. Hg L_{III} EXAFS Curve-fitting results.

Interaction	*fraction*	*N*	*R* (Å)	σ^2 (Å^2)	ΔE_0 (eV)
Hg–C_1	0.78	1	2.111(5)	0.0027(3)	–15.6
Hg–S_1		1	2.371(3)	0.0026(3)	
Hg–S_2	0.22	4	2.546(3)	0.0023(3)	
Hg⋯Hg_2		4.2(1)	4.127(4)	0.0040(5)	
Hg⋯S_2		4.2(1)	4.841(8)	0.0050(6)	

Structural parameters for the best fit of the EXAFS spectrum of cat 717 cerebellum, as shown in Figure 9.4. Interactions Hg–C_1 and Hg–S_1 are attributed to organometallic mercury (first component), and Hg–S_2, Hg•••S_2 and Hg•••Hg_2 to β–HgS. Values are given for the effective coordination numbers *N*, inter-atomic distances *R*, and the mean square deviation in *R*, σ^2, an index of thermal and static disorder. The threshold energy shift ΔE_0 was taken from fits to standard compounds of known structure, and was fixed at the same value for all interactions included in the analysis. Values in parentheses are the estimated standard deviations in the last digits obtained from the diagonal of the variance-covariance matrix (precisions). Amplitude reduction factor (S_0^2) set to 1.0. Coordination numbers in the fit for first-shell interactions were fixed according to the known value for the phase multiplied by the fraction determined from the HERFD XAS analysis. For the outer shell interactions (beyond 4 Å) both *N* and σ^2 were allowed to vary and are not thought to be structurally representative. This is typical for disordered non-crystalline amorphous systems, such as mercury chalcogenides (Gailer et al., 2000) including amorphous β–HgS, because the material will contain both disordered and ordered components, with the latter dominating the EXAFS. The interatomic distances (*R*) are, however, sensitive indicators of the nature of the material concerned.

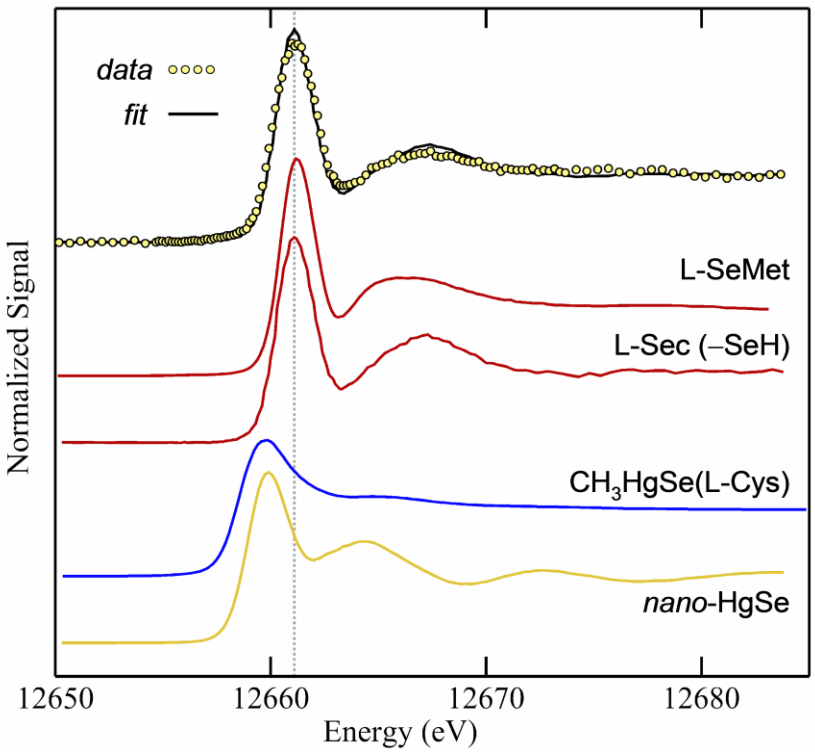

Figure 9.3. High energy resolution fluorescence detected Se Kα$_1$ X-ray absorption near-edge spectra of cat 717, compared with the spectra selected standard compounds; L-selenomethionine (aqueous, pH 7.4), L-selenocysteine (aqueous, pH 4.0), methylmercury L-selenocysteinate (solid), and nanoparticulate–HgSe (colloidal). The fit shows no contributions from the two mercury-containing species.

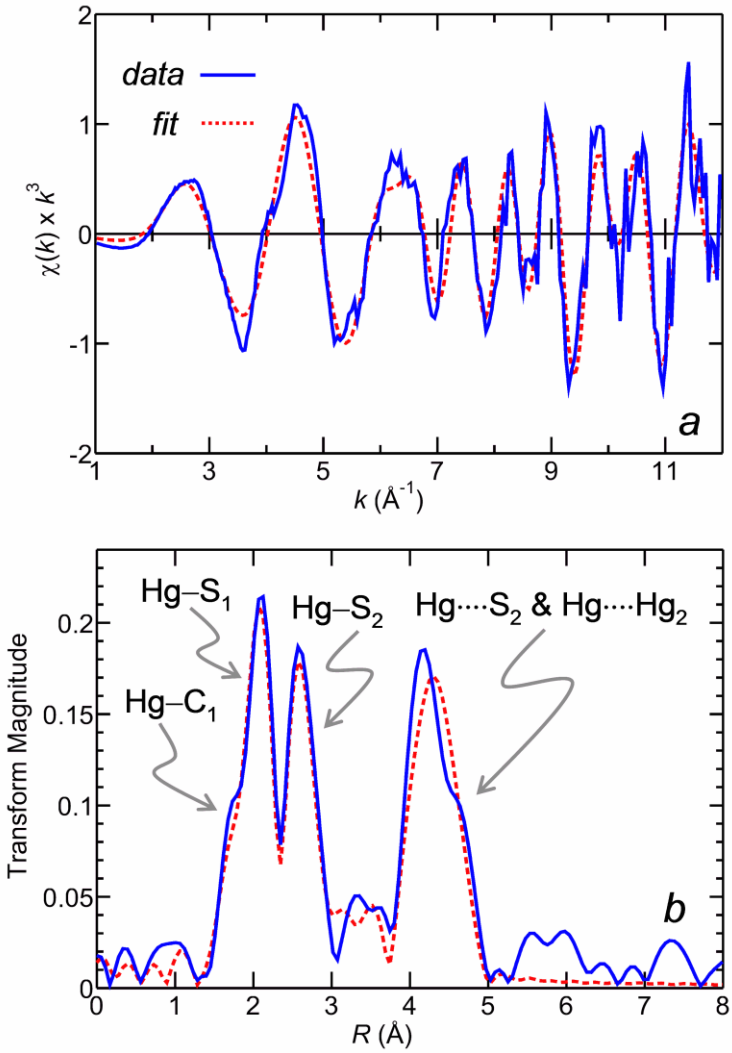

Figure 9.4. Extended X-ray absorption fine structure (EXAFS) spectra of cat 717 cerebellum. The EXAFS (*a*) and Fourier transforms (*b*) of cat 717 cerebellum are compared with the best fits calculated using the structural parameters given in Table 9.2. EXAFS Fourier transforms (*b*) are phase-corrected for Hg–S backscattering, with the various backscattering interactions included in the curve-fitting analysis indicated in the figure. Hg–C_1 and Hg–S_1 are attributed to sulfur-bound organometallic mercury (first component), and Hg–S_2, Hg•••S_2 and Hg•••Hg_2 to β–HgS.

Since the published analysis of the original waste was performed after storage at room temperature for decades and presumably had degraded (Eto et al., 2001b), we have used computational chemistry to consider the chemical plant processes and expected side-products. The Chisso plant employed mercury catalysts to manufacture acetaldehyde through hydration of acetylene (Eto et al., 2010; Othmer et al., 1948) using a catalytic method known as alkyne oxymercuration (Larock, 2013). The plant also supported a much smaller activity to manufacture vinyl chloride, also using mercury catalysts, which is not considered here. This factory, and others in Japan, had been using these methods since the early 1930's. However, no human poisonings were recognized in Minamata before 1953. Prior to that recognition in August 1952, the Chisso plant had modified their procedures, altering a catalyst regeneration process.

Figure 9.5 summarizes the major chemical reactions, together with some reaction energies from our DFT calculations. Acetylene is bound to Hg^{2+} by a η^2 bond to both carbon atoms to form compound **1**, in which the carbon atoms are activated for attack by water to form **2** an α-mercuri-vinyl alcohol. Under acidic conditions protonolysis of the Hg–C bond regenerates inorganic catalyst forming vinyl alcohol, which undergoes acid-catalyzed keto-enol tautomerization with 1,3-hydrogen migration to form the desired product acetaldehyde. However, **2** also undergoes similar keto-enol tautomerization to form the α-mercuri-acetaldehyde **3**, a stable compound of known structure (Halfpenny and Small, 1979). Although **3** can also undergo protonolysis to form acetaldehyde, it is less susceptible to this reaction than **2**. Therefore, an energetically-favoured by-product of the Chisso plant, expected under low-acid conditions, is **3**, an α-mercuri-acetaldehyde which is distinct from methylmercury. It has been suggested that **3** oxidizes to α-mercuri-acetic acid species **4**, which might spontaneously lose CO_2 to form methylmercury species **5** (Takeuchi et al., 1999). While the former is plausible, particularly in the presence of oxidizing nitric acid, our calculations suggest that decarboxylation is improbable due to a substantial activation barrier of 316 $kJ \cdot mol^{-1}$. In agreement with this, α-mercuri-acetic acids are known from the literature (Grdenić et al., 1991) to exhibit a stable C–C bond under oxidizing and acidic conditions (Grdenić et al., 1984), and only insignificant methylmercury yields have been reported (Kitamura et al., 1968). Taken together, the evidence is strong that the compound entering the waters of Minamata bay, that gave rise to the tragedy of Minamata disease, was species **3** or possibly **4**.

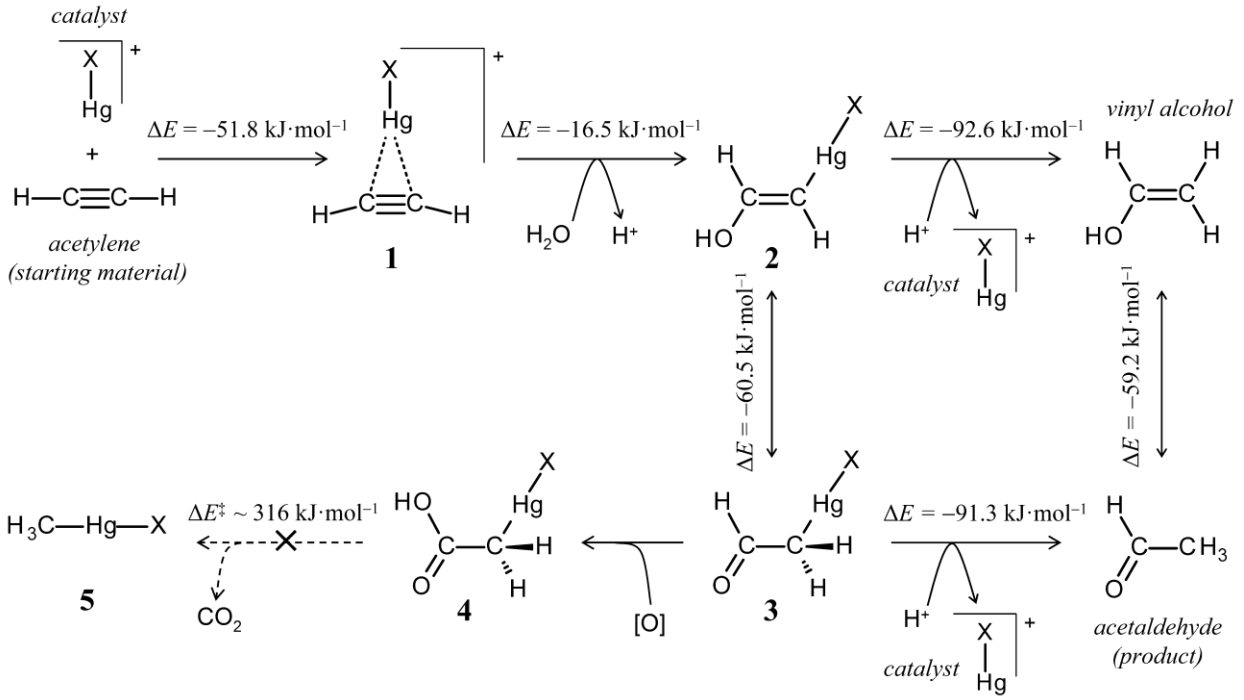

Figure 9.5. Chemistry of the Chisso chemical plant and its potential side-products. DFT computed energy changes kJ·mol^{-1} are shown adjacent to each of the central reactions. The suggested loss of CO_2 from **4** to form methylmercury **5** is chemically very unlikely due to the very high activation energy of 316 kJ·mol^{-1}. X represents a general substituent of mercury, like chloride, which was used for computations. The oxidation **3** to **4** might occur in the environment, after waste emission had occurred.

In living brain tissue organic mercury species are known to convert to inorganic forms over time, being converted to highly insoluble HgSe (Korbas et al., 2010b). However, since cat 717 lived only a short time after initiation of dosing, these protective processes had no time to occur *in vivo*, likely accounting for the notable absence of HgSe. Exposure of the brain to formaldehyde preservative over decades would be expected to change its forms of selenium, but not of Hg. Selenocysteine residues (either selenolate R–Se^- or selenol R–SeH) would react to form selanylmethanol derivatives, or cyclizing with the selenocysteine amino group to form 1,3-selenazolidine species. However, Hg–Se bonds would be expected to be stable, and their absence may be significant in relation to recent suggestions of inhibition of selenoenzymes as a contributor to mercury's toxicity (Ralston et al., 2007). Plausibly, the presence of β-HgS in the cerebellum of cat 717 may result from degradation of the original organometallic compounds during storage. Conversely, our finding of a majority organometallic mercury species is unlikely to be an artifact of storage because there is no chemically plausible method of organometallic mercury derivatives forming.

We have shown through newly developed X-ray spectroscopic techniques that cat 717 was exposed to primarily organometallic mercury compounds, and hence we can conclude that these were the dominant mercury species in the acetaldehyde plant waste. This is in agreement with the signs exhibited by the cat and with subsequent pathology investigations (Eto et al., 2001b). Our analysis of the chemistry indicates that the plant effluent probably contained an α-mercuri-acetaldehyde species (**3** or **4** in Figure 9.5) and that that was the species that gave rise to the tragedy of Minamata disease. We believe this evidence indicates that natural biomethylative processes within Minmata Bay initially played no major role in the tragedy, and suggests that exposure to methylmercury compounds were not specifically involved. The consequences of a different organometallic mercury species being the cause of the Minamata poisoning should be re-evaluated.

9.6 Acknowledgments

Funding: We thank Professors Eric Block (University of Albany, State University of New York) and Dale Ward (University of Saskatchewan) for helpful comments on the manuscript. We also thank Professor Kaori Tanaka (University of Saskatchewan) for additional help. Funding: We acknowledge grant support from the Natural Sciences and Engineering Research Council of Canada (I.J.P., P.H.K., and G.N.G.), a Canada Foundation for Innovation John Evans leader's

Fund Award (I.J.P.) and Canada Research Chairs (I.J.P. and G.N.G.). S.N. acknowledges a Dr. Rui Feng Scholarship; A.K.J. and S.N. were Fellows and N.V.D. an Associate in the Canadian Institutes of Health Research-Training grant in Health Research Using Synchrotron Techniques (THRUST). Use of the Stanford Synchrotron Radiation Lightsource, SLAC National Accelerator Laboratory, is supported by the U.S. Department of Energy, Office of Science, Office of Basic Energy Sciences under Contract No. DE-AC02-76SF00515. The SSRL Structural Molecular Biology Program is supported by the DOE Office of Biological and Environmental Research, and by the National Institutes of Health, National Institute of General Medical Sciences (including P41GM103393). The contents of this publication are solely the responsibility of the authors and do not necessarily represent the official views of NIGMS or NIH.

CHAPTER 10. General Discussion and Future Directions

The results in this dissertation address questions relating to mercury toxicity using the structural information gained from spectroscopic and computation chemistry tools. Structural knowledge of toxic compounds is important in the understanding of toxicological mechanisms and can be useful in managing the strategic efforts of environmental remediation and the design of optimal sequestering agents. XAS is a powerful structural tool that can serve to answer molecular toxicology questions and probe element-specific structural information. This was evident in Chapter 4 with the structural identification of the solution chemistry responsible for the drastic changes in toxicity observed using a standard laboratory reagent. XAS does however have its limitation as was seen in Chapter 5 which is that XAS on its own was unable to identify the possible chelating properties of a compound like AB9 and its labile ligands when analyzing the solution structure. Using newly available advanced synchrotron techniques, the chemical and concentration sensitivities of XAS are improved with HERFD XAS. These new advancements in structural characterization were used to identify important species of mercury possibly involved in the mutagenic activity of Hg(II) and the devastating symptoms associated with Minamata Disease. The following sections expand on aspects of the preceding chapters and surveys the prospect of future directions.

10.1 Mercury Sequestration

Molecular studies on mercury toxicity are complex due to the variable chemical forms and varied toxicological profiles. This was evident in the molecular studies on the extreme modification of toxicity presented in zebrafish larvae with both organic and inorganic forms of mercury with 1-phenyl-2-thiourea (PTU). Due to this unsuited effect, we discontinued the use of PTU in studies of mercury in zebrafish larvae. The dithiol AB9 was considered for its suitability in effectively treating acute inorganic mercury accumulation in zebrafish larvae. XFI was conducted to visualize the fate of mercury in zebrafish larvae, and results showed the unloading of mercury from custom accumulation patterns. Mortality studies however showed an increase in zebrafish larvae deaths which may indicate harmful redistribution of mercury to other parts of the body. EXAFS and DFT results showed that AB9 could provide the necessary framework to chelate

mercury in a close-to-linear two-coordinate geometry. Future work into the fate of redistributed mercury from the livers of zebrafish larvae is merited to establish answers to the increased mortality. As well, the effectiveness of AB9 in ameliorating acute methylmercury exposures in zebrafish would be worth pursuing as the toxicological fate of methylmercury species in zebrafish is different from inorganic mercury species. Korbas et al. (2012) reported highest methylmercury accumulation in the eye lens epithelial cells, as opposed to the olfactory epithelium and kidney for inorganic mercury accumulation (Korbas et al., 2012). An interesting extension of the work in this dissertation would be to pursue studies that compare the effectiveness of AB9 with both acute and chronic doses of mercury compounds. The patterns of mercury accumulation with chronic exposure are not well studied.

Multidentate thiols are still the leading treatment option for sequestering agents used in mercury poisoning cases. *Meso*-2,3-dimercaptosuccinic acid (DMSA) and 2,3-dimercapto-1-propanesulfonic acid (DMPS) (Figure 1.1) are often prescribed for treatment of mercury toxicity (Aaseth et al., 2018). These compounds are structurally similar with vicinal dithiols, however as was previously mentioned, neither dithiol was found to form true chelates with Hg^{2+} (George et al., 2004). This could be due to the small bite angle between the vicinal dithiols which is unable to accommodate the two-coordinate, linear geometry preferred for mercuric ions, without the penalty of high steric strain. Reports have also shown success with combination treatments using lipophilic and hydrophilic agents in unison to target different physiological criteria (Aeseth et al., 2018). Researchers proposed British antilewisite (BAL) (Figure 1.1) for lipophilic targets such as tubulin in the brain, followed by activity of DMSA or DMPS for assistance with excretion from the body (Aeseth et al., 2018). Ligands with high affinity towards mercury and with a binding environment flexible and accommodating to mercury ions is essential, as seen with all three ligand types presented in this dissertation – PTU, AB9, and thymine bases.

The metalloregulatory protein MerR exhibits exceptional ultrasensitivity towards mercuric ions as high as $1.0 \pm 0.3 \times 10^{-8}$, even in the presence of competitive dithiols (Watton et al., 1990). The binding geometry is through three cysteinate residues to produce a trigonal planar geometry (Wright et al., 1990). Fu et al. (2011) designed a multidentate thiolate compound, using a biomimetic approach from the MerR model and from extending the AB9 compound (Fu et al., 2011). The custom chelator is a close analogue of B9 with a few modifications which include the addition of a third ligand and extension of the ligand chain length to provide a protracted

coordination environment to accommodate mercury ions very close to ideal trigonal geometry (Fu et al., 2011). The computed structural parameters for this custom chelator to a mercuric ion were 2.429 Å Hg–S bond-lengths and 120.0° for S–Hg–S angles (Fu et al., 2011). It would be interesting to study molecular coordination using XAS or HERFD XAS of this custom chelator with inorganic and organic forms of mercury. Also, vertebrate treatment studies of this custom chelator following the exposure of either organic or inorganic forms of mercury would be worth performing. Results may aid in the design and development of a true chelator of mercury that could prove useful in therapeutic settings.

10.2 Theoretical Excited States Methods

Sophisticated computational methods using quantum mechanical theory calculate excited states of molecules which provide electronic structural information of molecules that can aid in understanding experimental near-edge spectra. The software used in this dissertation calculate based on *ab initio* wavefunctions and each program has their own strengths and limitations. StoBe-deMon software use the linear combination of atomic orbitals (LCAO) to solve Kohn-Sham DFT calculations. Regarding near-edge spectral interpretation, the energy position of spectral features are a result of the eigenstates of final state Hamiltonians in the presence of a core hole and the X-ray transition intensity is as a result of the valence states in the initial ground states (Cavalleri et al., 2005). StoBe-deMon code use half-core-hole (HCH) approximations that aim to balance the contribution between initial and final state effects. One of the limitations of StoBe-deMon code is the inability to apply all electron-relativistic effects to the wavefunction approximations which is imperative with larger atoms, such as mercury. ORCA software is another suitable computational chemistry package which provides flexibility with user-defined parameters such as all-electron relativistic contracted basis sets. With increasing popularity, time-dependent density functional theory (TDDFT) is a system modelling many-body systems with time-dependent potentials. Based on the Hohenberg-Kohn (HK) theorem, TDDFT simulates one electron excitations. The TDDFT method is not ideal for theoretical L-edge spectroscopy due to the neglect in multiplet structures. Restricted-open-shell configuration interaction with single excitation (ROCIS) method is yet another approach which incorporates multiplet structure and spin orbit coupling (SOC) and is therefore most appropriate in L and M-edge simulations. ROCIS constructs approximations accounting for the many multiplets in the $2p^5nd^{n+1}$ (for 2p excitations) configuration together with

corrections from SOC effects. A preliminary comparison of the various methods described above, to calculate the excited states of Se K-edge using an R-Se-S-R model is shown in Figure 10.1. The experimental data is seleno-sulfocystine shown in black. All three *ab initio* methods produce similar excited stick spectra and seemingly identical excited state molecular orbital diagrams to the 4p antibonding molecular orbitals (σ*) of sulfur (LUMO) and carbon (LUMO + 1) (Figure 10.2). Further work with a rigorous evaluation comparing various computational methods, accompanied with near-edge standard models would be worthwhile to establish the best practices in understanding mercury and selenium near-edges.

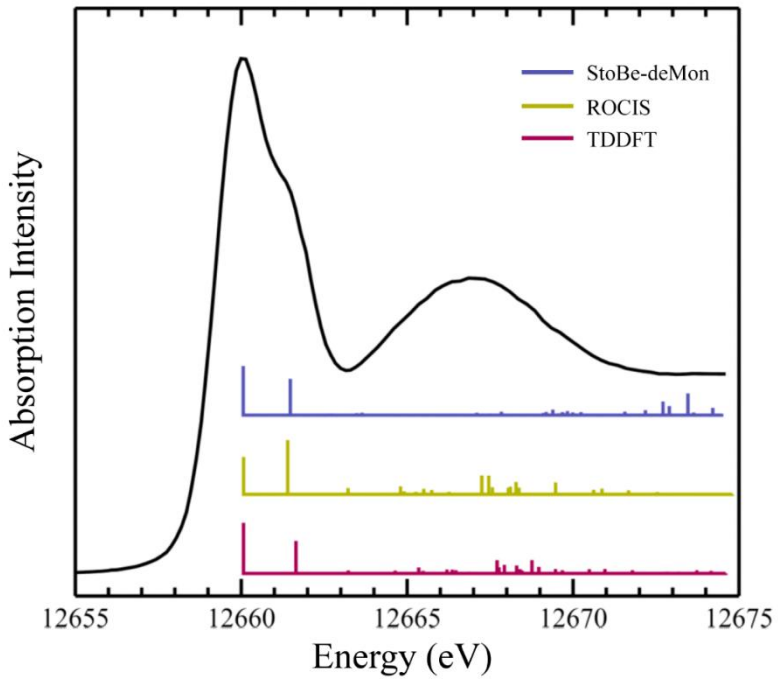

Figure 10.1. Comparison of Se K-edge excited state transitions of R-Se-S-R model using different *ab initio* based code. Near-edge spectrum is of seleno-sulfocystine (*black line*). Note: ROCIS calculation is without SOC correction.

Molecular Orbital	Stobe-deMon	ROCIS	TDDFT
LUMO	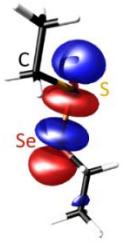	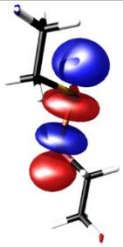	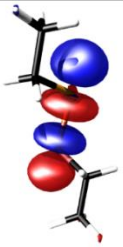
LUMO + 1	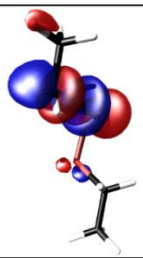	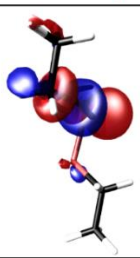	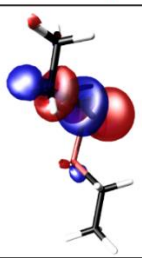

Figure 10.2. Molecular orbital diagrams from *ab initio* calculations comparing results from different codes.

10.3 Advanced Spectroscopic Techniques

The results of this dissertation established the development of new methodologies to investigate distinctive signatures in near-edge spectra of mercury and selenium compounds, as well as methods to probe dilute, biologically, and environmentally relevant levels. With respect to spectral resolution, HERFD XAS improved the observed Hg L_{III}-$L\alpha_1$ edge spectra considerably compared to the Se $K\alpha_1$ edge spectra. Yet regarding concentration sensitivity, HERFD XAS improved the capabilities of detecting dilute levels with Se $K\alpha_1$ edge spectra with better background signal rejection compared to the Hg L_{III}-$L\alpha_1$ edge spectra. And favourably, the HERFD XAS Hg L_{III}-$L\alpha_1$ emission peak was broader and showed less variability between different chemical forms compared to the HERFD XAS Se $K\alpha_1$ emission peak. All things considered, there is no doubt that HERFD XAS will significantly advance molecular studies of mercury toxicity. With the improvements in modern spectroscopic techniques achieving better detection limits, the ability to probe the natural limits of elements comes with great enthusiasm. The utility of HERFD type spectrometers to probe with great selectivity and sensitivity has already shown profound improvements in the measurements at unforeseen levels.

A further development from this would be the targeting of minor-line X-ray emission spectroscopy (XES) which has recently demonstrated high potential. Doonan et al. (2005) assigned the $K\beta_4$ and $K\beta''$ valence-to-core (VtC) transitions of oxo-Mo, correlating to a metal 4d to metal 1s transition and crossover ligand 2s to metal 1s transition, respectively. The intensity of the latter transition was reported to directly correlate to the bond-length and the position correlate to the ligand binding (Glatzel and Bergmann, 2005). Furthermore, the energy of the large $K\beta_{2,5}$ feature represents the Fermi level (Glatzel and Bergmann, 2005). Because these crossover transitions involve ligand-valence to metal-core transitions, distinguishing between ligands with close atomic numbers, for example carbon, nitrogen or oxygen, is feasible since valence orbitals possess the information on the binding energies of the atomic species. This sensitivity to distinguish between similar atomic species is highly valuable since such a distinction is not feasible with EXAFS. VtC XES has been successfully applied to a number of experiments. Hall et al. (2014) used VtC XES spectra for ligand identity and electronic structure of a number of manganese nitride and oxo complexes. Experimental results showed pre-edge features with distinct energetic shifts for different oxygen and nitrogen ligands (Hall et al., 2014). March et al. (2015) also detected time-

resolved transient intermediates of solution-phase ferrocyanide redox reactions. Their results lacked signal strength but they theorized improved counting statistics would help gather meaningful information from the spectrum. A future extension of this dissertation might be in monitoring the intensity and ratio between different satellite emission energies. Table 10.1 lists a series of satellite K and L emission lines with their corresponding electronic transitions. As these transitions involve the frontier molecular orbitals of selenium and mercury, examination of these emission lines might give insights into the electron occupancy of difference compounds and hence their bonding.

Table 10.1. Minor emission lines and corresponding electronic transitions.

Selenium		**Mercury**	
Line	Transition	Line	Transition
$K\beta_1$	$3p_{3/2} \rightarrow 1s$	$L\beta_5$	$5d \rightarrow 2p_{3/2}$
$K\beta_2$	$4p \rightarrow 1s$	$L\gamma_6$	$5d \rightarrow 2p_{1/2}$
$K\beta_3$	$3p_{1/2} \rightarrow 1s$	$L\beta_7$	$5s \rightarrow 2p_{3/2}$
$K\beta_4$	$4d \rightarrow 1s$	$L\gamma_8$	$5s \rightarrow 2p_{1/2}$
$K\beta_5$	$3d \rightarrow 1s$	$L\gamma_4$	$5p \rightarrow 2p$ (both L_{III} and L_{II})
$K\beta''$	Ligand $2s \rightarrow 1s$		

Doonan et al. (2005) compared the emission rate of $K\beta_4/K\beta_1$ and $K\beta''/K\beta_1$ transitions to recognize the different ligand contributions to the molecular orbitals of oxo-molybdenum compounds (Doonan et al., 2005). VtC XES has been probed for 3d (Glatzel and Bergmann, 2005) and 4d (Doonan et al., 2005) metals, and could feasibly be applied to Se and Hg satellite emission lines. The major requirement for this to be practical is to achieve a high resolving power of energy.

Finally, the optics used to apply high-energy resolution X-ray spectrometry can be adapted for enhanced results. The HERFD XAS spectrometer at SSRL utilizes Johann-type geometry crystals which compared to Johansson-type geometry lacks energy resolution because it is not exact point-to-point imaging. Utilizing Johansson ground-bent crystals may further improve the speciating and sensitivity capabilities of HERFD XAS. Furthermore, energy dispersive operations which collect the whole spectrum simultaneously in a single shot (Alonso-Mori et al., 2012) compared to the scanning setup at SSRL would not only save time, but also provide a whole RIXS spectrum of the scan which would alleviate the uncertainty when it comes to choosing the emission

energy to set when scanning composite samples or ultra-dilute samples and accompanying poorer signal-to-noise.

Molecular studies into mercury toxicity has its challenges, though we are achieving great success implementing advanced methodologies. New analytical tools are just beginning to fulfill the gaps and uncover great potential in mercury research, making the future in molecular studies into mercury toxicity very promising.

REFERENCES

Aaseth, J., Ajsuvakova, O.P., Skalny, A.V., Skalnaya, M.G., and Tinkov, A.A. (2018) Chelator combination as therapeutic strategy in mercury and lead poisoning. *Coord Chem Rev*, **358**, 1-12.

Allen, F.H. (2002) The Cambridge Structural Database: A quarter of a million crystal structures and rising. *Acta Cryst B,* **58**, 380–388.

APEX2; 2014.3-0 ed.; Bruker AXS Inc., Madison, Wisconsin, 2014.

Aposhian, H.V., Morgan, D.L., Sam Queen, H.L., Maiorino, R.M., and Aposhian, M.M. (2003) Vitamin C, glutathione, or lipoic acid did not decrease brain or kidney mercury in rats exposed to mercury vapor. *J Toxicol Clin Toxicol,* **41**, 339-347.

Ariya, P.A., Amyot, M., Dastoor, A., Deeds, D., Feinberg, A., Kos, G., Poulain, A., Ryjkov, A., Semeniuk, K., Subir, M., and Toyota, K. (2015) Mercury physicochemical and biochemical transformation in the atmosphere and at atmospheric interfaces: A review and future directions. *Chem Rev*, **115**, 3760-3802.

Ariza, M.E. and Williams, M.V. (1999) Lead and mercury mutagenesis: Type of mutation dependent upon metal concentration. *J Biochem Mol Toxicol,* **13**, 102-112.

Aschner, M. and Ceccatelli, S. (2010) Are neuropathological conditions relevant to ethylmercury exposure? *Neurotox Res,* **18**, 59-68.

Atkins, A.J., Jacob, C.R., and Bauer, M. (2012) Probing the electronic structure of substituted ferrocenes with high-resolution XANES spectroscopy. *Chem Eur J,* **18**, 7021-7025.

Avery, J.C. and Hoffmann, P.R. (2018) Selenium, selenoproteins, and immunity. *Nutrients,* **10,** 1-20.

Bacquart, T., Devès, G., and Ortega, R. (2010) Direct speciation analysis of arsenic in sub-cellular compartments using micro-X-ray absorption spectroscopy. *Environ Res*, **110**, 413-416.

Bakir, F., Damluji, S.F., Amin-Zaki, L., Murtadha, M., Khalidi, A., Al-Rawi, N.Y., Tikriti, S., Dhahir, H.I., Clarkson, T.W., Smith, J.C., and Doherty, R.A. (1973) Methylmercury poisoning in Iraq, *Science*, **181,** 230-241.

Ballatori, N. and Truong, A.T. (1995) Mechanisms of hepatic methylmercury uptake. *J Toxicol Environ Health*, **46**, 343-353.

Bauer, M. (2014) HERFD-XAS and valence-to-core-XES: New tools to push the limits in research with hard X-rays. *Phys Chem Chem Phys,* **16**, 13827-13837.

Behne, D., Pfeifer, H., Röthlein, D., and Kyriakopoulos, A. (2002) A cellular and subcellular distribution of selenium and selenium-containing proteins in the rat. In: Roussel, A.M., Anderson, R.A., and Favrier A.E. (Eds.) *Trace Elements in Man and Animals 10*. Boston: Springer

Beijer, K. and Jernelöv A. (1978) Ecological aspects of mercury-selenium interactions in the marine environment. *Environ Health Perspect*, **25**, 43-45.

Berman H.M., Westbrook, J., Feng, Z., Gilliland, G., Bhat, T.N., Weissig, H., Shindyalov, I.N., Shindyalov, and Bourne, P.E. (2000) The Protein Data Bank. *Nucleic Acids Res,* **28**, 235-242.

Bernhoft, R.A. (2012) Mercury toxicity and treatment: A review of the literature. *J Environ Public Health*, **2012**, 1-10.

Bjørklund, G., Aaseth, J., Ajsuvakova, O.P., Nikonorov, A.A., Skalny. A.V., Skalnaya, M.G., and Tinkov, A.A. (2017) Molecular interaction between mercury and selenium in neurotoxicity. *Coord Chem Rev,* **332**, 30–37.

Blechinger, S.R., Warren Jr., J.T., Kuwada, J.Y., and Krone, P.H. (2002) Developmental toxicology of cadmium in living embryos of a stable transgenic zebrafish line. *Environ Health Persp*, **110**, 1041–1046.

Blum, J.D., Sherman, L.S., and Johnson, M.W. (2014) Mercury isotopes in Earth and environmental sciences. *Annu Rev Earth Planet Sci*, **42**, 249-269.

Boerner, L.J.K. and Zaleski, J.M. (2005) Metal complex-DNA interactions: From transcription inhibition to photoactivated cleavage. *Curr Opin Chem Biol,* **9**, 135-144.

Bohnsack, B.L., Gallina, D., and Kahana, A. (2011) Phenylthiourea sensitizes zebrafish cranial neural crest and extraocular muscle development to changes in retinoic acid and IGF signaling. *PLoS ONE,* **6**, e22991.

Boyer Jr., C.I., Andrews E.J., deLahunta A., Bache C.A., Gutenman W.H., Lisk, D.J. (1978) Accumulation of mercury and selenium in kittens fed commercial cat food. *Cornell Vet*, **68**, 365-374.

Brown, T.A. and Shrift, A. (1982) Selenium: Toxicity and tolerance in higher plants. *Biol Rev,* **57**, 59-84.

Bumbrah, G.S. and Sharma, R.M. (2016) Raman spectroscopy – Basic principle, instrumentation and selected applications for the characterization of drugs of abuse. *Egypt J Forensic Sci,* **6**, 209-215.

Cantor, M.O. (1951) Mercury lost in the gastrointentinal tract; Report of an unusual case. *JAMA*, **146**, 560-561.

Carty, A.J., Malone, S.F., Taylor, N.J., and Canty, A.J. (1983) Synthesis, spectroscopic, and X-ray structural characterization of methylmercury-D, L-selenocysteinate monohydrate, a key model for the methylmercury(II)-selenoprotein interaction. *J Inorg Biochem*, **18**, 291–300.

Cavalleri, M., Odelius M., Nordlund, D., Nilsson, A., Pettersson L.G.M. (2005) Half or full core hole in density functional theory X-ray absorption spectrum calculations of water? *Phys Chem Chem Phys*. **7**, 2854-2858.

Chen, F.M. (1992) Sr^{2+} facilitates intermolecular G-quadruplex formation of telomeric sequences. *Biochemistry*. **31**, 3769-3776.

Chun, H.J., Kim, S., Han, Y.D., Kim, D.W., Kim, K.R., Kim, H.S., Kim, J.H., and Yoon, H.C. (2018) Water-soluble mercury ion sensing based on the thymine-Hg^{2+}-thymine base pair using retroreflective Janus particle as an optical signaling probe. *Biosens Bioelectron*, **104**, 138-144.

Clarke, D., Buchanan, R., Gupta, N., and Haley, B. (2012) Amelioration of acute mercury toxicity by a novel, non-toxic lipid soluble chelator N,N'bis-(2-mercaptoethyl) isophthalamide: Effect on animal survival, health, mercury excretion, and organ accumulation, *Toxicol Environ Chem*, **94**, 616-640.

Clarkson, T.W., Magos, L., and Myers, G.J. (2003) The toxicology of mercury – Current exposures and clinical manifestations. *N Engl J Med*, **349**, 1731-1737.

Clarkson, T.W. and Magos, L. (2006) The toxicology of mercury and its chemical compounds. *Crit Rev Toxicol*, **36**, 609-662.

Clarkson, T.W., Vyas J.B., and Ballatori, N. (2007) Mechanisms of mercury disposition in the body. *Am J Ind Med*, **50**, 757-764.

Corminboeuf, C., Tran, F., and Weber, J. (2006) The role of density functional theory in chemistry: Some historical landmarks and applications to zeolites. *Theo Chem*, **762**, 1-7.

Cotelesage, J.J.H., Pushie, M.J., Grochulski, P., Pickering, I.J., and George, G.N. (2012) Metalloprotein active site structure determination: Synergy between X-ray absorption spectroscopy and X-ray crystallography. *J Inorg Biochem*, **115**, 127–137.

Craig, M.P., Gilday, S.D., Hove, J.R., (2006) Dose-dependent effects of chemical immobilization on the heart rate of embryonic zebrafish. *Lab Anim*, **35**, 41-47.

Cramer, S.P., Tench, O., Yocum, M., and George, G.N. (1988) A 13-element Ge detector for fluorescence EXAFS. *Nucl Instrum Meth A*, **266**, 586–591.

Cutsail III, G.E., Banerjee, R., Zhou, A., Que Jr, L., Lipscomb, J.D., and DeBeer, S. (2018) High-resolution extended X-ray absorption fine structure analysis provides evidence for a longer Fe•••Fe distance in the Q intermediate of methane monooxygenase. *J Am Chem Soc*, **140**, 16807-16820.

Dambly-Chaudière, C., Sapède, D., Soubiran, F., Decorde, K., Gompel, N. and Ghysen, A. (2003) The lateral line of zebrafish: A model system for the analysis of morphogenesis and neural development in vertebrates. *Biol Cell*, **95**, 579–587.

Dave, G., and Xiu, R. (1991) Toxicity of mercury, copper, nickel, lead, and cobalt to embryos and larvae of zebrafish, *Brachydanio rerio*. *Arch Environ Contam Toxicol*, **21**, 126–134.

Delley, B.J. (1990) An all-electron numerical method for solving the local density functional for polyatomic molecules. *Chem Phys*, **92**, 508–517.

Delley, B J. (2000) From molecules to solids with the $DMol^3$ approach. *Chem Phys*, **113**, 7756–7764.

Dolgova, N.V., Hackett, M.J., MacDonald, T.C., Nehzati, S., James, A.K., Krone, P.H., George, G.N., Pickering, I.J. (2016) Distribution of selenium in zebrafish larvae after exposure to organic and inorganic selenium forms. *Metallomics*, **8**, 305-312.

Doonan, C.J., Zhang, L., Young, C.G., George, S.J., Deb, A., Bergmann, U., George, G.N., and Cramer, S.P. (2005) High-resolution X-ray emission spectroscopy of molybdenum compounds. *Inorg Chem*, **44**, 2579-2581.

Doonan, C.J., Rubie, N.D., Peariso, K., Harris, H.H., Knottenbelt, S.Z., George, G.N., Young, C.G., and Kirk, M.L. (2008) Electronic structure description of the cis-MoOS unit in models for molybdenum hydroxylases. *J Am Chem Soc*, **130**, 55-65.

Dyrssen, D. and Wedborg, M. (1991) The sulfur-mercury(II) system in natural waters. *Water Air Soil Pollut*, **56**, 506-519.

Eckert, M., Fleischmann, G., Jira, R., Bolt, H.M., Golka, K., (2007) *Acetaldehyde* (in Ullmann's Encyclopedia of Industrial Chemistry, Wiley-VCH.

Eichhorn, G.L. and Clark, P. (1963) The reaction of mercury(II) with nucleosides. *J Am Chem Soc*, **85**, 4020-4024.

Eichhorn, G.L. and Shin, Y.A. (1968) Interaction of metal ions with polynucleotides and related compounds. XII. The relative effect of various metal ions on DNA helicity. *J Am Chem Soc*, **90**, 7323-7328.

Elsalini, O.A., and Rohr, K.B. (2003) Phenylthiourea disrupts thyroid function in developing zebrafish. *Dev Genes Evol*, **212**, 593–598.

Eto, K., Yasutake, A., Kuwana, T., Korogi, Y., Akima, M., Shimozeki, T., Tokunaga, H., Kaneko, Y. (2001a) Methylmercury poisoning in common marmosets – A study of selective vulnerability within the cerebral cortex. *Toxicol Pathol*, **29**, 565-573.

Eto, K., Yasutake, A., Nakano, A., Akagi, H., Tokunaga, H., and Kojima, T. (2001b) Reappraisal of the historic 1959 cat experiment in Minamata by the Chisso Factory. *Tohoku J Exp Med*, **194**, 197–203.

Eto, K., Marumoto, M., and Takeya, M. (2010) The pathology of methylmercury poisoning (Minamata disease). *Neuropathology*, **30**, 471–479.

Föhlisch, A., Vijayalakshmi, S., Hennies, F., Wurth, W., Medicherla, V.R.R., Drube, W. (2007) Verification of the core-hole-clock method using two different time differences: Attosecond charge transfer in c(4x2)S/Ru(0001), *Chem Phys Lett*, **434**, 214-217.

Fox, D.A. and Boyes, W.A. (2013) "[Toxic responses of the ocular and visual system]" in *Casarett & Doull's Toxicology: The basic science of poisons*, C.D. Klaassen, Ed., McGraw-Hill.

Fu, J., Hoffmeyer, R.E., Pushie, M.J., Singh, S.P., Pickering, I.J., and George, G.N. (2011) Towards a custom chelator for mercury: Evaluation of coordination environments by molecular modeling. *J Bio Inorg Chem*, **16**, 15-24.

Gailer, J., George, G.N., Pickering, I.J., Madden, S., Prince, R.C., Yu, E.Y., Denton, M.B., Younis, H.S., and Aposhian, H.V. (2000) Structural basis of the antagonism between inorganic mercury and selenium in mammals. *Chem Res Toxicol*, **13**, 1135-1142.

Gailer, J., George, G.N., Pickering, I.J., Buttigieg, G.A., Denton, M.B., and Glass, R.S. (2002) Synthesis, X-ray absorption spectroscopy and purification of the seleno-bis (*S*-glutathionyl) arsinium anion from selenide, arsenite and glutathione. *J Organomet Chem*, **650**, 108-113.

Gailer, J. (2007) Arsenic–selenium and mercury–selenium bonds in biology. *Coord Chem Rev*, **251**, 234–254.

Gale, J.D. (2005) GULP: Capabilities and prospects, *Z. Krist*., **220**, 552–554.

Gale, T.K., Lani, B.W., Offen, G.R. (2008) Mechanisms governing the fate of mercury in coal-fired power systems. *Fuel Process Technol*, **89**, 139-151.

George, G.N., Garrett, R.M., Prince, R.C., and Rajagopalan, K.V. (1996) The molybdenum site of sulfite oxidase: A comparison of wild-type and the cysteine 207 to serine mutant using X-ray absorption spectroscopy. *J Am Chem Soc*, **118**, 8588–8592.

George, G.N. (2000) http://ssrl.slac.stanfor.edu/exafspak.html

George, G.N., Prince, R.C., Gailer, J., Buttigieg, G.A., Denton, M.B., Harris, H.H., and Pickering, I.J. (2004) Mercury binding to the chelation therapy agents DMSA and DMPS and the rational design of custom chelators for mercury. *Chem Res Toxicol*, **17**, 999-1006.

George, G.N. and Pickering, I.J. (2007) X-ray absorption spectroscopy in biology and chemistry. In: Tsakanov, V. and Wiedmann, H. (Eds.) *Brilliant Light in Life and Material Sciences.* North Atlantic Treaty Organization: Springer.

George, G.N., Pickering, I.J., Doonan, C.J., Korbas, M., Singh, S.P, and Hoffmeyer, R. (2008) Inorganic molecular toxicology and chelation therapy of heavy metals and metalloids. *Adv Mol Toxicol*, **2**, 123–152.

George, G.N., Singh, S.P., Hoover, J., and Pickering, I.J. (2009) The chemical forms of mercury in aged and fresh dental amalgam. *Chem Res Toxicol*, **22**, 1761-1764.

George, G.N., Singh, S.P., Myers, G.J., Watson, G.E., and Pickering, I.J. (2010) The chemical forms of mercury in human hair: A study using X-ray absorption spectroscopy. *J Biol Inorg Chem*, **15**, 709-715.

George, G.N., Pickering, I.J., Pushie, M.J., Nienaber, K., Hackett, M.J., Ascone, I., Hedman, B., Hodgson, K.O., Aitken, J.B., Levina, A., Glover, C., and Lay, P.A. (2012) X-ray-induced photo-chemistry and X-ray absorption spectroscopy of biological samples. *J Synchrotron Rad* **19**, 875-886.

George, M.J. (2000) XAS-Collect: A computer program for X-ray absorption spectroscopic data acquisition *J. Synchrotron Radiat*. **7**, 283–286.

Gladyshev, V.N. (2006) Chapter 9. Selenoproteins and selenoproteomes. In. Hatfield D.L., Berry M.J., and Gladyshev V.N. (Eds.) *Selenium. Its molecular biology and role in human health.* New York: Springer.

Glatzel, P. and Bergmann, U. (2005) High resolution 1s core hole X-ray spectroscopy in 3d transition metal complexes – electronic and structural information. *Coord Chem Rev*, **249**, 65-95.

Glatzel, P., Sikora, M., Fernández-García, M. (2009a) Resonant X-ray spectroscopy to study K absorption pre-edges in 3d transition metal compounds. *Eur Phys J*, **169**, 207-214.

Glatzel, P., Sikora, M., Smolentsev, G., and Fernández-García, M. (2009b) Hard X-ray photon-in-photon-out spectroscopy. *Catal Today*, **145**, 294-299.

Global Mercury Assessment 2013: Sources, Emissions, Releases and Environmental Transport, United Nations Environment Programme, Geneva Switzerland.

Gochfield, M. (2003) Cases of mercury exposure, bioavailability, and absorption. *Ecotoxicol Environ Safe*, **56**, 174-179.

Gonzalez-Raymat, H., Liu, G., Liriano, C., Li, Y., Yin, Y., Shi, J., Jiang, G., and Cai, Y. (2017) Elemental mercury: Its unique properties affect its behavior and fate in the environment. *Environ Pollut*, **229**, 69-86.

Greenwood, M.R. (1985) Methylmercury poisoning in Iraq. An epidemiological study of the 1971-1972 outbreak. *J Appl Toxicol*, **5**, 148–159.

Grdenić, D., Korpar-Čolig, B., and Sikirica, M. (1984) Mercuretin as the condensation polymer of tris(acetoxymercuri)acetic acid. The crystal structure of $(ClHg)_3CCOOH \cdot DMSO$. *J Organomet Chem*, **276**, 1–8.

Grdenić, D., Korpar-Čolig, B., Matković-Čalogović, D., Sikirica, M., Popović, Z. (1991) Monomercurated acetic acid. The crystal structure of NO_3HgCH_2COOH. *J Organomet Chem*, **411**, 19–23.

Grégoire, D.S. and Poulain, A.J. (2016) A physiological role for Hg^{II} during phototrophic growth. *Nat Geosci*, **9**, 121-127.

Groner, P., Gillies, C.W., Gillies, J.Z., Zhang, Y., and Block, E. (2004) Microwave structural studies of organoselenium compounds 1. Microwave spectra, molecular structure, and methyl barrier to internal rotation of dimethyl diselenide. *J Mol Spectrosc*, **226**, 169-181.

Guschlbauer, W., Chantot, J.F., and Thiele, D. (1990) Four-stranded nucleic acid structures 25 years later: From guanosine gels to telomere DNA. *J Biomol Struct Dyn*, **8**, 491-511.

Guzzi, G., La Porta, C.A.M. (2008) Molecular mechanisms triggered by mercury. *Toxicol,* **244**, 1-12.

Halfpenny, J., and Small, R.W.H. (1979) Structure of (chloromercurio)acetaldehyde. *Acta Cryst. B* **35**, 1239–1241.

Hall, E.R., Pollock, C.J., Bendix, J., Collins, T.J., Glatzel, P., and DeBeer, S. (2014) Valence-to-core-detected X-ray absorption spectroscopy: Targeting ligand selectivity. *J Am Chem Soc*, **136**, 10076-10084.

Hämäläinen, K., Siddons, D.P., Hastings, J.B., and Berman, L.E. (1991) Elimination of the inner-shell lifetime broadening in X-ray-absorption spectroscopy. *Phys Rev Lett,* **67**, 2850-2853.

Hansen, K. and Stern, R.M. (1984) A survey of metal-induced mutagenicity in vitro and in vivo. *Int J Toxicol*, **3**, 381-430.

Harper, B.L. and Harris, S.G. (2008) A possible approach for setting a mercury risk-based action level based on tribal fish ingestion rates. *Environ Res*, **107**, 60-68.

Harris, H.H., Pickering, I.J., and George, G.N. (2003) The chemical form of mercury in fish. *Science*, **301**, 1203-1203.

Henke, K.R., Robertson, D., Krepps, M.K., and Atwood, D.A. (2000) Chemistry and stability of precipitates from aqueous solutions of 2,4,6-trimercaptotriazine, trisodium salt, nonahydrate (TMT-55) and mercury (II) chloride, *Water Res*, **34**, 3005-3013.

Hermann, K., Pettersson, L.G.M., Casida, M.E., Daul, C., Goursot, A., Koester, A., Proynov, E., St-Amant, A., Salahub, D.R., Carravetta, V., Duarte, H., Godbout, N., Guan, J., Jamorski, C., Leboeuf, M., Malkin, V., Malkina, O., Nyberg, M., Pedocchi, L., Sim, F., Triguero, L., and Vela, A. (2001) StoBe-deMon Code.

Hoffmeyer, R., Singh, S.P., Doonan, C.J., Ross, A.R.S., Hughes, R.J., Pickering, I.J., and George, G.N. (2006) Molecular mimicry in mercury toxicology. *Chem Res Toxicol*, **19**, 753–759.

Hohenberg, P. and Kohn, W. (1964) Inhomogeneous Electron Gas. *Phys Rev*, **136**, B864-B871.

Hoogsteen, K. (1963) The crystal structure of 1-methylthymine. *Acta Cryst*, **16**, 28-38.

Hűbner, M., Koziej, D., Grunwaldt, J.D., Weimar, U., and Barsan, N. (2012) An Au clusters related spill-over sensitization mechanism in SnO_2-based gas sensors identified by operando HERFD-XAS, work function changes, DC resistance and catalytic conversion studies. *Phys Chem Chem Phys*, **14**, 13249-13254.

Hunter, F. and Russell D.S. (1954) Focal cerebral and cerebellar atrophy in a human subject due to organic mercury compounds. *J Neurol Neurosurg Psychiat*, **17**, 235-241.

Hursh, J.B., Clarkson, T.W., Cherian, M.G., Vostal, J.J., and Mallie, R.V. (1976) Clearance of mercury (Hg-197, Hg-203) vapor inhaled by human subjects. *Arch Environ Occup Health*, **31**, 302-309.

Hussain, R.A., Badshah, A., and Shah, A. (2014) Synthesis and biological applications of selenoureas. *Appl Organomet Chem*, **28**, 61-73.

Isab, A.A. and Perzanowski, H.P. (1990) ^{1}H, ^{13}C and ^{199}Hg NMR studies of the complexation of $HgCl_2$ by imidazolidine-2-thione and its derivatives. *J Coord Chem*, **21**, 247-252.

Jacob, C., Maret, W., and Vallee, B.L. (1999) Selenium redox biochemistry of zinc-sulfur coordination sites in proteins and enzymes. *Proc Natl Acad Sci*, **96**, 1910-1914.

Jalilehvand, F., Leung, B.O., Izadifard, M., and Damian, E. (2006) Mercury(II) cysteine complexes in alkaline aqueous solution. *Inorg Chem*, **45,** 66-73.

Jalilehvand, F., Parmar, K., and Zielke, S. (2013) Mercury(II) complex formation with *N*-acetylcysteine. *Metallomics*, **5**, 1368-1376.

Johnson, C.C., Ge, X., Green, K.A., and Liu, X. (2000) Selenium distribution in the local environment of selected villages of the Keshan Disease belt, Zhangjiakou District, Hebei Province, People's Republic of China. *App Geochem*, **15**, 385-401.

Kari, G., Rodeck, U., and Dicker, A.P. (2007) Zebrafish: An emerging model system for human disease and drug discovery. *Clin Pharmacol Ther*, **82**, 70–80.

Karlsson, J., von Hofsten, J., and Olsson, P.E. (2001) Generating transparent zebrafish: A refined method to improve detection of gene expression during embryonic development. *Mar Biotechnol*, **3**, 522–527.

Kerper, L.E., Ballatori, N., and Clarkson, T.W. (1992) Methylmercury transport across the blood-brain barrier by an amino acid carrier. *Am J Physiol*, **262**, R761-R765.

Khan, M.A.K. and Wang, F. (2010) Chemical demethylation of methylmercury by selenoamino acids. *Chem Res Toxicol*, **23**, 1202-1206.

Kim, Y.O., Bae, H.J., Cho, E., and Kang, H. (2017) Exogenous glutathione enhances mercury tolerance by inhibiting mercury entry into plant cells. *Front Plant Sci*, **8**, 1-10.

Kitamura, S., Sebe, E., Hayakawa, K., Sumino, K., (1968) Side reactions accompanying catalytic hydration of acetylene. IV. Miscellaneous reactions yielding alkyl mercury compounds. *Nippon Yakurigaku Zasshi*, **64**, 531–543.

Klamt A., and Schüürmann, G. (1993) COSMO: A new approach to dielectric screening in solvents with explicit expressions for the screening energy and its gradient. *Chem Soc Perkin Trans*, **2**, 799–805.

Kleimenov, E., Bergamaschi, A., van Bokhoven, J., Janousch, M., Schmitt, B., and Nachtegaal, M. (2009) High-resolution hard-X-ray fluorescence spectrometer. *J Phys Conf Ser*, **190**, e012035/1-6.

Kleymenov, E., Sa, J., Abu-Dahrieh, J., Rooney, D., van Bokhoven, J.A., Troussard, E., Szlachetko, J., Safonova, O.V., and Nachtegaal, M. (2012) Structure of the methanol synthesis catalyst determined by *in situ* HERFD XAS and EXAFS. *Catal Sci Technol*, **2**, 373-378.

Kohn, W. and Sham, L.J. (1965a) Self-consistent equations including exchange and correlation effects. *Phys Rev A,* **140**, 1133-1138.

Kohn, W. and Sham, L.J. (1965b) Quantum density oscillations in an inhomogeneous electron gas. *Phys Rev A,* **137,** 1697-1705.

Kondo, J., Yamada, T., Hirose, C., Okamoto, I., Tanaka, Y., and Ono, A. (2014) Crystal structure of metallo DNA duplex containing consecutive Watson-Crick-like T-Hg^{II}-T base pairs. *Angewandte Chemie*, **126**, 2417-2420.

Korbas, M., Blechinger, S.R., Krone, P.H., Pickering I.J., and George, G.N. (2008) Localizing organomercury uptake and accumulation in zebrafish larvae at the tissue and cellular level. *Proc Natl Acad Sci*, 1**05**, 12108–12112.

Korbas, M., Krone, P.H., Pickering, I.J., and George, G.N. (2010a) Dynamic accumulation and redistribution of methylmercury in the lens of developing zebrafish embryos and larvae. *J Biol Inorg Chem*, **15**, 1137–1145.

Korbas, M., O'Donoghue, J.L., Watson, G.E., Pickering, I.J., Singh, S.P., Myers, G.J., Clarkson, T.W., and George, G.N. (2010b) The chemical nature of mercury in human brain following poisoning or environmental exposure. *ACS Chem Neurosci*, **1**, 810-818.

Korbas, M., MacDonald, T.C., Pickering, I.J., George, G.N., and Krone, P.H. (2012) Chemical form matters: Differential accumulation of mercury following inorganic and organic mercury exposures in zebrafish larvae. *ACS Chem Biol*, **7**, 411-420.

Korbas, M., Lai, B., Vogt, S., Gleber, S.-C., Karunakaran, C., Pickering, I.J., Krone, P.H., and George, G.N. (2013) Methylmercury targets photoreceptor outer segments. *ACS Chem Biol*, **8**, 2256–2263.

Kosturko, L.D., Folzer, C., and Stewart, R.F. (1974) The Crystal and Molecular Structure of a 2:1 Complex of 1-Methylthymine-Mercury(II). *Biochemistry*, **13**, 3949-3952.

Kotch, F.W., Fettinger, J.C., and Davis, J.T. (2000) A lead-filled G-quadruplex: Insight into the G-quartet's selectivity for Pb^{2+} over K^{+}. *Org Lett*, **2**, 3277-3280.

Krause, M.O. and Oliver, J.H. (1979) Natural widths of atomic K and L levels, Kα X-ray lines and several KLL Auger lines. *J Phys Chem Ref Data*, **8**, 329-338.

Krzyżyńska, R., Hutson, N.D., Zhao, Y., Szeliga, Z., and Regucki, P. (2018) Mercury removal and its fate in oxidant enhanced wet flue gas desulphurization slurry. *Fuel*, **211**, 876-882.

Kuehnelt, D., Juresa, D., Francesconi, K.A., Fakih, M., Reid, and M.E. (2007) Selenium metabolites in urine of cancer patients receiving L-selenomethionine at high doses. *Toxicol Appl Pharmacol.* **220**, 211-215.

Kurland, L.T., Faro, S.N., and Siedler, H. (1960) Minamata disease. The outbreak of a neurologic disorder in Minamata, Japan, and its relationship to the ingestion of seafood contaminated by mercuric compounds. *World Neurol*, **1**, 370–395.

Kvashnina, K.O., Butorin, S.M., Martin, P., and Glatzel, P. (2013) Chemical state of complex uranium oxides. *Phys Rev Lett*, **111**, e253002/1-5.

Larock, J. and Small, R.W.H. (2013) *Solvomercuration/demercuration reactions in organic synthesis*, Springer.

Leaner, J.J. and Mason, R.P. (2002) Methylmercury accumulation and fluxes across the intestine of channel catfish, *Ictalurus punctatus*. *Comp Biochem Physiol B-Biochem Mol Biol*, **132**, 247-259.

Leermakers, M., Baeyens, W., Quevauviller, P., and Horvat, M. (2005) Mercury in environmental samples: Speciation, artifacts and validation. *Trends Analyt Chem*, **24**, 383-393.

Lehmann, W. (1924) Röntgenographische untersuchungen an natürlichem und synthetischem metacinnabarit (HgS). *Z. Krystallog*, **60,** 379–413.

Li, Z., Ptak, D., Zhang, L., Walls, E. K., Zhong, W. and Leung, Y. F. (2012) Phenylthiourea specifically reduces zebrafish eye size. *PLoS ONE*, **7**, e40132.

Li, B., Zhang, Y., Ma, D., Shi, Z., and Ma, S. (2014) Mercury nano-trap for effective and efficient removal of mercury(II) from aqueous solution. *Nat Commun*, **5**, 5537/1-7.

Liang, L., Horvat, M., and Bloom, N.S. (1994) An improved speciation method for mercury by GC/CVAFS after aqueous phase ethylation and room temperature precollection. *Talanta*, **41**, 371-379.

Lieschke G.J. and Currie, P.D. (2007) Animal models of human disease: Zebrafish swim into view, *Nature Rev*, **8**, 353-367.

Lister, J.A., Robertson, C.P., Lepage, T., Johnson, S.L., and Raible, D.W. (1999) Nacre encodes a zebrafish microphthalmia-related protein that regulates neural-crest-derived pigment cell fate. *Development*, **126**, 3757–3767.

Liu, C. W.; Huang, C. C.; Chang, H. T. (2009) Highly selective DNA-based sensor for lead(II) and mercury(II) ions. *Anal. Chem*., **81**, 2383–2387.

Liu, G., Li, Z., Zhu, J., Liu, Y., Zhou, Y., and He, J. (2015) Studies on the thymine-mercury-thymine base pairing in parallel and anti-parallel DNA duplexes. *New J Chem*, **39**, 8752-8762.

Liu, H., Cai, C., Haruehanroengra, P., Yao, Q., Chen, Y., Yang, C., Luo, Q., Wu, B., Li, J., Ma, J., Sheng, J., and Gan, J. (2017) Flexibility and stabilization of Hg^{II}-mediated C:T and T:T base pairs in DNA duplex. *Nuc Acids Res*, **45**, 2910-2918.

Lu, J. and Holmgren, A. (2008) Selenoproteins. *J Biol Chem*, **284**, 723-727.

Lyons, G., Stangoulis, J., and Graham, R. (2003) High-selenium wheat: Biofortification for better health. *Nutr Res Rev*, **16**, 45-60.

MacDonald, T.C., Korbas, M., James, A.K., Sylvain, N.J., Hackett, M.J., Nehzati, S., Krone, P.H., George, G.N., and Pickering, I.J. (2015a) Interaction of mercury and selenium in the larval stage zebrafish vertebrate model. *Metallomics*, **7**, 1247-1255.

MacDonald, T.C., Nehzati, S., Sylvain, N.J., James, A.K., Korbas, M., Caine, S., Pickering, I.J., George, G.N., and Krone, P.H. (2015b) Phenylthiourea alters toxicity of mercury compounds in zebrafish larvae. *J Inorg Biochem*, **151**, 10-17.

Magos, L., Halbach, S., and Clarkson, T.W. (1977) Role of catalase in the oxidation of mercury vapor. *Biochem Pharmaco*l. **27**, 1373-1377.

Magos, L. and Clarkson, T.W. (2006) Overview of the clinical toxicity of mercury. *Ann Clin Biochem*, **43**, 257-268.

Manceau, A., Lemouchi, C., Rovezzi, M., Lanson, M., Glatzel, P., Nagy, K.L., Gautier-Luneau, I., Joly, Y., and Enescu, M. (2015) Structure, bonding, and stability of mercury complexes with thiolate and thioether ligands from high-energy XANES spectroscopy and first-principles calculations. *Inorg Chem*, **54**, 11776-11791.

Manceau, A., Enescu, M., Simionovici, A., Lanson, M., Gonzalez-Rey, M., Rovezzi, M., Tucoulou, R., Glatzel, P., Nagy, K.L., and Bourdineaud, J.P. (2016) Chemical forms of mercury in human hair reveal sources of exposure. *Environ Sci Technol*, **50**, 10721-10729.

March, A.M., Assefa, T.A., Bressler, C., Doumy, G., Galler, A., Gawelda, W., Kanter, E.P., Nemeth, Z., Papai, M., Southworth, S.H., Young, L., and Vanko, G. (2015) Feasibility of valence-to-core x-ray emission spectroscopy for tracking transient species. *J Phys Chem C*, 1**19**, 14571-14578.

Marino, T. (2014) DFT Investigation of the mismatched base pairs $(T–Hg–T)_3$, $(U–Hg–U)_3$, $d(T–Hg–T)_2$, and $d(U–Hg–U)_2$. *J. Mol. Model*, **20**, 2303/1–5.

Mason, R.P., Fitzgerald, W.F., and Morel, F.M.M. (1994) The biogeochemical cycling of elemental mercury: Anthropogenic influences. *Geochim Cosmochim Ac,* **58**, 3191-3198.

Mason, R.P., Abbott, M.L., Bodaly, R.A., Bullock, O.R., Evers, D., Lindberg, S.E., Murray, M., and Swain, E.B. (2005) Monitoring the response to changing mercury deposition. *Environ Sci Technol,* **1**, 15A-22A.

Matlock, M.M., Henke, K.R., and Atwood, D.A. (2002) Effectiveness of commercial reagents for heavy metal removal from water with new insights for future chelate design, *J Hazard Mater*, **B92**, 129-142.

Matlock, M.M., Howerton, B.S., Aelstyn, M.V., Henke K.R., and Atwood, D.A. (2003) Soft metal preferences of 1,3-benzenediamidoethanethiol, *Water Res*, 3**7**, 579-584.

McGrath, P. and Li, C.Q. (2008) Zebrafish: A predictive model for assessing drug-induced toxicity, *Drug Discov Today*, **13**, 394-401.

Melnick, J.G. and Parkin, G. (2007) Cleaving mercury-alkyl bonds: A functional model for mercury detoxification by *MerB. Science*, **317**, 225-227.

Melnick, J.G., Yurkerwich, K., and Parkin, G. (2009) Synthesis, structure, and reactivity of two-coordinate mercury alkyl compounds with sulfur ligands: Relevance to mercury detoxification. *Inorg Chem*, **48**, 6763-6772.

Minamata Convention on Mercury. (2019) www.mercuryconvention.org

Morel, F.M.M., Kraepiel, A.M.L., and Amyot, M. (1998) The chemical cycle and bioaccumulation of mercury. *Annu Rev Ecol Syst*, **29**, 543-566.

Mustre de Leon, J., Rehr, J.J., Zabinsky, S.I., and Albers, R.C. (1991) Ab initio curved-wave X-ray-absorption fine structure. *Phys Rev B*, **44**, 4146–4156.

Nandi, U. S.; Wang, J. C.; Davidson, N. (1965) Separation of Deoxyribonucleic Acids by Hg(II) Binding and Cs_2SO_4 Density-Gradient Centrifugation. *Biochemistry*, ***4***, 1687–1696.

Navarro-Alarcon, M. and Cabrera-Vique, C. (2008) Selenium in food and the human body: A review. *Sci Total Environ,* **400**, 115-141.

Nehzati, S., Dolgova, N.V., Sokaras, D., Kroll, T., Cotelesage, J.J.H., Pickering, I.J., and George, G.N. (2018) A photochemically generated selenyl free radical observed by high energy resolution fluorescence detected X-ray absorption spectroscopy. *Inorg Chem*, **57**, 10867-10876.

Neese, F. (2017) Software update: The ORCA program system, version 4.0. *WIREs Comput Mol Sci*, **8**, e1327

Nienaber, K. H., Nehzati, S., Cotelesage, J. J. H., Pickering, I. J., George, G. N. (2018) X-ray induced photoreduction of Hg(II) in aqueous frozen solution yields nearly monatomic Hg(0). *Inorg Chem*, **57**, 8205–8210.

Nishigaki, S. and Harada, M. (1975) Methylmercury and selenium in umbilical cords of inhabitants of the Minamata area. *Nature*, **258**, 324-325.

Ohlendorf, H.M., Hothem, R.L., Bunck, C.M., and Marois, K.C. (1990) Bioaccumulation of selenium in birds at Kesterson Reservoir, California. *Arch Environ Contam Toxicol*, **19**, 495-507.

Ohta, Y. and Suzuki, K.T. (2008) Methylation and demethylation of intermediates selenide and methylselenol in the metabolism of selenium. *Toxicol Appl Pharmacol*, **226**, 169-177.

Onyido, I., Norris, A.R., and Buncel, E. (2004) Biomolecule-mercury interactions: Modalities of DNA base-mercury binding mechanisms. Remediation Strategies. *Chem Rev*, **104**, 5911-5929.

Orio, M., Pantazis, D.A., and Neese, F. (2009) Density functional theory. *Photosynth Res*, **102**, 443-453.

Othmer, D.F., Kon, K., and Igarashi, T. (1948) Acetaldehyde by the Chisso process. *Ind Eng Chem*, **48**, 1258–1262.

Packer, L., Witt, E.H., and Tritschler, H.J. (1995) Alpha-lipoic acid as a biological antioxidant. *Free Radic Biol Med*, **19**, 227-250.

Pantazi, D.A., Chen, X.Y., Landis, C.R., and Neese, F. (2008) All-electron scalar relativistic basis sets for third-row transition metal atoms. *J Chem Theory Comput*, **4**, 980-919.

Parker, M.O., Brock, A.J., Millington, M.E., and Brennan, C.H. (2013) Behavioral phenotyping of Casper mutant and 1-pheny-2-thiourea treated adult zebrafish. *Zebrafish*, **10**, 466–471.

Parízek, J. and Ostádalová I. (1967) The protective effect of small amounts of selenite in sublimate intoxication. *Experientia*, **23,** 142-143.

Peak, D. (2006) Adsorption mechanisms of selenium oxyanions at the aluminum oxide/water interface. *J Colloid Interface Sci***, 303**, 337-345.

Perdew, J.P., Chevary, J.A., Vosko, S.H., Jackson, K.A., Pederson, M.R., Singh, D.J., and Fiolhais, C. (1992) Atoms, molecules, solids, and surfaces: Applications of the generalized gradient approximation for exchange and correlation. *Phys Rev B*, **46**, 6672-6687.

Perdew, J.P., Burke, K., and Ernzerhof, M. (1996) Generalized gradient approximation made simple. *Phys Rev Lett* **77**, 3865–3868; (1997) Erratum, **78**, 1396.

Peverati, R. and Truhlar, D.G. (2012) M11-L: A local density functional that provides improved accuracy for electronic structure calculations in chemistry and physics. *J Phys Chem Lett*, **3**, 117–124.

Pickering, I.J., George, G.N., Van Fleet-Stalder, V., Chasteen, T.G., and Prince, R.C. (1999) X-ray absorption spectroscopy of selenium-containing amino acids *J Biol Inorg Chem*, **4**, 791-794.

Pickering, I.J., Prince, R.C., George, M.J., Smith, R.D., Geoge, G.N., and Salt, D.E. (2000a) Reduction and coordination of arsenic in Indian mustard. *Plant Physiol*, **122**, 1171-1177.

Pickering, I.J., Prince, R.C., Salt, D.E., and George, G.N. (2000b) Quantitative, chemically specific imaging of selenium transformation in plants. *PNAS*, **97**, 10717-10722.

Pickering, I.J., Wright, C., Bubner, B., Ellis, D., Persans, M.W., Yu, E.Y., George, G.N., Prince, R.C., and Salt, D.E. (2003) Chemical form and distribution of selenium and sulfur in the selenium hyperaccumulatory *Astragalus bisulcatus*. *Plant Physiol*, **131**, 1460-1467.

Pickering, I.J., Sneeden, E.Y., Prince, R.C., Block, E., Harris, H.H., Hirsch, G., and George, G.N. (2009) Localizing the chemical forms of sulfur in vivo using X-ray fluorescence spectroscopic imaging: applications to onion (*Allium cepa*) tissues. *Biochemistry*, **48**, 6846-6853.

Pilon-Smith, E.A.H., Quinn, C.F., Taken, W., Malagoli, M., and Schiavon, M. (2009) Physiological functions of beneficial elements. *Current Opinion in Plant Biology*, **12**, 267-174.

Pires, S., Habjanič, J., Sezer, M., Soares, C.M., Hemmingsen, L., Iranzo, O. (2012) Design of a peptidic turn with high affinity for Hg^{II}. *Inorg Chem*, **51**, 11339-11348.

Pirrone, N., Cinnirella, S., Feng, X., Finkelman, R.B., Friedli, H.R., Leaner, J., Mason, R., Mukherjee, A.B., Stracher, G.B., Streets, D.G., and Telmer, K. (2010) Global mercury emissions to the atmosphere from anthropogenic and natural sources. *Atmospheric Chem Phys*, **10**, 5951-5964.

Proux, O., Lahera, E., Del Net, W., Kieffer, I., Rovezzi, M., Testemale, D., Irar, M., Thomas, S., Aguilar-Tapia, A., Bazarkina, E.F., Prat, A., Tella, M., Auffin, M., Rose, J., Hazemann, J.L. (2017) High-energy resolution fluorescence detected X-ray absorption spectroscopy: A powerful new structural tool in environmental biogeochemistry sciences. *J Environ Qual*, **46**, 1146-1157.

Puk, R. and Weber, J.H. (1994) Critical review of analytical methods for determination of inorganic mercury and methylmercury compounds. *Appl Organomet Chem*, **8**, 293-302.

Pushie, M.J., Pickering, I.J., Korbas, M., Hackett, M.J., and George, G.N. (2014) Elemental and chemical specific X-ray fluorescence imaging of biological samples. *Chem Rev*, **114**, 8499-8541.

Raldua, D. and Pina, B. (2014) In vivo zebrafish assays for analyzing drug toxicity, *Expert Opin Drug Metab Toxicol*, **10**, 685-697.

Ralston, N.V.C., Blackwell III, J.L.B., and Raymond, L.J. (2007) Importance of molar ratios in selenium-dependent protection against methylmercury toxicity. *Biol Trace Elem Res*, **119**, 255-268.

Raptis, S.E., Kaiser, G., and Tolg, G. (1983) A survey of selenium in the environment and a critical review of its determination at trace levels. *Fresenius Z Anal Chem*, **316**, 105-123.

Rappe, A. K.; Casewit, C. J.; Colwell, K. S.; Goddard III, W. A.; Skiff, W. M. (1992) UFF, a full periodic table force field for molecular mechanics and molecular dynamics simulations. *J. Am. Chem. Soc*., **114**, 10024–10035.

Rawls, J.F., Mellgren, E.M. and Johnson, S.L. (2001) How the zebrafish gets its stripes. *Dev Biol*, **240**, 301–314.

Rayman, M.P. (2012) Selenium and human health. *Lancet*, **379**, 1256-1268.

Raymond, L.J. and Ralston, N.V.C. (2004) Mercury: Selenium interactions and health implications. *Seychelles Med Dent J*, **7**, 72-77.

Rehr, J.J., Mustre de Leon, J., Zabinsky, S.I., and Albers, R.C. (1991) Theoretical X-ray absorption fine-structure standards. *J Am Chem Soc*, **113**, 5135-5140.

Rehr, J.J. and Albers, R.C. (2000) Theoretical approaches to X-ray absorption fine structure. *Rev Mod Phys*, **72**, 621-654.

Reich, H.J. and Hondal, R.J. (2016) Why nature chose selenium. *ACS Chem Bio*, **11**, 821-841.

Reith, F., Etschmann, B., Grosse, C., Moors, H., Benotmane, M.A., Monsieurs, P., Grass, G., Doonan, C., Vogt, S., Lai, B., Martinez-Criado, G., George, G.N., Nies, D.H., Mergeay, M., Pring, A., Southam, G., and Brugger, J. (2009) Mechanisms of gold biomineralization in the bacterium Cupriavidus metallidurans. *PNAS*, **42**, 17757-17762.

Roemelt, M. and Neese, F. (2013a) Excited states of large open-shell molecules: An efficient, general, and spin-adapted approach based on a restricted open-shell ground state wave function. *J Phys Chem A*, **117**, 3069-3083.

Roemelt, M., Maganas, D., DeBeer, S., and Neese, F. (2013b) A combined DFT and restricted open-shell configuration interaction method including spin-orbit coupling: Application to transition metal L-edge X-ray absorption spectroscopy. *J Chem Phys*, **138**, 204101-22.

Roman, M., Jitaru, P., and Barbante, C. (2014) Selenium biochemistry and its role for human health. *Metallomics*, **6**, 25-54.

Rooney, J.P.K. (2007) The role of thiols, dithiols, nutritional factors and interacting ligands in the toxicology of mercury. *Toxicology*, ***234***, 145-156.

Sa, J., Barrabes, N., Kleymenov, E., Lin, C., Fottinger, K., Safonova, O.V., Szlachetko, J., van Bokhoven, J.A., Nachtegaal, M., Urakawa, A., Crespo, G.A., and Rupprechter, G. (2012) The oxidation state of copper in bimetallic (Pt-Cu, Pd-Cu) catalysts during water denitration. *Catal Sci Technol*, **2**, 794-799.

SAINT and SADABS; v8.34a ed.; Bruker AXS Inc., Madison, WI, USA, 2013.

Sandhoefer, B and Neese F. (2012) One-electron contribution to the g-tensor for second-order Douglas-Kroll-Hess theory. *J Chem Phys*, **137**, 094102/1-15.

Santos, S., Ungureanu, G., Boaventura, R., and Botelho, C. (2015) Selenium contaminated waters: An overview of analytical methods, treatment options and recent advances in sorption methods. *Sci Total Environ*, **512-522**, 246-260.

Schiavon, M. and Pilon-Smits, E.A.H. (2017) The fascinating facets of plant selenium accumulation – biochemistry, physiology, evolution and ecology. *New Phytol*, **213**, 1582-1596.

Selin, N.E. (2009) Global biogeochemical cycling of mercury: A review. *Annu Rev Environ Resour*, **34**, 43-63.

Selin, H. (2014) Global environmental law and treaty-making on hazardous substances: The Minamata Convention and mercury abatement. *Global Environ Politics*, **14**, 1-19.

Sharma, S. and Uttam, K.N. (2017) Early diagnosis of mercury stress of wheat seedlings using attenuated total reflection Fourier transform infrared spectroscopy. *Anal Lett*, **51**, 1544-1563.

Sharma, V.K., McDonald, T.J., Sohn, M., Anquandah, G.A.K., Pettine, M., and Zboril, R. (2015) Biogeochemistry of selenium. A review. *Environ Chem Lett*, 1**3**, 49-58.

Sheldrick, G. M. (2008) A short history of *SHELX*. *Acta Cryst.. A*, ***64***, 112–122.

Sheldrick, G. M.; *SHELXL, Program for the Solution of Crystal Structures,* Version 2014/7, University of Göttingen, Göttingen, Germany.

Sheldrick, G.M. (2015) Crystal structure refinement with *SHELXL*. *Acta Cryst.. C*, ***71***, 3–8.

Shi, X., Fettinger, J.C., and Davis, J.T. (2001) Homochiral G-quadruplexes with Ba^{2+} but not with K^{+}: The cation programs enantiomeric self-recognition *J Am Chem Soc*, **123**, 6738-6739.

Shrift, A. (1969) Aspects of selenium metabolism in higher plants. *Annu Rev Plant Physiol*, **20**, 475-494.

Simmons-Willis, T.A., Koh, A.S., Clarkson, T.W., and Ballatori, N. (2002) Transport of a neurotoxicant by molecular mimicry: The methylmercury-L-cysteine complex is a substrate for human L-type large neutral amino acid transporter (LAT) 1 and LAT2. *Biochem J*, **367**, 239-246.

Simpson, R.B. (1964) Association constants of methylmercuric and mercuric ions with nucleosides. *J Am Chem Soc*, **86**, 2059-2065.

Smirnov, I.V., Kotch, F.W., Pickering, I.J., Davis, J.T., and Shafer, R.H. (2002) Pb EXAFS Studies on DNA Quadruplexes: Identificaiton of Metal Ion Binding Site. *Biochemistry,* **41**, 12133-12139.

Sneeden E.Y., Harris, H.H., Pickering, I.J., Prince, R.C., Johnson, S., Li, X., Block, E., George, G.N. (2004) The sulfur chemistry of shiitake mushroom. *J Am Chem Soc, **126**, 458-459.*

Sokaras, D., Weng, T.C., Nordlund, D., Alonso-Mori, R., Velikov, P., Wenger, D., Garachtchenko, A., George, M., Borzenets, V., Johnson, B., Rabedeau, T., and Bergmann, U. (2013) A seven-crystal Johann-type hard x-ray spectrometer at the Stanford Synchrotron Radiation Lightsource. *Rev Sci Inst,* **84**, 053102/1-8.

Soler- Lopez, M.; Malinina, L.; Subirana, J. A. (2000) Solvent organization in an oligonucleotide crystal. The structure of d(GCGAATTCG)2 at atomic resolution. *J Biol Chem*, **275**, 23034–23044.

Sors, T.G., Martin, C.P., and Salt, D.E. (2009) Characterization of selenocysteine methyltransferases form *Astragalus* species with contrasting selenium accumulation capacity. *Plant J,* **59**, 110-122.

Streets, D.G.; Lu, Z.; Levin, L.; ter Schure, A.F.H., Sunderland, E. M. (2018) Historical releases of mercury to air, land, and water from coal combustion. *Sci Total Environ*, **615**, 131–140.

Sugiura, Y., Tamai, Y., and Tanaka, H. (1978) Selenium protection against mercury toxicity: High binding affinity of methylmercury by selenium-containing ligands in comparison with sulfur-containing ligands. *J Inorg Biochem,* **9**, 167-180.

Sullivan-Brown, J., Bisher, M.E., and Burdine, R.D. (2011) Embedding, serial sectioning and staining of zebrafish embryos using JB-4 resin. *Nat Protoc*, **6**, 46-55.

Swanston, T., Varney, T.L., Kozachuk, M., Choudhury, S., Bewer, B., Coulthard, I., Keenleyside, A., Nelson, A., Martin, R.R., Stenton, D.R., and Cooper, D.M.L. (2018) Franklin expedition lead exposure: New insights from high resolution confocal X-ray fluorescence imaging of skeletal microstructure. *PLoS ONE*, **13**, e0202983.

Swedish Expert Group (1971) Methylmercury in fish: A toxicological-epidemiological evaluation of risks. Nord Hyg Tidskr4(suppl):19-364.

Takeuchi, T., Morikawa, N., Matsumoto, H., and Shiraishi, Y. (1962) A pathological study of Minamata Disease in Japan. *Acta Neuropathol,* **2**, 40–57.

Takeuchi, T., Eto, K., Nakayama, H., Sumiyoshi, A. (1999) The Pathology of Minamata Disease: A Tragic Story of Water Pollution. Kyushu University Press Inc.

Tanaka- Kagawa, T., Naganuma, A., and Imura, N. (1993) Tubular secretion and reabsorption of mercury compounds in mouse kidney. *J Pharmacol Exp Ther*, **264**, 776-782.

Tanzer, T. and Heumann, K.G. (1990) GC determination of dimethyl selenide and trimethyl selenonium ions in aquatic systems using element specific detection. *Atmos Environ*, **24**, 2099-2102.

Taylor, N. J. and Carty, A. J. (1977) Nature of mercury(2+) ion-L-cysteine complexes implicated in mercury biochemistry. *J. Am. Chem. Soc*., **99**, 6143–6145.

Terkhi, M.C., Taleb, F., Gossart, P., Semmoud, A., Addou, A. (2008) Fourier transform infrared study of mercury interaction with carboxyl groups in humic acids. *J Photochem Photobiol A*. **198**, 205-214.

Thanigaimalai, P., Lee, K.C., Sharma, V.K., Joo, C., Cho, W.J., Roh, E., Kim, Y., and Jung, S-H. (2011) Structural requirement of phenylthiourea analogs for their inhibitory activity of melanogenesis and tyrosinase. *Bioorg Med Chem Lett*, **21**, 6824–6828.

Thavarajah, D., Vanderberg, A., George, G.N., and Pickering, I.J. (2007) Chemical form of selenium in naturally selenium-rich lentils (*Lens culinaris* L.) from Saskatchewan *J Agric Food Chem*, **55**, 7337-7341.

Thomas, CA. (1954) The interaction of $HgCl_2$ with sodium thymonucleate. *J Am Chem Soc*, **74**, 6032-6034.

Torigoe, H., Ono, A., Kozasa, T. (2010) Hg^{II} ion specifically binds with T:T mismatched base pair in duplex DNA. *Chem Eur J*, **16**, 3218-13225.

Torres, J., Pintos, V., Gonzatto, L., Domínguez, S., Kremer, C., and Kremer, E. (2011) Selenium chemical speciation in natural waters: Protonation and complexation behavior of selenite and selenate in the presence of environmentally relevant cations. *Chem Geol*, **288**, 32-38.

Turanov, A.A., Xu, X.M., Carlson, B.A., Yoo, M.H., Gladyshev, V.N., and Hatfield, D.L. (2011) Biosynthesis of selenocysteine, the 21^{st} amino acid in the genetic code, and a novel pathway for cysteine biosynthesis. *Adv Nutr*, **2**, 122-128.

Tse, J.J., George, G.N., and Pickering, I.J. (2011) Use of soller slits to remove reference foil fluorescence from transmission spectra. *J Synchrotron Rad*, **18**, 527-529.

Uchiyama, T., Miura, T., Takeuchi, H., Dairaku, T., Komuro, T., Kawamura, T., Kondo, Y., Benda, L., Sychrovsky, V., Bour, P., Okamoto, I., Ono, A., and Tanaka, Y. (2001) Raman spectroscopic detection of the T-Hg^{II}-T base pair and the ionic characteristics of mercury. *Nuc Acids Res*, **40**, 5766-5774.

van den Berg, B.M., Nieuwdorp, M., Stroes, E.S.G., and Vink, H. (2006) Glycocalyx and endothelial (dys) function: from mice to men. *Pharmacol Rep*, **58**, 75–80.

Van Der Wijst, T., Guerra, C.F., Swart, M., Bickelhaupt, F.M., and Lippert, B. (2009) Rare tautomers of 1-methyluracil and 1-methylthymine: tuning relative stabilities through coordination to Pt^{II} complexes. *Chem Eur J*, **15**, 209-218.

Vermeulen, M., Nuyts, G., Sanyova, J., Vila, A., Buti, D., Surronen, J.P., and Janssens, K. (2016) Visualization of As(III) and As(V) distributions in degraded paint micro-samples from Baroque- and Rococo-era paintings. *J Anal At Spectrom*, **31**, 1913-1921.

Vriens, B., Ammann, A.A., Hagendorfer, H., Lenz, M., Berg, M., and Winkel, L.H.E. (2014) Quantification of methylated selenium, sulfur, and arsenic in the environment. *PLoS ONE*, **9**, e102906/1-9.

Wagida, A.A. and Gabal, M.S. (1991) Cytogenic study in workers occupationally exposed to mercury fulminate. *Mutagenesis*, **6**, 189-192.

Wang, Q., Kim, D., Dionysiou, D.D., Sorial, G.A., and Timberlake, D. (2004) Sources and remediation for mercury contamination in aquatic systems – A literature review. *Environ Pollu*, **131**, 323-336.

Watton, S.P., Wright, J.G., MacDonnell, F.M., Bryson, J.W., Sabat, M., and O'Halloran, T.V. (1990) Trigonal mercuric complex of an aliphatic thiolate: A spectroscopic and structural model for the receptor site in the Hg(II) biosensor MerR. *J Am Chem Soc*, **112**, 2924-2826.

Webb, S.M. (2016) https://www.sams-xrays.com/smak

Weigend, F. and Ahlrichs, R. (2005) Balanced basis sets of split valence, triple zeta valence and quadruple zeta valence for H to Rn: Design and assessment of accuracy. *Phys Chem Chem Phys*, **7**, 3297-3305.

Westerfield, M. (1995) The zebrafish book: a guide for the laboratory use of zebrafish (*Brachydanio rerio*). University of Oregon Press, Eugene.

White, R.M., Sessa, A., Burke, C., Bowman, T., LeBlanc, J., Ceol, C., Bourque, C., Dovey, M., Goessling, W., Burns, C.E., and Zon, L.I. (2008) Transparent adult zebrafish as a tool for in vivo transplantation analysis. *Cell Stem Cell*, **2**, 183–189.

Whittaker, J.R. (1966) An analysis of melanogenesis in differentiating pigment cells of ascidian embryos. *Dev Biol*, **14**, 1–39.

Wierzbicki, D., Baran, R., Dębek, R., Motak, M., Gálvez, M.E., Grzybek, T., Da Costa, P., Glatzel, P. (2018) Examination of the influence of La promotion on Ni state in hydrotalcite-derived catalysts under CO_2 methanation reaction conditions: Operando X-ray absorption and emission spectroscopy investigations. *Appl. Catal. B-Environ*, **232**, 409-419.

Winkel, L.H.E., Vriens, B., Jones, G.D., Schneider, L.S., Pilon-Smits, E., Baňuelos, G.S. (2015) Selenium cycling across soil-plant-atmosphere interfaces: A critical review. *Nutrients*, **7**, 4199-4239.

Wright, J.G., Tsang, H.T., Penner-Hahn, J.E., and O'Halloran, T.V. (1990) Coordination chemistry of the Hg-MerR metalloregulatory protein: Evidence for a novel tridentate mercury-cysteine receptor site. *J Am Chem Soc,* **112**, 2434-2435.

Yamaguchi, H., Sebera, J., Kondo, J., Oda, S, Komuro, T., Kawamura, T., Dairaku, T., Kondo, Y., Okamoto, I., Ono, A., Burda, J.V., Kojima, C., Sychrovsky, V., and Tanaka, Y. (2014) The structure of metallo-DNA with consecutive thymine-Hg^{II}-thymine base pairs explains positive entropy for the metallo base pair formation *Nuc Acids Res*, **42**, 4094-4099.

Yang, G., Liu, G-F., Zheng, S-L., and Chen, X-M. (2001) Synthesis and structures of dichlorotetrakis(phenylthiourea) Cadmium(II) and catena-bis(thiocyanate) bis(phenylthiourea) Cadmium(II). *J Coord Chem*, **53**, 269–279.

Yang, L., Ho, N.Y., Alshut, R., Legradi, J., Weiss, C., Reischl, M., Mikut, R., Liebel, U., Müller, F., and Strähle, U. (2009) Zebrafish embryos as models for embryotoxic and teratological effects of chemicals. *Reprod Toxicol,* **28**, 245–253.

Yano, J. and Yachandra, V.K. (2009) X-ray absorption spectroscopy, *Photosynth Res*, **102**, 241-254.

Yokoyama, Y., 2018. *Mercury Pollution in Minamata* (Springer Briefs in Environmental Science, Springer.

Zahir, F., Rizwi, S.J., Haq, S.K., and Khan, R.H. (2005) Low dose mercury toxicity and human health. *Environ Toxicol Pharmaco,* **20**, 351-360.

Zaman, K.M., Blue, L.Y., Huggins, F.E., and Atwood, D.A. (2007) Cd, Hg, and Pb compounds of benzene-1,3-diamidoethanethiol ($BDETH_2$). *Inorg Chem*, **46**, 1975-1980.

Zhang, H., Feng, X., Chan, H.M., and Larssen, T. (2013) New insights into traditional health risk assessments of mercury exposure: Implications of selenium. *Env Sci Tech,* **48**, 1206-1212.

Zhao, Q.X., Chen, Y.W., Montaut, S., Joly, H.A., Wang, M., and Belzile, N. (2010) Synthesis, identification and chemical features of high-purity trimethylselenonium iodide. *J Sulfur Chem*, **31**, 373-385.

APPENDICES

Appendix A: Supplementary Information for Chapter 4

Table A.1. Statistical significance values for comparison of deaths in $HgCl_2$ versus $HgCl_2$ with phenylthiourea groups.

	2 µM $HgCl_2$ *vs* 2 µM $HgCl_2$ + 100 µM PTU	**4 µM $HgCl_2$ *vs* 4 µM $HgCl_2$ + 100 µM PTU**
Day 1	$P < 0.001$	$P < 0.0001$
Day 2	$P < 0.0001$	$P < 0.0001$
Day 3	$P < 0.0001$	$P < 0.0001$

Table A.2. Statistical significance values for comparison of deaths in CH_3HgCl versus CH_3HgCl with phenylthiourea groups.

	0.5 µM CH_3HgCl *vs* 0.5 µM CH_3HgCl + 100 µM PTU
Day 1	Not significant
Day 2	$P < 0.0001$
Day 3	$P < 0.0001$

Table A.3. *T*-test values.

	4 µM $HgCl_2$	**4 µM $HgCl_2$ + PTU**	**0.2 µM CH_3HgCl + PTU**	**0.2 µM CH_3HgCl + PTU**
Fish 1	0.1297	0.002200	0.04589	0.07668
Fish 2	0.1225	0.00161	0.06792	0.12224
Fish 3	0.1132	0.00234	0.05066	0.08737
Mean	0.1218	0.00198	0.05482	0.09421
P value	0.001662		0.028974	

Appendix B: Supplementary Information for Chapter 8

Table B.1. Crystal data and structure refinement.

Hg-*bis*(1-methylthymine)				
Empirical formula	C12 H14 Hg N4 O4		**Crystal size**	0.190 x 0.070 x 0.040 mm^3
Formula weight	478.86		**Theta range for data collection**	3.065 to 27.438°
Temperature	173(2) K		**Index ranges**	$-5 \leq h \leq 5$, $-11 \leq k \leq 15$, $-17 \leq l \leq 16$
Wavelength	0.71073 Å		**Reflections collected**	6670
Crystal system	Monoclinic		**Independent reflections**	1560 [R(int) = 0.0172]
Space group	$P2_1/c$		**Completeness to theta = 25.242°**	99.90%
Unit cell dimensions	a = 4.3903(2) Å	α = 90°	**Absorption correction**	Multi-scan
	b = 11.7232(4) Å	β = 91.5640(10)°	**Refinement method**	Full-matrix least-squares on F2
	c = 13.2976(5) Å	γ = 90°	**Data / restraints / parameters**	1560 / 0 / 99
Volume	684.15(5) $Å^3$		**Goodness-of-fit on F2**	1.193
Z	2		**Final R indices [I > 2sigma(I)]**	R1 = 0.0124, wR2 = 0.0272
Density (calculated)	2.325 mg/m^3		**R indices (all data)**	R1 = 0.0147, wR2 = 0.0280
Absorption coefficient	11.271 mm^{-1}		**Largest diff. peak and hole**	0.455 and -0.364 $e.Å^{-3}$
F(000)	452			

Table B.2. Atomic coordinates (x 10^4) and equivalent isotropic displacement parameters ($Å^2$x 10^3) for Hg-*bis*(1-methylthymine. U (eq) is defined as one third of the trace of the orthogonalized U^{ij} tensor. Anisotropic displacement parameters ($Å^2$x 10^3) for Hg-*bis*(1-methylthymine. The anisotropic displacement factor exponent takes the form: $-2p^2$ [h2 $a^{*2}U^{11}$ + ... + 2 h k a* b* U^{12}].

	x	y	z	U(eq)	U^{11}	U^{22}	U^{33}	U^{23}	U^{13}	U^{12}
Hg(1)	5000	5000	5000	15(1)	17(1)	16(1)	13(1)	3(1)	1(1)	-2(1)
N(1)	9521(5)	7465(2)	3284(2)	21(1)	21(1)	18(1)	23(1)	5(1)	2(1)	0(1)
O(2)	10035(4)	6770(2)	4908(1)	24(1)	27(1)	28(1)	18(1)	0(1)	-4(1)	-4(1)
N(3)	6614(4)	5924(2)	3845(1)	15(1)	18(1)	15(1)	13(1)	4(1)	2(1)	-2(1)
O(4)	3274(4)	5001(2)	2810(1)	26(1)	28(1)	22(1)	27(1)	-2(1)	-3(1)	-7(1)
C(2)	8814(5)	6722(2)	4063(2)	17(1)	18(1)	16(1)	19(1)	1(1)	3(1)	3(1)
C(4)	5234(5)	5742(2)	2910(2)	17(1)	19(1)	14(1)	18(1)	0(1)	1(1)	5(1)
C(5)	6223(5)	6474(2)	2123(2)	16(1)	19(1)	16(1)	14(1)	4(1)	1(1)	3(1)
C(6)	8243(5)	7310(2)	2342(2)	20(1)	21(1)	20(1)	19(1)	8(1)	3(1)	4(1)
C(9)	11559(6)	8440(2)	3503(2)	26(1)	25(1)	22(1)	32(1)	7(1)	-1(1)	-4(1)
C(10)	4916(6)	6297(3)	1083(2)	28(1)	34(1)	33(2)	17(1)	5(1)	-3(1)	2(1)
H(6)	8806	7814	1819	24						
H(9A)	11856	8877	2885	39						
H(9B)	13531	8158	3761	39						
H(9C)	10644	8932	4008	39						
H(10A)	5560	6921	647	42						
H(10B)	2686	6285	1104	42						
H(10C)	5644	5570	817	42						

Table B.3. Bond-lengths for Hg-*bis*(1-methylthymine).

Atoms	Bond-lengths (Å)
Hg(1)-N(3)	2.0235(18)
Hg(1)-N(3)#1	2.0235(18)
O(2)-C(2)	1.233(3)
O(4)-C(4)	1.228(3)
N(1)-C(6)	1.371(3)
N(1)-C(2)	1.395(3)
N(1)-C(9)	1.475(3)
N(3)-C(2)	1.370(3)
N(3)-C(4)	1.384(3)
C(4)-C(5)	1.431(3)
C(5)-C(6)	1.348(3)
C(5)-C(10)	1.497(3)
C(6)-H(6)	0.9500
C(9)-H(9A)	0.9800
C(9)-H(9B)	0.9800
C(9)-H(9C)	0.9800
C(10)-H(10A)	0.9800
C(10)-H(10B)	0.9800
C(10)-H(10C)	0.9800

#1 -x+1, -y+1, -z+1 symmetry transformations

Table B.4. Bond angles for Hg-*bis*(1-methylthymine).

Atoms	Angles (°)
N(3)-Hg(1)-N(3)#1	180.0
C(6)-N(1)-C(2)	120.1(2)
C(6)-N(1)-C(9)	121.0(2)
C(2)-N(1)-C(9)	118.9(2)
C(2)-N(3)-C(4)	125.74(19)
C(2)-N(3)-Hg(1)	117.67(15)
C(4)-N(3)-Hg(1)	116.45(15)
O(2)-C(2)-N(3)	120.7(2)
O(2)-C(2)-N(1)	123.2(2)
N(3)-C(2)-N(1)	116.1(2)
O(4)-C(4)-N(3)	119.7(2)
O(4)-C(4)-C(5)	124.8(2)
N(3)-C(4)-C(5)	115.5(2)
C(6)-C(5)-C(4)	119.3(2)
C(6)-C(5)-C(10)	122.3(2)
C(4)-C(5)-C(10)	118.5(2)
C(5)-C(6)-N(1)	123.0(2)
C(5)-C(6)-H(6)	118.5
N(1)-C(6)-H(6)	118.5
N(1)-C(9)-H(9A)	109.5
N(1)-C(9)-H(9B)	109.5
H(9A)-C(9)-H(9B)	109.5
N(1)-C(9)-H(9C)	109.5
H(9A)-C(9)-H(9C)	109.5
H(9B)-C(9)-H(9C)	109.5
C(5)-C(10)-H(10A)	109.5
C(5)-C(10)-H(10B)	109.5
H(10A)-C(10)-H(10B)	109.5
C(5)-C(10)-H(10C)	109.5
H(10A)-C(10)-H(10C)	109.5

#1 -x+1, -y+1, -z+1 symmetry transformations